ISTANBUL TECHNICAL UNIVERSITY ★ GRADUATE SCHOOL OF SCIENCE ENGINEERING AND TECHNOLOGY

DESIGN, ANALYSIS AND VERIFICATION OF CONVENTIONAL AND NON-CONVENTIONAL CYLINDRICAL CFRP COMPOSITE SHELL WITH OPTIMIZED CUTOUT UNDER THE EFFECT OF COMBINED LOADING

Ph.D. THESIS

Mansur ÇELEBİ

Aeronautics and Astronautics Engineering Department

Aeronautics and Astronautics Engineering

AUGUST 2017

ISTANBUL TECHNICAL UNIVERSITY ★ GRADUATE SCHOOL OF SCIENCE ENGINEERING AND TECHNOLOGY

DESIGN, ANALYSIS AND VERIFICATION OF CONVENTIONAL AND NON-CONVENTIONAL CYLINDRICAL CFRP COMPOSITE SHELL WITH OPTIMIZED CUTOUT UNDER THE EFFECT OF COMBINED LOADING

Ph.D. THESIS

Mansur ÇELEBİ
(511092116)

Aeronautics and Astronautics Engineering Department

Aeronautics and Astronautics Engineering

Thesis Advisor: Prof. Dr. Halit Süleyman TÜRKMEN
Co-advisor: Prof. Dr. Zafer GÜRDAL

AUGUST 2017

İSTANBUL TEKNİK ÜNİVERSİTESİ ★ FEN BİLİMLERİ ENSTİTÜSÜ

ÜZERİNDE KESİTLER OLAN GELENEKSEL VE GELENEKSEL OLMAYAN SİLİNDİRİK KARBON FİBER KOMPOZİT POLİMER KABUĞUN BİLEŞİK YÜKLEME ALTINDA TASARIM, ANALİZ VE DOĞRULANMASI

DOKTORA TEZİ

Mansur ÇELEBİ
(511092116)

Uçak ve Uzay Mühendisliği Anabilim Dalı

Uçak ve Uzay Mühendisliği

Tez Danışmanı: Prof. Dr. Halit Süleyman TÜRKMEN
Eş Danışman: Prof. Dr. Zafer GÜRDAL

AĞUSTOS 2017

Mansur ÇELEBİ, a Ph.D. student of ITU Graduate School of Science Engineering and Technology 511092116 successfully defended the thesis entitled "DESIGN, ANALYSIS AND VERIFICATION OF CONVENTIONAL AND NON-CONVENTIONAL CYLINDRICAL CFRP COMPOSITE SHELL WITH OPTIMIZED CUTOUT UNDER THE EFFECT OF COMBINED LOADING", which he/she prepared after fulfilling the requirements specified in the associated legislations, before the jury whose signatures are below.

Thesis Advisor :	**Prof. Dr. Halit Süleyman TÜRKMEN** Istanbul Technical University	.....
Co-advisor :	**Prof. Dr. Zafer GÜRDAL** University of South Carolina	.....
Jury Members :	**Prof. Dr. Zahit MECİTOĞLU** Istanbul Technical University	.....
	Prof. Dr. Vedat Ziya DOĞAN Istanbul Technical University	.....
	Prof. Dr. Mehmet YILDIZ Sabancı University	.....
	Assoc. Prof. Dr. Bahattin KOÇ Sabancı University	.....
	Assist. Prof. Dr. Özge ÖZDEMİR Istanbul Technical University	.....

Date of Submission : **29 July 2017**
Date of Defense : **18 August 2017**

To my wife Burcu and sweety daughter İpek,

FOREWORD

My Ph.D. study has been a very long and exhausting period of my life. On the other hand, I have met and interacted many respectable and valued people from whom I learned a lot. I really like to thank to all the contributing people for their support and guidance, although, it will not be possible to mention everyone individually.

I would like to first start with my advisor and motivator Prof.Dr. Süleyman Halit Türkmen who motivated me to start to work on laminated composite materials which were always very attractive to me. The laminated composites were whole different world with new areas to discover. Dr. Türkmen always supported and motivated me throughout all my works.

The other very important person is my co-advisor Prof.Dr. Zafer Gürdal from University of South Carolina and director of McNAIR Aerospace Center. When I was in search of finding an institute to perform manufacturing and testing of specimens about my study, I decided to contact to Dr. Gürdal who is one of the best known academicians in the field of composite materials. He accepted me as a researcher in McNAIR center to work on mechanical and failure analysis of carbon fiber composite cylindrical shells. All I can say in short, without Dr. Gürdal it would not be possible to complete my thesis within that period of time. In addition to that, I was also motivated more with being involved in a project that was funded by The Boeing Company. My thesis mostly composed of part of the project. Therefore, I would like to thank also to Dr. Agnes Blom-Schieber, Mostafa Rassaian and Steven Wanthal from The Boeing Company for their critical comments and questions that improved the quality of my work.

Specifically, Dr. Agnes Blom-Schieber's thesis and studies became a very important basis for my study. Therefore, Dr. Blom-Schieber contributed a lot to my study and I am graceful for making my Ph.D. work such a success.

Dr. Brian Tatting has a special importance in my Ph.D. work. I really enjoyed all our discussions, both related to my thesis and the general engineering and the personal discussions. Brian, I learned a lot from you and thank you very much for all the effort you set forth.

Special thanks to Prof. Dr. Chiara Bisagni, Chairholder of Aerospace Structures and Computational Mechanics and Dr. Edgars Labans from Delft University of Technology (TU Delft) for performing the bending tests in their facilities.

I would like to express my gratitude to my thesis committee members Prof.Dr Zahit Mecitoğlu, Prof Dr. Vedat Ziya Doğan, Prof.Dr. Mehmet Yıldız for the fruitful discussions and for the advices they gave me over the course of my study.

Another person whom I can not pass without mentioning is Mr. Özdemir Bayraktar from Baykar Technologies. He gave me great support to manufacture composite specimen parts and testing tools in his company. I am very grateful for his support and informative discussions we made.

I would like to also thank to Dr. Carlos Davila from NASA Langley Research Center and Dr. Claudia Lopez from IMDEA about their comments on progressive failure analysis that enriched my work.

ITU research assistant Dr. Erdem Akay and Lab. Tech. Müslüm Çakır, I would like to also thank you for your support and assistance during my manufacturing and tests in ITU labratories.

Finally, I would like to present my appreciation to all my family members who always trusted and believed in me during my long period of Ph.D. study. Especially, my wife Burcu and my tactful daughter İpek, you always have become very patient and respectful. My parents Şimşat and Mehmet Çelebi, and all my family members thank you very much for all your support and encouragements.

August 2017 Mansur ÇELEBİ

TABLE OF CONTENTS

Page

FOREWORD ..... **x**
TABLE OF CONTENTS ..... **xi**
ABBREVIATIONS ..... **xv**
SYMBOLS ..... **xvii**
LIST OF TABLES ..... **xix**
LIST OF FIGURES ..... **xxi**
SUMMARY ..... **xxvii**
ÖZET ..... **xxxi**
1. INTRODUCTION **1**
1.1 Purpose of Thesis 2
1.2 Literature Review 6
1.3 Hypothesis 14
2. NON-CONVENTIONAL CFRP COMPOSITES **15**
2.1 Fiber Placement Technology 16
2.2 Variable Stiffness Laminate Design and Manufacturing Constraints 19
2.2.1 Turning radius of the course 19
2.2.2 Tow cut length 20
2.2.3 Coverage parameter 20
2.3 Construction and Manufacturing of Variable Stiffness Laminates 21
2.3.1 Coordinate definition on a cylinder 22
2.4 Ply Construction Methods 27
2.4.1 Parallel ply construction method 27
2.4.2 Shifted ply construction method 28
2.4.2.1 Tow-drop and overlap ply construction methods 28
2.4.2.2 Point-wise ply construction method 29
3. PROGRESSIVE FAILURE ANALYSIS **31**
3.1 Multicontinuum Theory 32
3.2 The Nonlinear Analysis Method 35
4. FINITE ELEMENT ANALYSIS CASES AND FORMAT OF RESULTS **37**
4.1 Cylinder Geometry and Cutout Configurations 37
4.1.1 Basic Shell Geometry 37
4.1.2 Cutout Size and Configurations 38
4.2 Modeling and meshing 39
4.3 Analysis options 43
4.4 Presentation of analysis results 44
5. BENDING ANALYSIS OF CONSTANT STIFFNESS CYLINDRICAL SHELL WITH CUTOUTS AT 90° POSITION UNDER BENDING **47**

5.1 Linear Buckling and Nonlinear Failure Analysis for Various Cutout Sizes... 47
5.2 Imperfection Analysis 49
5.3 Non-Linear Analysis of the Cylindrical Shell with Cutouts and Imperfection 53
5.4 Non-Linear Analysis Results at the Cutout Edge 58
6. BUCKLING AND STRENGTH ANALYSIS OF CONSTANT STIFFNESS SHELL WITH CUTOUTS UNDER BENDING 61
6.1 Baseline Case Examples 61
6.1.1 Non-linear analysis of non-cutout cylindrical shell 61
6.2 Failure Mode Classifications for Cutouts 62
6.2.1 Failure mode I 63
6.2.2 Failure mode II 64
6.2.3 Failure mode III 67
6.3 Design Study Results 69
6.3.1 Eigenvalue analysis 69
6.3.2 Failure limits and mode designations 71
6.4 Extended Analysis of Cylindrical Shell with Cutouts 74
6.4.1 Eigenvalue and failure mode analysis 74
6.4.2 Imperfection investigation 77
6.4.3 Extended design study results 79
6.4.4 Discussion on $\pm 75^{\circ}$ location 81
6.5 Cutout Recommendation Considerations 83
7. BUCKLING AND STRENGTH ANALYSIS OF VARIABLE STIFFNESS SHELL WITH CUTOUTS UNDER BENDING 87
7.1 Geometry and Variation Definition 87
7.2 Implementation within FEM Solution 89
7.3 Baseline Case Comparison 91
7.4 Variable Stiffness Design Study Results 93
7.4.1 Cutout configurations 93
7.4.2 Eigenvalue analysis 94
7.4.3 Failure limits and mode designations 96
7.5 Cutout Configuration for Testing 99
8. BUCKLING AND STRENGTH ANALYSIS OF CONSTANT STIFFNESS AND VARIABLE STIFFNESS CYLINDRICAL SHELLS UNDER COMBINED LOADING 103
8.1 Loading Conditions 103
8.1.1 Pure bending moment 104
8.1.2 Vertical shear force 107
8.2 Combined Bending Moment and Vertical Shear Force Loading 113
8.2.1 Combined Loading Results 117
9. BENDING TEST 121
9.1 Test Setup 121
9.2 Machining and Inspection of the Cutouts 123
9.2.1 Specimen Preparation and Installation 127
9.2.2 Bending moment calculation 129
9.2.3 Measurement of the displacements 130

9.2.4 Measurement of the geometric imperfections 131
9.3 Instrumentation and Data Acquisition 134
9.4 Test Procedure 137
9.5 Finite Element Predictions 137
9.6 Test Results 141
9.6.1 Strain Results 145
10. CONCLUSIONS AND RECOMMENDATIONS 151
10.1 Practical Application of This Study 155
REFERENCES 157
APPENDICES 163
APPENDIX A: CS Cylinder Linear Buckling Results for Cutout Configurations 165
APPENDIX B: CS, 0.1R Cutout Analysis Results 167
APPENDIX C: CS, 0.3R Cutout Analysis Results 177
APPENDIX D: CS, 0.5R Cutout Analysis Results 187
APPENDIX E: CS, 0.3R Cutout Detail Analysis Results 197
APPENDIX F: CS, 0.4R Cutout Detail Analysis Results 203
APPENDIX G: CS, 0.5R Cutout Detail Analysis Results 209
APPENDIX H: CS, 0.6R Cutout Detail Analysis Results 215
APPENDIX I: The Centroid Calculation of the Elements 221
APPENDIX J: VS Cylinder Linear Buckling Results for Cutout Configurations 223
APPENDIX K: VS, 0.1R Cutout Analysis Results 227
APPENDIX L: VS, 0.3R Cutout Analysis Results 237
APPENDIX M: VS, 0.5R Cutout Analysis Results 247
APPENDIX N: Drawing for Machining of Planned Cutout Configurations 257

ABBREVIATIONS

AFP : Automated Fiber Placement
CC : Circular Cutout
CFRP : Carbon Fiber Reinforced Polymer
CS : Constant-Stiffness
CDM : Continuum Damage Mechanics
DIC : Digital Image Correlation
FEA : Finite Element Analysis
FEM : Finite Element Modeling
FAA : Faculty of Aeronautics and Astronautics
FL : Failure Load
FPFF : First Ply Fiber Failure
FRP : Fiber Reinforced Polymer
IMP : Imperfection
ITU : Istanbul Technical University
LVDT : Linear Variable Differential Transformer
LwPFA : Linear Progressive Failure Analysis
NDT : Non-Destructive Testing
NLwPFA : Nonlinear Progressive Failure Analysis
PFA : Progressive Failure Analysis
SHM : Structural Health Monitoring
TU Delft : Technology University of Delft
USC : University of South Carolina
UTM : Universal Testing Machine
VS : Variable-Stiffness

SYMBOLS

A	**:** Cutout size
E	**:** Modulus of Elasticity
M	**:** Bending Moment
β	**:** Cutout location
θ	**:** Circumferential position of the fibers
R	**:** Radius of the shell
t	**:** Ply thickness
κ	**:** Curvature of the steered fibers
ρ	**:** Density
σ_x, σ_y, $\sigma_{x,y}$	**:** Shell internal stresses
ξ	**:** The fiber path normal
ε	**:** Strain
λ	**:** Eigenvalue
γ	**:** Load proportionality factor
α	**:** End rotation
φ	**:** Fiber angle orientation at θ circumferential position rotation

LIST OF TABLES

Page

Table 4.1 : IM7/8552 (190 g/m^2) Lamina Mechanical Properties **38**
Table 4.2 : Buckling analysis of non-cutout cylindrical shell with given mesh sizes. **41**
Table 5.1 : Buckling analysis of cylindrical shell with cutouts at $\pm 90^{\circ}$. **48**
Table 6.1 : Critical buckling mode summary for initial set of cutout configurations. **69**
Table 6.2 : Failure mode summary for initial set of cutout configurations. **71**
Table 6.3 : Eigenvalue analysis with respect to cutout positions (view from bottom of the cylinder. **75**
Table 6.4 : Linear eigenvalue results (view from bottom of the cylinder). **78**
Table 6.5 : NLwPFA results (0.3R/105). **78**
Table 6.6 : NLwPFA results (0.4R/90). **79**
Table 6.7 : NLwPFA results (0.5R/90). **79**
Table 6.8 : NLwPFA Failure Modes. **80**
Table 6.9 : Linear Buckling Modes. **80**
Table 6.10 : Detail NLwPFA Failure Modes. **80**
Table 6.11 : Detail Critical Buckling Modes. **80**
Table 6.12 : Linear eigenvalue results (view from bottom of the cylinder). **82**
Table 6.13 : NLwPFA results (0.7R/75). **83**
Table 7.1 : Fiber orientation angle value for the VS cylinder design. **89**
Table 7.2 : Critical buckling mode summary for VS cutout configurations. **95**
Table 7.3 : Critical buckling mode summary for CS cutout configurations. **96**
Table 7.4 : Failure mode summary for VS cylinder cutout configurations. **96**
Table 8.1 : Critical buckling and failure mode summary for 0.3R cutout configurations under constant vertical shear force only. **118**
Table 8.2 : Critical buckling and failure mode summary for 0.3R cutout configurations under $R_L = 0.2$ load ratio combined loading. **118**
Table A.1 : Eigenvalue and mode shapes according to cutout positions. **165**
Table A.2 : Eigenvalue and mode shapes according to cutout positions (cont.). .. **166**
Table J.1 : VS cylinder eigenvalue and mode shapes for cutout positions. **223**
Table J.2 : VS cylinder eigenvalue and mode shapes for cutout positions (cont.) **224**
Table J.3 : VS cylinder eigenvalue and mode shapes for cutout positions (cont.) **225**

LIST OF FIGURES

Page

Figure 1.1 : Airplanes by percentage of composite and materials in Boeing 787 [1]. **2**
Figure 1.2 : Boeing 787 Structure [2]. **3**
Figure 1.3 : One-piece composite barrel construction in Boeing 787 [2]. **3**
Figure 1.4 : Rear Fuselage of Boeing 787 [2]. **4**
Figure 1.5 : MTS Test Bench with the bending fixture [3]. **6**
Figure 2.1 : Fiber-steered panels built by Tatting and Gürdal in 2002 [4]. **15**
Figure 2.2 : Gentry type automated fiber placement machine. **17**
Figure 2.3 : A view of an Ingersoll AFP machine, mandrel and the head in McNAIR Center. **18**
Figure 2.4 : Tow placement process. **18**
Figure 2.5 : Gaps and overlaps between four courses. **19**
Figure 2.6 : Straight-line orientation with respect to fabrication coordinates [5] **23**
Figure 2.7 : Axes rotation for stiffness variation definition [6] **23**
Figure 2.8 : Cylindrical surface path coordinate definition. **25**
Figure 2.9 : Coordinate transformation from cylindrical surface **25**
Figure 2.10 : Laminate construction by shifting courses [7]. **26**
Figure 2.11 : Effective course width definition. **26**
Figure 2.12 : Depiction of the parallel method ply [8]. **27**
Figure 2.13 : Shifted configuration for courses with gaps and overlaps [8]. **28**
Figure 2.14 : Contours of fiber orientation angles for tow drop method [8]. **29**
Figure 2.15 : Point-wise method [8]. **30**
Figure 3.1 : Multi-continuum Theory approach [9]. **33**
Figure 3.2 : The proportional loading with unstable response [10]. **35**
Figure 4.1 : Cylinder Geometry. **38**
Figure 4.2 : Cutout configuration possibilities and example geometry (0.3R/45) **39**
Figure 4.3 : S4 and S4R elements. **40**
Figure 4.4 : Mesh Size Convergence. **40**
Figure 4.5 : Example section view and finite element mesh for 0.3R/45 cutout configuration. **42**
Figure 4.6 : Finite element solutions for non-cutout case. **45**
Figure 5.1 : Buckling moment and strength results for given cutout dimensions **49**
Figure 5.2 : Percent decrease in the buckling moment due to increase in the cutout dimension. **49**
Figure 5.3 : The rotation of the end plates with varying imperfections in bending **51**
Figure 5.4 : Top and bottom node locations. **51**
Figure 5.5 : The displacement of the top mid node in the vertical direction. **52**

Figure 5.6 : The displacement of the bottom mid node in the vertical direction. **52**
Figure 5.7 : The percent deflection difference between the bottom and top nodes of the cylinder per cylinder radius. **53**
Figure 5.8 : The axial strain values of the upper mid node. **53**
Figure 5.9 : The axial strain values of the bottom mid node. **54**
Figure 5.10 : The transverse strain values of the upper mid node. **54**
Figure 5.11 : The transverse strain values of the bottom mid node. **55**
Figure 5.12 : The rotation of the end plates under the effect of the bending load **55**
Figure 5.13 : The axial strain values of the top mid node. **56**
Figure 5.14 : The axial strain values of the bottom mid node. **56**
Figure 5.15 : The transverse strain values of the upper mid node. **57**
Figure 5.16 : The transverse strain values of the bottom mid node. **57**
Figure 5.17 : The displacement of the upper mid node in the vertical direction. .. **57**
Figure 5.18 : The displacement of the lower mid node in the vertical direction. .. **58**
Figure 5.19 : The percentage deflection difference between the bottom and top nodes of the cylinder normalized per cylinder radius. **58**
Figure 5.20 : Top and Bottom Nodes of the Cutout Edge. **59**
Figure 5.21 : The axial strain values of the top and bottom mid nodes. **59**
Figure 5.22 : The transverse strain values of the top and bottom mid nodes. **60**
Figure 5.23 : The top and bottom nodes displacement in the x direction **60**
Figure 6.1 : Finite element solutions for non-cutout case. **62**
Figure 6.2 : Demonstration of Mode I failure. **63**
Figure 6.3 : 0.1R/60 cutout failure initiation and ultimate failure depiction (Mode I). **64**
Figure 6.4 : Demonstration of Mode II failure. **65**
Figure 6.5 : Demonstration of Mode II failure (close-up view). **66**
Figure 6.6 : 0.3R/105 cutout failure initiation and ultimate failure (Mode II)..... **66**
Figure 6.7 : Demonstration of Mode III failure. **67**
Figure 6.8 : Demonstration of Mode III failure (close-up view). **68**
Figure 6.9 : 0.5R/0 cutout failure initiation and ultimate failure views (Mode III). **68**
Figure 6.10 : Critical eigenvalues vs. cutout position for representative cutout sizes. **70**
Figure 6.11 : Failure loads versus cutout position β for representative cutout sizes. **72**
Figure 6.12 : Nonlinear analysis results with and without progressive failure. **73**
Figure 6.13 : Detail Linear Buckling and NL with PFA Results. **76**
Figure 6.14 : Linear Buckling and NL with PFA Results. **81**
Figure 6.15 : Suggested cutout configuration. **84**
Figure 7.1 : The cylinder with circumferential variation of fiber orientation angle [7]. **88**
Figure 7.2 : Contour plots of the fiber orientation angles for the three VS plies. **91**
Figure 7.3 : Ply angle variations shown in Blom's study [11]. **91**
Figure 7.4 : Finite element solutions for VS non-cutout case. **92**
Figure 7.5 : Cutout configuration possibilities and example geometry (0.3R/45) **94**

Figure 7.6 : Critical eigenvalues versus cutout position for representative cutout sizes. **95**
Figure 7.7 : Failure loads versus cutout position β for representative cutout sizes. **97**
Figure 7.8 : Failure loads versus cutout position β for 0.1R cutout size. **98**
Figure 7.9 : Failure loads versus cutout position β for 0.3R cutout size. **98**
Figure 7.10: Failure loads versus cutout position β for 0.5R cutout size. **99**
Figure 7.11: Recommended cutout configuration. **100**
Figure 7.12: Detailed results for 0.3R/120 cutout configurations. **100**
Figure 8.1 : Combined Loading Configuration. **103**
Figure 8.2 : Boundary and Loading Conditions. **104**
Figure 8.3 : CS shell failure and buckling loads for 0.3R size cutouts under pure bending **105**
Figure 8.4 : VS shell failure and buckling loads for 0.3R size cutouts under pure bending **105**
Figure 8.5 : Nonlinear PFA load/end vertical displacement curve. **106**
Figure 8.6 : CS shell failure and buckling loads for 0.3R size cutouts under shear force. **107**
Figure 8.7 : VS shell failure and buckling loads for 0.3R size cutouts under shear force. **108**
Figure 8.8 : Load/displacement curve for non-cutout CS shell under vertical shear force. **109**
Figure 8.9 : Load/displacement curve for 0.3R/45 cutout, CS shell under vertical shear force. **110**
Figure 8.10: Load/displacement curve for 0.3R/90 cutout, CS shell under vertical shear force. **111**
Figure 8.11: Load/displacement curve for 0.3R/180 cutout, CS shell under vertical shear force. **112**
Figure 8.12: Normalized combined loading results for 0.3R/90 cutout case. **114**
Figure 8.13: CS shell $R_L = 0.2$ combined load ratio for 0.3R cutout cases. **115**
Figure 8.14: VS shell $R_L = 0.2$ combined load ratio for 0.3R cutout cases. **115**
Figure 8.15: CS shell $R_L = 0.2$ combined load ratio for 0.3R/90 cutout position **116**
Figure 8.16: CS shell $R_L = 1.0$ combined load ratio for 0.3R/90 cutout position **117**
Figure 9.1 : Manufacturing of cylindrical shells (Photo courtesy of A. Blom). .. **122**
Figure 9.2 : MTS test bench. **122**
Figure 9.3 : Test fixture. **123**
Figure 9.4 : Planned cutout configurations. **124**
Figure 9.5 : Dimensions of cut-outs of the CS cylinder. **124**
Figure 9.6 : Dimensions of cut-outs of the VS cylinder. **125**
Figure 9.7 : Pulled fibres near the cut-out 1 for VS cylinder. **125**
Figure 9.8 : Inner side of the VS cylinder. **126**
Figure 9.9 : Scanning along the edge of the cutout. **126**
Figure 9.10: Location of the damaged surfaces in VS cylinder. **127**
Figure 9.11: Dimensions of the end tabs. **127**
Figure 9.12: End tab view. **128**
Figure 9.13: Connection between the two support structures. **129**

Figure 9.14: Schematic for the determination of the bending moment..... **130**
Figure 9.15: Imperfection data for CS cylinder with cutouts..... **131**
Figure 9.16: Imperfection data for VS cylinder with cutouts. **132**
Figure 9.17: Imperfection data for non-cutout CS and VS cylinders. **133**
Figure 9.18: 3D view of imperfection data for non-cutout CS cylinder. **133**
Figure 9.19: Test set-up on MTS 3500 machine- side 1. ..... **135**
Figure 9.20: Test set-up on MTS 3500 machine- side 2. ..... **135**
Figure 9.21: Top and side view of the locations for the DIC systems. **136**
Figure 9.22: Location of the attached strain-gauges. **136**
Figure 9.23: Spring type BCs. **138**
Figure 9.24: Nonlinear PFA with real imperfection for CS cylinder with cutouts **138**
Figure 9.25: Nonlinear PFA with real imperfection for VS cylinder with cutouts **139**
Figure 9.26: Non-cutout CS test results. **140**
Figure 9.27: Non-cutout VS test results. **141**
Figure 9.28: Test result for CS cylinder with cutouts. **142**
Figure 9.29: The picture of the failed CS cylinder. **143**
Figure 9.30: The picture of the failed VS cylinder from outside. **143**
Figure 9.31: The picture of the failed VS cylinder from inside. **143**
Figure 9.32: Test result for VS cylinder with cutouts. **144**
Figure 9.33: The strain results for CS cylinder for top and bottom mid nodes..... **145**
Figure 9.34: The strain results for VS cylinder for top and bottom mid nodes. ... **146**
Figure 9.35: The strain results around left cutout for CS cylinder. **147**
Figure 9.36: The strain results around right cutout for CS cylinder..... **147**
Figure 9.37: The strain results around left cutout for VS cylinder..... **148**
Figure 9.38: The strain results around right cutout for VS cylinder. **148**
Figure 9.39: The axial DIC results comparison with FEM results for VS cylinder **149**
Figure 9.40: The circumferential DIC results comparison with FEM results for VS cylinder..... **150**
Figure B.1 : 0.1R/0 analysis result. **167**
Figure B.2 : 0.1R/45 analysis result. **168**
Figure B.3 : 0.1R/60 analysis result. **169**
Figure B.4 : 0.1R/75 analysis result. **170**
Figure B.5 : 0.1R/90 analysis result. **171**
Figure B.6 : 0.1R/105 analysis result. **172**
Figure B.7 : 0.1R/120 analysis result. **173**
Figure B.8 : 0.1R/135 analysis result. **174**
Figure B.9 : 0.1R/180 analysis result. **175**
Figure C.1 : 0.3R/0 analysis result. **177**
Figure C.2 : 0.3R/45 analysis result. **178**
Figure C.3 : 0.3R/60 analysis result. **179**
Figure C.4 : 0.3R/75 analysis result. **180**
Figure C.5 : 0.3R/90 analysis result. **181**
Figure C.6 : 0.3R/105 analysis result. **182**
Figure C.7 : 0.3R/120 analysis result. **183**
Figure C.8 : 0.3R/135 analysis result. **184**
Figure C.9 : 0.3R/180 analysis result. **185**

Figure D.1 : 0.5R/0 analysis result. **187**
Figure D.2 : 0.5R/45 analysis result. **188**
Figure D.3 : 0.5R/60 analysis result. **189**
Figure D.4 : 0.5R/75 analysis result. **190**
Figure D.5 : 0.5R/90 analysis result. **191**
Figure D.6 : 0.5R/105 analysis result. **192**
Figure D.7 : 0.5R/120 analysis result. **193**
Figure D.8 : 0.5R/135 analysis result. **194**
Figure D.9 : 0.5R/180 analysis result. **195**
Figure E.1 : 0.3R/90 analysis result. **197**
Figure E.2 : 0.3R/105 analysis result. **198**
Figure E.3 : 0.3R/110 analysis result. **199**
Figure E.4 : 0.3R/115 analysis result. **200**
Figure E.5 : 0.3R/120 analysis result. **201**
Figure F.1 : 0.4R/90 analysis result. **203**
Figure F.2 : 0.4R/105 analysis result. **204**
Figure F.3 : 0.4R/110 analysis result. **205**
Figure F.4 : 0.4R/115 analysis result. **206**
Figure F.5 : 0.4R/120 analysis result. **207**
Figure G.1 : 0.5R/90 analysis result. **209**
Figure G.2 : 0.5R/105 analysis result. **210**
Figure G.3 : 0.5R/110 analysis result. **211**
Figure G.4 : 0.5R/115 analysis result. **212**
Figure G.5 : 0.5R/120 analysis result. **213**
Figure H.1 : 0.6R/90 analysis result. **215**
Figure H.2 : 0.6R/105 analysis result. **216**
Figure H.3 : 0.6R/110 analysis result. **217**
Figure H.4 : 0.6R/115 analysis result. **218**
Figure H.5 : 0.6R/120 analysis result. **219**
Figure I.1 : Cylindrical and Cartesian coordinate representations. **221**
Figure K.1 : 0.1R/0 analysis result. **227**
Figure K.2 : 0.1R/45 analysis result. **228**
Figure K.3 : 0.1R/60 analysis result. **229**
Figure K.4 : 0.1R/75 analysis result. **230**
Figure K.5 : 0.1R/90 analysis result. **231**
Figure K.6 : 0.1R/105 analysis result. **232**
Figure K.7 : 0.1R/120 analysis result. **233**
Figure K.8 : 0.1R/135 analysis result. **234**
Figure K.9 : 0.1R/180 analysis result. **235**
Figure L.1 : 0.3R/0 analysis result. **237**
Figure L.2 : 0.3R/45 analysis result. **238**
Figure L.3 : 0.3R/60 analysis result. **239**
Figure L.4 : 0.3R/75 analysis result. **240**
Figure L.5 : 0.3R/90 analysis result. **241**
Figure L.6 : 0.3R/105 analysis result. **242**

Figure L.7 : 0.3R/120 analysis result..... **243**
Figure L.8 : 0.3R/135 analysis result..... **244**
Figure L.9 : 0.3R/180 analysis result..... **245**
Figure M.1 : 0.5R/0 analysis result..... **247**
Figure M.2 : 0.5R/45 analysis result..... **248**
Figure M.3 : 0.5R/60 analysis result..... **249**
Figure M.4 : 0.5R/75 analysis result..... **250**
Figure M.5 : 0.5R/90 analysis result..... **251**
Figure M.6 : 0.5R/105 analysis result..... **252**
Figure M.7 : 0.5R/120 analysis result..... **253**
Figure M.8 : 0.5R/135 analysis result..... **254**
Figure M.9 : 0.5R/180 analysis result..... **255**
Figure N.1 : Planned cutout configurations and machining dimensions..... **257**

DESIGN, ANALYSIS AND VERIFICATION OF CONVENTIONAL AND NON-CONVENTIONAL CYLINDRICAL CFRP COMPOSITE SHELL WITH OPTIMIZED CUTOUT UNDER THE EFFECT OF COMBINED LOADING

SUMMARY

The rate of the usage of fiber reinforced composite structures both in aerospace and automotive industries has been increasing very rapidly over the past few decades. In addition to conventional fiber orientation laminate composites, the steered fiber layup composites have also become in the center of interests. Having higher specific strength and stiffness and being light-weight compare to metallic structures give polymer composites an important advantage over metals.

Traditional fiber-reinforced composite laminates are composed of 0°, 90° and ±45° plies and are called as constant stiffness (CS) composites. Those specific fiber orientation selections are due to the ease of manufacturing, since at the initial times of composite manufacturing the only way was to manufacture manually. On the other hand, with the development of automated fiber placement machines, recently designed steered fiber composites have been able to put into service. This manufacturing technique allows fibers to be oriented other than 0°, 90° and ±45° such that the curved fiber orientation within a ply changes continuously. Due to spatially oriented fibers within a ply, the laminate has spatially varying stiffness and therefore, those fiber composites are called as variable-stiffness (VS) composites. The purpose of having VS is to improve the mechanical properties of the composite. There have been various researches on the VS composites including flat panels, conical and cylindrical shells with some of the works including cutouts as well.

The work presented in this dissertation includes the effect of cutouts varying circumferentially and geometrically on both CS and VS cylindrical shells under pure bending and combined loading. The geometry and cutout configurations of the CFRP cylindrical composite shell was selected to simulate the fuselage of the airframe. The structure under consideration is a circular cylinder with a radius R of 304.5 mm (12 in), length L of 813 mm (32 in), and an overall shell thickness H of 4.392 mm (0.173 in). Loading is introduced at each end of the cylinder and for this study is confined to a pure bending, applied in a direction so that the bottom of the cylinder is under compression and the top in tension. The manufactured shells are composed of 24 plies of BMS8/276 material. This material is considered Boeing proprietary and since the design studies undertaken here are intended for future publication, a similar material (IM7/8552) is substituted that is suitable for publication yet provides acceptable agreement with the material properties of the actual test specimen (for modeling of the actual mechanical tests, the BMS8/276 material properties were be used). The stacking sequence of the constant stiffness shell is given as $[\pm 45/0_2/90_2/0/\pm 45_2/90]_s$. The material properties were that of Hexcel IM7/8552 unidirectional prepreg.

In the combined loading study, in addition to bending moment, vertical shear force applied from one end of the cylinder while applying encastre boundary condition

to the other end. The results of a parametric study, concerning on the effects of a pair of cutouts symmetrically located with respect to the vertical axis perpendicular to the bending axis, varying both the location and size of the cutouts and evaluating their effects on the maximum load levels and predominant failure modes of a circular cylindrical shell were presented. Several baseline cases were presented to illustrate the type of results that were encountered. Overall failure trends from the study were introduced, and a supplemental study to highlight an interesting aspect of the results was demonstrated.

The analysis methods that were used for the evaluation of the buckling and failure characteristics of shells include linear buckling analysis, nonlinear analysis using Riks method and nonlinear progressive failure analysis using Riks method. During the nonlinear analysis, the imperfections coming from the buckling analysis were also included at a rate of 10% of the shell thickness. Analyses were performed using the commercial FEM solution ABAQUS using S4R element. In that model, the stacking sequence was defined using the COMPOSITE option of the SHELL SECTION designator to define the fiber orientation angle of each layer. For the VS case, additional computations were required due to the spatial variation of the fiber orientation angle within the plies. Subroutines were generated with FORTRAN coding to produce fiber orientation angles for each ply. The fiber angle values were introduced into the model through the DISTRIBUTION TABLE designator within ABAQUS. This feature allows the user to construct tables to list specified values for each element or node. In this case, one table was used for each distinct ply and default values were used for the CS plies. During finite element analysis S4R shell element which possesses one integration point at the centroid of the element was used. The centroid was calculated from the four connected nodes of each element and the fiber orientation angle values were calculated there based on the parametric formulation of the circumferential variation. A Python script was used to construct both the input file and the tables based on the model parameters (geometry, mesh size, material properties, stacking sequence, and cutout configuration), where the tables used the FORTRAN subroutines interactively to calculate the fiber orientation angles. The tables were written to external files so they could be easily changed without having to alter the original input file.

During nonlinear progressive failure analysis, Helius PFA commercial tool was used. It is composed of a set of software modules and a composite material library that integrates with the ABAQUS finite element analysis system. Helius PFA utilizes a form of material modeling that is based on Multi-continuum Theory in addition to other common composite failure criteria like Tsi-wu, Hashin, Larc etc.

In the analysis of cylindrical shell model with cutouts, failure modes were defined and tables of failure modes were generated for the prescribed cutout size and locations. It was discovered that, there are generally three types of failure modes, which appears under pure bending for cylindrical shells with cutouts. To classify them; Failure Mode I may be defined as strength failure driven by global buckling of the cylinder. Failure Mode II can be defined as; strength failure around the cutout driven by local cutout edge buckling. As third mode, in Failure Mode III, before global buckling, material strength failure starts due to high stress concentration and therefore, it was defined as the strength failure initiated around the cutout without buckling.

Finally, comparison of the finite element predictions with the experimental results were realized by matching the end rotations and strains. Although, the VS cylinder was designed to be stiffer than the CS cylinder and expected to have higher failure load in bending, after placing cutouts with certain size and locations on the cylinder, the effect of steered fiber laminae reduced dramatically. The effect of steered fiber is reduced due to the change in the failure mode as a result of applied cutouts. When the cutouts are below the neutral axis, that is the compression side of the cylinder, failures are usually driven by local buckling around the holes in contrast to global buckling from the bottom of the cylinder. The steered fiber laminate were designed to increase the failure load under pure bending and it can be effective in global buckling since the VS shell was optimized without cutouts. Therefore under local buckling conditions failure load were dropped for both CS and VS laminates.

After completing the nonlinear analyses and finalizing the cutout size and locations, the cylinders without cutouts were machined with the 0.3R/120 cutout configurations. Following the machining, real imperfections were measured with Digital Image Correlation method. A final improvement of the finite element predictions was achieved by including real geometric imperfections in the model and by performing nonlinear progressive failure analysis using Riks method.

Testing of cylindrical shells with cutouts was performed in TU Delft using a fixture that was designed to test the constant-stiffness and the variable-stiffness cylinders in pure bending. Strains and displacements were measured using strain gauges, digital image correlation, LVDT's and lasers. Two cylinders were tested: one with conventional layup laminate baseline cylinder (CS) and one with circumferentially varying laminate stiffness (VS). A comparison of the experimental response of the two cylindrical shells with the finite element predictions showed that the experimental boundary conditions has almost the same flexibility as modeled in the finite element model and resulted in good agreement between the experimental and the numerical results. The ultimate failure loads of testing also showed very good correlations with the finite element predictions.

The results of this study show that, during the numerical analyses of composite structures it is important to apply nonlinear progressive failure analyses in order to obtain realistic results close to the test results. It was also proved that there are basically three failure modes of the cylindrical shells with cutouts. Although, the failure resulting from the global buckling of the cylinder has the highest failure load, generally the cylinders with moderate cutout size will tend to either buckle or tear up from the cutout edge. Therefore, in the design of cylindrical aerospace structures the window or door cutouts, the sizes and locations of the cutouts should be adjusted so that the buckling will tend to start from cutout edge to increase the post buckling strength of the cylindrical shells .

ÜZERİNDE KESİTLER OLAN GELENEKSEL VE GELENEKSEL OLMAYAN SİLİNDİRİK KARBON FİBER KOMPOZİT POLİMER KABUĞUN BİLEŞİK YÜKLEME ALTINDA TASARIM, ANALİZ VE DOĞRULANMASI

ÖZET

Havacılık, uzay ve otomotiv sektöründe, karbon fiber takviyeli kompozit malzemelerin kullanımı son yıllarda ivmelenerek artmaktadır. Geleneksel fiber oryantasyonu ile üretilmiş olan olan kompozitlerin yanında, fiber açıları uzaysal olarak değişen yönlendirilmiş fiber oryantasyonlu kompozitlere olan ilgi hızla artmakta ve birçok araştırmacı ve ticari firma bu konularda çalışmaktadırlar. Karbon fiber takviyeli kompozitler metallere göre daha yüksek özgül mukavemet ve katılığa sahiptirler, ayrıca daha hafif olmalarından dolayı da, kompozitler metallere göre önemli avantajlara sahiptirler.

Geleneksel fiber takviyeli katmanlı kompozitlerde, katmanlar standart 0°, 90° and $\pm 45^\circ$'lik katmanlardan oluşurlar. Bu fiber açılarının kullanılmasının sebebi, fiber takviyeli polimer kompozit malzemelerin ilk kullanıma başladığı dönemlerde üretimlerin elle yapılmasından dolayı karşılaşılan üretim zorluklarından kaynaklanmaktadır. Son yıllarda geliştirilen otomatik fiber yerleştirme makineleri ile standart açılı fiber katmanlara ilave olarak istenen her açıda fiber yerleşimi sağlanabildiği gibi, yönlendirilmiş fiberlere sahip kompozit malzemelerin üretilmesine de olanak sağlanmış oldu. Yönlendirilmiş fiberler, bir katmandaki fiberlerin açılarının sabit olmayıp uzaysal olarak değişmesini içermektedir. Bu nedenle yönlendirilmiş şekilde tasarlanmış olan kompozitlerde katılık da uzaysal olarak değişmektedir ve değişken-katılığa sahip kompozitler olarak adlandırılırlar. Değişken-katılıklı kompozitlerde amaç yapının mekanik özelliklerinin iyileştirilmesi, kompozitin kalınlık veya ağırlığının azaltılmasıdır.

Değişken katılıklı sahip kompozitlerle ilgili düz paneller, konik yapılar ve silindirik kompozit yapılarla ilgili gerçekleştirilmiş olan çeşitli çalışmalar bulunmaktadır. Bu çalışmalardan bazılarında üzerinde delikler bulunan kompozit paneller ile değişken katılık yöntemi ile tasarlanarak hasar yükünün artırılmasını hedefleyen örnekler de mevcuttur.

Bu tezde, silindirik katmanlı kompozit bir yapıda, silindirin her iki yanına simetrik olarak açılan dairesel pencerelerin bileşik yükleme altındaki, sabit-katılıklı (geleneksel) ve değişken-katılıklı (geleneksel olmayan) kompozitlerde hasar yükü ve hasar şekline olan etkisi incelenmiştir. Silindirik kabuk üzerine açılan dairesel pencerelerin yerleşimi ve çapları değiştirilerek analizler gerçekleştirilmiş ve sonuçları tablolar ve grafikler halinde sunulmuştur. Yapılan çalışmada elde edilen hasar durumlarına göre hasar modları oluşturulmuştur. Bu modlar incelendiğinde hasarın pencere ölçüsü ve yerleşimine göre farlı eğilimler izlediği tespit edilmiştir. Silindirlerin burkulma ve hasar karakteristiklerinin tespit edilebilmesi amacıyla lineer burkulma analizi, Riks metodu kullanılarak lineer olmayan analizler ve ilerlemeli hasar

analizleri gerçekleştirilmiştir. Lineer olmayan analizler gerçekleştirilirken burkulma analizinden teorik olarak elde edilen geometrik kusurlar silindirik kabuğun kalınlığının % 10'u oranında analize dahil edilmiştir.

Seçilen geometri ve pencere konfigürasyonun amacı bir uçak gövdesine benzer bir yapının simüle edilmesi nedeniyledir. Dairesel kompozit silindir 304.5 mm (12 in) çap ve 813 mm (32 in) uzunluğa sahiptir. Silindirin toplam kalınlığı ise 4.392 mm (0.173 in) dir. Eğilme yükü silindirin her iki ucundan uygulanarak, silindirin üst bölgesinin çekme, alt bölgesinin ise basma yüküne maruz kalması sağlanmıştır. 24 katmandan oluşan silindir, BMS8/276 malzemesinden imal edilmiştir. Bu malzeme Boeing firmasına ait bir ticari gizliliğe sahip olduğundan malzeme özellikleri teze konulmamış, çalışmalar ise benzer mekanik özelliklere sahip bir malzeme olan IM7/8552 prepreg malzeme ile gerçekleştirilmiştir. Ancak, testler için üretilen silindir BMS8/276 malzemesinden imal edildiğinden, bu malzeme için de moddelleme ve analizler yapılmış ve sonuçlar test sonuçları ile malzeme özellikleri verilmeden karşılaştırılmıştır. Sabit katılıklı silindir için katma dizilimi $[\pm 45/0_2/90_2/0/\pm 45_2/90]_s$ olarak belirlenmiş ve malzeme özellikleri Hexcel IM7/8552 prepreg olarak seçilmiştir.

Sayısal analizler gerçekleştirilirken ticari Sonlu Elemanlar Metodu (SEM) olan ABAQUS ve S4R eleman tipi kullanılmıştır. Modelleme yapılırken, sabit katılıklı silindirik kabuk için, her katmanda, katmanların dizilim sırası ve fiber oryantasyonlarının belirlendiği KOMPOZİT modülü kullanılmıştır. Ancak yönledirilmiş fiberlere sahip değişken katılıklı silindirik kompozit için ilave hesaplamaların yaplması ve her katmanda bulunan tüm elemanlar için fiber oryantasyonunun ayrı ayrı hesaplanması gerekmektedir. Bu amaçla Pyhton kodu ve FORTRAN kullanılarak programlar yazılmış ve ABAQUS tarafından kullanılacak olan eleman oryantasyon bilgilerini içeren "DISTRIBUTION TABLE" oluşturulmuştur. Bu tezde yapılan çalışmada, silindirde çevresel olarak belirlenen noktalarda fiber oryantasyonları belirlenmiş ve daha sonra sabit eğim yöntemi kullanılarak bu noktalar arasında kalan herbir eleman için fiber oryantasyonları belirlenerek tablolar oluşturulmuştur.

Modelde kullanılan S4R eleman tipi geometrik merkezinde bir integrasyon noktasına sahiptir. Tek integrasyon noktasına sahip olan bu eleman tipinin seçilmesinin sebebi, ilerlemeli hasar hesaplaması sırasında bir integrasyon noktasında hasarın tespit edilmesi durumunda hasarlanan elemanın kolaylıkla çıkarılmasının sağlanması ve böylelikle daha doğru bir sonuca ulaşabilmek içindir. Herbir elemanın fiber oryantasyonunun aktarılması için gerekli olan bu noktanın koordinatlarının tespiti için ise elemanın düğüm noktalarının koordinat bilgilerinden faydalanılmıştır. Python dilinde yazılmış bir programla, modele ait parametre değerleri (model geometrisi, mesh ölçüsü, malzeme özellikleri, katman dizilimleri, geometrik kusur oranı ve pencere ölçü ve lokasyonları) kullanılarak fiber oryantasyon tabloları ve ABAQUS'ün girdi dosyası oluşturulmuştur. Bahsedilen Pyhton kodu FORTRAN'da yazılan bir kodla interaktif olarak çalışmakta ve fiber oryantasyon tablolarını oluşturmaktadır. Bu tablolar ayrı bir dosyada oluşturulduğundan herhangi bir değişiklik durumunda orjinal ABAQUS girdi dosyasının değiştirilmesine gerek kalmamaktadır.

İlerlemeli hasar analizleri sırasında ise Helius PFA ticari programı kullanılmıştır. Bu program, ABAQUS yazılımı ile entegre olmakta ve hasar analizi yapmasını sağlayacak olan çeşitli modül ve malzeme veri bankasından oluşmaktadır. Helius PFA hasar analizi Multi-continuum teorisine dayalı bir hasar kriterini kullanmaktadır. Ayrıca,

bu programla Tsi-wu, Hashin, Larc gibi bilinen hasar kriterleri ile de analiz yapmak mümkün olmaktadır.

Bu teze konu olan silindirik kompozitlerdeki pencereler için tanımlanan herbir ölçü ve lokasyon için ilerlemeli hasar analizleri yapılarak hasar modlarını içeren tablo ve grafikler oluşturulmuştur. Bu çalışmanın sonucunda eğilme yükü veya bileşik yükleme altındaki silindirler için temelde üç farklı hasar modunun olduğu tespit edilmiştir. Bunlardan ilki olan Mod I hasar tipi, silindirde oluşan global burkulmadan kaynaklı mukavemet kaybı sonucu oluşan hasar olarak tanımlanabilir. Mod II hasar tipi genel olarak, delik çevresinde oluşan burkulmadan kaynaklı mukavemet kaybı sonucu oluşan hasar olarak tanımlanabilir. Mod III hasar modunda ise, global veya yerel herhangi bir burkulma olmadan önce malzeme mukavemet hasarının delik çevresinde oluşan yüksek çekme veya basma gerilmelerinden dolayı hasarlanma oluşmasıdır.

Test sonuçları ile sayısal analiz sonuçlarının karşılaştırılması, eğilme yükü altındaki silindirin uçlarındaki dönme miktarları ile belirli noktalardaki gerinimlerin karşılaştırılması ile gerçekleştirilmiştir. Değişken katılıklı silindir, eğilme yükü altında sabit katılıklı silindire göre daha mukavemetli olarak tasarlanmış olmasına ve daha yüksek eğilme yüküne dayanmasına rağmen, silindirlere belirli ölçülerde, örneğin 0.3R/120 (0.3R yarıçap ve 120°'lik oryantasyon) ölçülerindeki pencere açıldığında, değişken katılıklı silindirde yönlendirilmiş fiberlerin mukavemete olan katkısının önemli ölçüde azaldığı anlaşılmıştır. Bunun sebebi, hasar modunda meydana gelen değişimden kaynaklanmaktadır. Pencereler silindirin tarafsız ekseninin altında, basmaya maruz kalan tarafta yer aldığında, hasar oluşumu, global burkulmanın aksine, deliklerin etrafında meydana gelen burkulma sonucunda meydana gelmektedir. Başlangıçta silindirler, üzerlerinde herhangi bir delik açılmamış halleriyle, eğilme yükü altında hasar yükünü artımaya yönelik olarak yönlendirilmiş fiberlerin optimizasyonu ile tasarlanmışlardır ve genel olarak global burkulma sonucu oluşan hasar modlarında (Mod I) etkili olmaktadırlar. Bu nedenle, belli bir çapın üzerinde ve silindirin basmaya maruz kalan tarafında silindirler üzerine delikler açıldığında yönlendirilmiş fiberlerin mukavemete olan katkısı önemli ölçüde azalmaktadır.

Basit eğilme yükü altında yapılan bu analizlerden sonra bileşik yükleme altındaki analizler gerçekleştirildi. Bu analizler sırasında eğilme yüküne ilave olarak, bir ucundan ankastre sabitlenmiş silindirin diğer ucundan kesme kuvveti uygulandı. Kesme kuvveti neticesinde silindirin orta kısmında oluşan momentin değeri ugulanan eğilme momentinin 0.2 oranına ulaştığında, oluşan hasarda kesme kuvvetinin etkisinin daha yüksek olduğu görülmüştür. Bileşik yükleme sırasında, kesme kuvvetinden dolayı silindirde burkulma meydana gelerek hasar oluşmasına sebep olmaktadır.

Sayısal analizlerin tamamlanmasının ardından silindirler üzerine açılacak deliklerin yerleşimi ve ölçülerine karar verilmiş ve deliksiz olarak üretilmiş olan silindirlere bu pencereler açılmıştır. Sayısal analizler yapılırken teorik olarak hesaplanan kusurlar kullanıldığından, silindirlere delikler açıldıktan sonra DIC yöntemi kullanılarak silindirlerdeki gerçek kusurlar ölçülmüş ve sayısal analizler gerçek kusur değerleri kullanılarak tekrarlanmıştır.

Eğilme testi yapılacak olan silindirler Boeing firması tarafından desteklenen bir proje ile otomatik fiber yerleştirme makinesi ile üretilmiştir. Ayrıca, eğilme testinin yapılabilmesi için gerekli olan fikstürler de daha önce bir doktora tezi kapsamında TU Delft üniversitesinde üretildiğinden bu fikstürler kullanılmıştır. Bu nedenle, oluşturulan bu model daha sonra Boeing firması ile TU Delft üniversitesine

gönderilerek modeli incelemeleri ve silindirlere açılması için karar verilen pencere ölçülerinde kesimlerin yapılması sağlanmıştır.

Testler sırasında silindir üzerindeki gerinimler ve yer değiştirmeler gerinim ölçerler ve DIC ile ölçülmüştür. Test sonuçları ile sayısal analiz sonuçları karşılaştırıldığında sonuçların birbirine oldukça yakın olduğu ve böylece model ve analizlerin geçerliliği doğrulanmış oldu.

Bu tezde, üzerinde pencere kesitleri olan karbon fiber kompozit silindirlerin sonlu elemanlar yöntemiyle analizleri ve sonrasında da testleri yapılarak bu kesitlerin mukavemete ve hasar oluşumuna olan etkileri incelenmiş oldu. Sayısal analizler gerçekleştirilirken, ilerlemeli hasar analizlerinin dahil edilmesinin gerçeğe yakın sonuçların elde edilmesi için önemli olduğu tespit edilmiş oldu. Aksi takdirde test sonuçlarından daha yüksek hasar sonuçlarına ulaşılmaktadır. Bu sonuçlar gösterdi ki, üzerinde pencere kesitleri olan silindirik kompozit yapılar temel olarak üç tip hasar modu altında hasarlanmaktadırlar. Bu nedenle, üzerinde büyük ölçülerde delik olan silindirik havacılık yapılarının bu deliklerin ölçü ve oryantasyonlarının, hasarın delik kenarından burkularak başlayacak şekilde ayarlanmasının yapının hasar dayanımının artırılmasında önemli olduğu tespit edilmiştir.

1. INTRODUCTION

Carbon fiber reinforced polymer (CFRP) composite materials have many advantages when compared to metallic structures; therefore, they have become very popular and their usage has been inevitable for many applications especially in aerospace and automotive industries. They have better mechanical properties compare to metals, like having higher specific stiffness and strength in addition to higher fatigue strength and better impact properties. Composites can also be manufactured as smart materials to be used in structural health monitoring systems with the help of embedded sensors. In addition, they offer higher corrosion and chemical resistance, better dimensional stability and design flexibility over metallic materials. On the other hand, the manufacture cost of the composite materials is high and manufacturing high quality composite material depends on the experience.

Composite materials have been used in wide variety of applications. They are being used for decades in both transport and military aircraft components, but they have been mostly used in wing edges or control surfaces. In recent years, the uses of composites have been extended to the fuselage and wings because of its lightweight and resistance to corrosion compared to the metallic materials that have traditionally been used in aircraft. The use of composites will not only help to save the weight but there will be benefits to the passengers as well. Due to the properties of composites, airlines will be able to increase cabin pressure and the humidity that will result more comfortable flight and prevent jet lag [12].

One of the latest commercial aircraft, The Boeing 787 is about 50 percent composite by weight and soon it is followed by the Airbus A350, having composite material roughly in the same proportion as dreamliner as shown in the Figure 1.1. However, the airworthiness authorities such as FAA in US and EASA in Europe still have some safety concern due to the use of large percentage of composite materials, that their mechanical behavior and the proper failure criteria are still under investigation. Therefore, it is important to investigate the mechanical properties of the composites

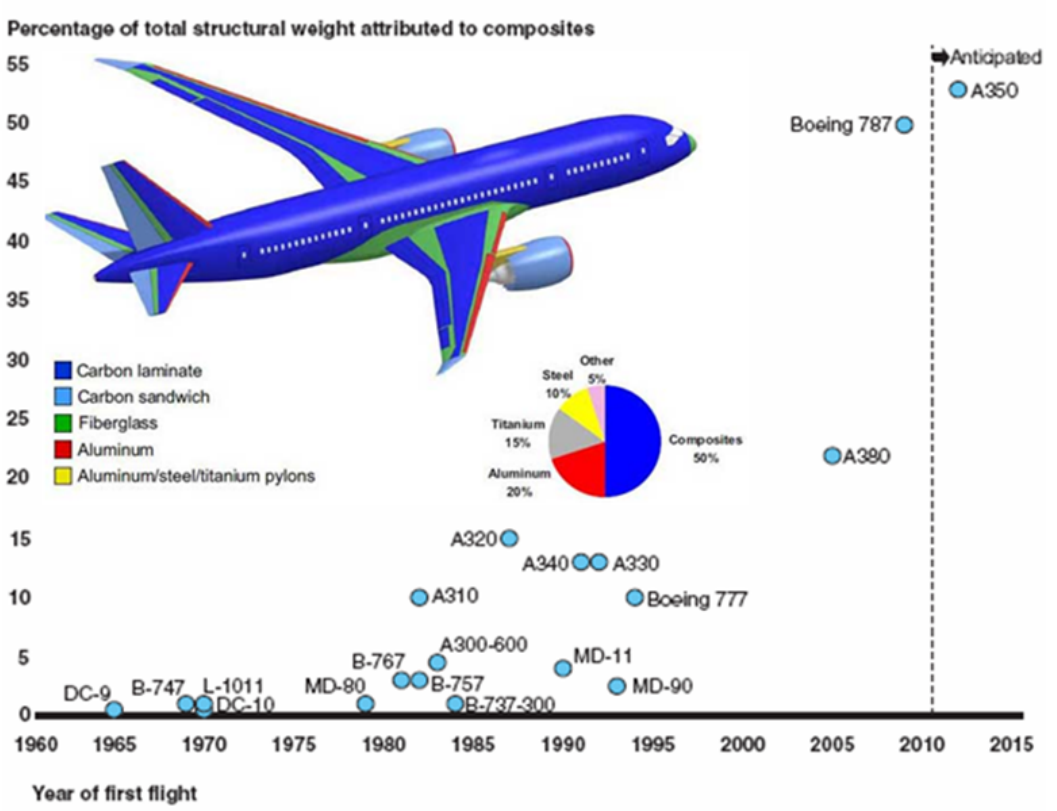


Figure 1.1 : Airplanes by percentage of composite and materials in Boeing 787 [1].

under various combined loading and increase the reliability with some proper testing.

1.1 Purpose of Thesis

It is well known that in recently designed aircraft, the rate of the usage of laminated composites are increasing as shown in the Figure 1.2. The research in the area of cylindrical CFRP composite shells is an important area especially for airworthiness, and the amount of experimental data and information available requires reliable verifications. Especially, when the cylinders have certain cutouts. Therefore, the purpose of this study is defined as to investigate effects of size and location of circular cutouts on buckling and failure behavior of a cylindrical CFRP laminated composite shell under combined loading.

Generally, the fuselage of an aircraft has circular cylindrical geometry with door and window cutouts having elliptical or rectangular shapes as illustrated in Figure 1.3; therefore, cylindrical shell was selected for the study.

The purpose of selecting cylindrical geometry is because, generally the fuselage of the aircraft have circular cylindrical geometry with door and window cutouts. The

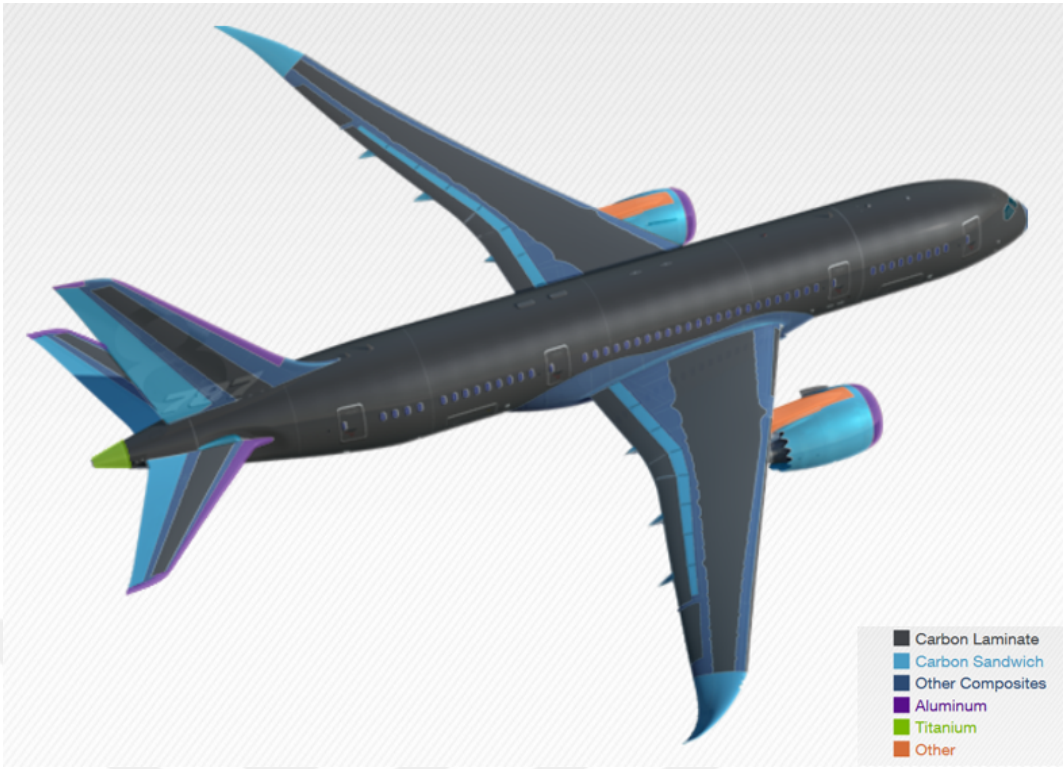


Figure 1.2 : Boeing 787 Structure [2].

geometry of the cutouts is mostly of rectangular or elliptical shapes as illustrated in Figure 1.3. In addition to B787 also in A350, composites are applied extensively

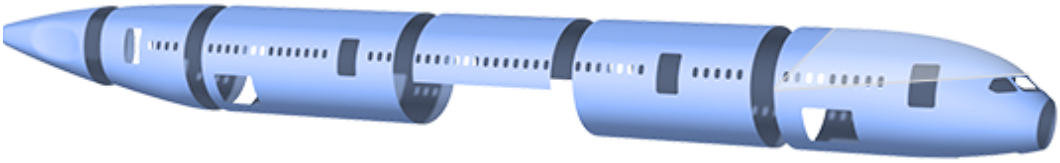


Figure 1.3 : One-piece composite barrel construction in Boeing 787 [2].

throughout the fuselage. According to Airbus, there are many advantages of polymer composites: "The 53% of composites utilized in the A350 XWB's fuselage and wing reduces the need for fatigue-related inspections required on more traditional aluminum jetliners. Composites and titanium also diminish the requirement for corrosion-related maintenance checks on the A350 XWB. These two factors reduce the new aircraft's overall fatigue and corrosion maintenance related tasks by 60 per cent" [13]. With the use of automated fiber placement (AFP) machines, almost the complete structural shell of the aircraft can be built using composite materials. As shown in Figure 1.4 the rear fuselage of Boeing 787 is almost completely made of CFRP.

It should be noted that as with any structural design, a key feature in the design is the selection of an appropriate failure criterion. For the case of metals, it is sufficient to



Figure 1.4 : Rear Fuselage of Boeing 787 [2].

use one observable metric such as the ultimate tensile, compressive or shear stress to describe failure. For composites, however, there is a challenge of selecting a suitable failure criteria based upon a number of observable stress metrics.

In contrast to metallic materials, composite structures fail under different failure modes such as matrix and fiber failures or delamination. The initiation of damage in a composite laminate occurs when a single ply or part of the ply in the laminate fails in any of these failure modes [14]. The crack propagation and damage tolerance known for metallic structures can be applied for the composite structures until certain level. For composite structures that can accumulate damage before structural collapse, the use of failure initiation criteria is not sufficient to predict ultimate structural failure since they only predict onset of the damage. Therefore, an accurate determination of failure modes and the progression of the failure within the structure until critical failure are important.

Several progressive failure models were developed by researchers, LaRC failure criteria is a type of continuum damage model that is able to predict the initiation and propagation of ply failure mechanisms as well as the final failure load of composite structures [15]. In a typical progressive failure analysis, at each load step, a non-linear analysis is performed to account for the geometrically nonlinear response of the structure. Using this nonlinear solution, the local lamina stresses are determined and checked against a failure criterion to determine whether any failures have occurred for

this load increment. If no failure is detected, the applied load is increased and the analysis continues. When failure in the lamina occurs, a change in the stiffness tensor is calculated based on the material degradation model. This process is repeated until no additional lamina failures are detected. The load step is then incremented until final failure of the structure is detected [15].

The overall aim of the thesis is to investigate the mechanical response and failure characteristics of introducing varying cutouts into both conventional and non-conventional CFRP cylindrical shells. Two shells without cutouts were previously designed, manufactured, and tested at TU Delft as part of Ph.D. work of Blom [3]. One shell used a conventional laminate layup and is referred to as the constant stiffness (CS) shell, while the second utilized fiber steering during manufacture and is termed the variable stiffness (VS) shell. In this study cutouts will be introduced into the shells to investigate the failure results during testing and the effects of the cutout size and position on the failure characteristics under pure bending.

The geometries of the shells, the proposed cutouts and the analysis methods that were used for the design studies to determine a useful cutout configuration will be explained in detail. Alterations to these models for the VS shell and to provide better agreement with the mechanical testing boundary conditions will also be provided. The geometries of the shells and the cutouts will be described and the analysis methods that are used for the evaluation of the buckling and failure characteristics of shells will be detailed. The results of parametric study for both CS shell and VS shell, varying both the location and size of the cutout and determining the effect on the maximum load levels and predominant failure modes will be presented. It was intended to find a suitable cutout configuration for bending testing. The test was performed using the existing test fixture at TU Delft, as depicted in Figure 1.5. In the fixture, each end of the cylinder is attached to a rigid end plate, such that the edges of the cylinder are clamped to the plate, while the plates are able to move. Opposite and equal bending moments are applied to the centers of the plates. Several baseline cutout cases were presented first to illustrate the type of results that were encountered and detailed results from the study are discussed. Appendices include complete details of each cutout configuration. The results of the



(a) Picture (b) Model

Figure 1.5 : MTS Test Bench with the bending fixture [3].

design studies and recommendations for the cutout configuration along with test results were also provided.

1.2 Literature Review

The following literature survey has been performed to decide the level of study and to get benefits from previous works. The literature survey mostly includes the design of laminated conventional and steered fiber reinforced polymer composite materials, their optimization and linear and nonlinear progressive failure analysis. During failure analysis, many failure criteria are used by the researchers and some of those methods will be mentioned.

Tailoring of laminated composite structures by varying ply fiber angle and thickness locally provides a great opportunity to obtain full advantage of composite materials.

Variable stiffness design has become very popular with the development of industrial fiber placement machines.

During variable stiffness composite design, using lamination parameters which provide a compact definition of laminate stiffness, as design variables accepted as a good option. A method which incorporates the strength failure criteria in the lamination parameters by using a conservative failure envelope for all ply angles was developed by Khani et al. [16]. While designing composites, where strength constraints are considered, the failure load is usually desired to be greater than the buckling load in order to avoid buckling induced failure. Khani et al. used a conservative failure envelopes based on Tsai-Wu failure criterion for strength evaluation [17]. A circular cylinder under bending and an elliptical cylinder under axial compression, which were tailored circumferentially, were modeled and analyzed using nonlinear buckling analysis by means of commercial FEM tool Abaqus. Another finite element analysis on the response of composite cylinder shells with cutouts and subjected to internal pressure and axial compression were presented by Ismail et al. [18]. The objective of the study was to improve the buckling load by applying the internal pressure while the compression load is applied. They also investigated the effect of local stress concentration distributed around the cutout region. In addition, Shi et al. investigated the initial buckling and post-buckling responses of axially loaded composite cylindrical shells with reinforced rectangular or circular cutouts [19]. A nonlinear analysis procedure was proposed to predict the nonlinear buckling response of the cylindrical shell.

The design and optimization of steered fiber composite laminates has attracted the attention of the researchers and given industry new opportunities for design and manufacturing of novel structures. However, there exist several discrepancies and obstacles between the design and the manufacturing of composites. A review of fabrication issues encountered during the manufacture of tow-steered laminates was presented by Gürdal et al. [5]. Tow-steering laminate design concept tailors the stiffness of the composite laminate by using curvilinear fiber paths within the plane of a ply. The stiffness tailoring of the composite laminate was achieved by spatial variation of the fiber orientation angle. They used curvilinear tow paths based on constant curvature arcs. However, this construction technique generates gaps and/or overlaps

between neighboring tow courses. They showed that the issue must be considered during both the structural analysis and fabrication phases. Tatting and Gürdal showed that for structures with highly non-uniform stress states such as a flat panel with a central hole subjected to in plane loading, steered fiber concept provides substantial improvements in load carrying capability [4]. They tested the panels with hole to demonstrate that curvilinear fibers reduce stress concentrations around the hole and improve the load carrying capability of panels. They also presented a procedure for analyzing and designing elastically tailored composite laminates using the STAGS finite element solver [8] . The methodology used to produce computer-controlled steering of reinforced composite material tows. Tatting et al. also applied tow-steering design techniques for laminated composite structures, with implementation of novel weight-reduction methods [20].

A fiber placement method called 'continuous tow shearing' has been developed by Kim et al. in order to minimize manufacturing induced defects in a tow steering process [21]. They developed a computer-aided modelling tool to create ABAQUS finite element models showing the nonlinear fiber trajectories and thickness variations of variable stiffness composites.

Soremekun et al. presented a methodology for designing two-dimensional array of laminated composite panels with varying loads [22]. The design process is proposed to minimize the manufacturing effort and cost of the panels while meeting structural requirements at minimum weight. The methodology involves an automated optimization process using a commercial genetic algorithm software. A comparison between the individually optimized panel designs and the blended designs were presented.

A multi-step framework was proposed by IJsselmuiden et al. where the structure is optimized using panel thickness and lamination parameters as continuous design variables [23]. They performed continuous optimization and obtained discrete blended stacking sequences using a guide-based genetic algorithm.

The optimization of fiber-reinforced composite shells for maximum fundamental frequency was presented by Blom et al. [24]. Cylindrical shells using an advanced tow-placement machine that allows steering of the fibers, resulting in a VS structure

were built. They provided different path definitions for VS shells and optimized conical shells for maximum fundamental frequency, while taking into account the manufacturing constraints that apply for tow placement. The improvements of VS over conventional, CS shells were demonstrated. Blom et al. also presented the detailed derivation of four theoretical fiber path definitions for generalized conical shell surfaces, namely, geodesic path, constant angle path, linearly varying fiber angles path and constant curvature path [25]. Additionally, they demonstrated the implementation of fabrication details and constraints in terms of the steering radius of curvature based on advanced tow-placement technology.

VS laminates that have fiber orientation variation, can be manufactured using advanced fiber placement technology. In VS laminates, there may exist tow overlaps resulting in thickness build-up or gaps. If a constant thickness is needed, tows must be cut at the course boundary that will result in areas without any fibers. Blom et al. performed a theoretical, numerical investigation on the influence of tow width, laminate thickness and tow-drop areas on the strength and stiffness of variable-stiffness laminates [26]. Then, they performed progressive failure analyses using the LaRC failure criteria and showed that failure occurs at tow-drop locations. They also presented a method for designing composite plies with varying fiber angles with composite plates or panels in which the thickness build-up within a ply is predicted as function of ply angle variation using a streamline analogy. It was found that the thickness build-up is not unique and depends on the chosen start locations of fiber courses. Optimal fiber courses were formulated in terms of minimizing the maximum ply thickness, maximizing surface smoothness or combining these objectives with and without periodic boundary conditions [27]. On the other hand, in order to minimize the AFP induced defects as gaps and overlaps, the tow-drop method was developed by Marouene et al. [28]. Buckling tests were performed on panels containing gaps or overlaps. They showed that the tow-drop method significantly improved the structural performance in the pre-buckling stiffness, buckling load and the failure load.

White et. al presented a numerical investigation into the buckling and post-buckling of two variable-stiffness cylinders under axial compression [29]. The shells have continuous fiber-angle variation around the circumference. Dynamic analyses were

performed and the development of the initial nonlinear buckling, its dynamic snap-through, and the formation of a post-buckled configuration were monitored.

Senocak et al. presented a method to design the shape of a cutout and the reinforcement distribution of cutout edge for symmetrically laminated shells, when they were loaded by hydrostatic pressure and axial compression, respectively [30]. The designed shells were analyzed for stresses, displacements and its buckling load using the finite element method. It was demonstrated that the procedure was able to recover the buckling load of the shell compared to the uncut shell.

Van Tooren et al. performed an analysis of the curvature effects on the stress distribution around circular cutouts in sandwich cylinders [31]. The stresses in the cylinder were determined for uniformly distributed axial load and internal pressurization loading cases.

It is an important factor to accurately know the insitu composite properties in order to decide the appropriate failure model for polymer laminated composites. Based on that, Makeev et al. investigated the effect of nonlinear interlaminar shear stress-strain relations on delamination failure predictions for carbon fiber epoxy tape laminates [32]. A finite element model, which includes in-ply and delamination damage effects, was developed by Chen et al. for the progressive failure analysis of composite laminates [33]. A combined elastoplastic damage model which includes plasticity and damage effects was used to represent the mechanical response of composite layers and was implemented using Abaqus.

Angelico et al. investigated the intra-laminar progressive failure process of composite material under three-point bending [34]. The mechanical response was simulated using five failure modes: two for fiber-failures and three for inter-fiber-failures. Each failure mode has a failure criteria and an associated degradation function that decreases de engineering properties of the material.

Jaunky et al. presented progressive failure analyses results for composite panels with and without a cutout, subjected to in-plane shear loading and compression loading into their postbuckling regime [14]. Ply damage modes such as matrix and fiber failure and fiber-matrix shear failure were modeled and results from finite element analyses were compared with experimental results.

Lapczyk et al. presented an anisotropic damage model for predicting failure and post-failure behavior in fiber-reinforced materials [35]. The model was intended to predict mechanical behavior of elastic-brittle composite materials that show no significant plastic deformation before failure. The damage initiation was predicted using Hashin criteria and the progression of damage was controlled by a damage evolution law based on fracture energy dissipation during the damage process, and the increase in damage was controlled by equivalent displacements.

Analyses of postbuckling progressive damage behavior and final structural failure due to accumulation of fiber and matrix damage were performed by Lopes et al [15]. They implemented a user-developed continuum damage model in ABAQUS to simulate damage initiation and the stiffness degradation. They showed a success, by predicting ultimate failure of tow-steered panels in post buckling within 10% tolerance of the experimental results.

Stress analysis of composite cylindrical shells with an elliptical cutout was investigated by Öterkuş et al. [36]. They presented a semi analytical solution method for determining the stress and deformation fields in a thin, laminated-composite cylindrical shell with an elliptical cutout. The analysis includes the effects of cutout size, shape, and orientation; non-uniform wall thickness; oval cross-sectional eccentricity; and loading conditions with uniform tension, uniform torsion, and pure bending. In addition, Poore et al. also presented a semi-analytical solution method to find the natural frequencies and mode shapes of laminated cylindrical shells containing a circular cutout [37].

In order to avoid the stress concentrations around a cutout Lopes et al. suggested using fiber-steered laminates [38]. They showed that, it is possible to design and manufacture composite panels whose buckling and failure responses are insensitive to the existence of a central hole by steering of the fibers in the plane of the laminate.

Ambur et al. suggested that difficulty in developing an accurate and efficient numerical procedure to predict damage growth depends on analyzing the material microstructural changes and the response to those changes [39]. Due to uncertainty in the prediction of damage initiation and progression in composites, NASA Langley Research Center

developed a failure criteria, called LARC02. All the calculations were performed at lamina level with plane stress assumptions.

A set of failure criteria for fiber reinforced polymer laminates was described by Davila and Camanho derived from Puck's [40] action plane concept called as LaRC03 [41, 42]. It uses fracture mechanics models of matrix cracks to develop a criterion for matrix in tension and to calculate the associated in-situ strengths. Some examples to predict failure load envelopes and the failure mode for each region of the envelope were presented. The analysis results were compared to the predictions using other available failure criteria and with experimental results. Based on the comparison they claim that LaRC03 criterion has a significant improvement over the commonly used Hashin criteria [43].

A continuum damage model for the prediction of the initiation and evolution of inter laminar failure mechanisms and the collapse of structures manufactured in fiber-reinforced plastic laminates was proposed by Maimi et al [44]. The failures in the longitudinal and transverse directions of a ply were represented by a set of scalar damage variables. Damage activation functions based on the LaRC04 failure criteria were used to predict the different failure mechanisms occurring at the ply level.

Camanho investigated structural failure of laminated composites due to accumulation of several damage mechanisms such as matrix cracking, fiber fracture, fiber kinking, and delamination. He developed a tool for calculating the strength and damage tolerance of advanced composite structures based on Continuum Damage Mechanics [45]. The models were implemented in a non-linear Finite Element code ABAQUS and developed to predict the onset and type of damage, damage propagation, and structural collapse.

Progressive failure modeling methods used for structural analysis including failure initiation and material degradation were presented by Knight [46]. Different failure initiation criteria (maximum stress criteria, maximum strain criteria, Tsai-Wu criteria and the Hashin criteria) and material degradation models were described to define progressive failure formulations. The material degradation model was based on the ply-discounting approach and a parametric study for laminated composite structures was discussed.

For progressive failure analysis of composite structures under dynamic aeroelastic loading, a finite-element model was presented by Cardenas et al. [47]. The model, based on a shell formulation, was implemented in the commercial software tool GENOA.

An energy-based stiffness degradation method was proposed by Liu and Zheng to predict the progressive failure of the composite laminates, based on the continuum damage mechanics [48]. The calculated load–displacement curve and the final failure strength of structure were compared with experiments and other existing models.

Hansen and Garnich presented that a multicontinuum theory designed specifically for nonlinear progressive failure analysis of composite material systems [49]. A theory was developed to do structural analysis while allowing each constituent to retain its own identity. A finite element formulation for composite structures based on a volume fraction mixture theory was proposed . Later, Mayes and Hansen proposed a constituent stress-based failure criteria to construct a nonlinear progressive failure algorithm for investigating the material failure strengths of composite laminates [50]. The proposed failure analysis methodology was used to simulate the nonlinear laminate behavior and progressive damage of selected laminates under both uniaxial and biaxial load conditions up to their ultimate strength. This criteria, based on multicontinuum theory, uses Hashin criteria in constituent level. Additionally, a comparison of multicontinuum theory based failure analysis with experimental results was performed by Mayes and Hansen [51].

In the cases of cylindrical composite tubes, Levi et al. tested CFRP composite tubes under tensile axial loading up to failure related to lay-up configuration and evaluated strength properties as well as failure mechanisms [52]. Benamira et al. showed that in the composite tube the plane of failure was in line with the principal direction and under several loading conditions, the small damage was followed by brittle failure [53]. Fam et al. presented the behavior of GFRP composite thin-walled tubular poles subjected to combined lateral and axial loads [54]. A FEA model was developed and analysed for geometric nonlinearities. Two failure criteria, namely the Tsai-Wu material failure of composites and instability buckling failure were applied. Martins et al. studied the failure pressure of filament wound GFRP composite tubes subjected to internal pressure [55].

In case of testing of composite cylinders, two carbon-fiber-reinforced, CS and VS, composite cylinders were tested in bending by Blom et al. [11]. The cylinders were optimized for maximum buckling load carrying capability under bending. They showed that the VS cylinder was able to redistribute the applied loads around the circumference, resulting in lower strain values at both the tension and the compression side of the cylinder and an improvement of the buckling load by 18 percent compared to the constant stiffness conventional cylinder.

1.3 Hypothesis

In this thesis, the objective is to analyze laminated composite shells with varying cutouts under pure bending and combined loading. By applying nonlinear progressive failure analysis, it is aimed to find mechanical response and failure characteristics. It is expected to find different failure modes for the cylindrical fiber laminated composites with cutouts. The results of parametric study for both constant-stiffness shell and variable-stiffness shell, varying both the location and size of the cutout, on the maximum load levels and predominant failure modes are expected to provide a failure mode map. Finally, by performing bending test with specified cutout location and size, it is aimed to compare numerical analysis results with the testing results.

2. NON-CONVENTIONAL CFRP COMPOSITES

Laminated composites, especially carbon fiber reinforced composites that are mostly applied in the aerospace or automotive industries generally consist of conventional layers with 0°, 90° and ±45° fiber orientations. The use of specific limited fiber orientations is due to the times when composites were being manufactured manually, which made it very difficult to create distinct fiber orientations other than 0°, 90° and ±45°. If additional stiffness changes were needed, it was obtained by locally changing the number of plies within the laminate. However, with the introduction of automated fiber placement machines, any fiber orientations have been able to be applied including steered fiber orientations.

It is known that, the stiffness of a laminate depends on the orientation of plies; in conventional laminates since the fiber orientations do not change, the whole laminate has constant stiffness. On the other hand, with the use of steered fiber concept the fiber

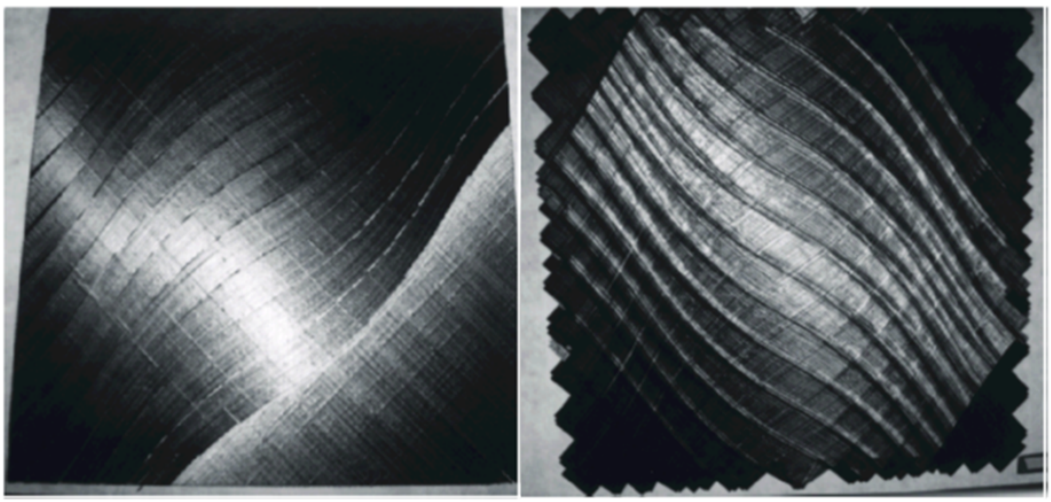


Figure 2.1 : Fiber-steered panels built by Tatting and Gürdal in 2002 [4].

orientations are changing from point to point in a ply causing the stiffness variation in the laminate. With the application of steered fibers, it has become possible to obtain variable stiffness properties within composite laminates. In a VS composite, the stiffness can be tailored to create more efficient load variation, resulting in lighter and stronger laminates compare to traditional laminates.

One of the initial studies that covers the tow-placement technology and fabrication of VS laminates were presented in the work of Tatting and Gürdal [4]. In that study, the flat panels shown in Figure 2.1 were optimized for in-plane compression and shear, taking into account manufacturability, based on advanced fiber placement technology. Improvements in load carrying capability increased up to 100% when compared to conventional laminates depending on the ply configuration, load condition and design method.

2.1 Fiber Placement Technology

Initially, the fiber reinforced composite material manufacturing were being implemented mostly by hand layup applications. However, high material cost in addition to the inefficient manual labor would increase the product cost and on the other hand will decrease the reliability due to varying quality of manual process depending on person. In addition to that, it was only possible to lay up certain fiber orientations. Therefore, automated fabrication processes has become a solution to resolve these problems, providing reliable and improved quality component production with a reduced production cycle time, in addition to the aforementioned steered fiber capabilities that will be possible to apply.

To be able to obtain very high weight efficiencies in aerospace applications, using CFRP composite materials became one of the primary motivations for the development of cost effective fabrication techniques for manufacturing of especially complex composite material parts. One of the most successful examples of a composite fabrication technique is filament winding, where pressure vessel can be fabricated. Filament winding has also been successfully extended to stiffened structural components such as grid-stiffened panels and geodesically stiffened shells. On the other hand, filament winding has some shape limitations, which are basically restricted to convex geometries [5].

For improving mechanical behavior of the composite structure by changing the fiber orientation angle spatially, a more automated fabrication technology was developed. That significant advancement in laminated composite manufacturing technology is the application of precise, repeatable, automated placement of prepreg composite tows. Those systems are generally called as advanced tow-placement, fiber-placement,

or tow-steering systems. They have been being used for fabrication of advanced composite structures. The system typically has a tow placement head with multiple degrees of freedom (DOF), which is mounted on a moving base with several translational DOF. A plate base or mandrel with additional rotational DOFs may provide a tool surface on which the tows are placed. Head of a gentry type of automated fiber placement machine is shown in Figure 2.2. Advanced fiber placement (AFP)

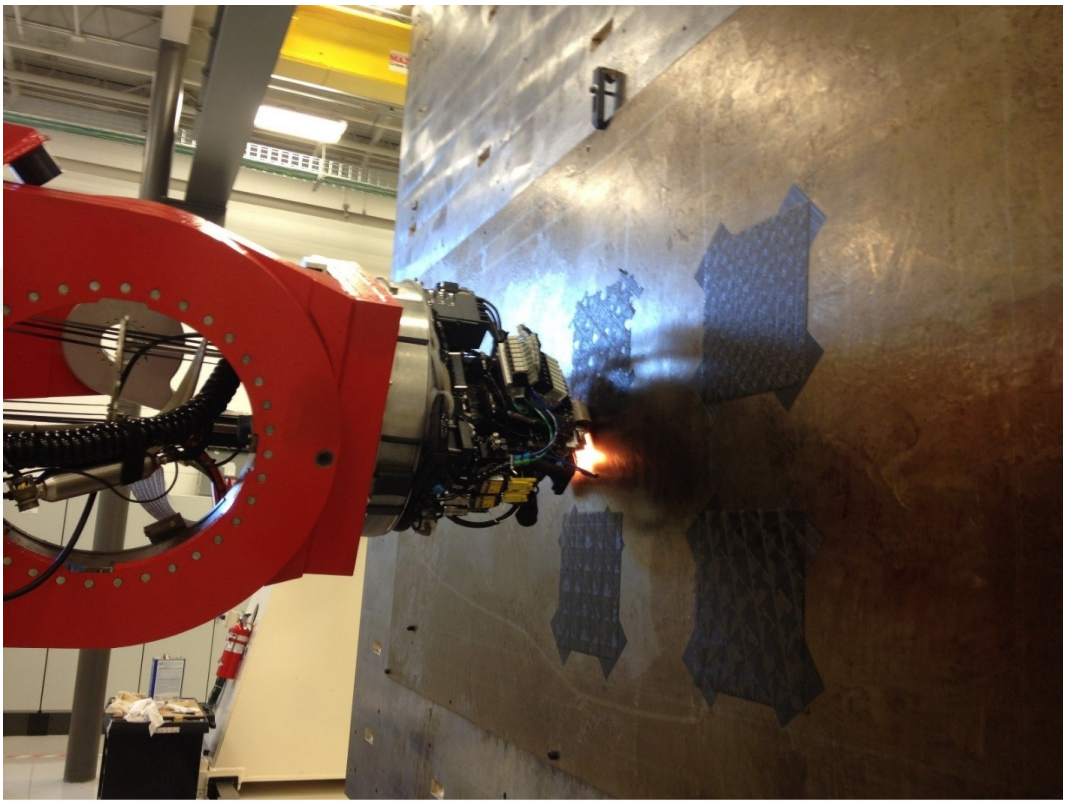


Figure 2.2 : Gentry type automated fiber placement machine.

can be defined as a fully automated process for the production of fiber reinforced composite laminates. Most of the currently available AFP machines deposit thermoset prepreg tow materials and thermoplastic materials. In addition, there are still some ongoing researches on using dry fibers during manufacturing of laminated composites that will eliminate shelf life of fiber tows and will help to keep the machine head clean. Currently, in aerospace industry, generally carbon fiber prepregs have been being used.

Most of the fiber placement systems have seven degrees of freedoms. The axes of freedoms are three translational axes, three rotational axes and one axis is the rotation of the specimen base. In addition, if robotic specimen base is used, the DOF of the fiber placement system maybe further increased. This provides the flexibility to position the fiber placement machine head onto the surface of the part and enabling the production

of complicated composite parts. A picture of an gentry type AFP machine located in McNAIR center/USC is shown in Figure 2.3. During the fiber placement process, tows



Figure 2.3 : A view of an Ingersoll AFP machine, mandrel and the head in McNAIR Center.

of prepreg tapes, shown in Figure 2.4, are placed on the surface in parallel fibers, called courses. Typical tow widths are 1/8 inch, 1/4 inch and 1/2 inch (3.175 mm, 6.35 mm and 12.7 mm). For a tow width of half inch, a maximum of 32 tows can be placed on the surface simultaneously, resulting in a course width of 16 inches.

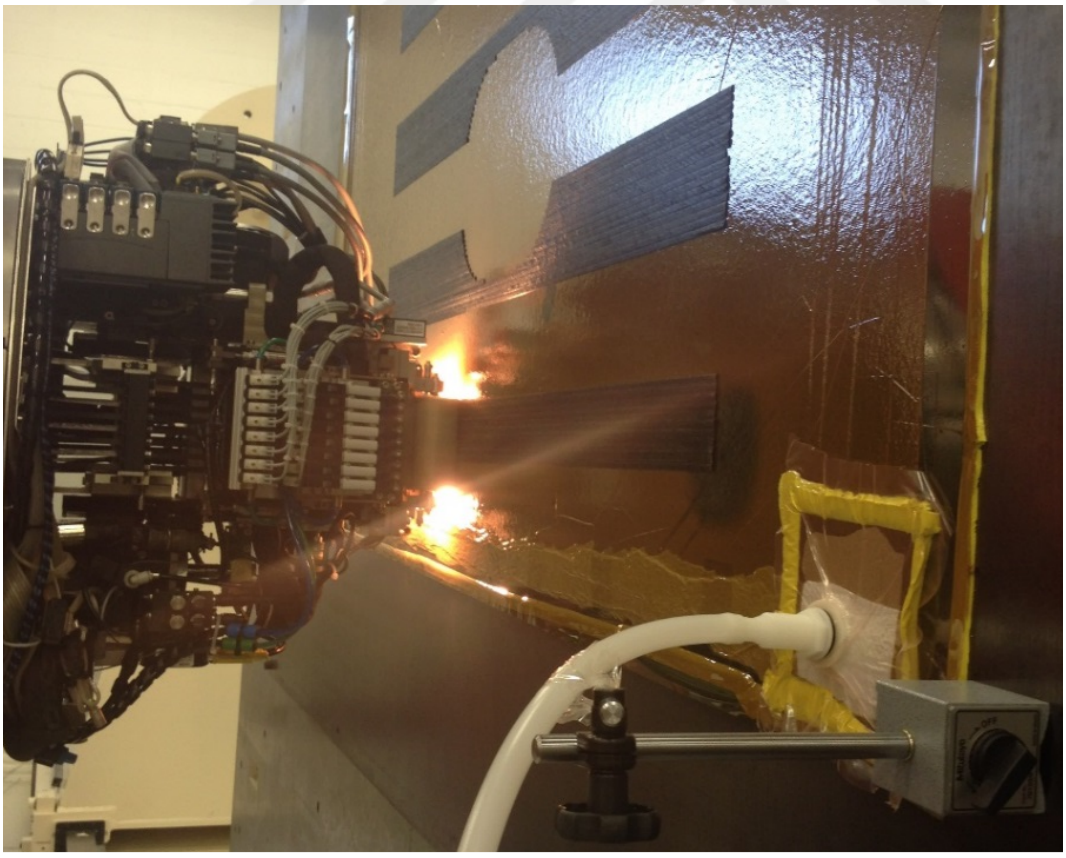


Figure 2.4 : Tow placement process.

2.2 Variable Stiffness Laminate Design and Manufacturing Constraints

In traditional design of fiber reinforced composite laminate, each ply within the laminate has constant fiber orientation resulting constant stiffness property throughout the composite. However, by allowing the fibers to steer allows a spatial stiffness variation in addition to non-uniform stress state and changes principal load paths. During the tow-steered laminate design, the aim is usually to spread the stress to non-critical locations by creating load paths.

On the other hand, steered fiber courses can cause overlaps or gaps if the course path kept constant. The tow cut and restart capability of fiber placement machines allows the variation of the course width, so that it can be used to reduce the gaps or overlaps between adjacent courses that resulting from the geometry or steered fiber courses. Gaps can be reduced by decreasing the distance between the course, while overlaps can be minimized by cutting and restarting tows. An example of a gap and overlap between four courses is shown in Figure 2.5 due to distance change between the centerlines of the courses. In manufacturing of the tow-steered laminated composites,

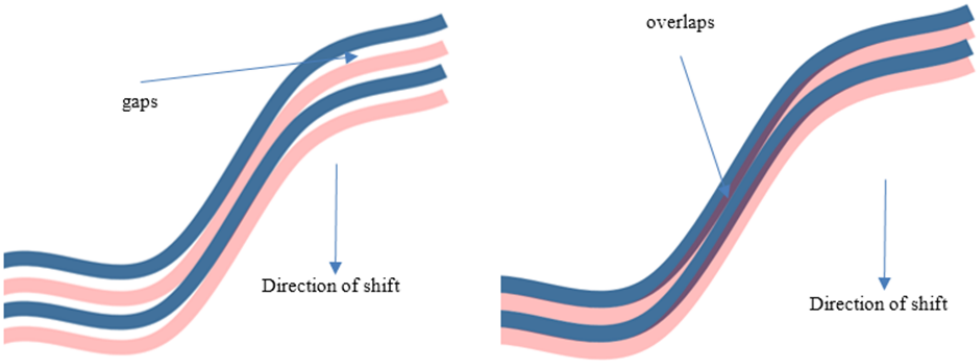


Figure 2.5 : Gaps and overlaps between four courses.

some constraints arise from the fiber placement machine capabilities as described in the following sections.

2.2.1 Turning radius of the course

In the tow-steering applications, the minimum turning radius of the machine head during fiber placement is an important limiting factor. For the application on curved surfaces or steered fiber application on any surface, the curvature of the surface or fiber generates a variation of the fiber orientation angle along the path. The turning radius required by the fiber placement head and relative placements of the inner and outer

tows depends on the radial location of the tow placement course. Minimum turning radius that the course can maintain is the limit of the fiber placement. Below that limit, the inner edge of the tow start to wrinkle causing the reduction in the strength of the structure due to cracks on the fibers and reduces the quality of the product. To be able to avoid this phenomenon a minimum turning radius for the fiber path is defined based on the geometry, material and tow width. This constraint is defined as the curvature constraint. For example, the AFP machine that used in this study has the allowable turning radius of 25 inches (635 mm) on a flat surface using 24 tows with a total head width of 3 inches (76.2 mm). It should be noted that the turning radius is defined based on the curvature of the center of the fiber placement head, not the inner tow. For courses with different number of tows, the minimum constraint value may change. In addition to that, for different materials the wrinkling properties may change, causing minimum turning radius value to change. Some of the pioneer researches on minimum turning radius of a curvilinear fibers were performed by Tatting and Gürdal [4], [5] on plate laminates. The studies were carried out in details to find out optimum curvilinear path to improve the structural response of the panels.

2.2.2 Tow cut length

This constraint is related to the minimum length of a tow that can be accurately placed onto a surface. The limit directly depends on the distance between the cutting mechanism and the clamps and rollers that hold the tows within the fiber placement head. The tow cut and restart must be accurately controlled enough to able to feed correctly the compaction roller and place the tow on the part [5].

2.2.3 Coverage parameter

In advanced fiber placement machines, cutting tows near a limiting curve or boundary can be defined as the coverage parameter. When the tow course approaches to the limiting curve or the boundary, tows are cut. The purpose is to ensure the necessary coverage of the course and do not waste the material. For 100% coverage, the dropping of the tows continue until the limiting curve is passed, ensuring that the entire area is covered with fiber material.

2.3 Construction and Manufacturing of Variable Stiffness Laminates

VS laminates have some major different properties when compared to traditional CS laminates. These differences can be noticed more clearly when laminate stiffness properties are calculated. These stiffness properties are referred to as the extensional stiffness matrix [A], coupling stiffness matrix [B], and bending stiffness matrix [D]. Each matrix is symmetrical and the terms are dependent on the unidirectional elastic material properties and stacking sequence of the laminate. Although, the classical laminates have constant stiffness within all composite, in the tow-steered laminates the stiffness varies spatially resulting the laminate to be named as variable stiffness laminate. Therefore, during numerical analysis the stiffness has to be calculated individually for each element.

In classical lamination theory, it is aimed to construct balanced laminates in order to avoid shearing effects resulting from coupling between in-plane extension and shear under normal loading. In that case, A_{16} and A_{26} terms in extensional stiffness matrix [A] become equal to zero $(A_{16} = A_{26} = 0)$ so that normal loading does not produce shearing effects. Usually, balancing is obtained by; for every $+\theta$ angle ply in the laminate, a corresponding -θ ply with identical thickness and material properties exists. This can be shown through the formulas for the A_{16} and A_{26} stiffness terms for a laminate constructed with identical materials for each ply:

$$A_{16}, A_{26} = -\Sigma_{k=1}^{N} \frac{U_2}{2} t_k \sin(2\theta_k) \pm \frac{U_4}{2} t_k \sin(4\theta_k) \tag{2.1}$$

The U_i terms in Eqn. (2.1) represent constants of the ply material, while t_k and θ_k represent the thickness and fiber orientation angle of each ply [5].

In tow-steered plies, balancing the laminate cannot be simply accomplished due to the variation of the fiber orientation angles. Therefore, balancing must be satisfied on a structural level by utilizing the mirror image approach presented by Gürdal and Tatting [5]. Mirroring a VS ply about the axial-axis and transverse-axis provides the extensional-shear coupling term A_{16} and A_{26} to be equal to zero. For conventional composite laminates, mirroring about one axis produces the same effect and removes both coupling terms.

Another important parameter during the construction of composite laminates is to have symmetrical plies. A symmetric laminate is that a stacking sequence is symmetrical

about the middle surface with having same material properties, ply thicknesses, and orientation angles. This symmetry eliminates the coupling between extension and bending so that the [B] matrix is identically zero, which is usually desired in the design and simplifies many analysis. For laminates that use the overlap construction method, coupling stiffness matrix [B] terms may exist locally.

During the design of the VS laminates, the capabilities or limitations of the AFP machines becomes important to provide choices of the design variables.

2.3.1 Coordinate definition on a cylinder

The manufacturing technique of automated fiber placement machines is based on laying down a series of plies over the surface of a plate or a mandrel. Therefore, for thin plate or shell laminates, it might be assumed that the working surface is two-dimensional. For the application of tow-steering manufacturing methods, tow courses can be defined in terms of these two-dimensional surface coordinates, and then converted to three-dimensional coordinates for manufacturing the part using the coordinate transformations. Principal directions are chosen to suit the geometry under consideration, and therefore can be based on a variety of possible coordinate systems such as rectangular, cylindrical, polar or spherical coordinates. For the simplest rectangular system, fiber orientations are not altered by the transformation from fabrication coordinates, so that a straight course aligned at a discrete angle with respect to the principal direction retains its original orientation. This basic case is demonstrated in Figure 2.6a, where the solid line represents a straight path orientation with respect to the fabrication coordinates of the rectangular domain. On the other hand, for the application of geodesic line on a polar coordinate system as displayed on Figure 2.6b, although the fabrication technique remains the same, the orientation of the line with respect to the principal directions changes as a function of location. Since the orientation of the fiber with respect to a specified axis defines the stiffness response of the structure, directly projecting the tow courses on the surface geometry may not necessarily generate the fiber orientation variation that is expected. The correct path producing a constant orientation angle for a circular plate is shown in gray in Figure 2.6b. For the curvilinear path, the orientation of the fiber with respect to the principal directions is constant at all points [5]. In the design of steered fiber ply laminates, a

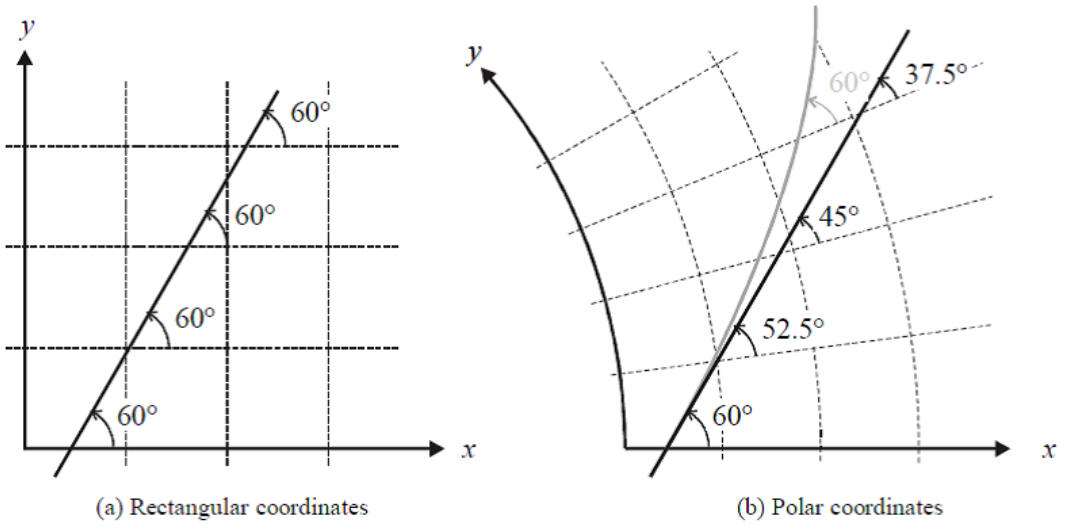


Figure 2.6 : Straight-line orientation with respect to fabrication coordinates [5].

basic method which has been first defined by Gürdal and Olmedo called directional method in which variables are based on a reference path that varies in one direction can be used [6]. Since, the coordinate system that is used for manufacturing is a two dimensional surface coordinate based on the surface geometry, the translation and rotation of steered fiber path are defined within the two-dimensional domain. This feature is also used for aligning the tow-steered plies to the structure's coordinate system, performing shifts for the fiber paths within steered fiber plies. The x', y' used for transformation are called directional coordinates for the stiffness variation [6]. The

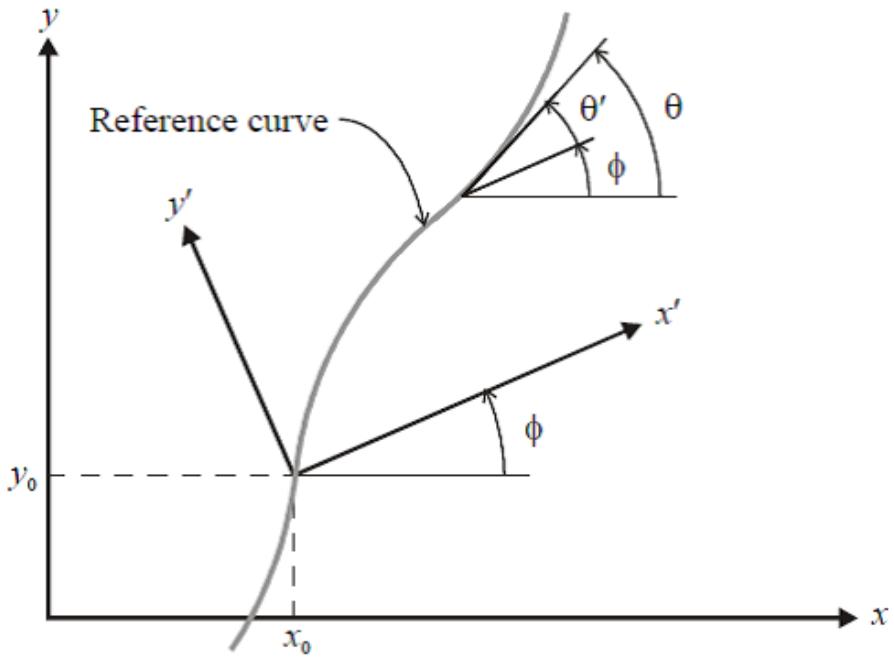


Figure 2.7 : Axes rotation for stiffness variation definition [6].

transformations of directional coordinates are shown in Figure 2.7 and for a translation of x_0, y_0 and a rotation ϕ along with equations that relate the local fiber orientation directions θ and curvatures κ are given in eqns. (2.2-2.5).

$$x' = (x - x_0)\cos\phi + (y - y_0)\sin\phi \tag{2.2}$$

$$y' = -(x - x_0)\sin\phi + (y - y_0)\cos\phi \tag{2.3}$$

$$\theta'(x', y') = \theta(x, y) - \phi \tag{2.4}$$

$$\kappa'(x', y') = \kappa(x, y) \tag{2.5}$$

The user-defined parameters x_0, y_0 and ϕ are used to place the tow course in the required position on the structure to build the remaining fiber courses. The reference curve that created in the directional coordinate system is used as a basis for the steered fibers.

Similarly, cylindrical surface can also be assumed as rectangular surface as shown in the Figure 2.8 and a rectangular coordinate system can be defined. Therefore, the vector showing an arbitrary point on the fiber path, as depicted in Figure 2.9, is defined by:

$$\vec{R_c} = x_c\vec{i} + R\theta_c\vec{j} \tag{2.6}$$

The path normal vector is:

$$\vec{\xi} = -\sin\phi\vec{i} + \cos\phi\vec{j} \tag{2.7}$$

Then, the vector pointing an edge of the course, with p is half of the course width becomes:

$$\vec{R_e} = \vec{R_c} + p\vec{\xi} \tag{2.8}$$

The effective course width (w_e) is defined as the course width in the direction of shift, which varies with the fiber angle if the course width w is kept constant, as can be seen in Figure 2.10. When no gaps are desired, the amount of shift is chosen to be smaller than the minimum effective course width, w_e. For example, the effective course width (w_e), shown in Figure 2.11, for a path with a constant fiber orientation on a cylinder can be calculated as equal to [3]:

$$w_e = w/\cos\phi \tag{2.9}$$

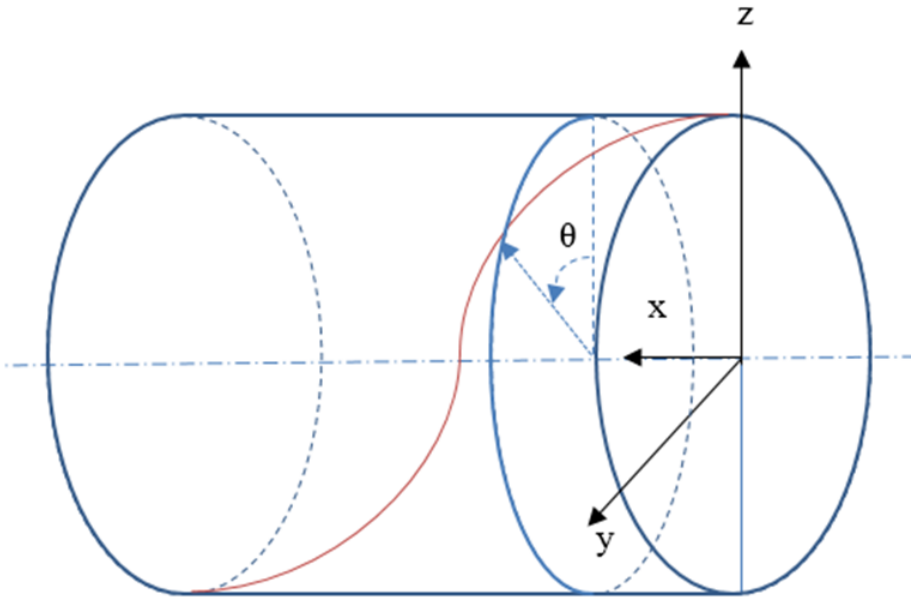


Figure 2.8 : Cylindrical surface path coordinate definition.

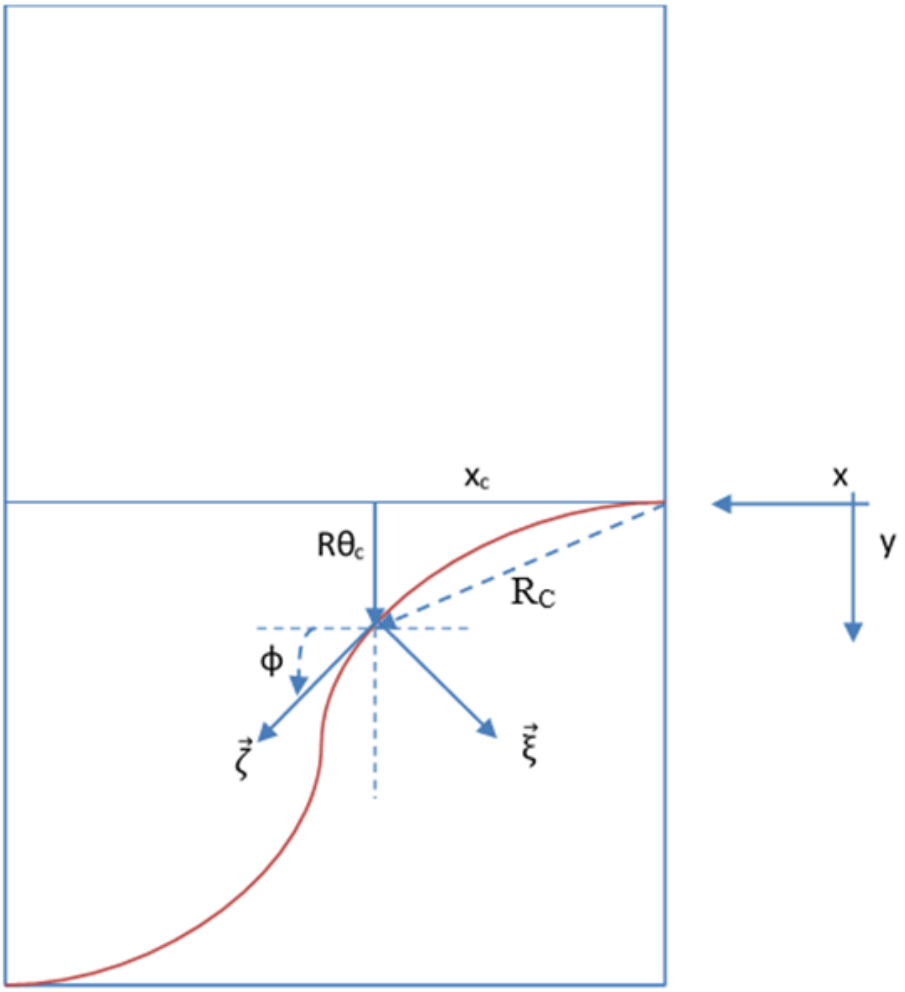


Figure 2.9 : Coordinate transformation from cylindrical surface.

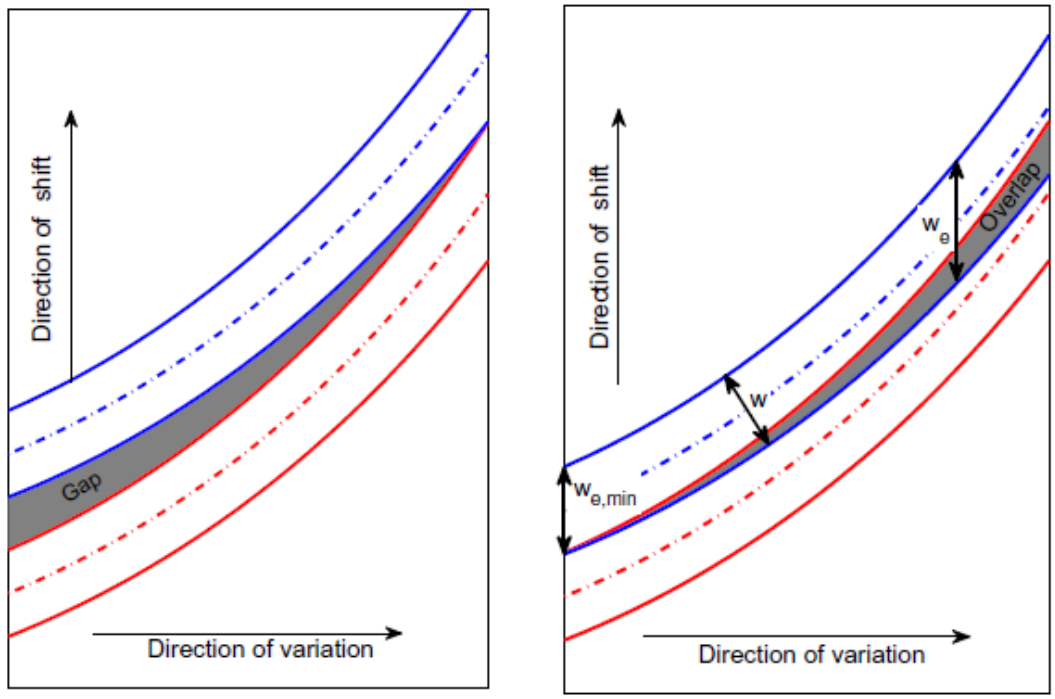


Figure 2.10 : Laminate construction by shifting courses [7].

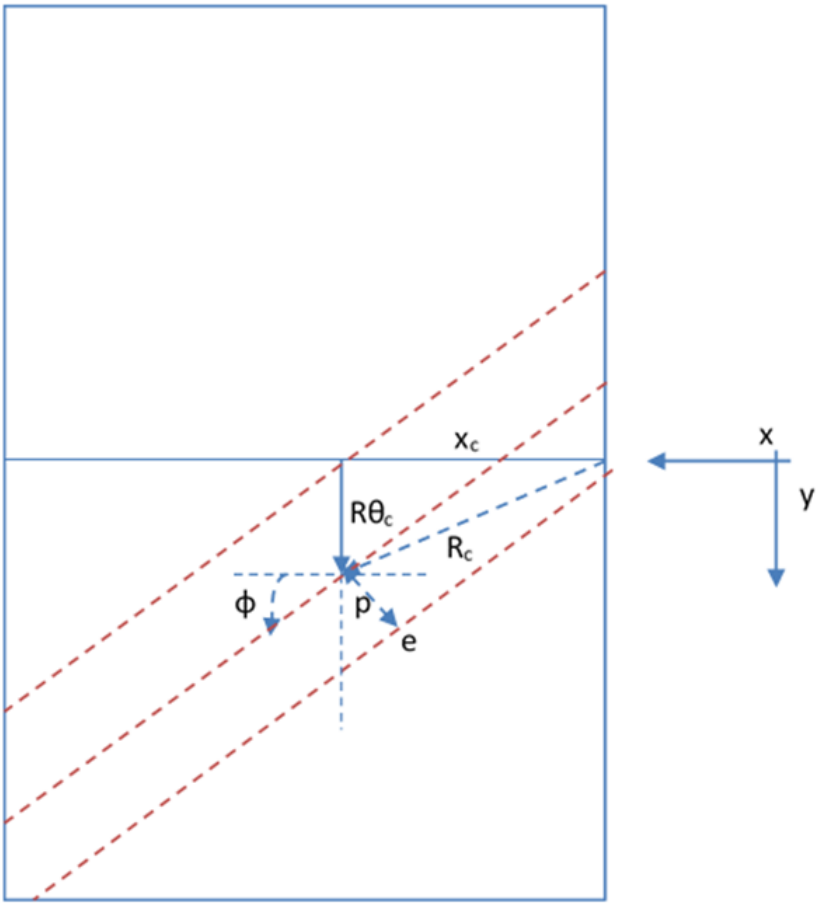


Figure 2.11 : Effective course width definition.

2.4 Ply Construction Methods

In order to completely cover the entire structure, depending on the number of tows, multiple courses must be laid up. These courses are defined with respect to a reference curve. There are several methods to apply those courses. The following sections describe some of the major techniques.

2.4.1 Parallel ply construction method

One of the most common ply construction technique is parallel ply construction method. It consists of laying down additional courses that line up with the edges of previous courses resulting no gaps or overlaps between courses and provides constant thickness ply. An example of the parallel method, with the courses including a contour plot of the fiber orientation angle, is displayed in Figure 2.12, where the dashed lines are the centerlines of each course. Since tows are positioned parallel to each other

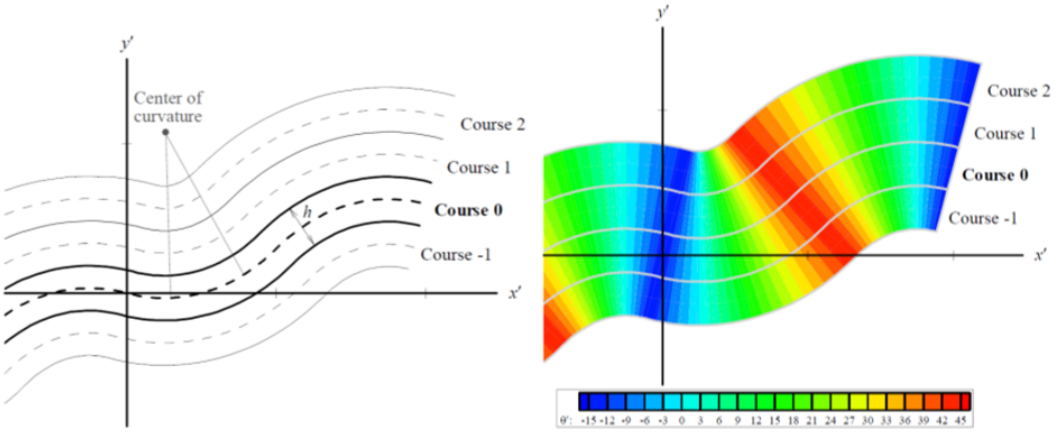


Figure 2.12 : Depiction of the parallel method ply [8].

within each individual course, the fiber angles vary smoothly along the path and all angles are identical perpendicular to the reference curve. In that case, the parallel courses on the inner side of the reference curves require smaller radius to remain aligned with the neighboring courses. To determine the fiber orientation angle for an arbitrary point within a parallel method ply, it can be referred to the equations from Gürdal and Tatting [5].

The main disadvantage of the parallel ply construction method is that tow-steered plies that possess a large stiffness variation may not be possible due to the smaller turning radius required for subsequent courses.

2.4.2 Shifted ply construction method

Shifted ply construction method utilizes copies of the reference path for the additional courses, which creates larger stiffness variation that may be more useful. Examples of shifted course are shown in Figure 2.13, where identical courses are placed next to the reference course with a shifted distance of s. Due to the curvature of the path, the top of one course does not match up with the bottom of a neighboring course, depending on the shift distance, gaps or overlaps may occur between courses. The rate of gaps and

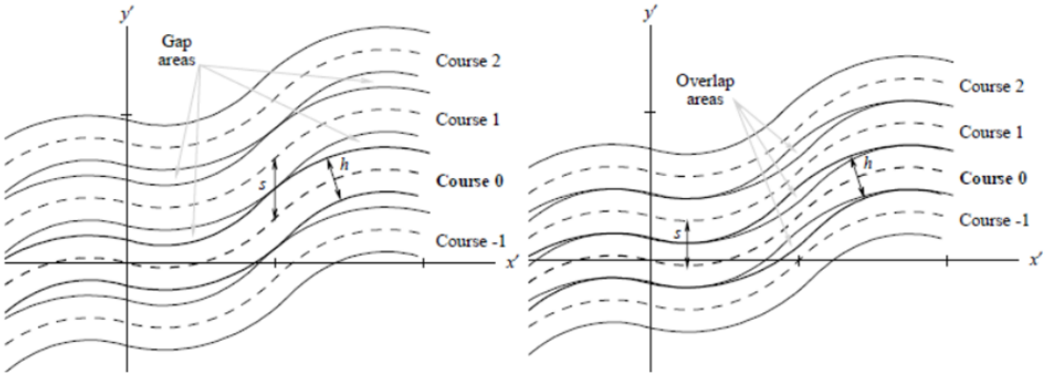


Figure 2.13 : Shifted configuration for courses with gaps and overlaps [8].

overlaps may be adjusted according to a desired configuration. In practice, allowing overlaps for curvilinear fiber paths produces regions that contain extra plies within the stacking sequence. Thus, the overlap method produces additional plies within the overlap regions, causing areas of higher stiffness through a change in thickness.

2.4.2.1 Tow-drop and overlap ply construction methods

Tow-drop method, utilizes the advantage of automated fiber placement machines to individually cut the tows within a course so that the overlap region is adequately covered without any overlapping of plies taking place. Decisions on when to drop tows from each course are made based on minimizing these gaps as well as some other fabrication requirements. The dropping of individual tows as the path approaches to the part boundaries or other tows is a very useful process for creating laminated structures. For this method, every laminate point will assume to be adequately covered by the course applied by the next shifted path. This produces a ply of constant thickness with small discontinuous jumps in the fiber angle from one course to the next. A contour plot of the fiber orientation angle for several courses that emphasizes these details is displayed in Figure 2.14. The overlap ply construction method is similar to

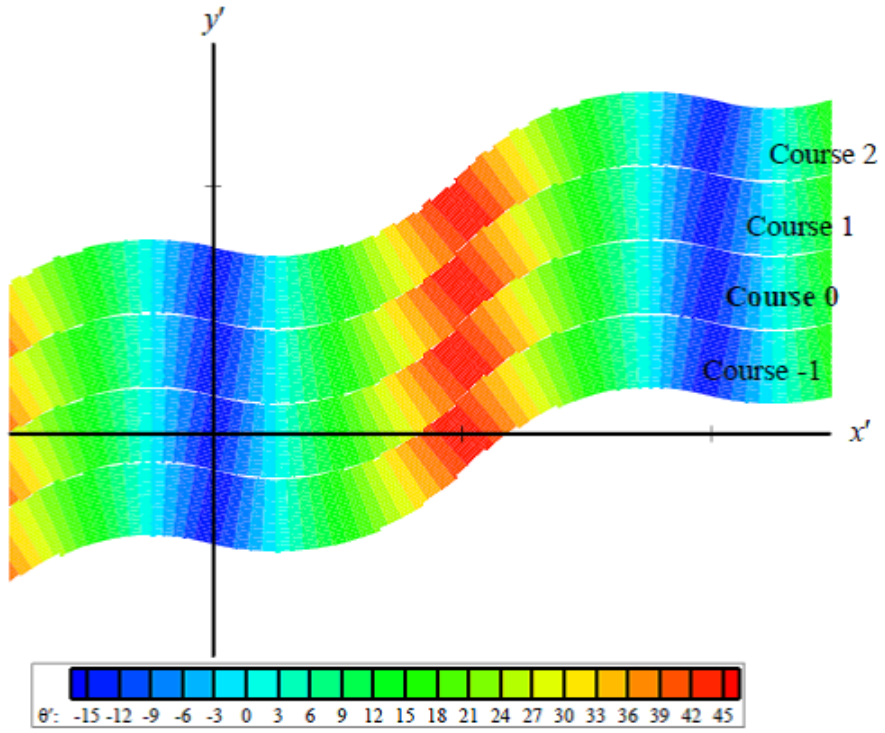


Figure 2.14 : Contours of fiber orientation angles for tow drop method [8].

the tow-drop construction method without the constraints of cut/restart for each tow. Instead, neighboring courses are allowed to overlap one another, producing areas that possess two or more layers within a single ply definition.

2.4.2.2 Point-wise ply construction method

It might be necessary to define specific fiber orientation angles at different points within a laminate to produce a transition between regions of a laminate that require varying orientation values. Figure 2.15 shows a rectangular domain for a flat panel, where the left and right sides are desired to have the particular fiber orientation angles of T_A and T_B, respectively. Since the angles do not match, tow steering is used within a transition region to vary the fiber orientation angle from one value to the other. The transition region uses circular arcs along with parallel courses, and the associated ply paths are indicated by dashed lines for the tow centers and solid lines for the tow edges. The resulting ply provides a seamless transition between the two regions, and is generally used to blend different laminates within a structure. Since the transition region is composed of simple arcs, simple trigonometry can be used to generate solutions to obtain the resulting fiber orientation angles. The center of the arcs is calculated by finding the intersection of the two lines drawn perpendicular to the

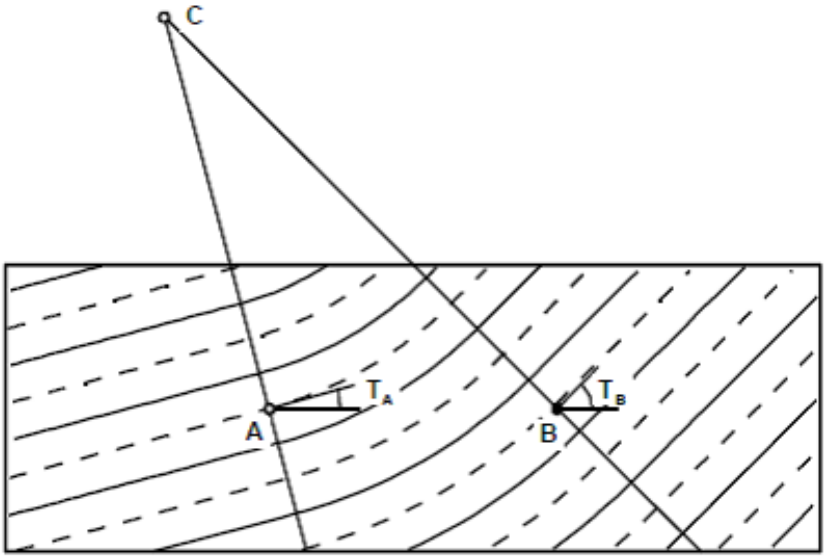


Figure 2.15 : Point-wise method [8].

desired fiber orientation values at their respective locations. Using the xy-coordinates at each point, the center point can be expressed as:

$$x_c = [-(x_B \cos T_B + y_B \sin T_B) \sin T_A + (x_A \cos T_A + y_A \sin T_A) \sin T_B] / \sin(T_B - TA) \tag{2.10}$$

$$y_c = [-(x_B \cos T_B + y_B \sin T_B) \cos T_A + (x_A \cos T_A + y_A \sin T_A) \cos T_B] / \sin(T_B - TA) \tag{2.11}$$

Lines connecting the center and the point locations divide the domain into three regions, for which the fiber orientation angle calculation can be performed. Note that, the points A and B do not necessarily have to exist within the same course, but have to be correctly oriented along the dividing lines. The main reference course is defined to run through point A. For the ease of manufacturability, the minimum turning radius can be calculated by determining the minimum distance from the center point to the domain of the part. Suitable selection of the variation locations and fiber angle values can lead to a smooth transition of variety of plies between two regions that require different angle ply orientations.

3. PROGRESSIVE FAILURE ANALYSIS

The numerical analysis of the CFRP cylindrical shell with cutouts is performed by applying a nonlinear progressive failure analysis (NLwPFA) method which best reflects the real failure conditions. During the NLwPFA, also theoretical and real geometric imperfections and more realistic flexible boundary conditions were included. In the following chapters, it can be seen that by including the progressive failure effect, the failure load level decreases close to the real test result. Therefore, it is important to include an efficient progressive failure analysis method.

For the application of the progressive failure analysis, ABAQUS supplies a capability to model anisotropic damage in fiber-reinforced materials. The response of the undamaged material is assumed linearly elastic, and the model is intended to predict behavior of fiber-reinforced materials for which damage can be initiated without a large amount of plastic deformation. The Hashin initiation criteria [43] are used to predict the onset of damage and the material stiffness is reduced gradually as deformation continues to accumulate after the initiation criterion is met. The damage evolution law is based on the energy dissipated during the damage process. However, this type of instantaneous, discrete stiffness reduction normally causes severe convergence difficulties for finite element codes. Since the aim of this study is not to develop a novel progressive failure model, it was decided to use the commercial Helius Progressive Failure Analysis (PFA) tool [9] to monitor this aspect of the solution.

Helius PFA is composed of a set of software modules and a composite material library that integrates with the ABAQUS finite element analysis, providing material modeling capability for unidirectional and woven fiber-reinforced composite materials. Helius PFA utilizes a form of multiscale material modeling based on Multi-continuum Theory (MCT) [50] that will be described in the following section.

In a finite element analysis of a composite structure, Helius PFA decomposes the composite average stress/strain field into constituent average stress/strain fields. The constituent average stress states are used by Helius PFA to predict damage evolution

and material failure individually for each constituent material in the microstructure level. Subsequently, the current damaged microstructure is homogenized to provide a more accurate assessment of the current composite average stiffness. Several predefined ABAQUS subroutines are utilized to analyze the model for damage, recompute the constitutive relations due to this damage, and update the response and stress levels within the model. These calculations were performed at each Gaussian integration point within the model, and failure counts for points within each layer were also tabulated. However, the method works best when an entire element is represented by one integration point as opposed to several points, since it is difficult to model partial failure within one element. This is the principal motivation for the use of the S4R element.

It is a widely accepted that a good convergence is difficult to achieve in a progressive failure simulation of a composite structure. In fact, many progressive failure simulations terminate early, not due to global structural failure, but rather due to the inability of the finite element code to obtain a converged solution at a particular load increment. Helius PFA was tested and it significantly improves the overall convergence rate and robustness of finite element simulations of progressive failure of composite structures. Therefore, it was chosen as a PFA tool for this study.

3.1 Multicontinuum Theory

Many enviable failure theories have been developed for composite laminates to determine both fiber and matrix failures initiated within a composite material. Hashin criteria [43] is one of the first criteria of such an approach in which fiber and matrix failures within a composite are based on the composite stress fields. Following the motivation of Hashin, the multicontinuum theory utilizes constituent stresses to predict constituent failure of the fiber and matrix rather than composite stresses to predict constituent failure [56]. Helius PFA was developed based on multi-continuum theory [50]. In traditional continuum mechanics, stress and strain quantities are averaged over the entire heterogeneous microstructure of the composite material. Whereas, in multi-continuum theory, the identities of the distinct material constituents within the microstructure as depicted in Figure 3.1 are retained. Consequently, the physical quantities are averaged over each individual constituent material. It automatically

calculates and inserts any extraneous stiffness parameters that are required by elements that use reduced integration [50].

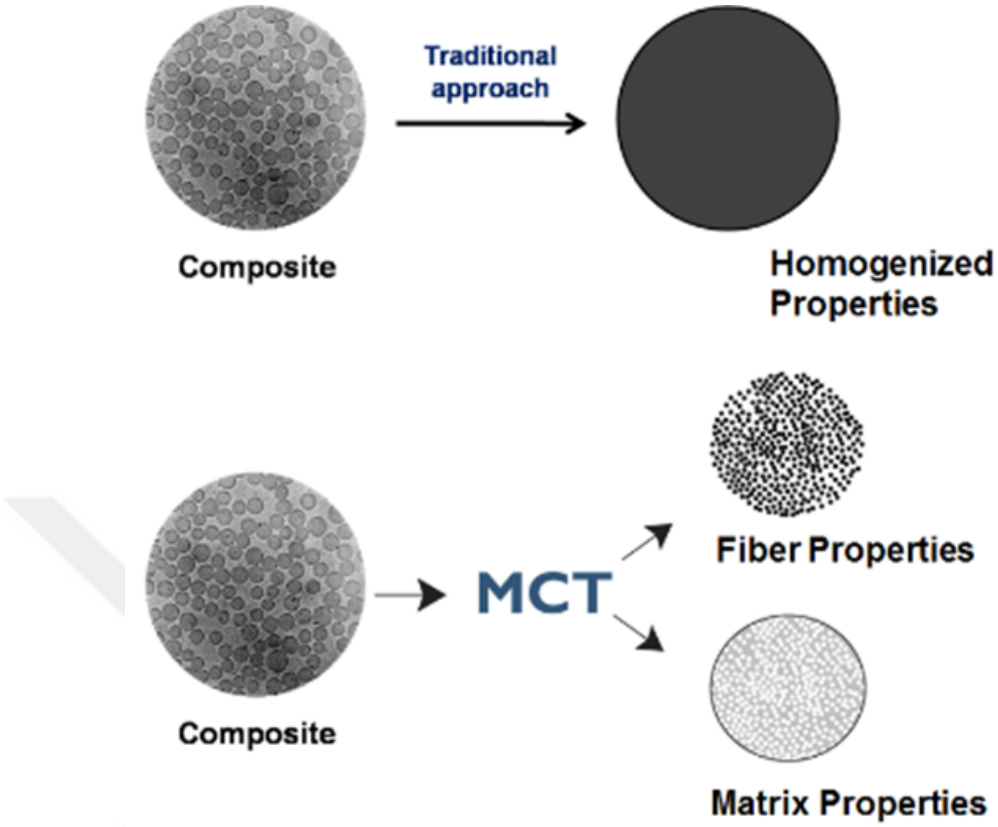


Figure 3.1 : Multi-continuum Theory approach [9].

Basically, MCT focuses on two concepts:

1) The development of relationships between the various constituent average quantities,

2) The development of relationships that link the composite average quantities to the constituent average quantities.

Multicontinuum theory similar to the Hashin failure criteria, account for stress interaction which is quadratic in stress and that choice of a quadratic polynomial is based on curve fitting considerations [51]. On the other hand, MCT applies the failure criteria at the constituent level rather than the composite laminate scale. Therefore, it can be assumed that MCT is based on Hashin criteria at constituent level.

Due to material symmetry, it is assumed to have transverse isotropy for each of the unidirectional lamina. Therefore, the constituents' failure criteria may be expressed in

terms of transversely isotropic stress invariants as follows [51]:

$$I_1 = \sigma_{11} \tag{3.1}$$

$$I_2 = \sigma_{22} + \sigma_{33} \tag{3.2}$$

$$I_3 = \sigma_{22}^2 + \sigma_{33}^2 + 2\sigma_{23}^2 \tag{3.3}$$

$$I_4 = \sigma_{12}^2 + \sigma_{13}^2 \tag{3.4}$$

$$I_5 = \sigma_{22}\sigma_{12}^2 + \sigma_{33}\sigma_{13}^2 + 2\sigma_{12}\sigma_{13}\sigma_{23} \tag{3.5}$$

The criterion for fiber failure is;

$$\pm K_{1f} I_{1f}^2 + K_{4f} I_{4f} = 1 \tag{3.6}$$

where

$$\pm K_{1f} = \frac{1}{\pm S_{11f}^2} \tag{3.7}$$

$$\pm K_{4f} = \frac{1}{\pm S_{12f}^2} \tag{3.8}$$

The $\pm$ symbol indicates that the appropriate tensile or compressive ultimate strength value is used depending on the constituent's stress state.

For the matrix constituent, the failure criterion is;

$$\pm K_{3m} I_{3m} + K_{4m} I_{4m} = 1 \tag{3.9}$$

where

$$\pm K_{3m} = \frac{1}{\pm S_{22m}^2 + \pm^{22} S_{33m}^2} \tag{3.10}$$

($\pm^{22} S_{33m}^2$ indicates stress in the 3,3 direction when stress $\pm$2,2 is applied.)

$$\pm K_{4m} = \frac{1}{\pm S_{12m}^2} \tag{3.11}$$

Constituent strength parameters, as well as constituent elastic constants, are obtained from experimentally determined composite results with the help of finite element micro-mechanics. Usually those strength parameters can be obtained from the literature, otherwise it is necessary to perform the required mechanical tests. On the other hand, sometimes the fiber and matrix manufacturers also provide the mechanical properties.

3.2 The Nonlinear Analysis Method

In simple cases, linear eigenvalue analysis may be sufficient for design evaluation; however, if there is concern about material nonlinearity, geometric nonlinearity prior to buckling or unstable post buckling response, a load-deflection (Riks) analysis is performed to investigate the problem further. The Riks method uses the load magnitude as an additional unknown; it solves simultaneously for loads and displacements. This approach provides solutions regardless of whether the response is stable or unstable [57]. The proportional loading with unstable response is shown in Figure 3.2. A load

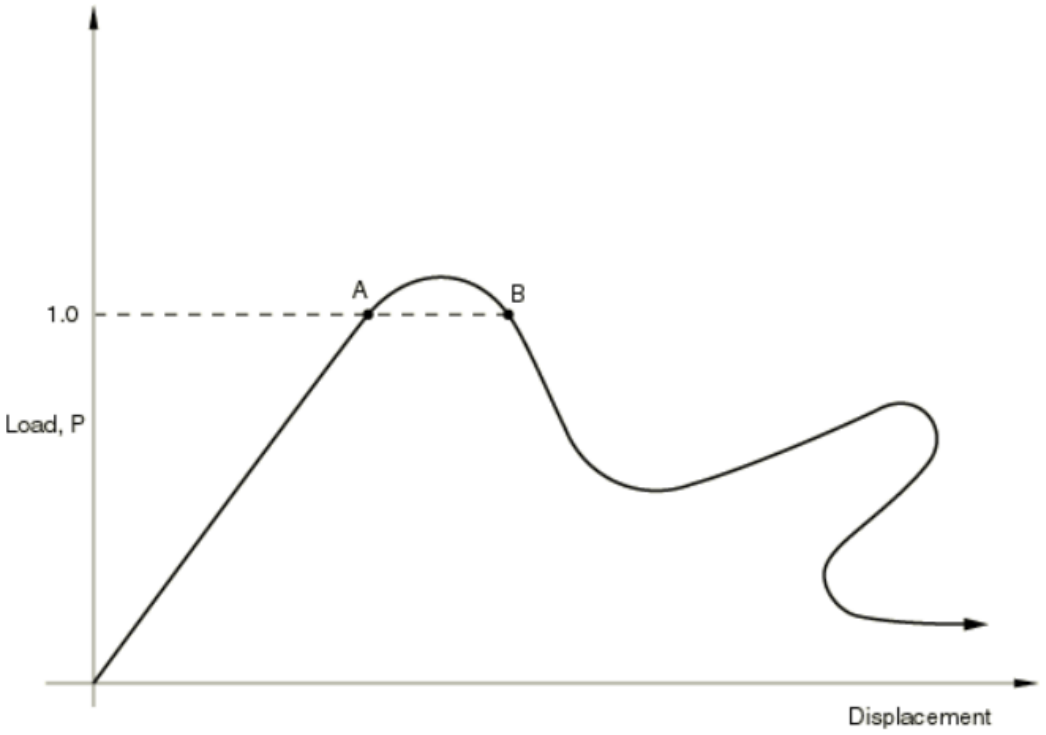


Figure 3.2 : The proportional loading with unstable response [10].

whose magnitude is defined in the Riks step is referred to as a "reference" load. This load is defined from the static buckling analysis and the loading during a Riks step is always proportional. The current load magnitude, P_{total} is defined by;

$$P_{total} = P_0 + \gamma(P_{ref} - P_0) \tag{3.12}$$

where P_0 is named as "dead load," P_{ref} is the reference load vector, and γ is the "load proportionality factor". The load proportionality factor is found as part of the solution and Abaqus uses Newton's method to solve the nonlinear equilibrium equations [10].

4. FINITE ELEMENT ANALYSIS CASES AND FORMAT OF RESULTS

This chapter explains the linear and nonlinear analyses cases and the results in details by giving some examples of the results. The commercial finite element solver ABAQUS [10] is used as the analysis tool. The generated models were compared with the models from Blom [3] including boundary conditions and measured imperfections. The following sections relate the details of the model generation and analysis options that were utilized.

4.1 Cylinder Geometry and Cutout Configurations

The geometry and cutout configurations of the CFRP cylindrical composite shell were defined in this section. The geometry was selected to simulate the fuselage of the airframe.

4.1.1 Basic Shell Geometry

The structure under consideration is a right circular cylinder with a radius R of 304.5 mm (12 in), length L of 813 mm (32 in), and an overall shell thickness H of 4.392 mm (0.173 in). The global and local coordinate systems are shown in Figure 4.1, where the local system is based on cylindrical coordinates with θ=0 at the top of the cylinder. Loading is introduced at each end of the cylinder and for this study is confined to a pure bending about the X-axis, applied in a direction so that the bottom of the cylinder is under compression and the top in tension.

The manufactured CS shell is composed of 24 plies of BMS8/276 material. This material is considered Boeing proprietary and since the design studies undertaken here are intended for future publication, a similar material (IM7/8552) is substituted that is suitable for publication yet provides acceptable agreement with the material properties of the actual test specimen (for modeling of the actual mechanical tests, the BMS8/276 material properties will be used). The stacking sequence of the CS shell is given as $[\pm 45/0_2/90_2/0/\pm 45_2/90]_s$ and the material properties used for the design studies

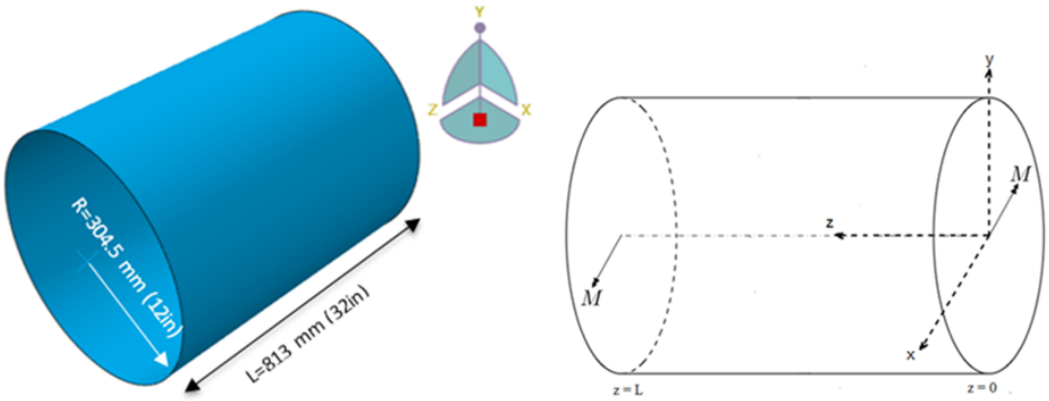


Figure 4.1 : Cylinder Geometry.

Table 4.1 : IM7/8552 (190 g/m^2) Lamina Mechanical Properties .

Property	Value
t_{ply}	0.183mm
E_1	158.510 GPa
E_2	8.963 GPa
G_{12}	4.688 GPa
G_{13}	4.688 GPa
G_{23}	3.974 GPa
ν_{12}	0.316
ρ	1580 kg/m^3
F_1^t	2500.7 MPa
F_2^t	64.05 MPa
F_1^c	1716.4 MPa
F_2^c	285.7 MPa
F_{12}^s	91.15 MPa

are provided in Table 4.1. The material properties were that of Hexcel IM7/8552 unidirectional prepreg with properties reported in qualification material property data report (NCAMP Test Report Number: CAM-RP-2009-015 Rev A) as given in Table 4.1 [58].

4.1.2 Cutout Size and Configurations

The cutout shape is defined as circular and centered longitudinally at the mid-length of the shell. The circumferential location is allowed to vary from the top to the bottom, with any configurations away from the top/bottom also containing a symmetric cutout on the opposite side to maintain left/right symmetry of the shell. The circumferential locations (β, starting from the top of the cylinder) are initially spaced at 15° intervals, with the locations near the top and bottom not utilized due to overlapping from the symmetric cutout on the opposite side. Figure 4.2 demonstrates the possible

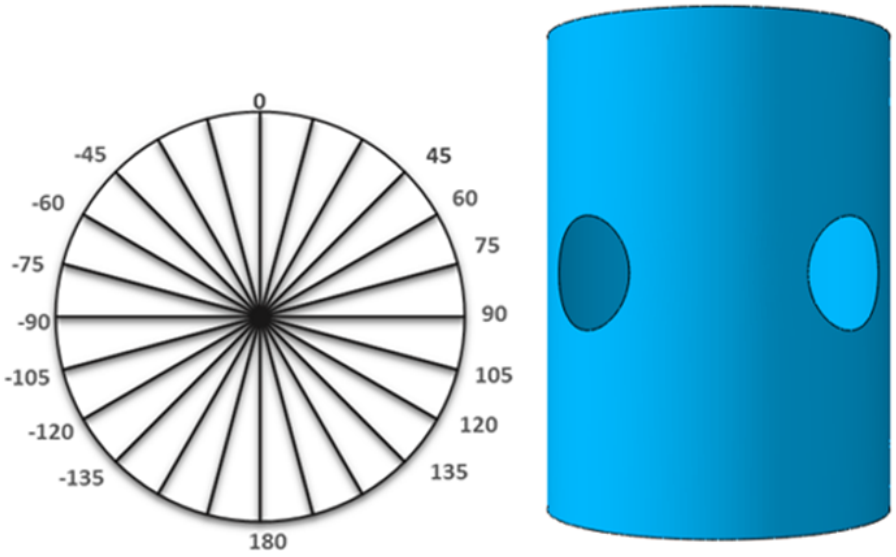


Figure 4.2 : Cutout configuration possibilities and example geometry (0.3R/45).

configurations considered in the initial design study and displays a cutout configuration located at 45°. Cutout size a=iR, represented by the radius of the circular cutout in relation to the radius of the cylindrical shell, is initially selected to represent small, medium, and large sizes (i=0.1,0.3,0.5, respectively). These sizes are meant to represent typical window or door sizes in an aircraft fuselage. Cutout configurations are represented as the size designation followed by the circumferential location in the form iR/β, such as '0.3R/90' for the medium-sized cutout located at the sides of the cylinder. After the initial design study, finer gradations of the cutout size and location are employed to zero in on the desired configuration to be selected.

4.2 Modeling and meshing

The cylinder is modeled using discrete S4R shell elements, which is a reduced integrated, general-purpose, finite-membrane-strain shell element with four nodes and one integration point. The fully integrated S4 shell element was also considered (representations displayed in Figure 4.3), however its increased computation-time and unsuitability for progressive failure analysis (discussed later) motivated the selection of the simpler S4R element. Hourglass control was used within ABAQUS for the S4R element to avoid the undesired hourglass deformation of the elements.

Mesh size convergence studies were performed using a linear eigenvalue analysis to determine an acceptable sizing for each element type. The convergence of the mesh

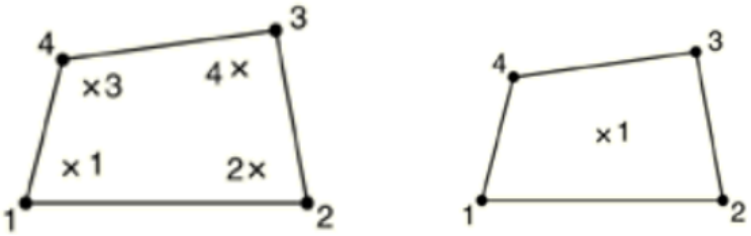


Figure 4.3 : S4 and S4R elements.

density is based on the relative change of the eigenvalues as the mesh is refined. During mesh size convergence analysis, S4 and S4R element type was used. The mesh sizes were selected as 30, 20, 15, 10, 7.5 and 5 mm. The analyses were run in a workstation and the analyses user times were taken as reference. The result is given in Table 4.2 and Figure 4.4.

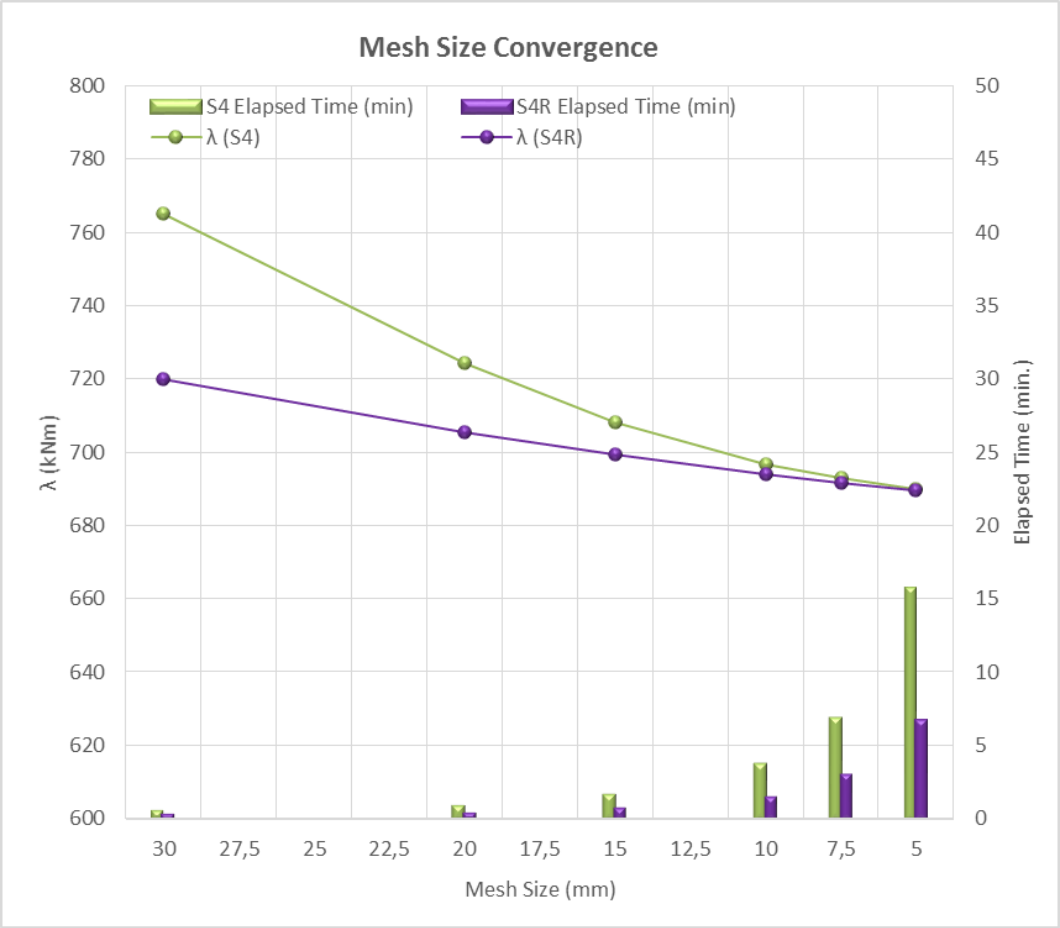
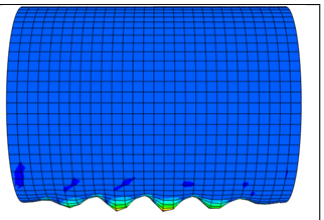
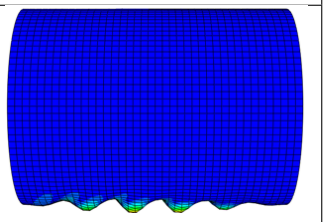
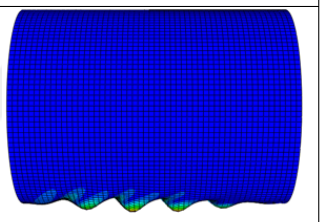
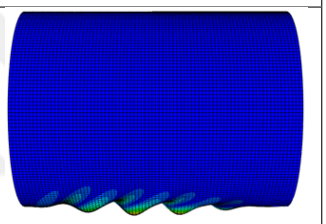
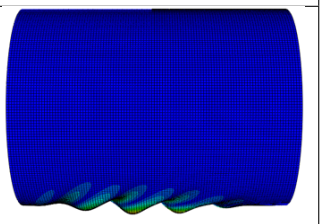
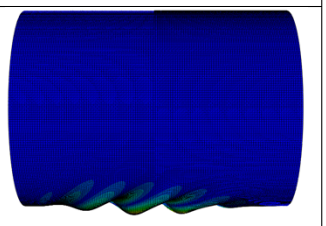


Figure 4.4 : Mesh Size Convergence.

While the reduced integration S4R element was used, it can be seen that the mesh convergence characteristic is much better compare to S4 element. As it can be seen from the Figure 4.4, the convergence after 10 mm mesh size is within acceptable limits, which the change in the result is less than 1% and the elapsed time for computation

Table 4.2 : Buckling analysis of non-cutout cylindrical shell with given mesh sizes.

Mesh Size (mm)	λ_{S4} (kNm)	λ_{S4R} (kNm)	Number of Elements	Elapsed Time (min.) S4/S4R	Mode Shape
30	765.15	720.06	1792	0.48/0.2	
20	724.41	704.45	3840	0.85/0.33	
15	708.20	699.27	6912	1.58/0.66	
10	696.79	693.80	15744	3.70/1.43	
7.5	692.88	691.43	27648	6.79/2.89	
5	690.03	689.49	61884	15.61/6.7	

is increasing which will be quite significant during non-linear analysis. Therefore, a suitable mesh size of 10 mm was chosen for the S4R element, which provides adequate accuracy without undue computational cost.

For meshing around the cutouts, a square section is constructed around the cutout location large enough to encompass its area, and all sections are meshed with the appropriate mesh size seed value to ensure compatibility along the section edges.

An example of this sectioning and the resulting mesh is shown for the 0.3R/45 configuration in Figure 4.5. The dark lines in the figure on the left represent the section lines constructed around the cutout and at the top and bottom of the cylinder. The continuity of the mesh is apparent in the figure on the right after identical seed values are used for mesh generation. The edges of the cutout are assumed to be stress free (no boundary conditions are applied there).

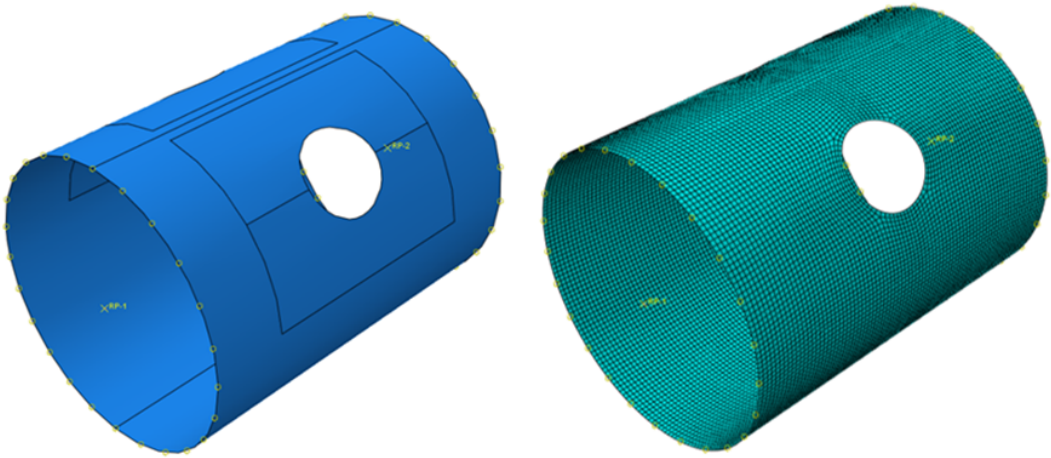


Figure 4.5 : Example section view and finite element mesh for 0.3R/45 cutout configuration.

Also shown in Figure 4.5 are the nodes used to introduce general loading. The small yellow circles around each end represent an edge constraint, where each node along the edge is tied to a reference point at the center of the end circle, denoted by the small yellow x and label at each end. Thus, each edge node is constrained to displace according to a rigid body displacement/rotation of the reference point. Rotation and displacement of the reference point, or application of forces and moments there, allows for combined loading of the cylinder (tension/compression, shear force, bending moments, and torsion). Pressurization of the cylindrical shell is also an option by enforcing lateral pressure for each shell element.

The boundary conditions at the edge of the shell are designated as clamped, restricting displacement and rotation in all directions except those imposed by the rigid body deformation. These conditions do not accurately reflect the boundary conditions during testing. Blom [3] utilized flexible boundary conditions using linear and rotational springs to better approximate the realistic interface between the shell and the testing apparatus, however their complexity is deemed unnecessary for the design study phase. Generation of the finite element model for each cutout configuration is automated using

Python scripts integrated with the ABAQUS environment. This enables rapid model generation and the ability to easily shift focus to interesting regions of the design study space.

4.3 Analysis options

To fully understand the response of the shell structure when cutouts are introduced, four different analysis types were used; namely linear static analysis, linear buckling analysis, nonlinear static analysis, and nonlinear static with progressive failure analysis. The first three types are discussed briefly here, while the addition of progressive failure analysis warrants more detail in chapter 3.

Linear static analysis is used to determine the likelihood of material failure based on the Hashin criterion [43]. This failure criterion investigates the stress state within each layer of the laminate for all elements in the structure, and determines if the values surpass the thresholds defined by the material failure constants. Distinctions are made concerning matrix or fiber failure and whether the mode is in tension, compression or shear. For most problems, matrix failure does not represent collapse of a structure since the stronger fibers are able to carry such a large proportion of the loading, therefore the failure load calculated using this analysis type is based on "first ply fiber failure" (FPFF), where the level is found where fiber failure is first encountered. The linear case used here serves well as a baseline for the more accurate progressive failure analysis using nonlinear static response, in that it helps pinpoint the onset of failure and the contribution from the cutout configuration.

Linear buckling analysis is used to calculate the critical eigenvalues and mode shapes for a shell under compressive loading. For this pure bending case, the compressive bottom half is the region of interest, though the mode shapes generated there are highly dependent on the location and size of the cutout. The linear buckling analysis assumes a "perfect" structure without any imperfections present and neglects any material or geometric nonlinearity. However, the eigenvalue analysis is extremely useful in determining the underlying causes of collapse and also serves as a worst-case imperfection for the nonlinear results. Within this analysis run, the five lowest eigenvalues and their associated mode shapes are calculated using the Lanczos option within ABAQUS.

Nonlinear static analysis is generally required for thin shells undergoing compressive loading, since these structures are highly dependent on geometric nonlinearity resulting from initial shape imperfections. Without the introduction of imperfections, the nonlinear analysis tends to follow the linear buckling solution until an unstable load value (eigenvalue) is reached and then the structure deforms into a post-buckled state. With the presence of imperfections, thin-walled structures under compression often attain a much lower maximum load due to the triggering of post-buckled mode shapes arising from the initial shape imperfections. Therefore, the nonlinear analysis introduces a non-zero imperfection into the model and a Riks method [57] is used to follow this nonlinear paths into the post-buckled range. The shape of the imperfection is, in ideal circumstances, based on actual measurements of the structure. This information also were obtained after the machining of a cutout into the specimen and the imperfection data were used in the numerical analyses. However, for the design study the typical worst-case scenario is used, where the imperfection assumes the form of the critical eigenvalue. This effectively activates the nonlinear solution and allows investigation into the post-buckled range.

To complete this nonlinear analysis, the linear buckling solution is found in the usual manner and the mode shapes of the first five eigenvalues were preserved. The nonlinear solution defines the imperfection as a small factor of the critical buckling mode or a linear combination of the calculated modes. Here we use the amplitude of the imperfection as 10% of the total shell thickness. The response is computed along the nonlinear load path, and the maximum load that is attained is recorded. Additionally, progressive failure analyses (PFA) also were assessed during this nonlinear solution, which provides the best overall estimate of the response of the shell.

4.4 Presentation of analysis results

A typical finite element result is displayed in Figure 4.6 for the non-cutout case, which provides the moment-curvature relation as well as cross-sectional deformation at significant points along the load path. The linear static solution is represented by the dark blue line and ends at the first ply fiber failure (FPFF) symbol and the lowest eigenvalue calculated by the linear buckling solution is denoted by the symbol marked by λ along the load path. Here the mode shape of the eigenvalue is shown by the

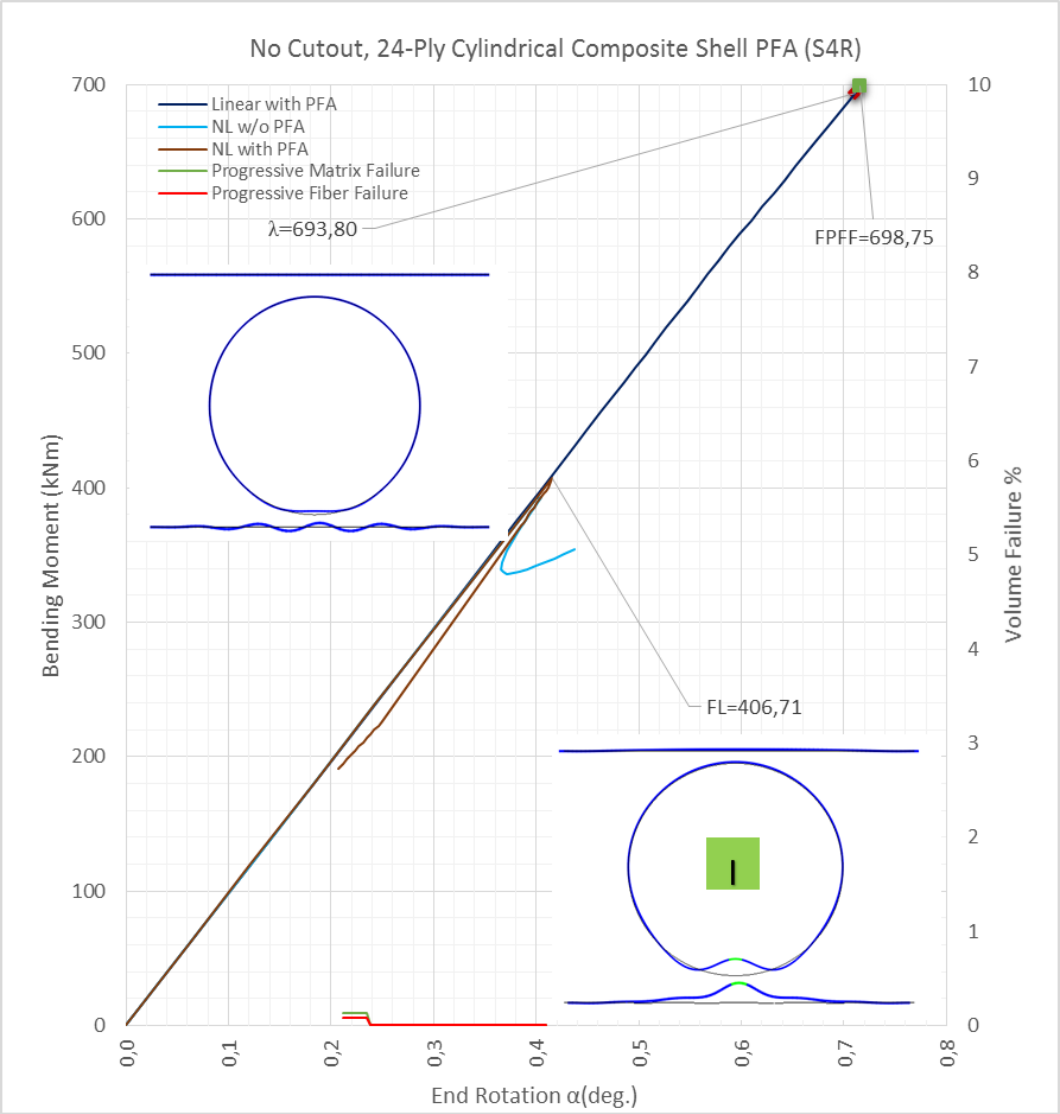


Figure 4.6 : Finite element solutions for non-cutout case.

inset cross-section to the left, where the cross-section is located at the mid-length and the lines above and below indicates the deformation of the top and bottom axial lines of the cylinder. These cross-sectional figures are also useful as indicators of the size and location of the cutouts. Responses for the nonlinear solution, with and without progressive failure analysis, are denoted by the light blue and dark brown paths, respectively. The failure load (FL) point is also indicated and the cross-sectional deformation displayed.

Additionally, the green and red lines at the bottom of the graph represent the percent of the shell volume that is considered failed due to the nonlinear with progressive failure analysis (NLwPFA) solution. These lines utilize the "Volume Failure %" axis on the right side of the graph. The initial onset of failure is often at the same point as the

failure load caused by the instability, as shown here, but can also arise before buckling for certain cutout configurations.

The green and red lines are meant to indicate these failure load values, and failure within the cross-section is also indicated, where applicable, by appropriate coloring within the cross-section. For example, one can see a green region within the post-buckled cross-section where matrix failure has initiated. Lastly, the cross-section at the FL point is also designated with a failure mode I, II, or III in green, yellow, red respectively. Figure 4.6 represents the principal elements of the response for a given cutout configuration. The appendices contain similar graphs for all configurations considered. In-depth, study of the results indicates that the overall failure estimations of the different cutout configurations can be classified into three distinct modes, described in Chapter 6 in detail.

5. BENDING ANALYSIS OF CONSTANT STIFFNESS CYLINDRICAL SHELL WITH CUTOUTS AT 90° POSITION UNDER BENDING

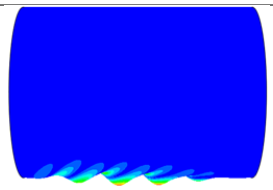
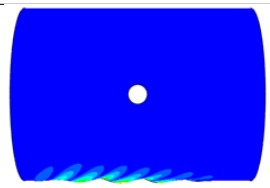
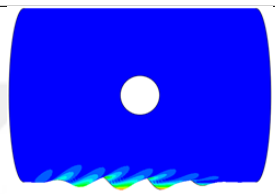
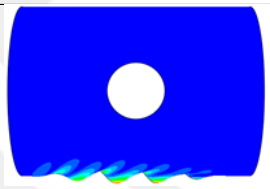
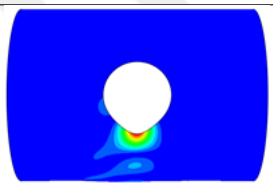
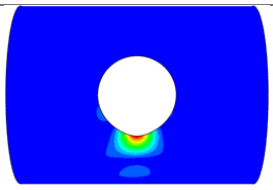
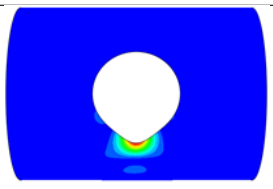
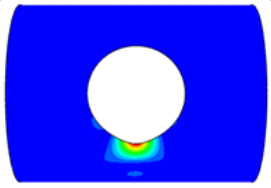
In order to analyze the cylindrical shell with cutouts, it was first decided to start the position of the cutouts at 90° position. Since the cutouts are at the symmetry axis, the only difference will be as a result of the cutout size. After the analyses at 90° position were completed, the positions of the cutouts were changed parametrically and the results will be given in the following chapters.

5.1 Linear Buckling and Nonlinear Failure Analysis for Various Cutout Sizes

Eigenvalue buckling analysis, which is a linear perturbation procedure, was used to estimate the critical (bifurcation) load of the structure. The cutout dimension is normalized with the radius of the cylinder up to normalized cutout size of 50% of the cylinder radius (0.5R). The cutout geometry is a circular cutout when you open the cylinder into a planar form. The cutout shapes also can be seen from Table 5.1. The result of the static buckling analysis as a function of cutout dimension and nonlinear failure analysis with 10% imperfection is given in Figure 5.1 where, the buckling load remains unaffected by the presence of the cutout until about 30% of the cylinder radius (0.3R), and then starts decreasing substantially after 35% of the radius (0.35R) [59].

On the other hand, the nonlinear (NL) analysis failure load also remains unchanged until 0.3R cutout radius and then start to increase until 0.35R. However, as the cutout size increases more the NL failure load also decreases following almost the same trend with linear buckling moment. Numerical results are tabulated in Table 5.1 along with the buckling mode shapes. It can be observed that until cutout dimension 0.3R the structure buckles from lower portion of the cylinder that is the compression side. However, after cutout dimension 0.35R the buckling initiates from the lower side of the cutout boundary and the buckling load decreases more than 20% compare to non-cutout buckling load as shown in Figure 5.2. Until this point, the decrement in the buckling load due to the increment in the cutout dimension is less than 4%. However,

Table 5.1 : Buckling analysis of cylindrical shell with cutouts at ±90°.

Dimension R=304.5 mm	Linear Buckling Moment (kNm)	NL with PFA (10% imp.)	Mode Shapes
0.00R	693.80	406.71	
0.10R	693.79	406.76	
0.20R	693.22	416.5	
0.30R	691.27	414.15	
0.35R	669.08	594.77	
0.40R	553.22	493.81	
0.45R	464.98	427.5	
0.50R	399.76	391.07	

after 0.35R, the buckling load start to decrease rapidly and at cutout dimension 0.5R the reduction reaches up to 40%.

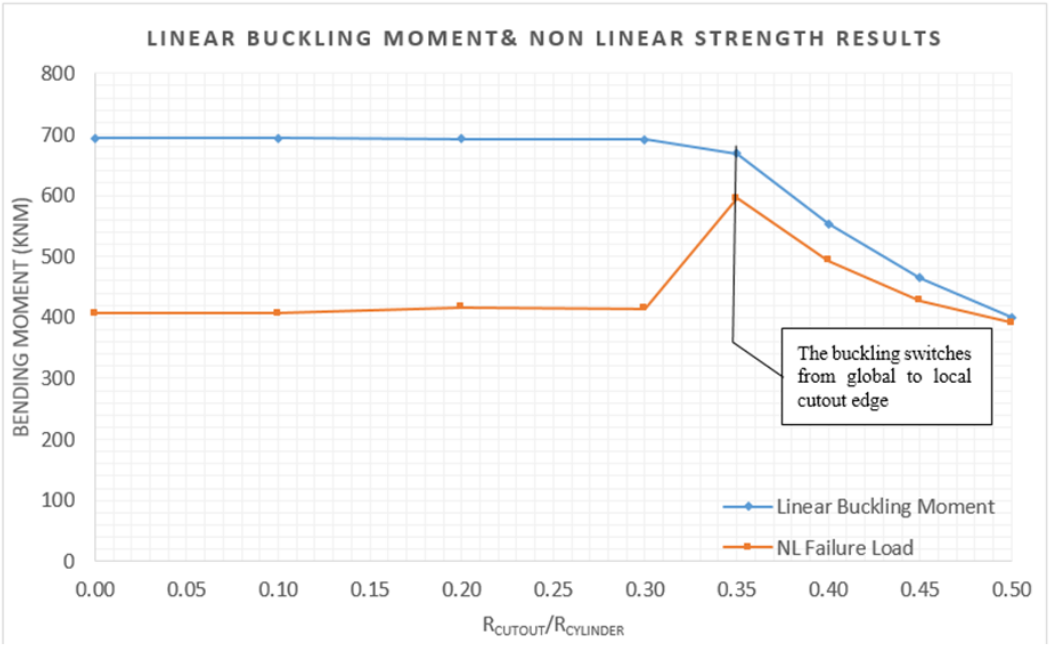


Figure 5.1 : Buckling moment and strength results for given cutout dimensions.

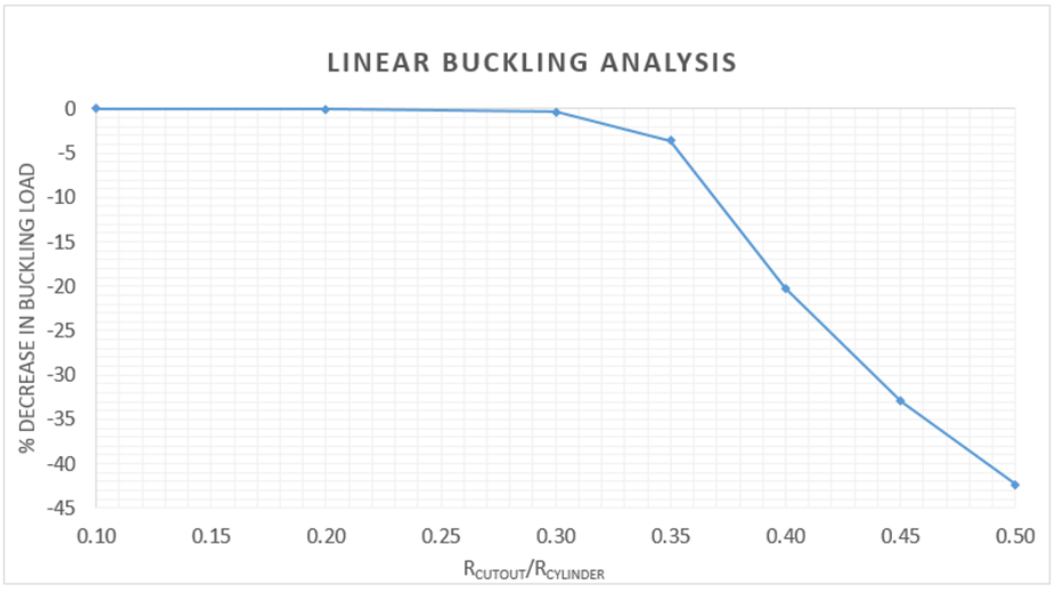


Figure 5.2 : Percent decrease in the buckling moment due to increase in the cutout dimension.

5.2 Imperfection Analysis

During the linear buckling analysis the presence of geometrical imperfections were not taken into account, and that could have a large influence on the experimental buckling load of thin-walled cylindrical shells. If the exact geometric imperfection is not known, an imperfection consisting of multiple superimposed buckling modes may be introduced and usually first buckling mode is the dominant one. The radial displacements of the nodes under the effect of the bending moment cause the cylinder

to deviate from perfect cylinder and create geometric imperfections. The first buckling mode is assumed to provide the most critical imperfections, therefore, usually these are scaled and added to the perfect geometry to create the perturbed mesh. The magnitudes of the perturbations used are typically a few percent of a relative structural dimension such as shell thickness [10]. In this case, Riks method can be used to perform a geometrically nonlinear load-displacement analysis to determine the collapse loads, especially for imperfection-sensitive structures in which the applied load produces significant geometric instability. Therefore, imperfections obtained from linear buckling analysis were applied in the nonlinear Riks analysis.

While performing the buckling stability study, initially, eigenvalue analysis is used to obtain estimates of the buckling loads and modes. Using imperfections suggested by the eigenvalue analysis, the second phase of the study is the performance of load-displacement analyses, using the Riks method. Before continuing to the nonlinear buckling analysis with cutout a series of analysis was performed on the cylinder that has no cutout to see the result of the imperfections in the shape of buckling eigenmodes from the linear buckling analysis. Imperfections, in the form of from of first buckling eigenmodes with 1%, 2.5%, 5% and 10% of the shell thickness were applied during Riks analysis. Linear and nonlinear finite element analyses were performed using an ABAQUS-Python script. During all analyses, the Hashin failure criterion was checked and no failure initiations were seen before buckling. The rotation of the end plates under the effect of the bending load is illustrated in Figure 5.3.

The end rotations decreases with the increasing imperfection values, but the behavior remains the same, the decrement in the end rotations is due to the decrease in the buckling load. The results show that there is a very important effect of imperfection on the failure load of cylindrical shells since shells are very imperfection sensitive. The displacements of the top and bottom mid nodes as shown in Figure 5.4 in the vertical direction under the effect of the bending moment are given in Figure 5.5 and Figure 5.6. Since the top node is in the tension side of the cylinder, the vertical displacement remains linear but due to the effect of the imperfection, that causes the decrease in the buckling load, vertical deflection also decreases. On the other hand, the bottom node has a vertical deflection greater than the top node and the increment is non-linear because of the compression of the bottom side of the cylinder. Although, after the

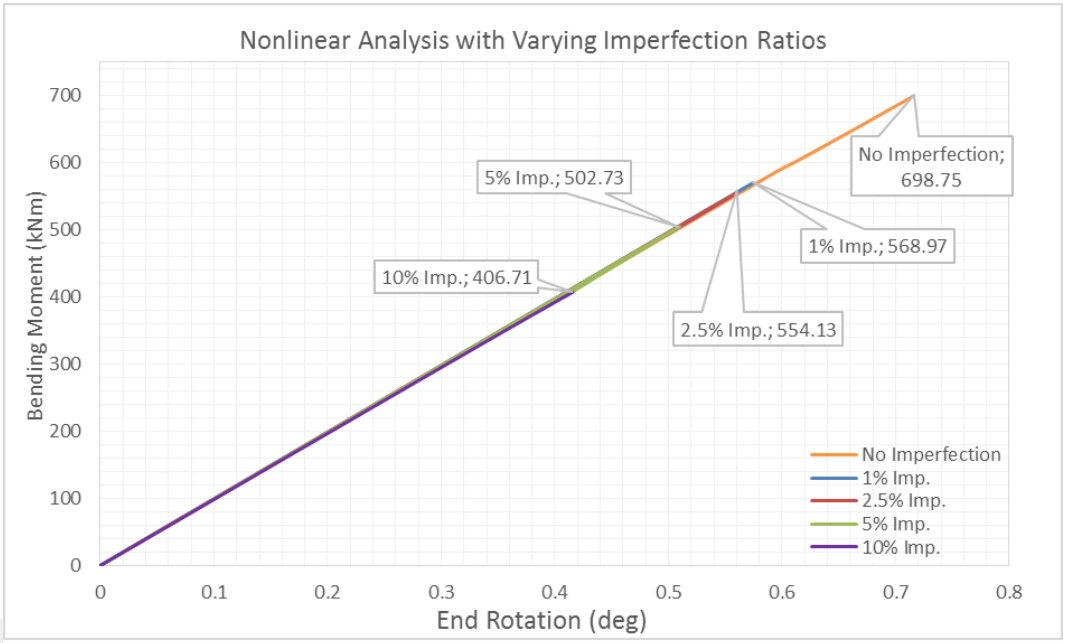


Figure 5.3 : The rotation of the end plates with varying imperfections in bending.

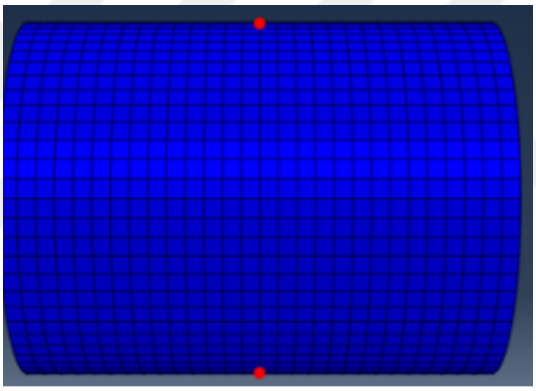


Figure 5.4 : Top and bottom node locations.

critical load the vertical displacement in top node stops, the bottom node continues to deflect.

The percentage deflection difference between the bottom and top nodes of the cylinder normalized per cylinder radius is given in Figure 5.7. The curvature in the graph shows the point when the instability, which cause the failure, starts. It can be deduced form Figure 5.7 that, for 10 % imperfection, collapse starts around 410 kNm, while this value is 500 kNm for 5% imperfection. It is obvious that the top node has linear positive strain values since it is under tension load; in contrast, the bottom node has negative strain value, which is nonlinear. The axial strain values of the upper and lower mid nodes under bending load are given in Figure 5.8 and Figure 5.9.

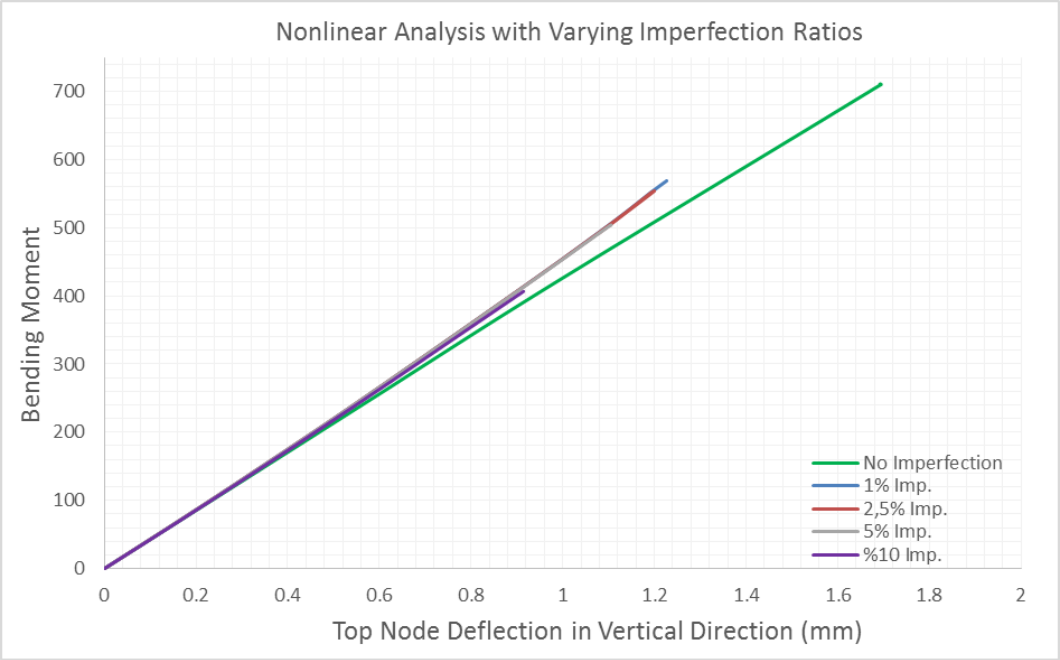


Figure 5.5 : The displacement of the top mid node in the vertical direction.

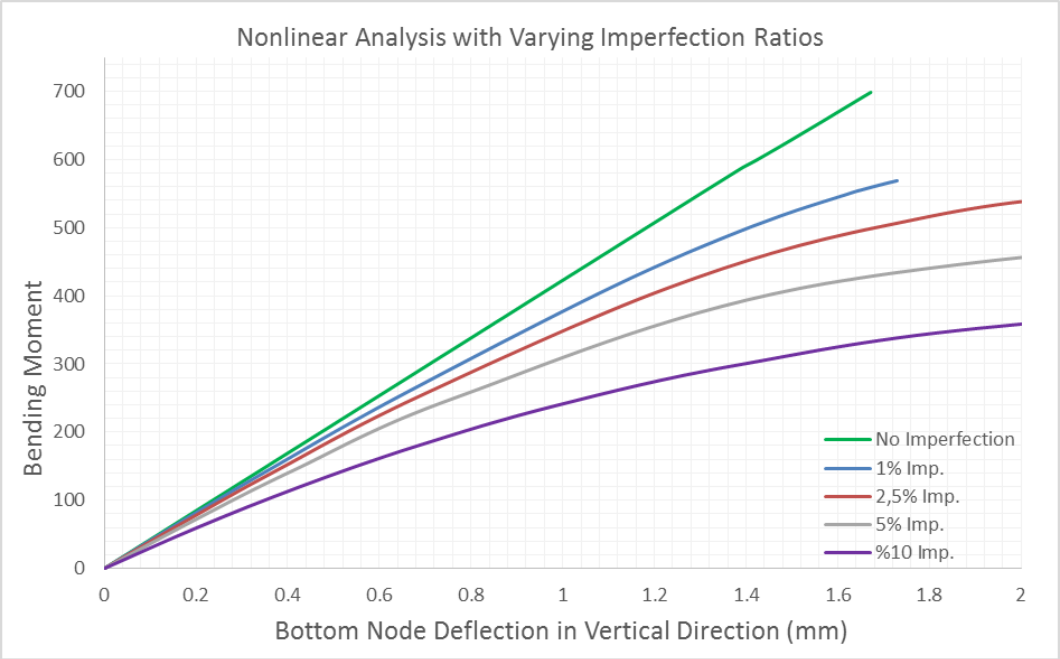


Figure 5.6 : The displacement of the bottom mid node in the vertical direction.

As it can be seen from the transverse strain values of the upper and lower mid nodes under bending load given in Figure 5.10 and Figure 5.11 that, the results for top node is linear and stays linear until the structure collapse. However, immediately after buckling starts the transverse strain for the bottom node decreases suddenly to negative values. This is due to the initation of the buckling on the compression side of the cylinder.

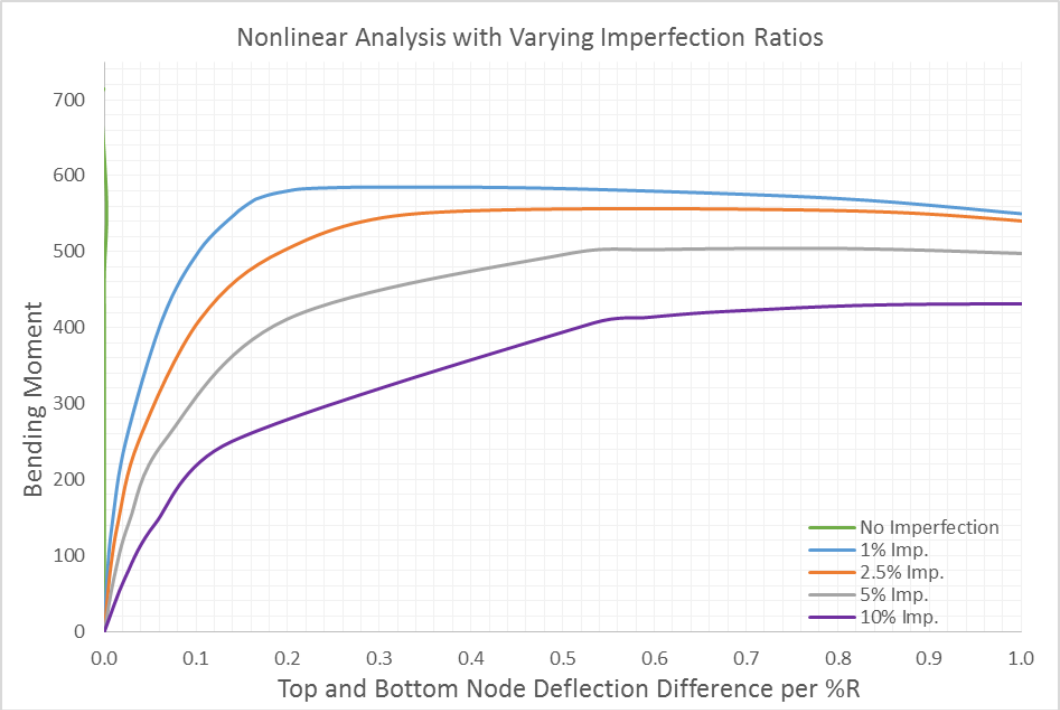


Figure 5.7 : The percent deflection difference between the bottom and top nodes of the cylinder per cylinder radius.

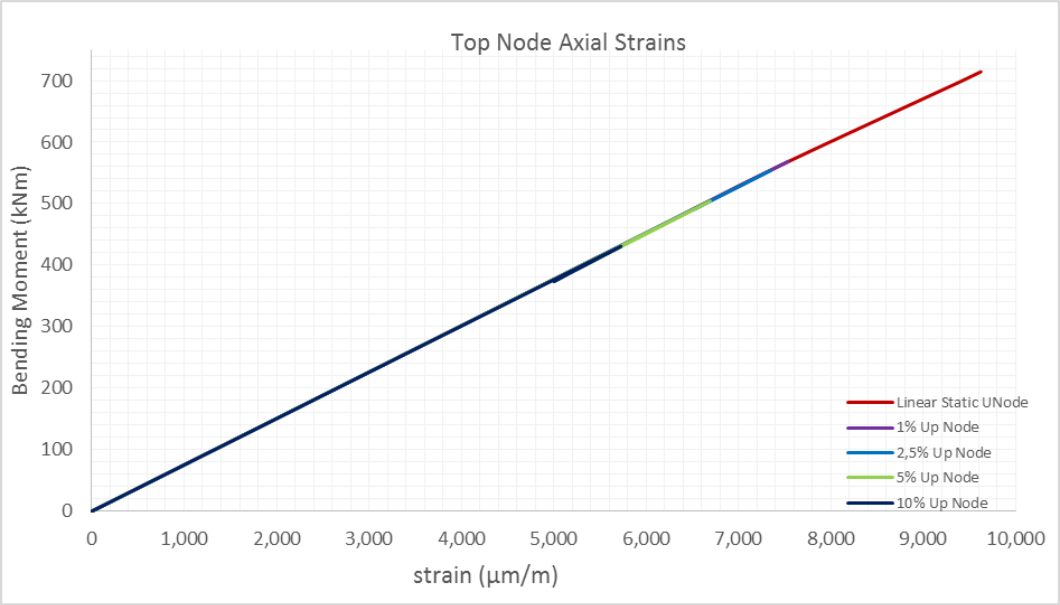


Figure 5.8 : The axial strain values of the upper mid node.

5.3 Non-Linear Analysis of the Cylindrical Shell with Cutouts and Imperfection

From the imperfection analyses results of the shell without cutouts, it was decided to continue with the geometrically nonlinear load-displacement analysis of the cylinder with cutouts containing the 10% of thickness imperfection using the Riks method.

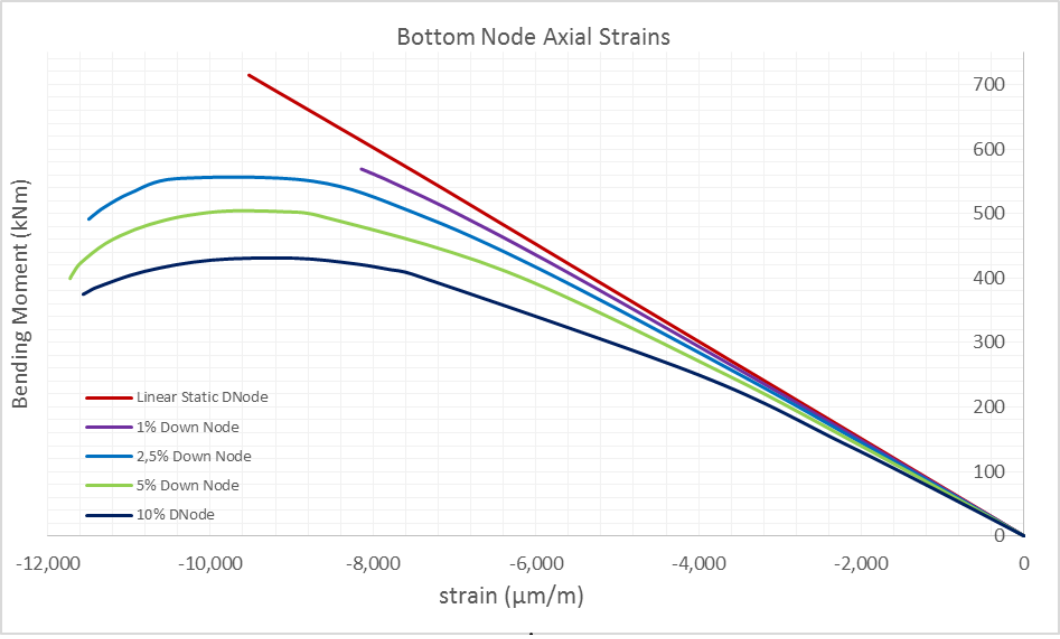


Figure 5.9 : The axial strain values of the bottom mid node.

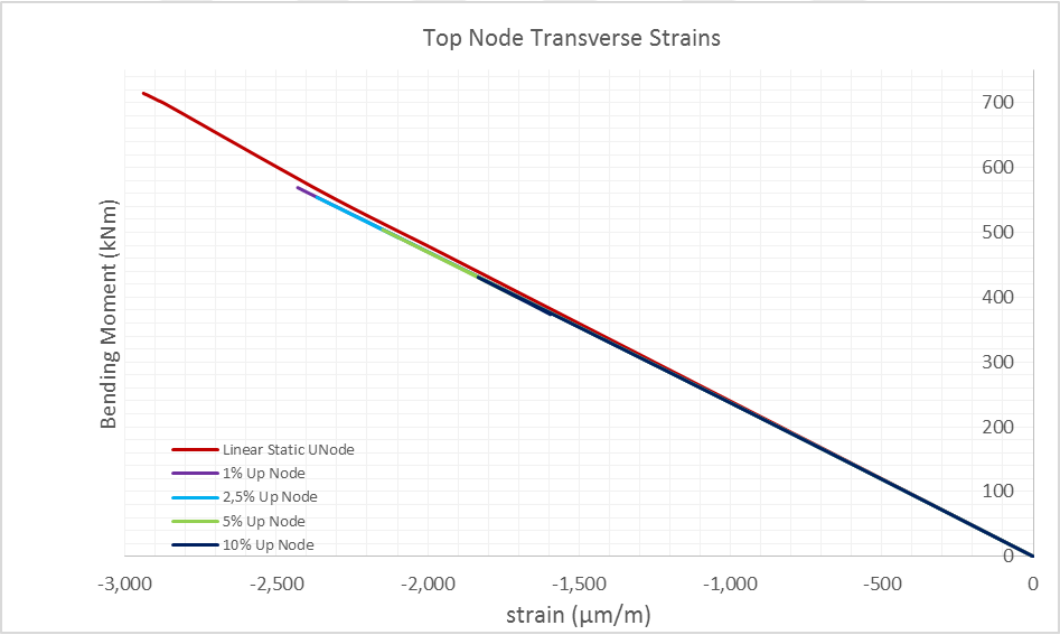


Figure 5.10 : The transverse strain values of the upper mid node.

During the analysis, the applied bending load and node displacements were obtained from linear buckling analysis. The rotation of the end plates under the effect of the bending load is given in Figure 5.12. It is clear that as cutout dimension increases, buckling starts at lower bending moments and therefore end rotation angle decreases. The axial strain values of the top and bottom mid nodes under bending load are given in Figures 5.13 and 5.14. The top node almost shows the same behavior with the case of no cutout condition since it always remains under tension. On the other hand, the

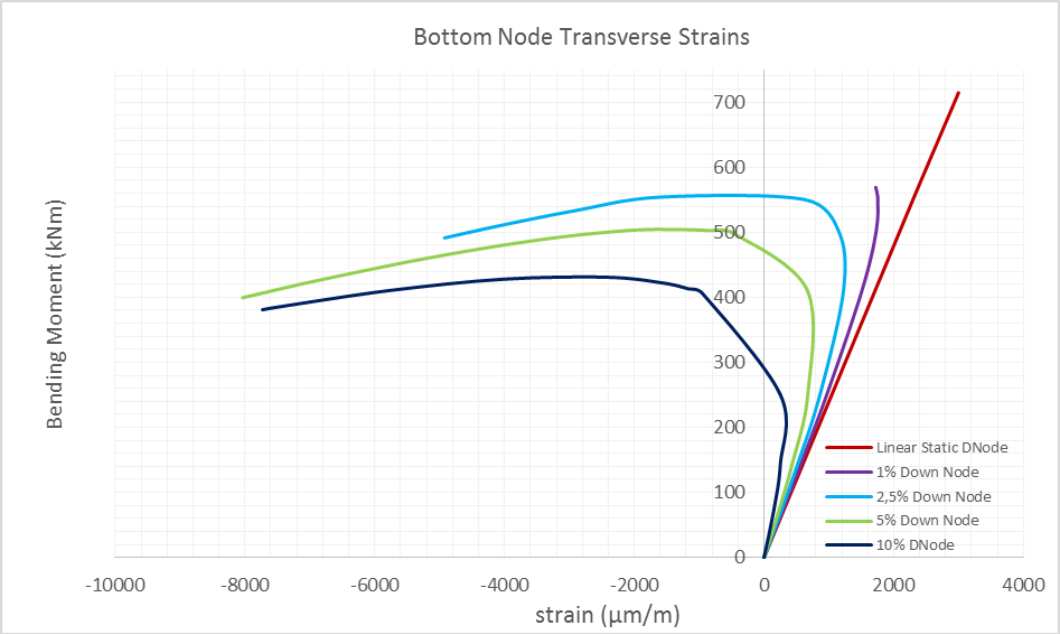


Figure 5.11 : The transverse strain values of the bottom mid node.

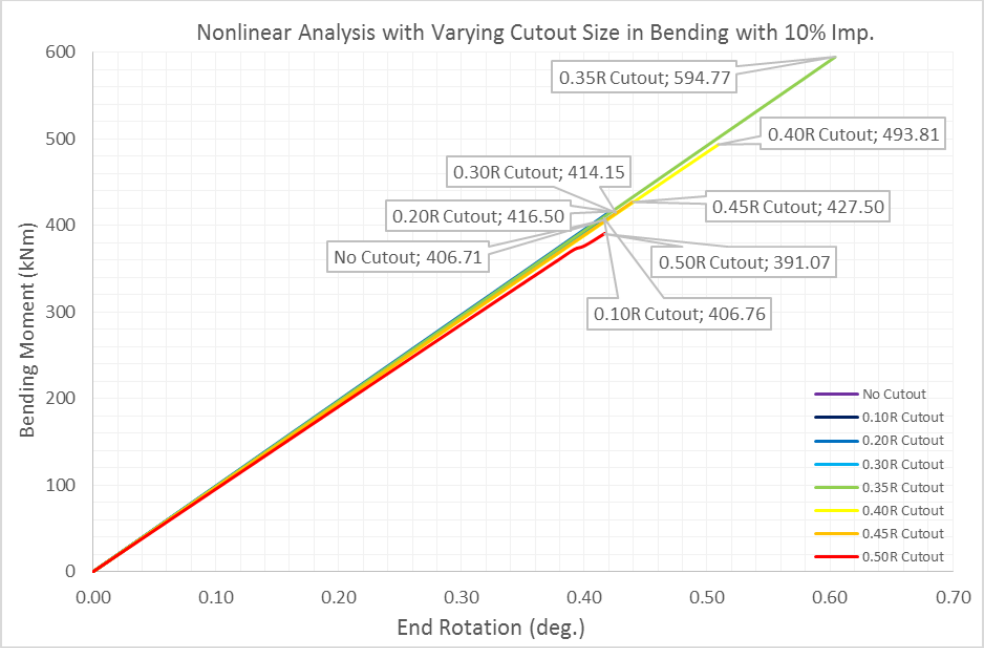


Figure 5.12 : The rotation of the end plates under the effect of the bending load .

bottom node diverges from Riks analysis of the cylinder without cutout, after cutout dimension 0.35R (Circular Cutout-CC0.35). This is because of the buckling starting from the lower edge of cutout and keeping the bottom node under linear compression in axial direction and tension in transverse direction. The transverse strain values of the top node are linear and have very close values for all cutouts as shown in Figure 5.15. The bottom mid node transverse strain value as in the axial strain values deviates from nonlinear behavior becoming linear after the cutout radius 0.35R and

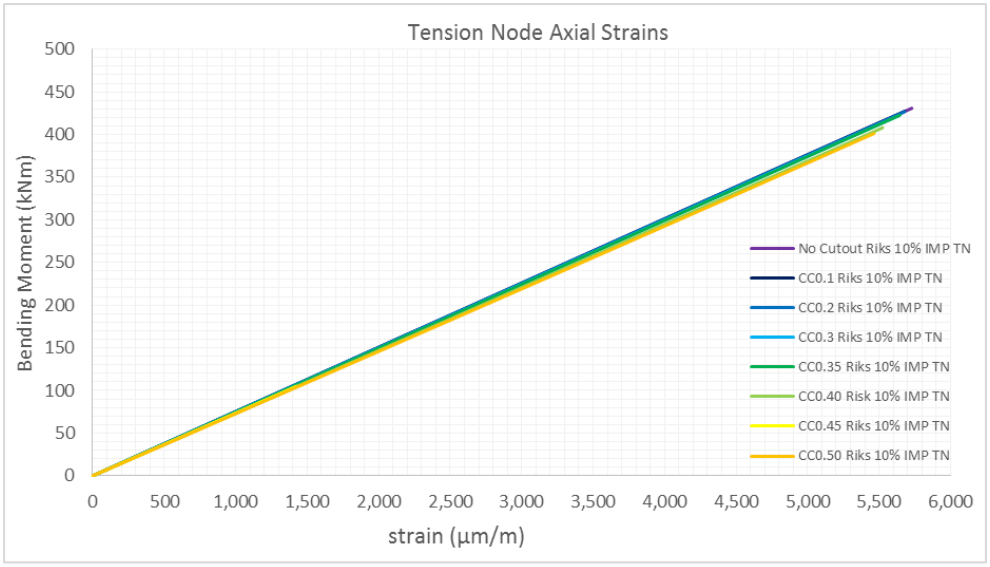


Figure 5.13 : The axial strain values of the top mid node.

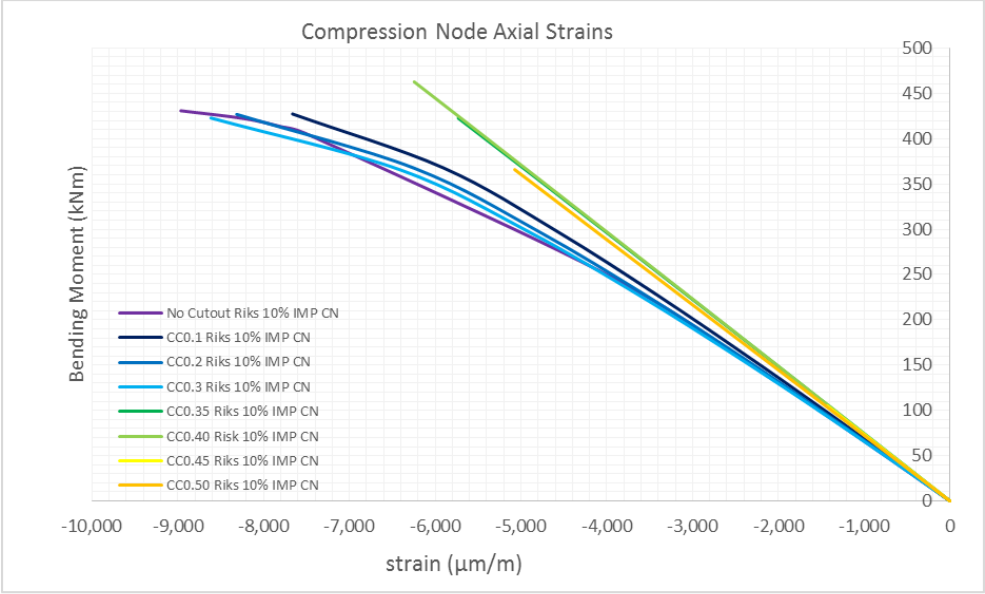


Figure 5.14 : The axial strain values of the bottom mid node.

again have very close strain values as shown in Figure 5.16. The displacements of the top node in vertical direction is almost same with the case of no cutout until cutout dimension 0.30R, however after that the vertical deflection increases slowly as the cutout dimension increases as shown in Figure 5.17. As for the bottom mid node, the behavior of the cutout until 0.30R is same with the no cutout condition and after the buckling load, deflection increases dramatically. However, for the cutout dimension greater than 0.35R deflection stops after buckling as illustrated in Figure 5.18. The percentage deflection difference between the bottom and top nodes of the cylinder normalized per cylinder radius is given in Figure 5.19. Since the buckling behavior

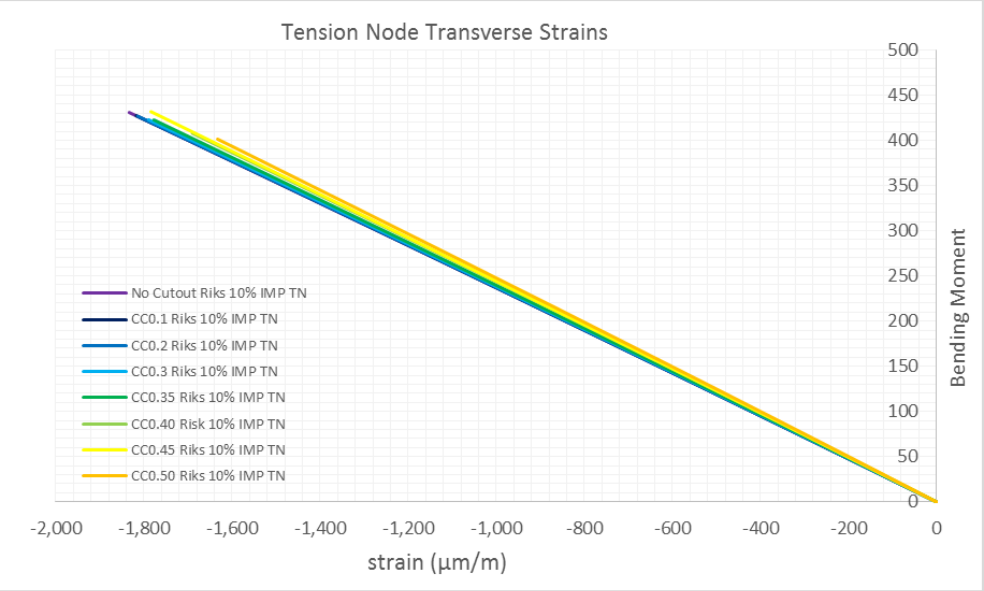


Figure 5.15 : The transverse strain values of the upper mid node.

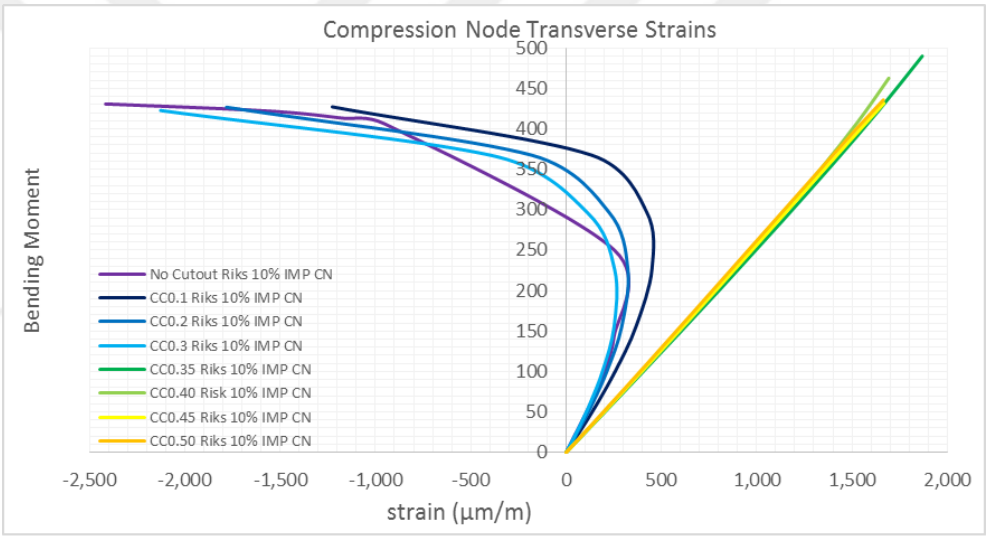


Figure 5.16 : The transverse strain values of the bottom mid node.

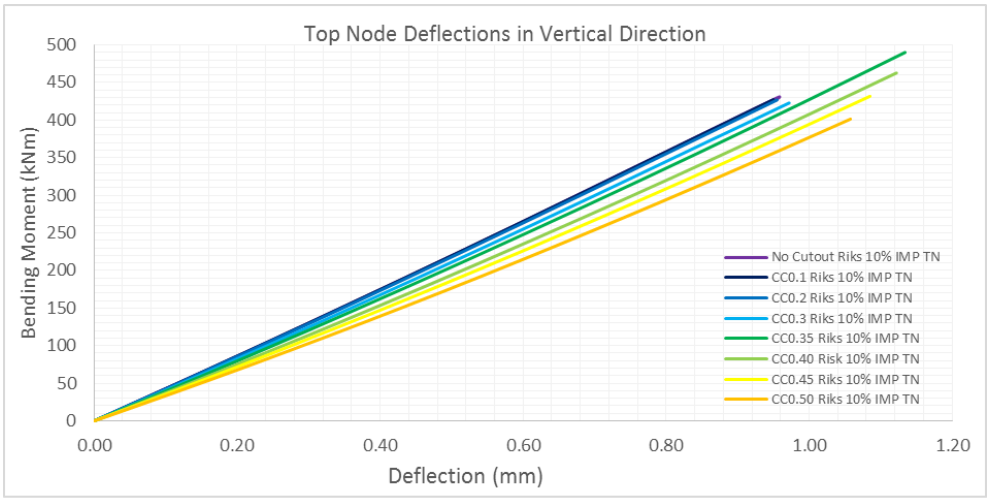


Figure 5.17 : The displacement of the upper mid node in the vertical direction.

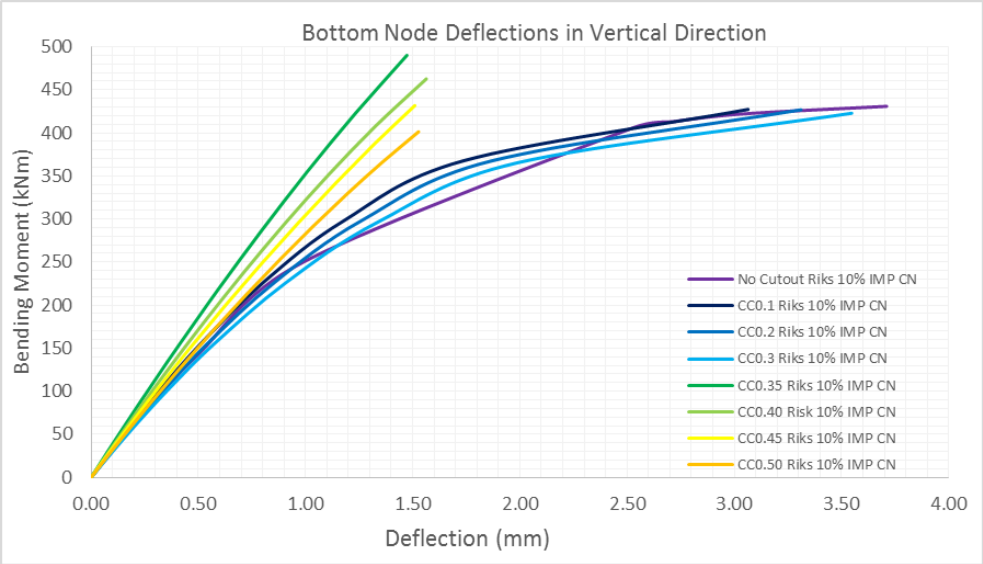


Figure 5.18 : The displacement of the lower mid node in the vertical direction.

changes after cutout 0.3R the deflection behavior of top and bottom nodes also changes and the deflection difference between top and bottom nodes becomes less.

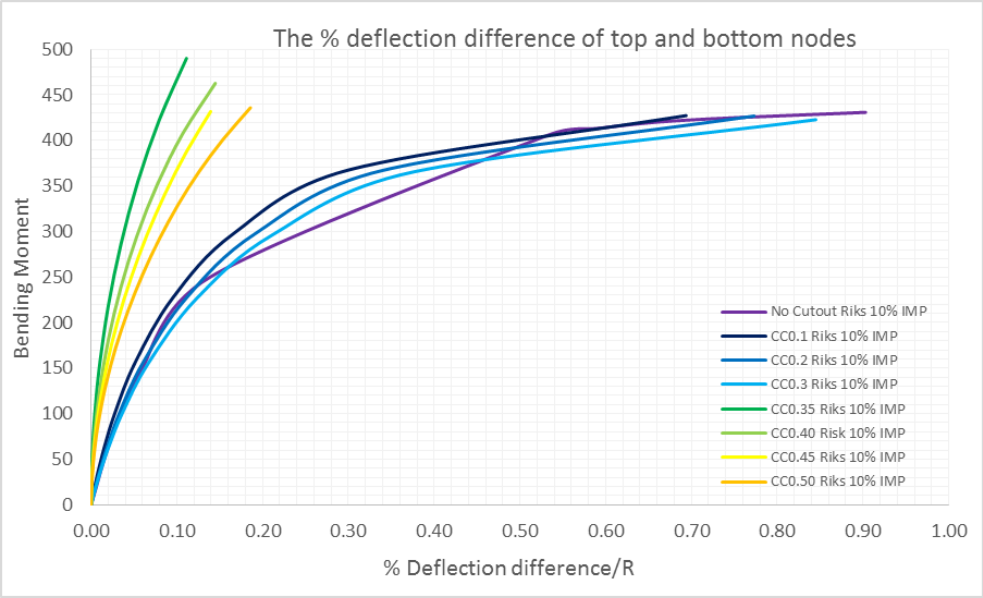


Figure 5.19 : The percentage deflection difference between the bottom and top nodes of the cylinder normalized per cylinder radius.

5.4 Non-Linear Analysis Results at the Cutout Edge

Since the behavior of global top and bottom nodes do not change with increase in cutout dimension, it was decided to analyze the top and bottom nodes behavior of the cutout edge as shown in Figure 5.20. The axial strain values of the top and bottom mid nodes until cutout dimension 0.35R increases linearly with the load and the values

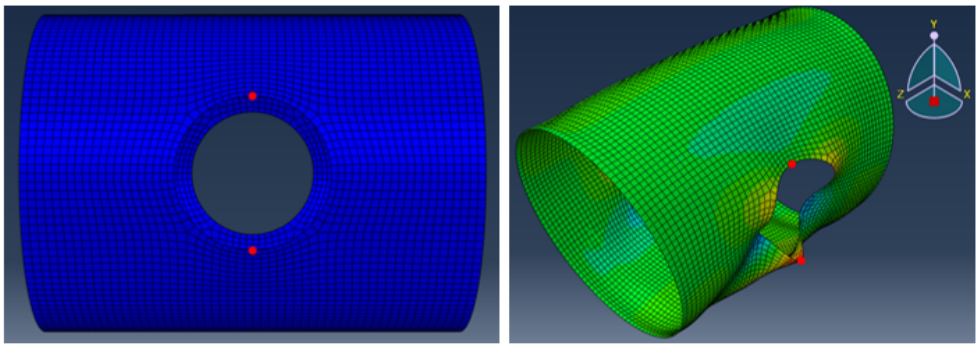


Figure 5.20 : Top and Bottom Nodes of the Cutout Edge.

of the top and bottom nodes are very close to each other as shown in Figure 5.21. In addition, the strain values increase with the cutout dimension increments. The

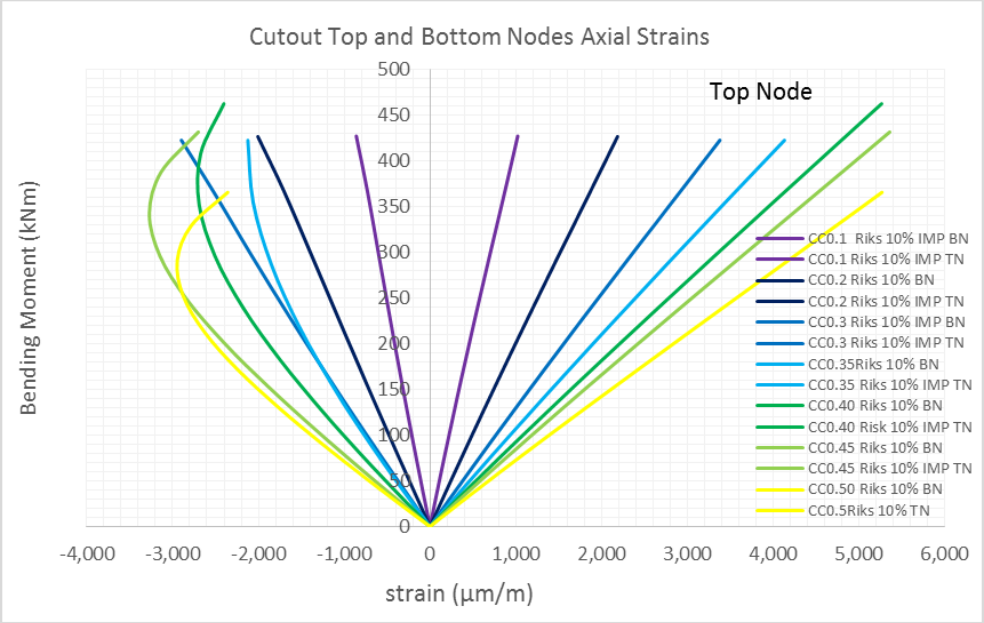


Figure 5.21 : The axial strain values of the top and bottom mid nodes.

transverse strain values of the top and bottom mid nodes given in Figure 5.22 are also consisted with the results of the axial strain values and as the cutout dimension increases, strain values increases in both nodes. Additionally, the nonlinearity starts at compression side after cutout 0.35R.

The displacements of the top and bottom mid nodes along-x direction under the effect of the bending moment are given in Figure 5.23. When the structure starts to buckle from the cutout edge, the cutout nodes displacement along x directions becomes more noticeable. Until cutout dimension 0.35R the horizontal displacement almost less than 0.1 mm, after 0.35R the deflection of the bottom node increases at each cutout

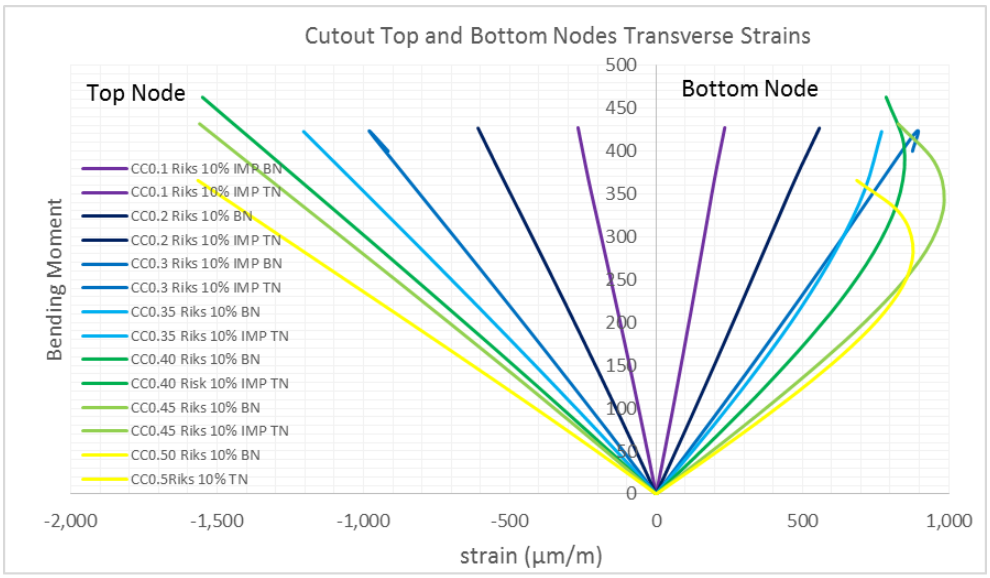


Figure 5.22 : The transverse strain values of the top and bottom mid nodes.

increment very sharply which shows that the buckling occurs actually at the lower edge of the cutout.

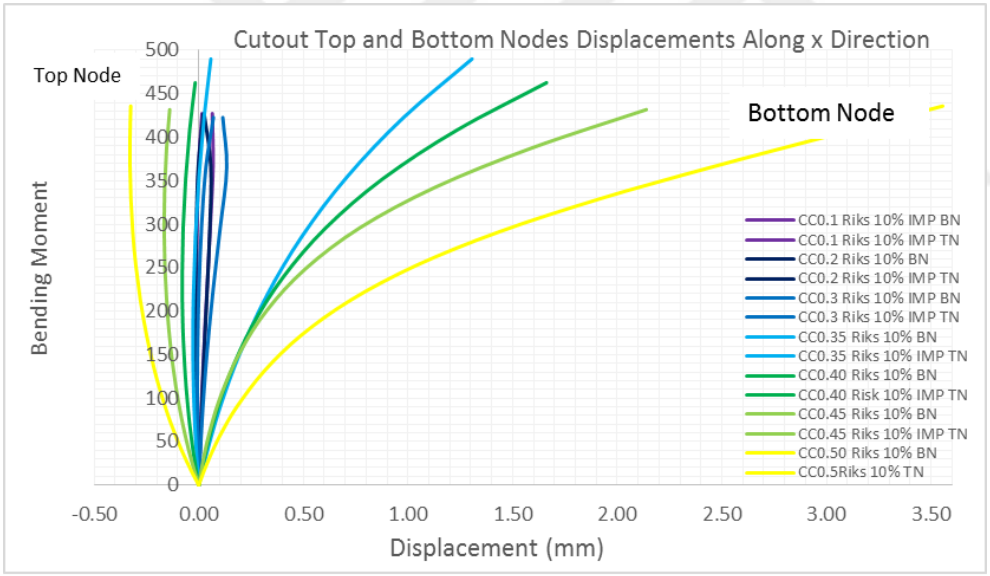


Figure 5.23 : The top and bottom nodes displacement in the x direction .

6. BUCKLING AND STRENGTH ANALYSIS OF CONSTANT STIFFNESS SHELL WITH CUTOUTS UNDER BENDING

In order to investigate the effect of the cutouts, 0.1R, 0.3R and 0.5R cutout dimensions were located to the positions shown previously in Figure 4.2. The shapes of the cutouts are in circular form when the cylinder is unwrapped into planar form. Both linear buckling eigenvalues along with buckling mode shapes and the failure loads obtained from nonlinear progressive failure analysis were given. Totally, in 28 location and sizes, liner progressive failure analysis and NLwPFA were performed including the non-cutout case. In the analyses, the bucklings occurred either from the compression side of the cylinder in global or from the cutout edge.

6.1 Baseline Case Examples

This section provides several baseline examples, which demonstrate the response of representative cutout configurations that correspond to three distinct failure mode classifications. Those classifications are used to understand the basic trends and effects of cutout size and location on the overall failure level and are the basis to decide which configuration to select for validation bending testing.

6.1.1 Non-linear analysis of non-cutout cylindrical shell

As an initial baseline for discussion, the results for the non-cutout case were shown in Figure 6.1 once again. Note that the response is linear up to the FL load, where instability occurs. This load is well below the expected linear eigenvalue due to the presence of the imperfection, which is introduced as 10% of the shell thickness in the form of the eigenmode shown at the top left cross-sectional inset. The NL without PFA line (blue line) is the best indicator of this phenomenon, and the resulting cross-section on the bottom right is the representation of the post-buckled shape after buckling. Moreover, the post-buckling deformation is concentrated at the bottom of the cylinder where the compressive stresses are the highest. Failure does not occur until the post-buckled deformation develops, as evidenced by the progressive failure

indicators. This is the “classical” mode of cylinder failure, where the buckling at the bottom of the cylinder initiates material failure. Figure 6.1 shows that even less than 0.5% fiber volume (red line) failure causes the ultimate failure under pure bending moment.

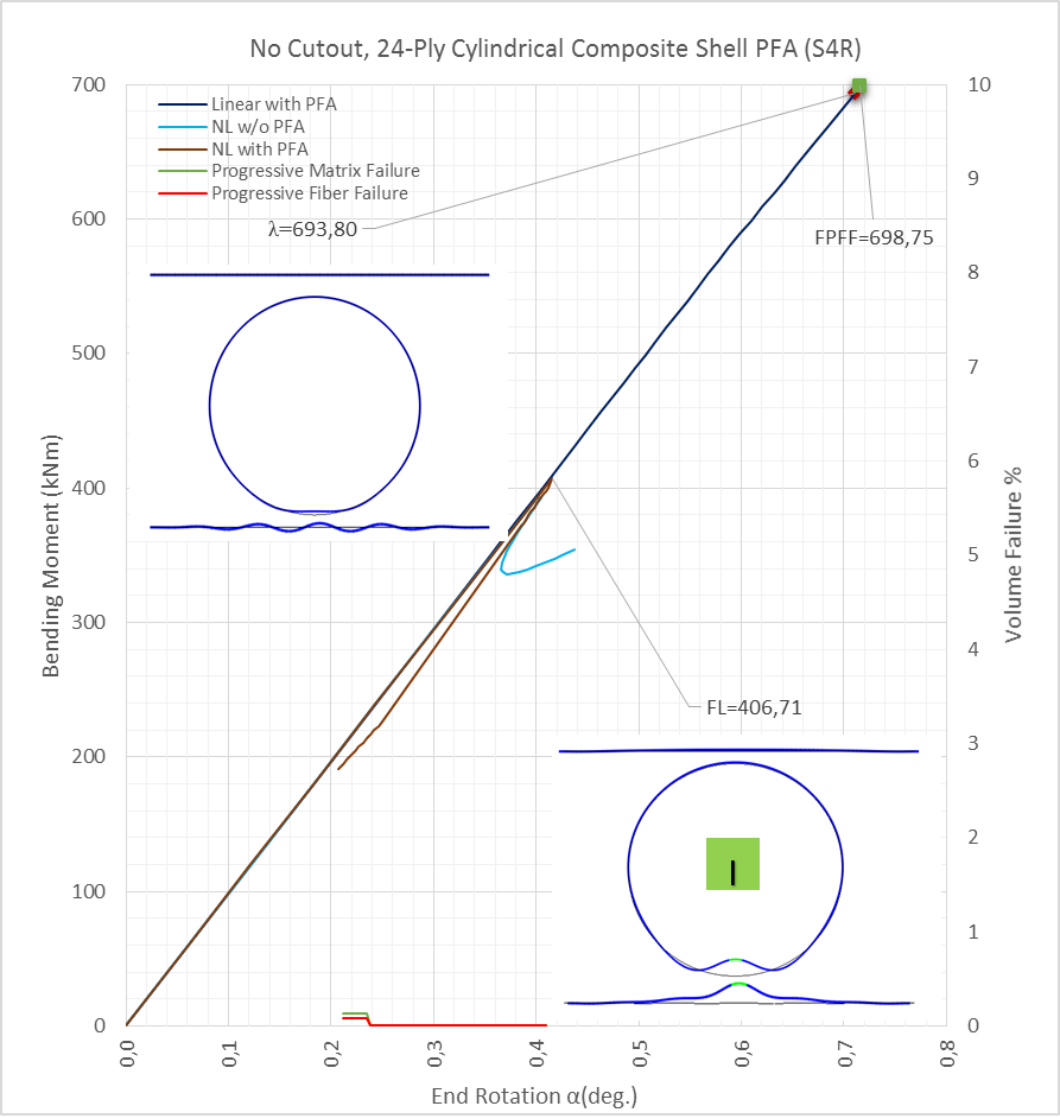


Figure 6.1 : Finite element solutions for non-cutout case.

6.2 Failure Mode Classifications for Cutouts

When the cutouts were introduced into the shell, it was realized that there are actually three distinct failure modes [60]. Therefore, due to the presence of the cutout, the classical failure mode described below as Failure Mode I is not always the resulting mode of failure. In the design study, two other modes were also defined. Examples

of each mode with failure initiation along with failure propagation are shown in the following sections

6.2.1 Failure mode I

The classic failure mode demonstrated by the non-cutout case was defined as Mode I. An additional example for the 0.1R/60 case is displayed in Figure 6.2. For these cases, buckling occurs well below the linear estimations for FPFF and buckling loads and the progressive failure load-displacement curve has the same maximum as the nonlinear case without PFA. Mode shapes and post-buckling deformation is concentrated at the bottom of the cylinder and the drop-off in load-carrying capability after buckling is often severe.

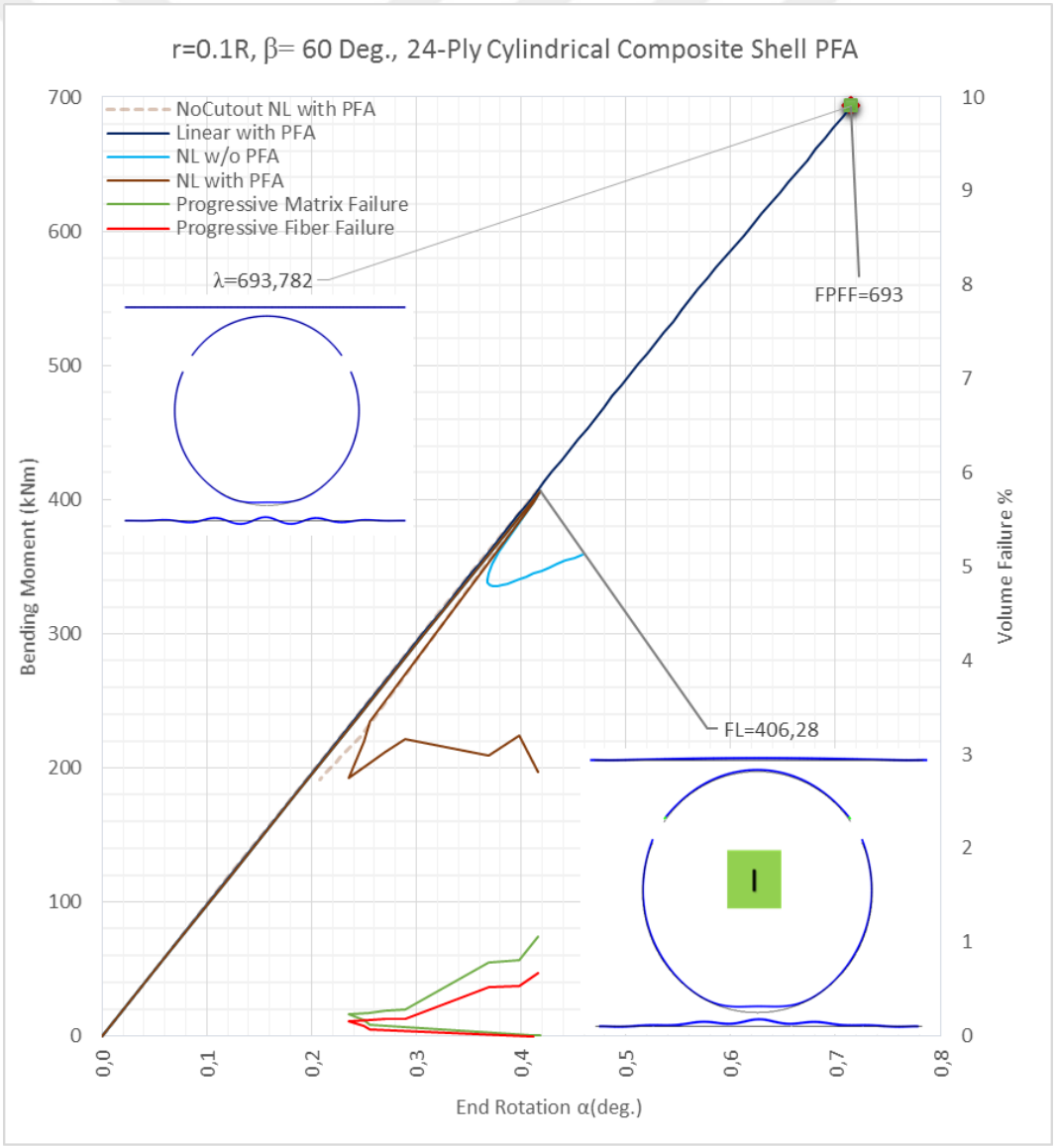


Figure 6.2 : Demonstration of Mode I failure.

The classical Mode I failure initiates from the compression side of the cylinder that is shown in Figure 6.3 with the ultimate failure view.

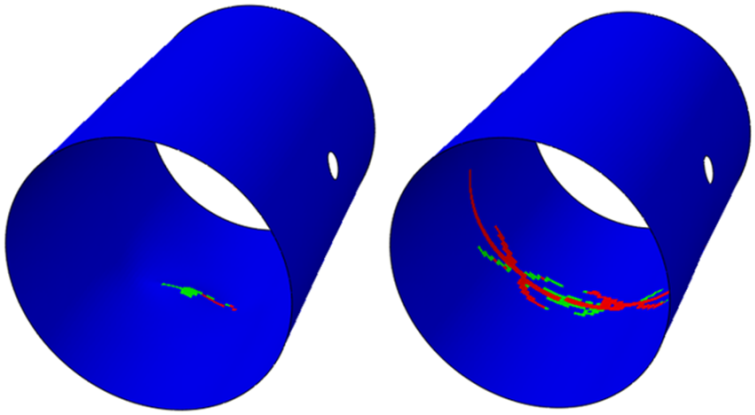


Figure 6.3 : 0.1R/60 cutout failure initiation and ultimate failure depiction (Mode I).

Briefly, Failure Mode I may be defined as strength failure driven by global buckling of the cylinder.

6.2.2 Failure mode II

The failure mode II is a transition between failure modes I and III, which is best thought of as local buckling around the cutout that leads to non-intuitive deformation and material failure progression. A representative plot is shown in Figure 6.4 for the 0.3R/105 configuration. Note that the eigenvalue is below the nonlinear load limit and the associated buckling shape is focused around the cutout as opposed to the classical mode of buckling at the bottom of the cylinder. The FPFF load level and progressive failure for the nonlinear solution greatly demonstrate the stress concentration around the hole, and it is the combination of the material failure and buckling deformation, which leads to the collapse of the cylinder. This failure mode provides the most interesting effect of the cutout configuration on the cylinder response, as evidenced by the forthcoming results for the design studies.

In Mode II failure, during non-linear analysis without PFA, from the Figure 6.4, it can be seen that although the out of plane deformations starts at lower load levels until certain amplitude of the deformation, the cylinder can carry the load and then buckles. However, during the NLwPFA the fiber failure initiates with the interaction of buckling from cutout edge and as shown in Figure 6.5.

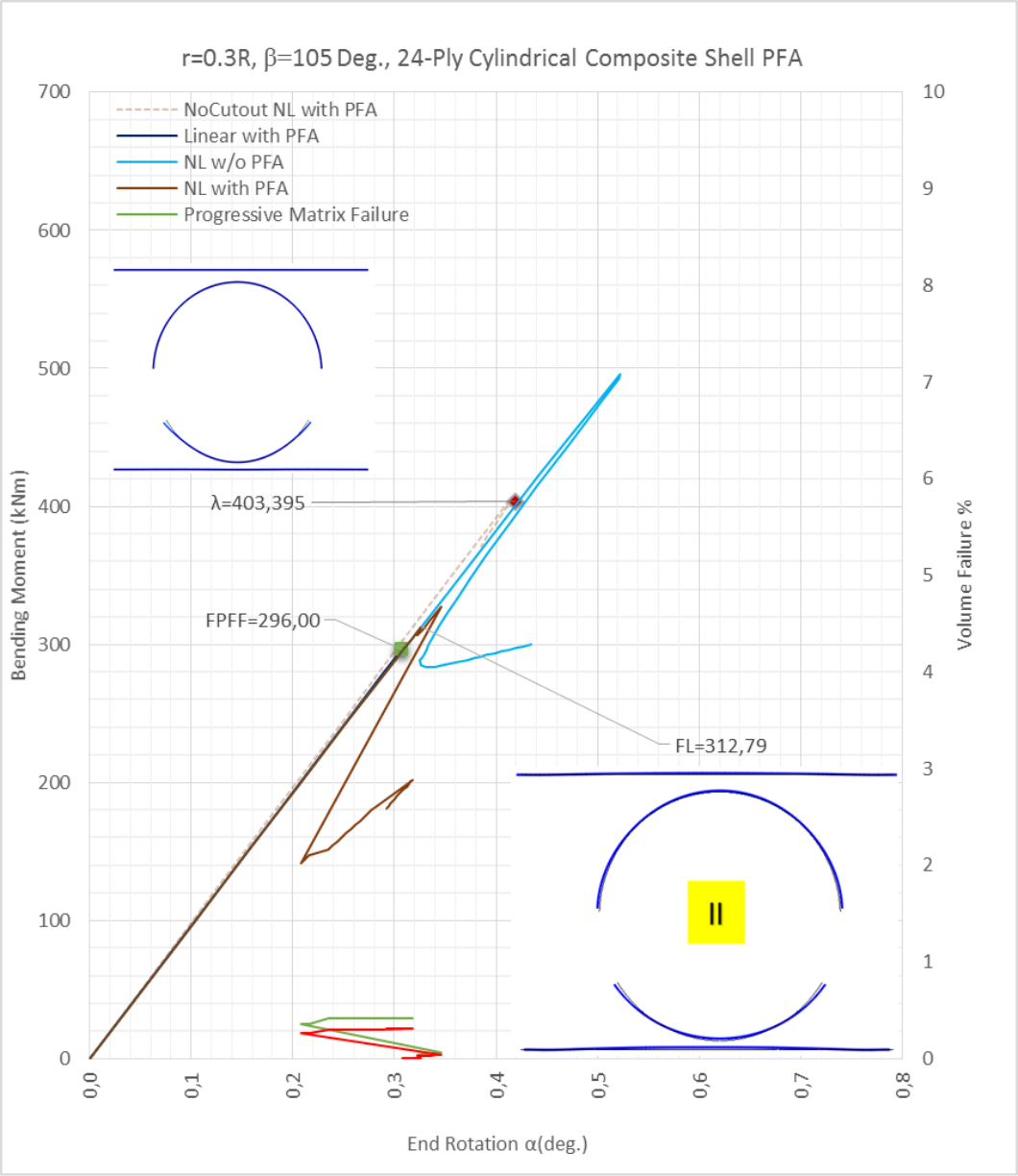


Figure 6.4 : Demonstration of Mode II failure.

In addition, although in the NLwPFA fiber failure initiates with FPFF, the cylinder is able to carry load until the buckling occurs at the cutout edge. Therefore, Failure Mode II generally can be defined as; strength failure around the cutout driven by local cutout edge buckling. The matrix and fiber failure initiation and the ultimate failure are shown in Figure 6.6. The failure initiates with the matrix and fiber breakages around the lower sides of the cutouts where they are under compression. After that, failure progresses towards the bottom of the cylinder from the both sides and causes ultimate failure. In spite of the failure starts cylinder still able to carry further load until catastrophic

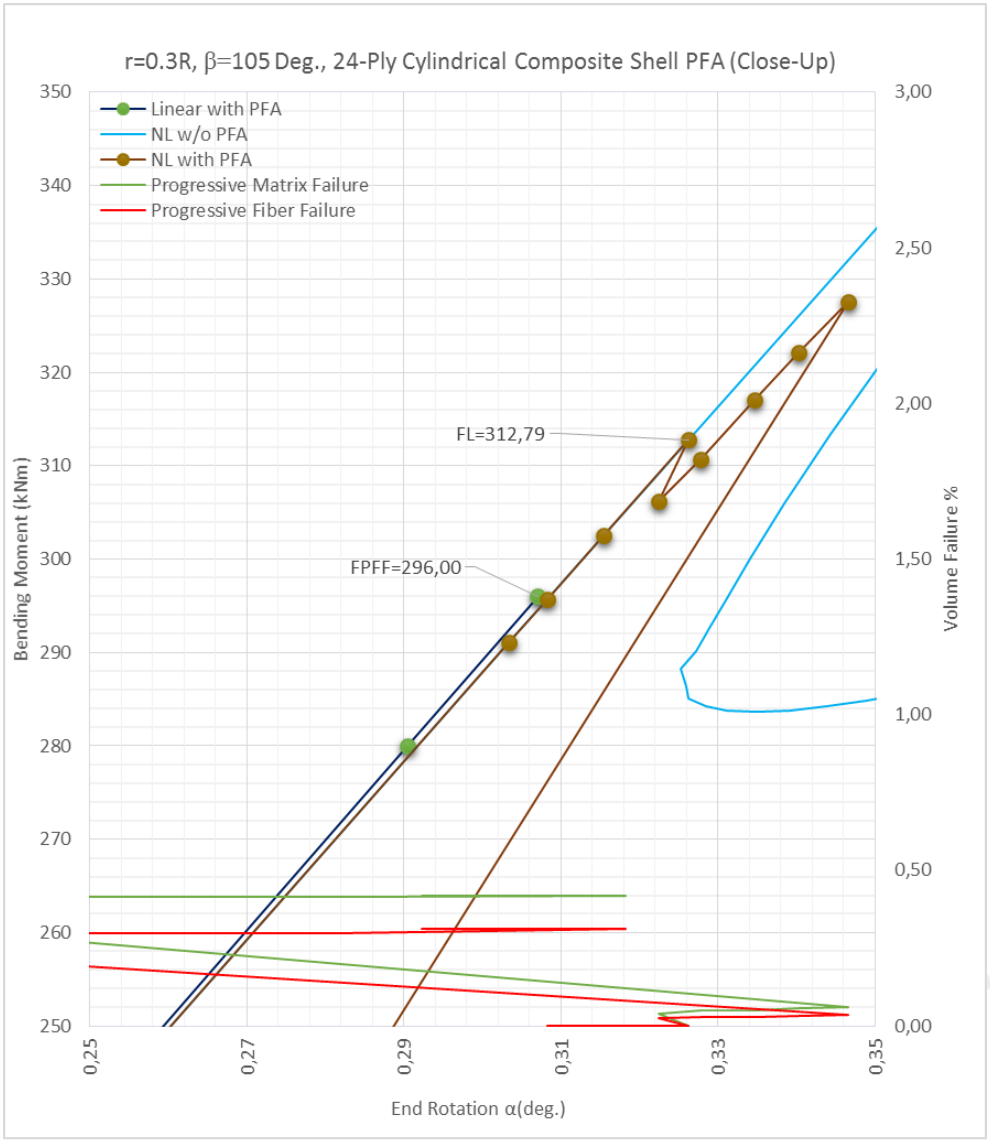


Figure 6.5 : Demonstration of Mode II failure (close-up view).

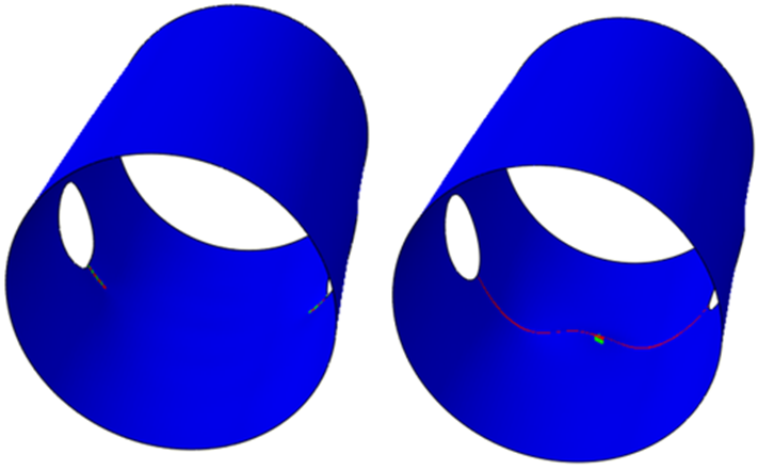


Figure 6.6 : 0.3R/105 cutout failure initiation and ultimate failure (Mode II).

failure. One can also observe a global buckling in addition to the local buckling around the cutouts, however, local buckling becomes dominant in order to cause the failure.

6.2.3 Failure mode III

The third failure mode generally occurs with the cutout at the extreme top or bottom of the cylinder and is characterized by catastrophic material failure before any buckling occurs. A typical example is shown in Figure 6.7 for the 0.5R/0 configuration.

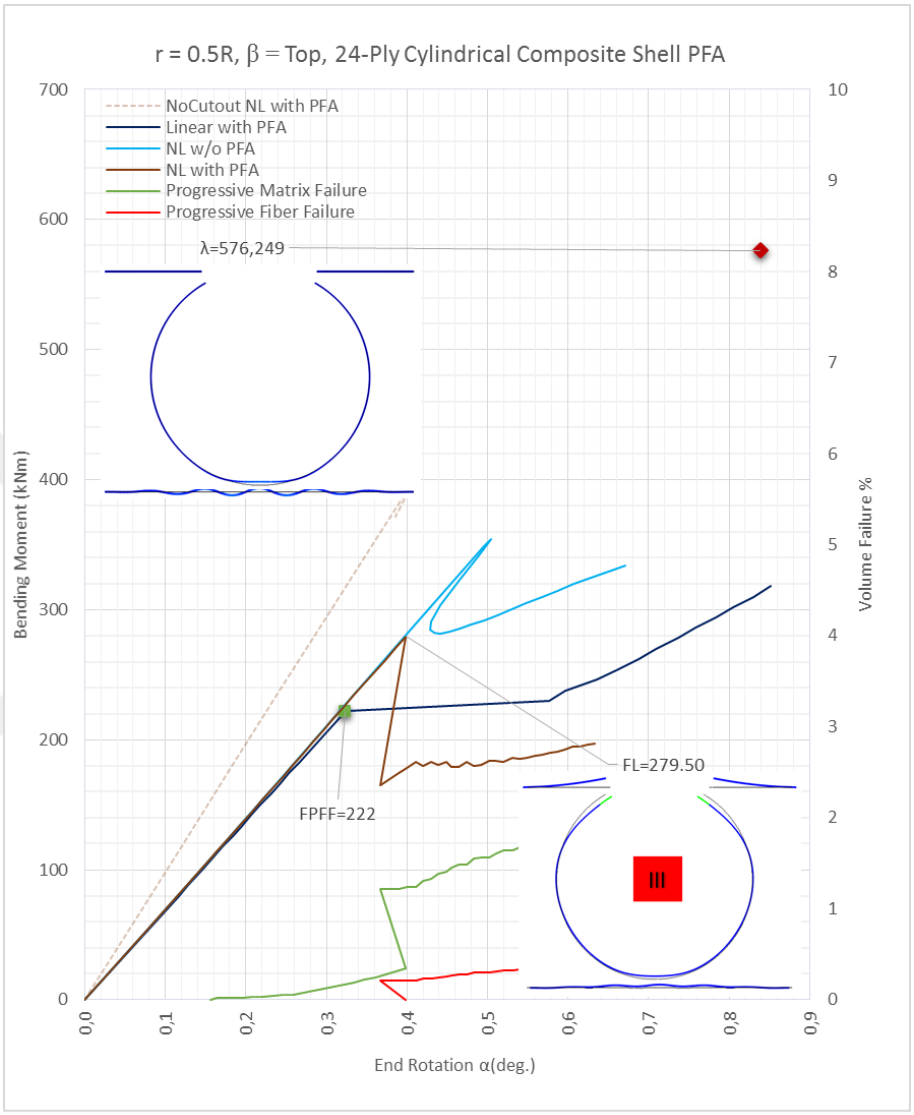


Figure 6.7 : Demonstration of Mode III failure.

The linear eigenvalue as indicated is well above the FL point, while the FPFF occurs at a much lower level due to the stress concentration around the cutout as can be seen more clearly from Figure 6.8. The nonlinear responses demonstrate the dominance of the progressive material failure around the hole, with the failure indicators quickly reaching high levels after initiation. This mode is thus dominated by material failure as opposed to the buckling of Mode I.

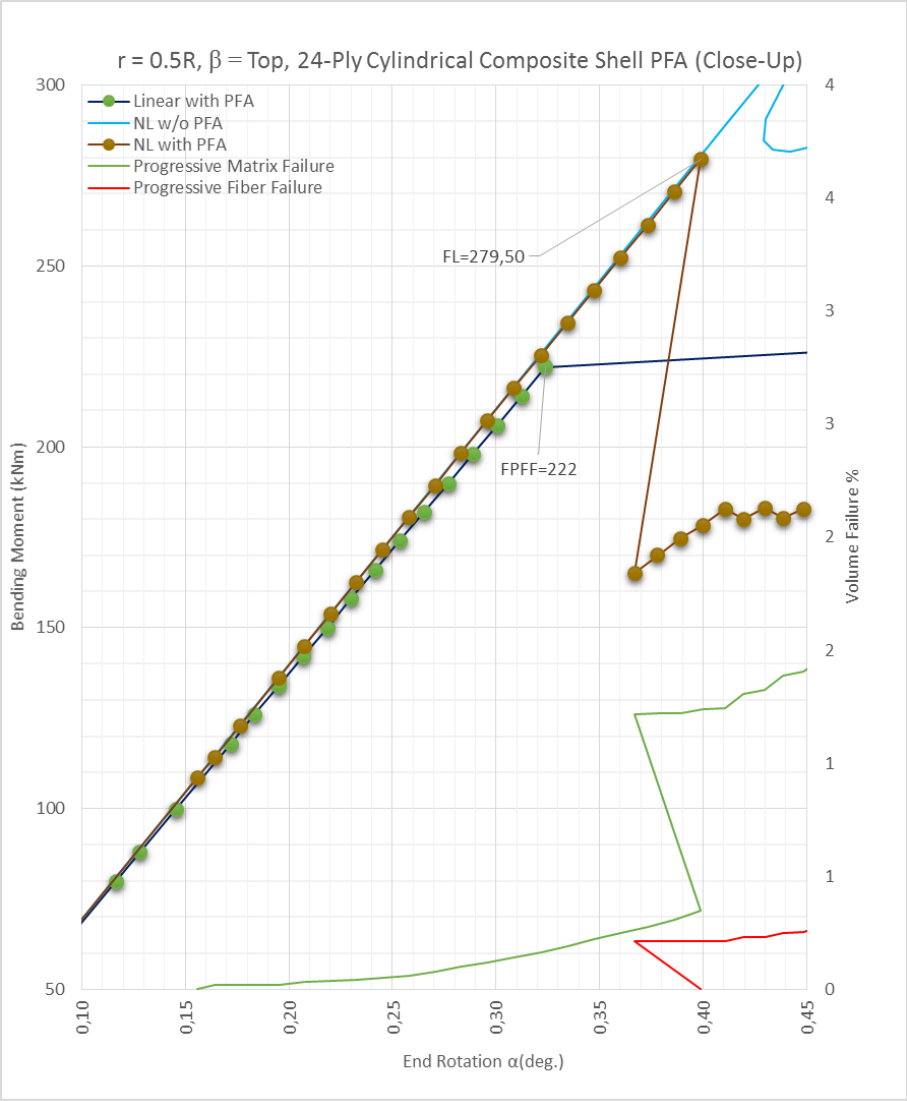


Figure 6.8 : Demonstration of Mode III failure (close-up view).

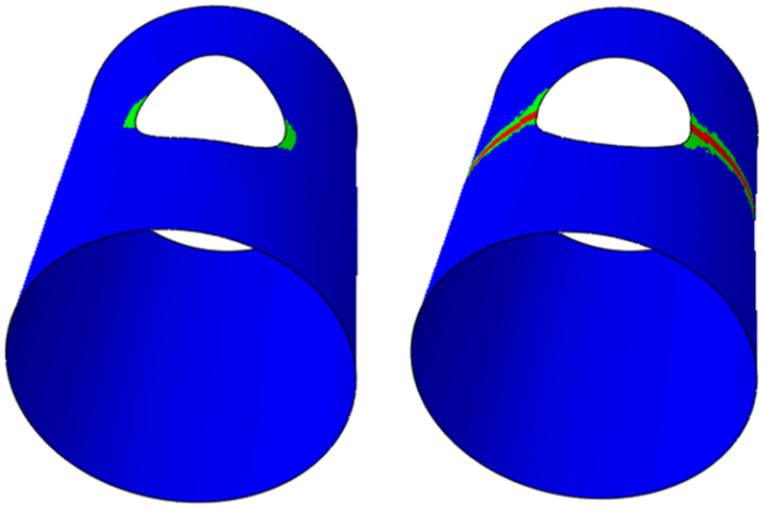


Figure 6.9 : 0.5R/0 cutout failure initiation and ultimate failure views (Mode III).

When the cutout is close to the upper portion of the cylinder, it is exposed to tension loading. Therefore, before global buckling material strength failure starts causing

Failure Mode III to be defined as strength failure around the cutout without buckling. As shown in Figure 6.9, the failure starts with matrix failure and as load level increases, the catastrophic failure occurs with large amount of fiber failures.

When a small size cutout is very close to the bottom side, before buckling induced failure, the fibers fails under compression. This is due to the stress concentration increase around the small diameter cutout beyond the strength of the fibers.

6.3 Design Study Results

When the study results were evaluated, it was discovered that for each cutout size and location we have a failure mode causing the structural failure either as a result of global or local buckling or loss of material failure. When those results were tabulated a map of failures were obtained given in the following sections.

6.3.1 Eigenvalue analysis

Part of the distinction between failure modes I and II is based on the type of mode shape for the lowest eigenvalue. Here, the classic mode of wrinkling at the bottom of the cylinder is labeled as the global (G) mode, while deformation that is centered around the edges of the cutout is be termed as local (L) buckling. A table listing the eigenvalues and displaying the critical modes for each of the cutout configurations is provided in APPENDIX A, while a summary of the critical buckling modes is shown in Table 6.1. Note that the 0.0R case corresponds to the non-cutout case. A plot of the eigenvalues as a function of cutout position is displayed in Figure 6.10, where each curve denotes a different hole size. From Table 6.1 it can be seen that as the cutout dimension increases, the local buckling start to initiate at the 90° position of the cylinder.

Table 6.1 : Critical buckling mode summary for initial set of cutout configurations.

LINEAR BUCKLING MODES									
0.0R	G	G	G	G	G	G	G	G	G
0.1R	G	G	G	G	G	G	G	L	L
0.3R	G	G	G	G	G	L	L	L	L
0.5R	G	G	G	G	L	L	L	L	L
$\beta =$	0(T)	45	60	75	90	105	120	135	180(B)

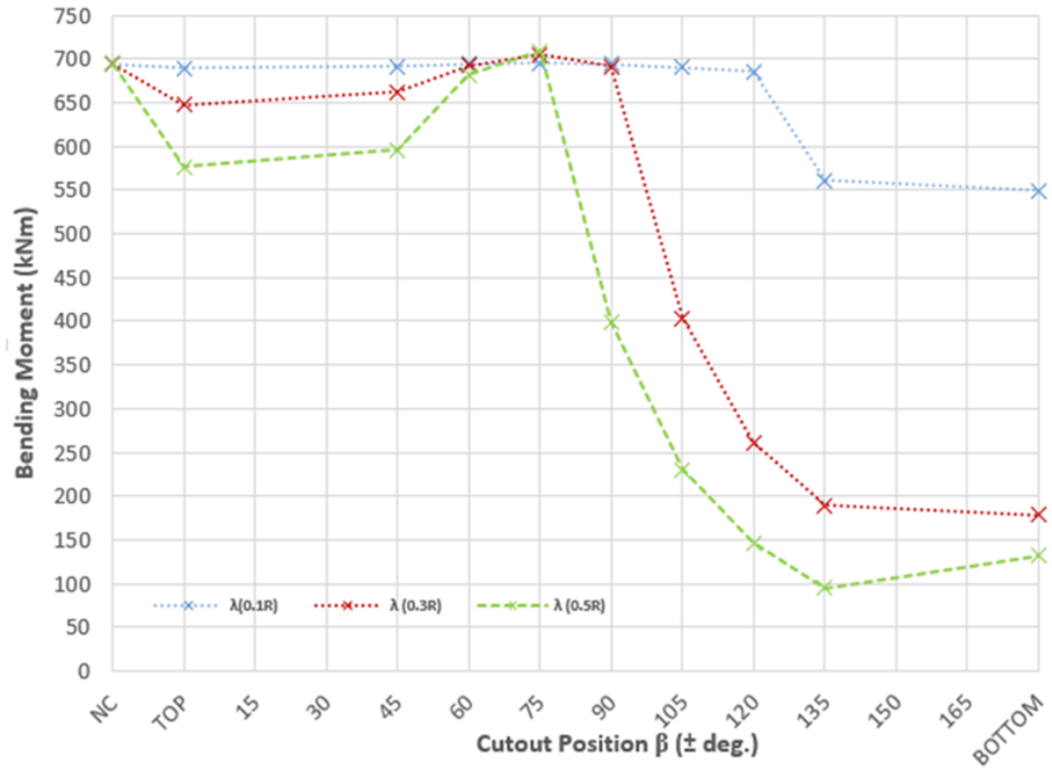


Figure 6.10 : Critical eigenvalues vs. cutout position for representative cutout sizes.

The results indicate that cutouts within the top half of the cylinder ($\beta < 75°$) do not have an effect on the type of the buckled mode, which remains in the usual global mode, but that the eigenvalues decrease from the non-cutout case load level depending on the size of the cutout. This is due to the fact that the cutouts generally decrease the overall bending stiffness of the shell, thereby producing higher stresses at the compressive region for an equivalent applied bending moment. This re-distribution of bending stresses also changes the effective neutral axis of the cylinder, which results in slight increases in buckling load for certain cases ($\beta = 75°$ for the two larger hole sizes). As the cutout location moves to the side of the shell ($\beta = 60°$, $75°$, $90°$), the cutout's effect on the bending stiffness is reduced and the critical loads converge back to the non-cutout value. The main exception is for the largest hole size at $90°$, where the eigenvalue has dropped considerably as the mode switches to the local one.

The curves for each of the hole size transition from the global mode to the local one as the location is moved closer to the bottom of the shell, though each change appears at a different value of β. The local modes exhibit greater influence on the load level as the size of the hole increases. Note that for most of the cutout configurations there is still a buckling mode that corresponds to the global one, however the key takeaway

is that the global mode no longer occurs at the lowest load level. This occurrence has several key effects on the forthcoming design study results, both changing the nature of the nonlinear deformation and altering the basic shape of the introduced imperfection which is based on the mode shape corresponding to the lowest eigenmode.

6.3.2 Failure limits and mode designations

The principal results for this design study are summarized in a similar fashion as the linear buckling results in Table 6.2 and Figure 6.11, where the designations in Table 6.2 are replaced with the failure mode type from section 6.2 and the graph includes the failure load levels as well as the previous eigenvalue results. The failure mode designations and load levels were discerned from the detailed load-displacement curves for each case, which are provided in the Appendices B through H.

Failure Mode I : Strength failure driven by global buckling mode.

Failure Mode II : Strength failure around cutout driven by local buckling.

Failure Mode III: Strength failure around cutout without buckling.

Table 6.2 : Failure mode summary for initial set of cutout configurations.

FAILURE MODES									
0.0R	I	I	I	I	I	I	I	I	I
0.1R	I	I	I	I	I	I	I	III	III
0.3R	III	III	I	I	I	II	II	II	II
0.5R	III	III	III	I	II	II	II	II	II
$\beta =$	0(T)	45	60	75	90	105	120	135	180(B)

The color-coding in Table 6.2 representing the three different failure modes is mirrored in Figure 6.11 through the shading of the symbols for each cutout configuration. The dark region in Figure 6.11 denotes the allowable load levels from the mechanical testing fixture and is helpful in determining which configurations can provide informative results from the testing phase. The design study results indicate that the smaller hole size (0.1R) has little effect on the failure of the cylinder except when it is located at the bottom locations. For the final two configurations from this set (0.1R/135 and 0.1R/180) the cutout generates stress concentrations from the large axial compressive stress state and the small radius hole which leads to considerable material failure before the buckling load levels are reached. This is a typical case of

mode III failure. For the medium and large hole sizes, the configurations with the cutout near the top also exhibit mode III failure due to the stress concentrations around the hole, though this time the region is under high tension instead of compression. The load-displacement configurations in the appendices demonstrate the nonlinear cross-sectional deformation and failure locations around the hole that lead to the overall failure. It seems to be a coincidence that the trends of the failure modes mimic the load level variation for the eigenvalues for cases 0.3R/0 $\rightarrow$ 0.3R/45 and 0.5R/0 $\rightarrow$ 0.5R/60 since the shells for these configurations do not experience any significant geometric instability. As the cutout moves toward the sides where the tensile and compressive stresses are lower, the stress concentration effects are diminished and the buckling modes tend to dominate the failure response. The focus of the results occurs

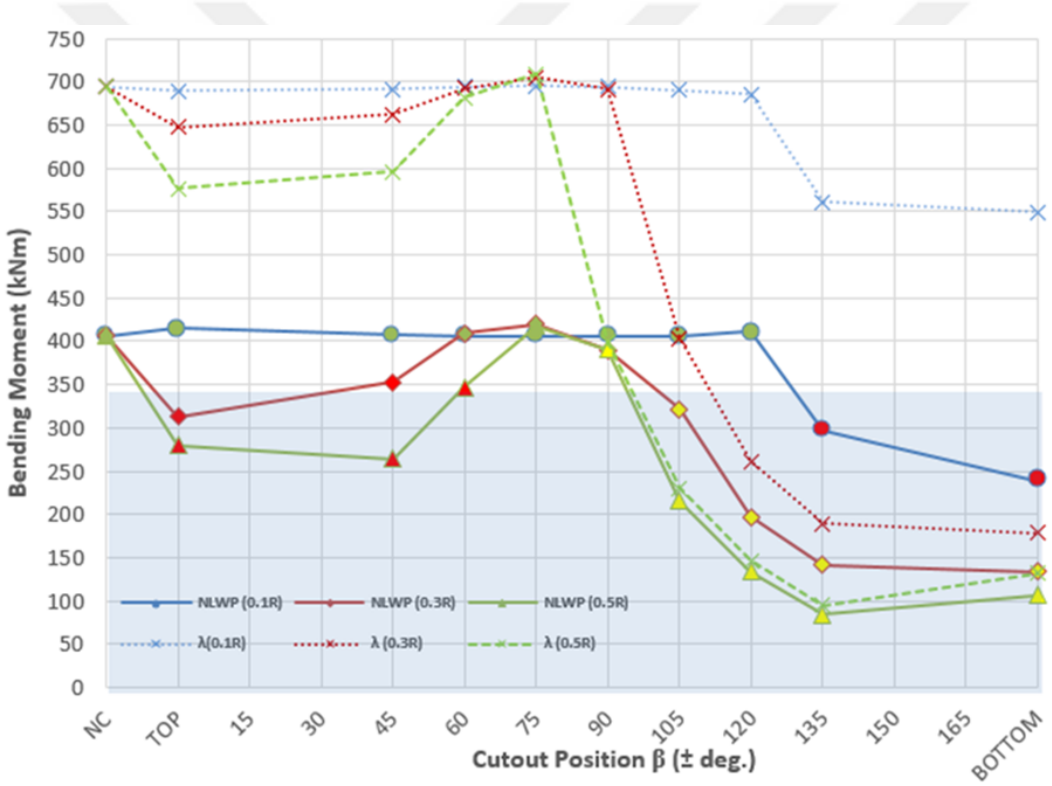


Figure 6.11 : Failure loads versus cutout position β for representative cutout sizes.

for the failure mode II cases where they transit from failure mode I (around the $\beta = 90^{\circ}$ mark for the two larger cutout sizes). The lower edge of the cutouts are within the compressive region of the cylinder, and the combination of the compressive state and the increased stress levels due to the stress concentration produce local buckling for the free edge of the cutout. As evidenced by Figure 6.11 the eigenvalues drop sharply from the global values and the failure load levels closely follow the trend of the eigenvalue variation.

A detailed investigation of this region of interest is provided in the next section. However, it is also significant that the cutout locations at 135° and 180° (bottom) undergo this local buckling as opposed to pure material failure (failure mode III) as exhibited by the 0.1R cases. The reason here is that the smaller hole produces higher stress concentrations to excite the material failure while also restricting the deformation of the local buckled mode shape. As the hole gets larger, the buckling mode shape's influence overtakes the decreasing stress concentration values and the mode II phenomenon dominates. The nonlinear analysis results with (NLwP) and without (NLnP) progressive failure is given in Figure 6.12. It is obvious that

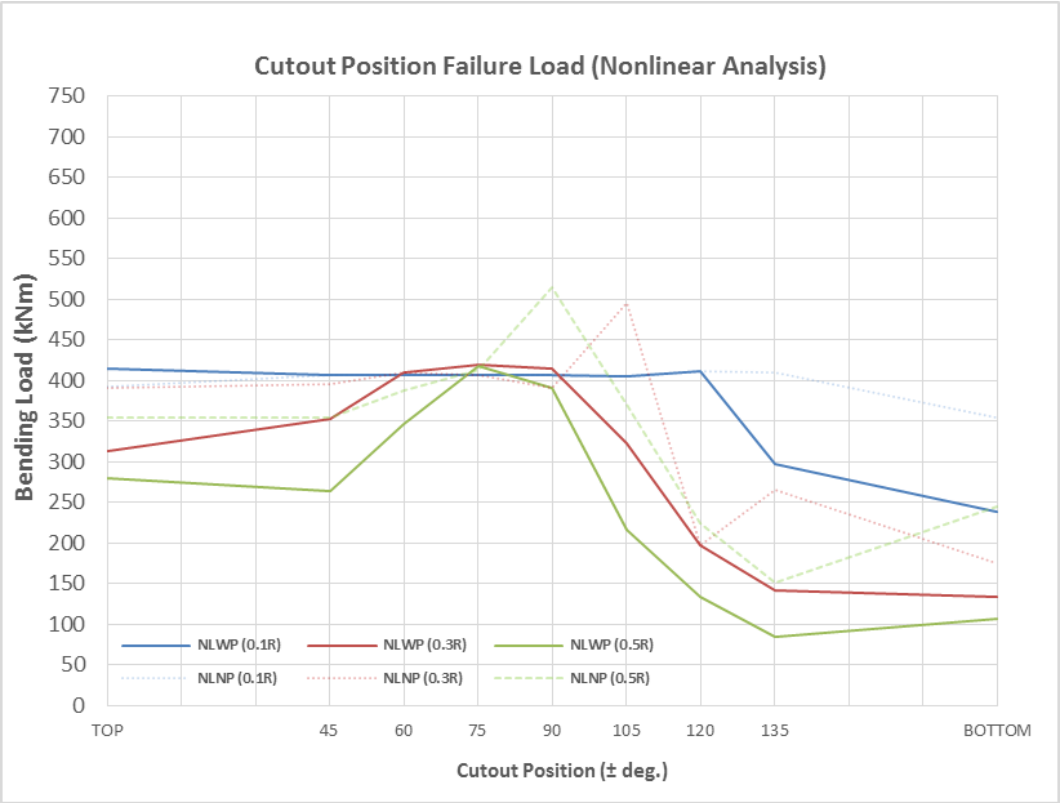


Figure 6.12 : Nonlinear analysis results with and without progressive failure.

while including progressive failure, the effect of reducing stiffness properties because of failure occurrence both in matrix and the fibers, reduces the critical load level substantially. Especially, in failure mode II and failure mode III cases the cylindrical shell fails before the ultimate load level of nonlinear analysis without progressive failure. Therefore, during nonlinear analyses, to be able to obtain more realistic analysis results close to the real test results, one must apply progressive failure analysis. Otherwise, one may get the ultimate failure load higher than the real failure load.

6.4 Extended Analysis of Cylindrical Shell with Cutouts

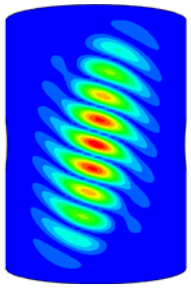
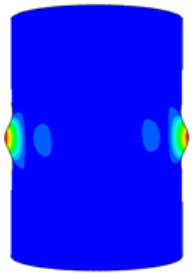
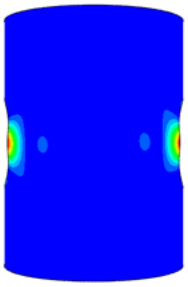
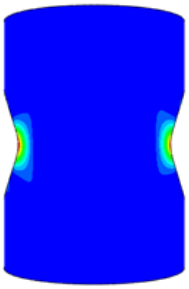
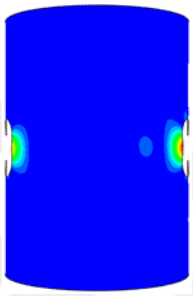
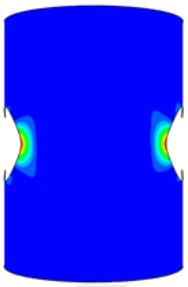
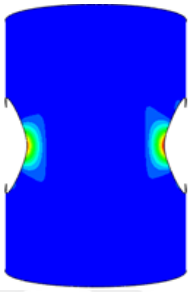
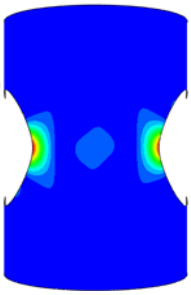
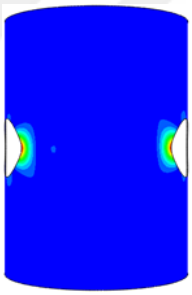
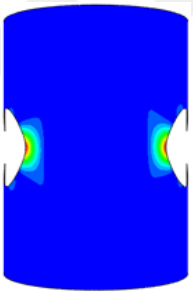
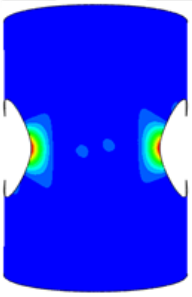
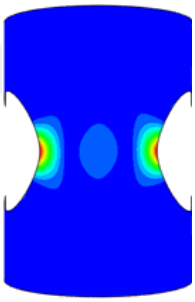
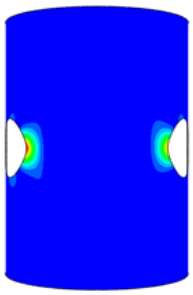
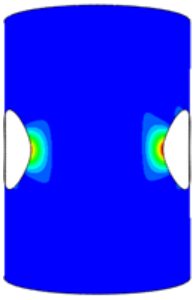
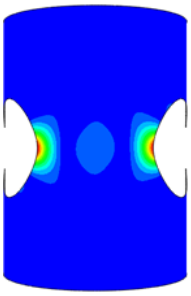
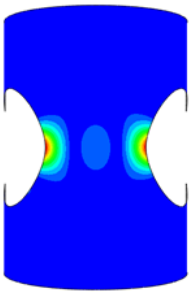
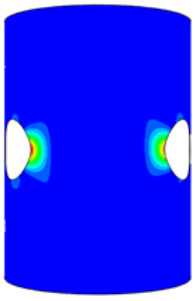
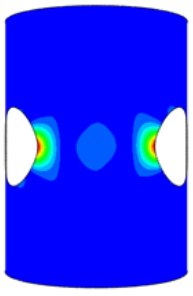
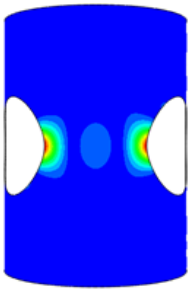
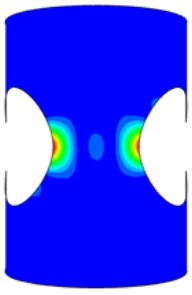
The results from the initial design study highlighted a specific area of interest, consisting of mode II failure below the upper load threshold of the testing machine. Therefore, an extended design study was undertaken to focus on the region to reinforce the trends observed there and aid in the selection of the final cutout configuration. Specifically, the range of the hole sizes was extended to include 0.4R and 0.6R and the locations were incremented every five degrees from 105° to 120° (including the 0.3R and 0.5R previous hole sizes). The 90° case was also included. The maximum design load, based on the test fixture's maximum bearing strength capacity, 415 kNm, which is very close to the calculated NLwPFA Mode I failure results. Therefore, it may not be possible to damage the cylinder with the Mode I failure cases. On the other hand, in Mode III failure cases, we have material strength failure and they are all catastrophic failures. Since the load limits of the test fixture is around 415 kNm the, as a result of previous analysis the cutout size and position was decided to be selected from Mode II failure. In all Mode I failure cases the load level is above the test fixture limit. On the other hand, in Mode III failure cases we have material strength failure and it is a catastrophic failure. The applied load increments during the analysis is adjusted so that intially it starts with 10 kNm for r=0.3R, 0.4R and 0.5R and 6 kNm for r=0.6R. After the first ply fiber failure the applied load increments were reduced to 5 kNm and 3 kNm. The study results are given in the following section.

6.4.1 Eigenvalue and failure mode analysis

The resulting plot of the failure levels, with the corresponding color-coding indicating the failure mode, is shown in Figure 6.13. Note that except for the 0.3R/90 cutout, the lowest eigenvalues are all local mode buckling as shown in Table 6.3.

The trends observed in the previous design study hold true for the locations of $\pm 105°$ to $\pm 120°$. As the hole size is increased, the load level for the local buckling decreases and the structure exhibits material failure closer to the buckling value. The smaller hole sizes have slightly increased failure load levels (compared to their eigenvalues) signifying some post-buckling strength after the initial local buckling. This is the preferred phenomena to observe during testing. Generally, thin cylindrical shells under compression loads do not exhibit such post-buckling strength, and in fact, the results

Table 6.3 : Eigenvalue analysis with respect to cutout positions (view from bottom of the cylinder.

β	0.3R:λ/FL	0.4R:λ/FL	0.5R:λ/FL	0.6R:λ/FL
$\pm 90^\circ$	691.27/389.88 	553.224/493.81 	399.761/391.07 	310.90/312.58 
$\pm 105^\circ$	403.39/312.79 	296.08/261.40 	230.52/215.77 	184.51/180.46 
$\pm 110^\circ$	341.99/293.31 	253.84/220.29 	197.83/183.51 	156.59/149.98 
$\pm 115^\circ$	296.57/239.71 	220.35/190.27 	170.17/154.45 	132.96/127.23 
$\pm 120^\circ$	260.90/197.07 	192.32/161.21 	146.50/133.53 	115.37/107.08 

for cutout configurations designated as mode I failure substantiate this claim. For mode I, the compressive load at the bottom of the cylinder leads quickly to material failure and usually catastrophic material failure, since the compressive region loses all ability to withstand load. In contrast, the mode II configurations buckle around the cutout but do not always degrade the high load-bearing compressive region, producing a structure that can go beyond its initial buckled state until ultimate failure.

An additional indication of this post-buckling phenomenon is provided by the additional purple dashed line in Figure 6.13, extending from the yellow-filled triangle at $\beta = 90°$ and a load of around 500 kNm to the yellow triangle at $\beta = 90°$ that is part of the 0.4R curve. This point was the initial result for 0.4R/90, failing in mode II and at a higher level than its hole size neighbors. This bucks the trend expected for the failure modes and therefore further discussion is required. The initial result is calculated

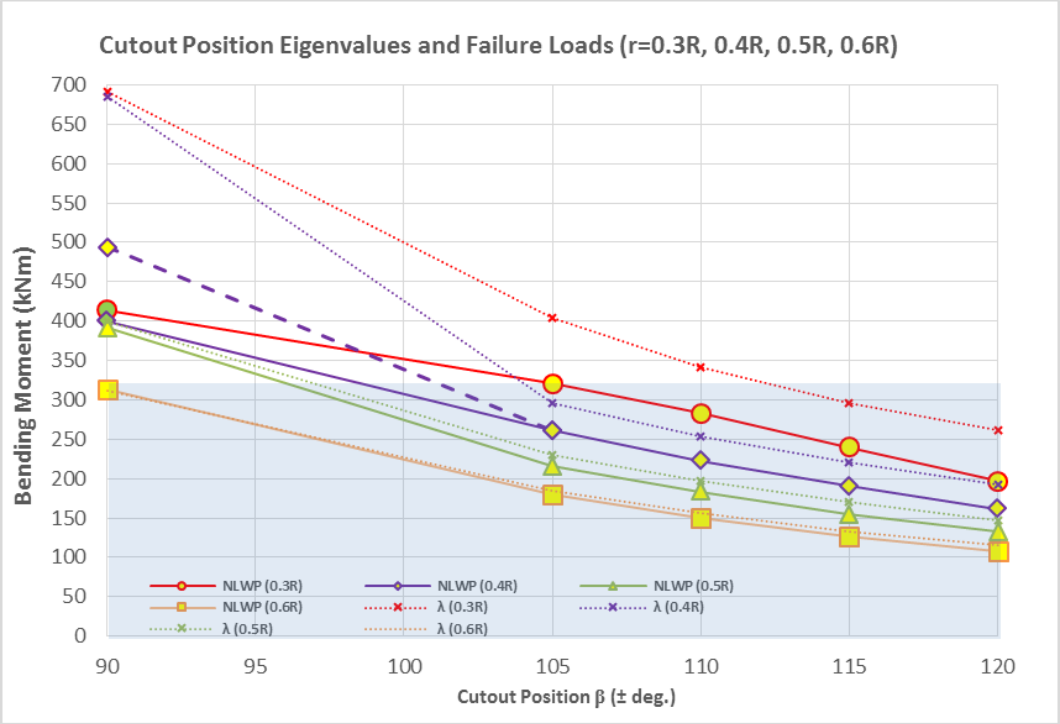


Figure 6.13 : Detail Linear Buckling and NL with PFA Results.

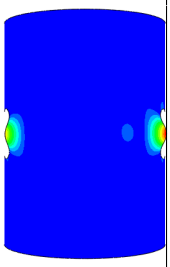
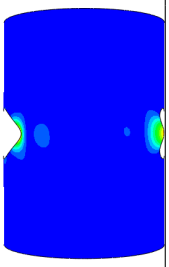
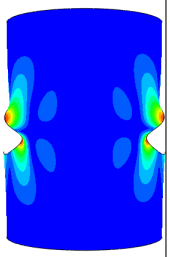
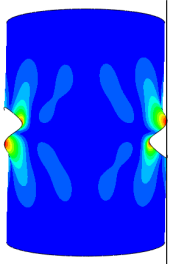
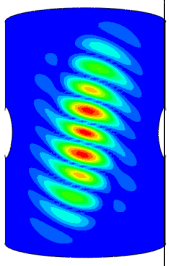
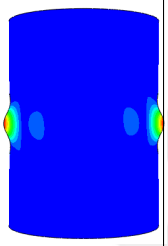
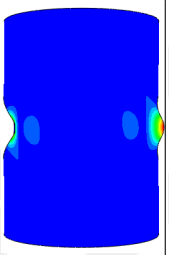
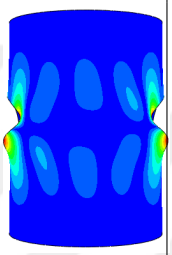
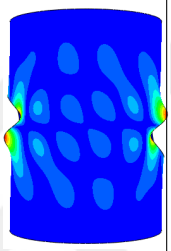
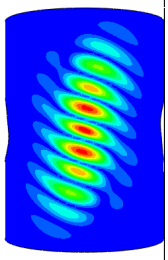
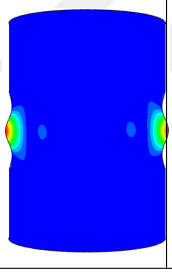
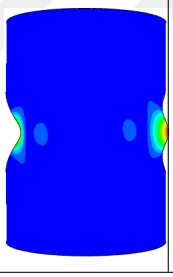
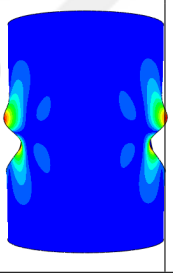
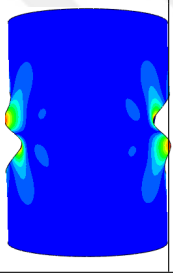
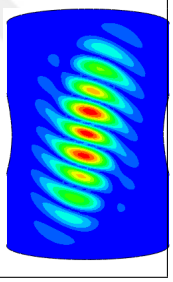
by assuming that the imperfection is based on the critical eigenvalue and associated buckling mode, which is a local mode around the cutout for this configuration. This produces a mode II failure and is thus designated by a yellow-filled symbol at the left end of the purple dashed line. However the slightly smaller hole (0.3R/90) has a global critical eigenvalue and fails due to mode I (green-filled circle), but at a lower level than the larger hole, which is inconsistent with our expected trends. Examination of

the 0.4R/90 configuration indicates that the global mode is actually the fifth smallest eigenvalue. Re-definition of the imperfection based on the global mode shape, as opposed to the lowest local buckling mode, excited the post-buckling shape and led the structure into the global mode of failure, represented above by the green-filled diamond for the purple curve. Thus, care must be taken when defining the "worst-case" mode shape for cylinders analyzed using nonlinear Riks analysis with imperfections. To ensure that this phenomenon did not alter any other results, potential configurations were re-analyzed with multiple modes included in the imperfection. However, the case detailed above was the single exception to the previously computed results.

6.4.2 Imperfection investigation

To ensure that 0.4R/90 cutout case phenomenon did not alter any other results, potential configurations were re-analyzed with multiple modes included in the imperfection. Since the cylindrical shells are imperfection sensitive, during the application of imperfections, until obtaining the real imperfection data, usually the first critical eigenmode was selected. However, when nonlinear analysis were performed for 0.4R cutout at 90° with 10% imperfection of the first critical eigenmode, it was seen that the failure load with the value of 493.8 kNm is much higher than the peak value of the even non-cutout case. After checking the other eigenmodes for all potential configurations, it was discovered that, there are three configurations with first critical eigenmode is at the cutout edge and the fifth eigenmode is completely distinct from the cutout edge with a much higher value than first four eigenvalues and located at the compression side of the cylinder, as seen in the Table 6.4. Since the first noticed configuration was 0.4R/90 cutout case it was first started to analyze this configuration as the NLwPFA results of combination of eigenmodes are given in Table 6.6. When the imperfection coming from the 5th eigenmode was included in addition to 1st eigenmode, during the non-linear analysis, it was seen that the failure load decreased to 399.6 kNm which is almost has the same peak value with other cutout sizes. Even, without including the first critical eigenmode and only using the imperfection coming from the 5th eigenmode failure load decreased to 397.8 kNm. In addition to failure load change, it also caused the failure mode to change from Failure Mode II to Failure Mode I. From Table 6.4 for 0.4R/90, it seems 3rd and 4th modes are also distinct from

Table 6.4 : Linear eigenvalue results (view from bottom of the cylinder).

r/β	1st (kNm)	2nd (kNm)	3rd (kNm)	4th (kNm)	5th (kNm)
r=0.3R, β=105	403.40 	405.32 	450.01 	477.08 	656.27 
r=0.4R, β=90	553.22 	554.56 	605.79 	644.48 	684.74 
r=0.5R, β=90	399.76 	401.75 	448.97 	471.90 	673.21 

the first two modes, however they are still interacting with the cutout edge allowing almost the same result with first two modes. On the other hand, the 5th modes is completely acting on a different location than first four modes and therefore it becomes crucial during nonlinear analysis. Note that during introduction of imperfection for each modes 10% of the shell thickness was included. There might be some cases that

Table 6.5 : NLwPFA results (0.3R/105).

Eigenmode Combinations	NLwPFA Failure Load (kNm)	Failure Mode
1st Mode only	312.79	Mode II
5th Mode only	313.50	Mode II
1st and 5th Modes	306.50	Mode II

the contribution coming from the distinct modes are equal and since the cylindrical shells are very imperfection sensitive they cause it fail either in failure mode I or II.

For example, as shown in Table 6.5 and Table 6.7, the failure modes are mode II in both cases, this might be due larger hole size and the being close to the compression side of the cylinder. When, we have a case in between as in Table 6.6, depending on the buckling mode, the failure location and failure load may change. Therefore, for a complete analysis, all distinct buckling modes must be taken into consideration during nonlinear analysis. This result showed that, during nonlinear analysis of a

Table 6.6 : NLwPFA results (0.4R/90).

Eigenmode Combinations	NLwPFA Failure Load (kNm)	Failure Mode
1st Mode only	493.81	Mode II
2nd Mode only	493.80	Mode II
4th Mode only	499.80	Mode II
5th Mode only	397.80	Mode I
1st and 5th Modes	399.60	Mode I
1st, 2nd and 5th Modes	399.00	Mode I

Table 6.7 : NLwPFA results (0.5R/90).

Eigenmode Combinations	NLwPFA Failure Load (kNm)	Failure Mode
1st Mode only	391.00	Mode II
5th Mode only	371.50	Mode II
1st and 5th Modes	367.50	Mode II

cylindrical shell under bending moment, although the first buckling eigenvalue seems critical, the imperfection coming from the remaining distinct mode shapes becomes very important for predicting the failure load. For a cylindrical shell under bending moment the critical failure location is either at compression side of the cylinder or at the cutout edge and the distinct modes at those two locations becomes dominant during the nonlinear analysis and it cannot be decided which one is going to be dominating the failure load. Therefore, during the introduction of geometrical imperfections coming from buckling mode shapes it is vital to include initial distinct mode shapes.

6.4.3 Extended design study results

In the extended design study in addition to the previous analysis also the 0.7R cutout size was added to investigate the failure modes of the largest cutout and see if the Mode I failure still exist at 75° position. The results are shown in Tables 6.8-6.11 and Figure 6.14.

Table 6.8 : NLwPFA Failure Modes.

FAILURE MODES									
0.0R	I	I	I	I	I	I	I	I	I
0.1R	I	I	I	I	I	I	I	III	III
0.3R	III	III	I	I	I	II	II	II	II
0.4R	III	III	I	I	I	II	II	II	II
0.5R	III	III	III	I	II	II	II	II	II
0.6R	III	III	III	I	II	II	II	II	II
0.7R	III	III	III	I	II	II	II	II	II
$\beta = \pm$	0(T)	45	60	75	90	105	120	135	180(B)

Table 6.9 : Linear Buckling Modes.

CRITICAL LINEAR BUCKLING MODES									
0.0R	G	G	G	G	G	G	G	G	G
0.1R	G	G	G	G	G	G	G	L	L
0.3R	G	G	G	G	G	L	L	L	L
0.4R	G	G	G	G	G	L	L	L	L
0.5R	G	G	G	G	L	L	L	L	L
0.6R	G	G	G	G	L	L	L	L	L
0.7R	G	G	G	G	L	L	L	L	L
$\beta =$	0(T)	45	60	75	90	105	120	135	180(B)

Table 6.10 : Detail NLwPFA Failure Modes.

FAILURE MODES					
0.3R	I	II	II	II	II
0.4R	I	II	II	II	II
0.5R	II	II	II	II	II
0.6R	II	II	II	II	II
$\beta = \pm$	90	105	110	115	120

Table 6.11 : Detail Critical Buckling Modes.

DETAIL CRITICAL BUCKLING MODES					
0.3R	G	L	L	L	L
0.4R	G	L	L	L	L
0.5R	L	L	L	L	L
0.6R	L	L	L	L	L
$\beta = \pm$	90	105	110	115	120

The results show that as the cutout size increases the failure is Mode III at the upper side of the cylinder and Mode II at the lower side of the cylinder. The only position that always has Mode I failure is 75° position. In addition, the failure load is also not changing at that position.

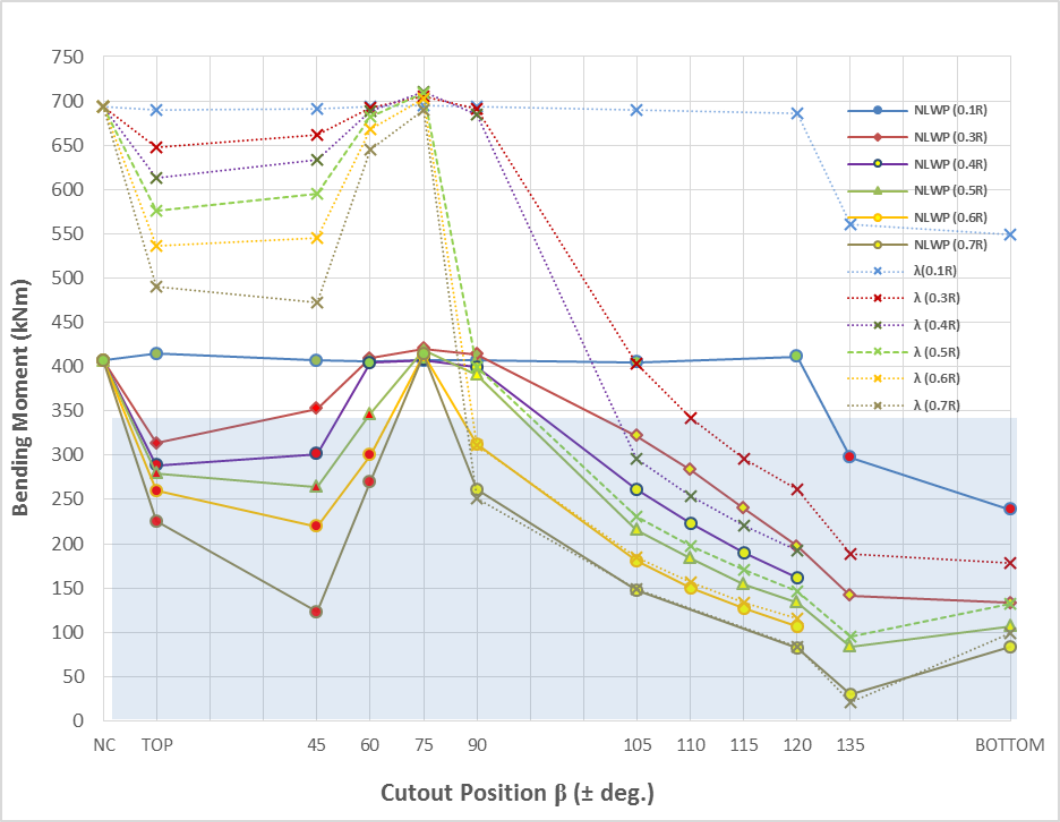


Figure 6.14 : Linear Buckling and NL with PFA Results.

6.4.4 Discussion on $\pm 75^{\circ}$ location

One point of interest along the way occurs at $\pm 75^{\circ}$ location. From Figure 6.14, one can easily notice that, the highest failure load level during both linear and nonlinear progressive failure analysis for all cutout sizes is $\pm 75^{\circ}$ location with corresponding values of equal to almost 700 kNm and 400 kNm. Therefore, it became important to examine $\pm 75^{\circ}$ specifically. Since the largest cutout size is 0.7R, it is expected to have lower failure load compared to smaller cutout size. Therefore, it was decided to start with the highest cutout size investigation to see if there is some other eigenmodes that may affect the failure load and not included during imperfection application coming from eigenmode analysis. For that purpose, first five critical eigenmodes were taken into consideration as shown in Table 6.12.

It can be observed that first two modes are at the cutout edges and they have very close eigenvalues, which are expected for thin walled cylindrical shells. Although, 3rd and 4th eigenvalues are higher, they are still interacting at the cutout edges. The only eigenmode is the 5th mode, having higher eigenvalue and acting on compression side

Table 6.12 : Linear eigenvalue results (view from bottom of the cylinder).

r/β	1st (kNm)	2nd (kNm)	3rd (kNm)	4th (kNm)	5th (kNm)
r=0.7R, β=75	563.09	564.63	612.38	652.91	689.55

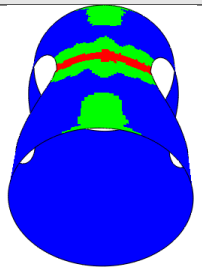
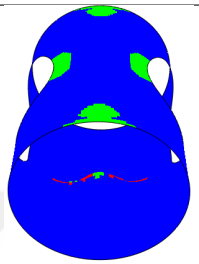
of the cylinder without interacting the cutout edge. Therefore, it was decided to include also the imperfection coming from 5th eigenmode during NLwPFA.

The results of the NLwPFA including imperfections coming from different eigenmode combinations, given in Table 6.13, show that even using imperfection from first five eigenmodes do not alter the critical failure load. The only change is in the failure mode; while including 5th eigenmode, it switches the failure mode from strength loss driven Failure Mode III to Failure Mode I which is failure driven by global buckling. For 0.7R cutout size, depending on the bifurcation, the cylindrical shell may select either of the stable path resulting either Mode III or Mode I failures. Since for both case the failure loads are very close to each other it may result any of the failure modes. The critical point is that the failure load remains almost the same that makes $\pm 75^{\circ}$ position important.

For the remaining cutout sizes smaller than 0.7R, all first five buckling eigenmodes are in global compression side; therefore, there are no any other distinct mode shapes that can alter the failure load.

For this configuration, the top of the cutout is within the tensile region of the cylinder, however the stress levels there are not large enough to generate material failure except for the 0.7R/75 with imperfection from 1st critical modes of buckling. Meanwhile the bottom of the cutout is near the neutral axis and does not threaten to buckle at all due to the low compressive stresses. Therefore, for every hole size investigated the $\pm 75^{\circ}$ location generates a standard mode I failure where the compressive stresses at the bottom of the cylinder initiate buckling and then material failure occurs. The slight differences between the failure levels for different hole sizes are due mainly due to

Table 6.13 : NLwPFA results (0.7R/75).

Eigenmode Combinations	NLwPFA Failure Load (kNm)	Failure Mode	Failure Depiction
1st Mode only	414	Mode III	
5th Mode only	404.5	Mode I	
1st and 5th Modes	407	Mode I	
1st, 2nd, 3rd, 4th and 5th Modes	407.5	Mode I	

re-distribution of the stresses around the cutout and slight re-location of the neutral axis, changing the bending stiffness and stress levels at the critical bottom region. This result indicates the ability of cylindrical shells to possess cutouts at certain locations without any great effect on the overall failure mode (at least considering the modes of failure included here).

6.5 Cutout Recommendation Considerations

To select a proper cutout configuration for testing, the two major considerations are the mode of failure that is desired to be observed and the limit of the testing fixture. These criteria are best represented in Figure 6.13 and Figure 6.14, which display the failure loads and limits for the initial and extended studies. The gray region in these figures represents the practical range of the testing fixture that will avoid pullout within the clamped ends.

With regard to the failure mode, the mode I failure possesses a few disadvantages. First, Figure 6.14 indicates that the level for this mode is clearly above the threshold allowed for by the test fixture. Several additional configurations using larger hole sizes were conducted and it was found that there was no suitable configuration that

would produce a viable test specimen that underwent the classic mode I failure. Once the hole became big enough to decrease the buckling load below the test fixture threshold, a different failure mode (mode II) occurred at a lower load level. Second, the classic buckling mode along the bottom edge of the cylinder does not generate any interesting new phenomena associated with cylindrical shells under buckling in that the effect of the cutout is not highlighted. Lastly, the progressive failure model indicates that many of these failures will be quite catastrophic (buckling quickly followed by material failure), which may not be as instructive during the testing phase. Mode

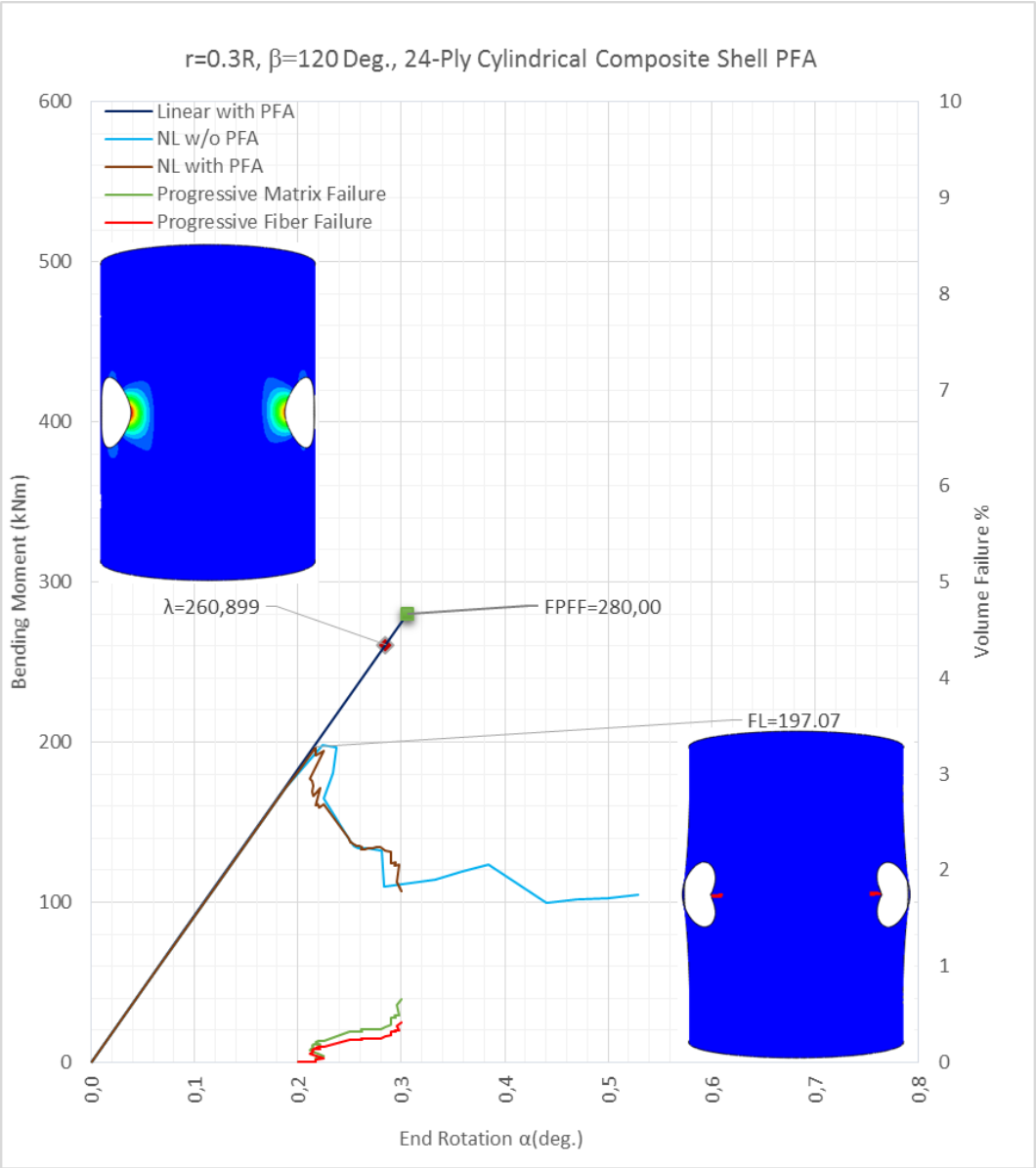


Figure 6.15 : Suggested cutout configuration.

III failure that represents material failure without any appreciable buckling effects has configurations below the appropriate test fixture threshold, however its response

may also be quite catastrophic from the tearing or crumpling of the failed regions around the cutout. Therefore, it was decided that the mode II failure will provide the most interesting case study and allow for sufficient leeway for the test fixture threshold. Specifically, the 0.3R/120 configuration shown in Figure 6.15 has several key advantages: some post-buckling strength after the initial buckling deformation; low ultimate failure load well below the test fixture threshold; and a smaller hole size, which may be more amenable to machining into the actual part and reducing additional shape imperfections.

With this general configuration selected, the next step is to generate a detailed ABAQUS model based on this configuration with the following improvements: actual material properties and layup of the existing part; flexible boundary conditions as documented by Blom [3]; and inclusion of the initial shape imperfections.

7. BUCKLING AND STRENGTH ANALYSIS OF VARIABLE STIFFNESS SHELL WITH CUTOUTS UNDER BENDING

The constant stiffness cylindrical shell that was investigated in Chapter 6 was optimized by Blom [3] for buckling under constant bending moment by varying the fiber orientation angle within a ply using steered fiber concept. Due to spatial variation of fiber orientation angels, the stiffness of the shell also vary spatially causing the shell to be called as variable stiffness (VS) shell. The aim was to improve the structural performance, since bending causes loads to vary around the circumference of the cylinder. By stiffness variation, the loads in the critical areas would be reduced by redistribution of the stresses and will change the buckling behavior of the structure. The same fiber orientation and stacking sequence was used as in Blom [3] study, however, in this study cutouts were introduced to see the effect of them and progressive failure analyses were performed. After deciding a proper cutout configuration the shell was tested under pure bending load.

7.1 Geometry and Variation Definition

The structure under consideration is a circular cylinder with a radius R of 304.5 mm (12 in), length L of 813 mm (32 in), and an overall shell thickness H of 4.392 mm (0.173 in) similar to CS study case. A local coordinate system is based on cylindrical coordinates with θ=0 at the top of the cylinder, as shown in Figure 7.1. Loading is introduced at each end of the cylinder and it is confined to pure bending about the X-axis, applied in a direction so that the bottom of the cylinder is under compression and the top in tension.

The layup of the conventional shell is $[\pm 45/0_2/90_2/0/\pm 45_2/90]_s$. The layup of the VS shell is combination of fiber-steered plies and constant-angle plies. The steered plies had an angle variation in the circumferential direction, as shown in Figure 7.1. The variation of the fiber angle within a ply was determined by design variables T_i, which keep constant fiber angle at 45° increments around the circumference, as

displayed in Figure 7.1. The fiber orientations in-between these locations are defined by a constant curvature path, such that the fiber angle varies as:

$$\cos\varphi(\theta) = \cos T_i + (\cos T_{i+1} - \cos T_i)\frac{\theta - \theta_i}{\theta_{i+1} - \theta_i} \tag{7.1}$$

where θ_i is the circumferential coordinate at which the fiber angle is defined as T_i. There is a fiber orientation transition between two segments, where the fiber angle itself is continuous, whereas the in-plane curvature changes. For a cylinder with radius R the in-plane curvature κ within one segment is [7]:

$$\kappa = \frac{\cos T_i - \cos T_{i+1}}{R(\theta_{i+1} - \theta_i)} \tag{7.2}$$

The figure on the right represents the cross-section of the cylinder and designates the locations where the circumferential variation $\varphi(\theta)$ of the fiber orientation angle is defined, where T_i represents the value of the fiber orientation angle at each location. Note that the variation is symmetric about the vertical axis, in agreement with both the loading conditions and ensuing cutout placement.

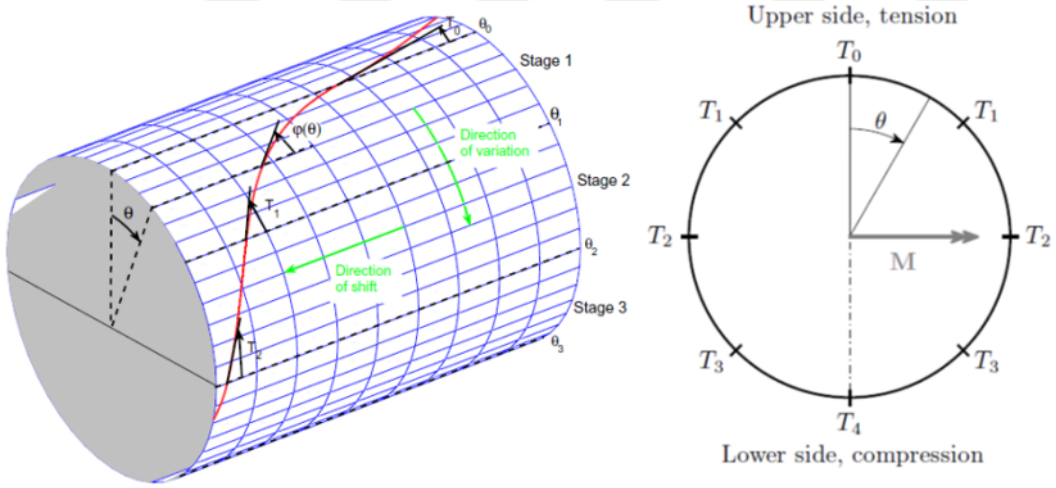


Figure 7.1 : The cylinder with circumferential variation of fiber orientation angle [7].

The stacking sequence of this VS carbon fiber reinforced cylindrical shell is given as $[\pm 45/\pm\varphi_1(\theta)/0/90/\pm\varphi_3(\theta)/0/90/\pm\varphi_5(\theta)]_s$, where the $\varphi_i(\theta)$ represent plies with an 8-segment piece-wise continuous constant curvature variation in the circumferential direction, as described by Blom [3]. Within that work, the stiffness variation was designed for maximum load carrying capability under pure bending. In this study, the stacking sequence and the fiber orientations were kept similar to the Blom's work to

see if the opening of the cutouts into the cylinder will still keep the failure load level of the VS cylinder to be higher than the CS cylinder. .

7.2 Implementation within FEM Solution

Analysis of the CS cylinder given in Chapter 6 was completed using the commercial FEM solution ABAQUS [10]. In that model, the stacking sequence was easily defined using the COMPOSITE option of the SHELL SECTION designator to define the fiber orientation angle of each layer. For the VS case here, additional computations are required due to the spatial variation of the fiber orientation angle within the plies defined in Table 7.1. For the non-cutout composite cylinder work by Blom [3], this

Table 7.1 : Fiber orientation angle value for the VS cylinder design.

Ply	$T_0(0^\circ)$	$T_1(\pm 45^\circ)$	$T_2(\pm 90^\circ)$	$T_3(\pm 135^\circ)$	$T_4(180^\circ)$
$\varphi_1(\theta)$	10.0°	10.0°	10.0°	10.0°	24.7°
$\varphi_3(\theta)$	10.0°	10.0°	10.6°	56.9°	61.7°
$\varphi_5(\theta)$	10.0°	12.0°	10.0°	34.2°	68.9°

was accomplished through a FORTRAN user-subroutine UGENS that computed the shell stiffness matrices [A], [B], [D] at each element integration point. Due to the fact that the chosen Progressive Failure Analysis procedure, the subroutines were modified to produce fiber orientation angles for each ply (as opposed to the fully computed [A], [B], [D] matrices). The fiber angle values were introduced into the model through the DISTRIBUTION TABLE designator within ABAQUS. This recent feature allows the user to construct tables to list specified values for each element or node. In this case, one table was used for each distinct ply (plies 1-12, the symmetric side used the same table as its symmetric counterpart), and default values were used for the CS plies. Each S4R shell element possesses one integration point, at the centroid of the element. The centroid was calculated from the four connected nodes of each element and the calculation procedure is given in Appendix I. The fiber orientation angle values were calculated there based on the parametric formulation of the circumferential variation derived by Blom [3] is given below.

$$\cos\varphi(\theta) = \cos T_0 + (\cos T_1 - \cos T_0)\frac{\theta - \theta_0}{\theta_1 - \theta_0} \tag{7.3}$$

Curvature is:

$$\kappa = \frac{\cos T_0 - \cos T_1}{R(\theta_1 - \theta_0)} \tag{7.4}$$

The fiber path is defined as:

$$x = \frac{\sin\varphi - \sin T_0}{\kappa} \tag{7.5}$$

where φ and θ is shown in Figure 7.1.

A Python script was used to construct both the input file and the tables based on the model parameters (geometry, mesh size, material properties, stacking sequence, and cutout configuration), where the tables used the FORTRAN subroutines interactively to calculate the fiber orientation angles. The tables were written to external files so they could be easily changed without having to alter the original input file. This technique proved to be quite beneficial for several reasons:

(1) Using the original FORTRAN subroutines ensured agreement with the manufactured shells and the previous results of Blom [3],

(2) Using fiber orientation angles for each ply instead of stiffness matrices for the entire shell element allowed the use of the chosen PFA solution,

(3) Hard-coding of the external table files allowed an easy switch between CS and VS configurations,

(4) Re-compiling of the ABAQUS program was not required.

To demonstrate the agreement with Blom's work, contour plots of the fiber orientation angles for the three VS plies defined in Table 7.1 are displayed in Figure 7.2 (designated by their ply numbers 3, 7 and 11, respectively). These plots are constructed from the subroutines that calculate the fiber orientation angles for regularly spaced grid points. The cylinder is unrolled for full visualization of the angle variation, and corresponds to the paths generated by Blom as shown in Figure 7.3. Each ply figure uses colors to denote the variation of the fiber orientation angle and is based on the actual courses that were used to build the parts. Thus, the edges for each course emerge as discontinuities in the color contours and the paths of the courses are easily discerned. The balanced ply counterparts (plies 4, 8, and 12, respectively) are a mirror image about the vertical axis of the images shown in Figure 7.2. The stiffness of the lower part of the cylinders were increased in order to carry more bending load on the mentioned plies.

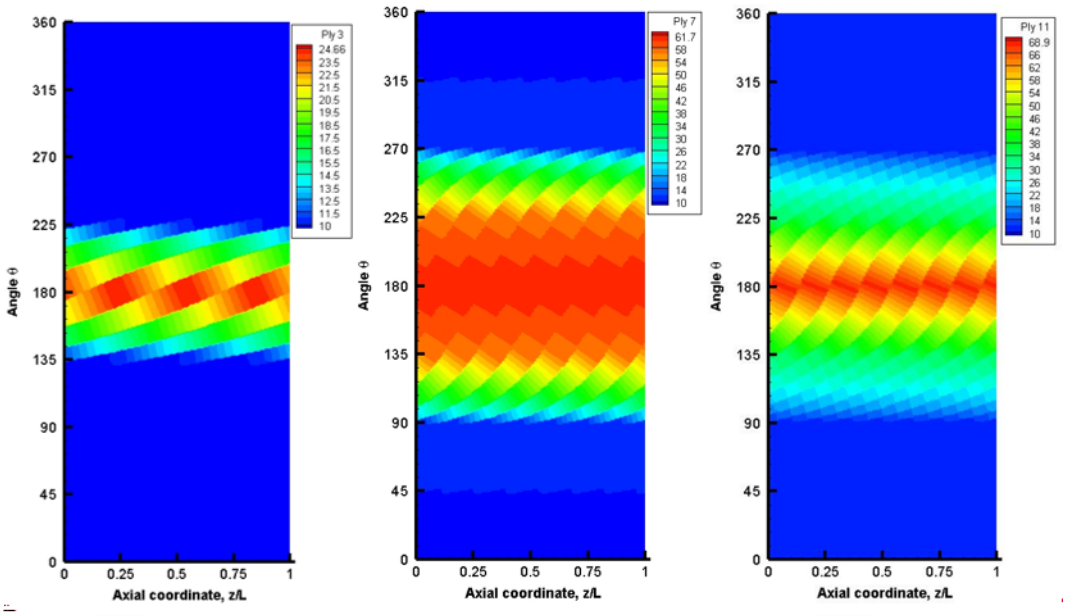


Figure 7.2 : Contour plots of the fiber orientation angles for the three VS plies.

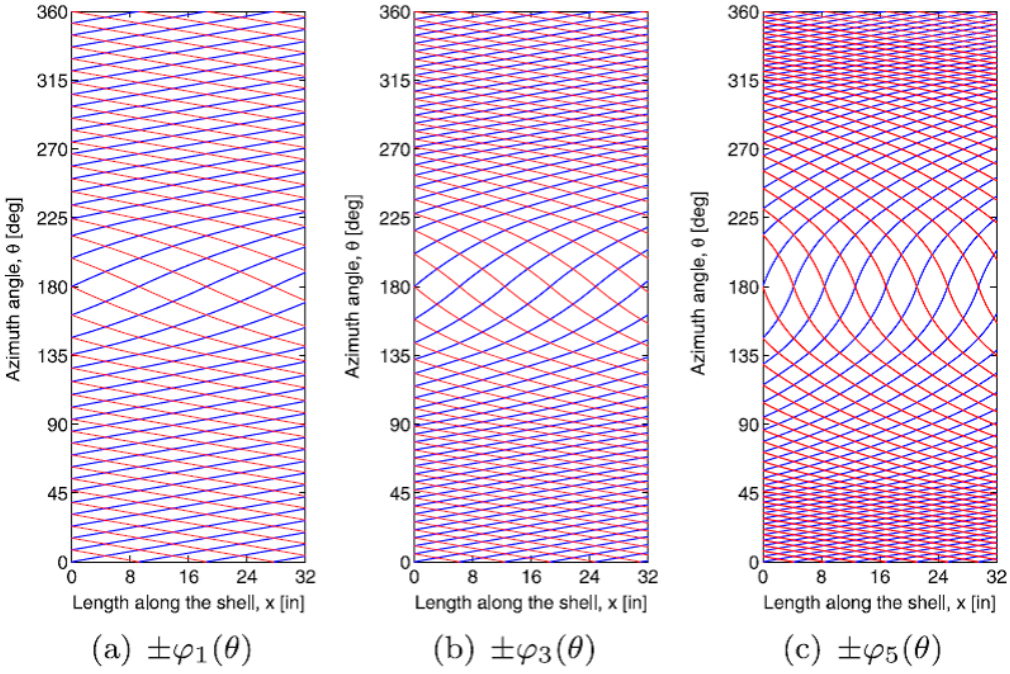


Figure 7.3 : Ply angle variations shown in Blom's study [11].

7.3 Baseline Case Comparison

Verification of the previous ply angle calculations is further demonstrated by comparison to the original calculations of Blom [3]. The usual four analysis cases (linear buckling, linear static, nonlinear Riks, and nonlinear Riks with PFA) were performed for the non-cutout case and the bending moment-end rotation curvature relations are displayed in Figure 7.4.

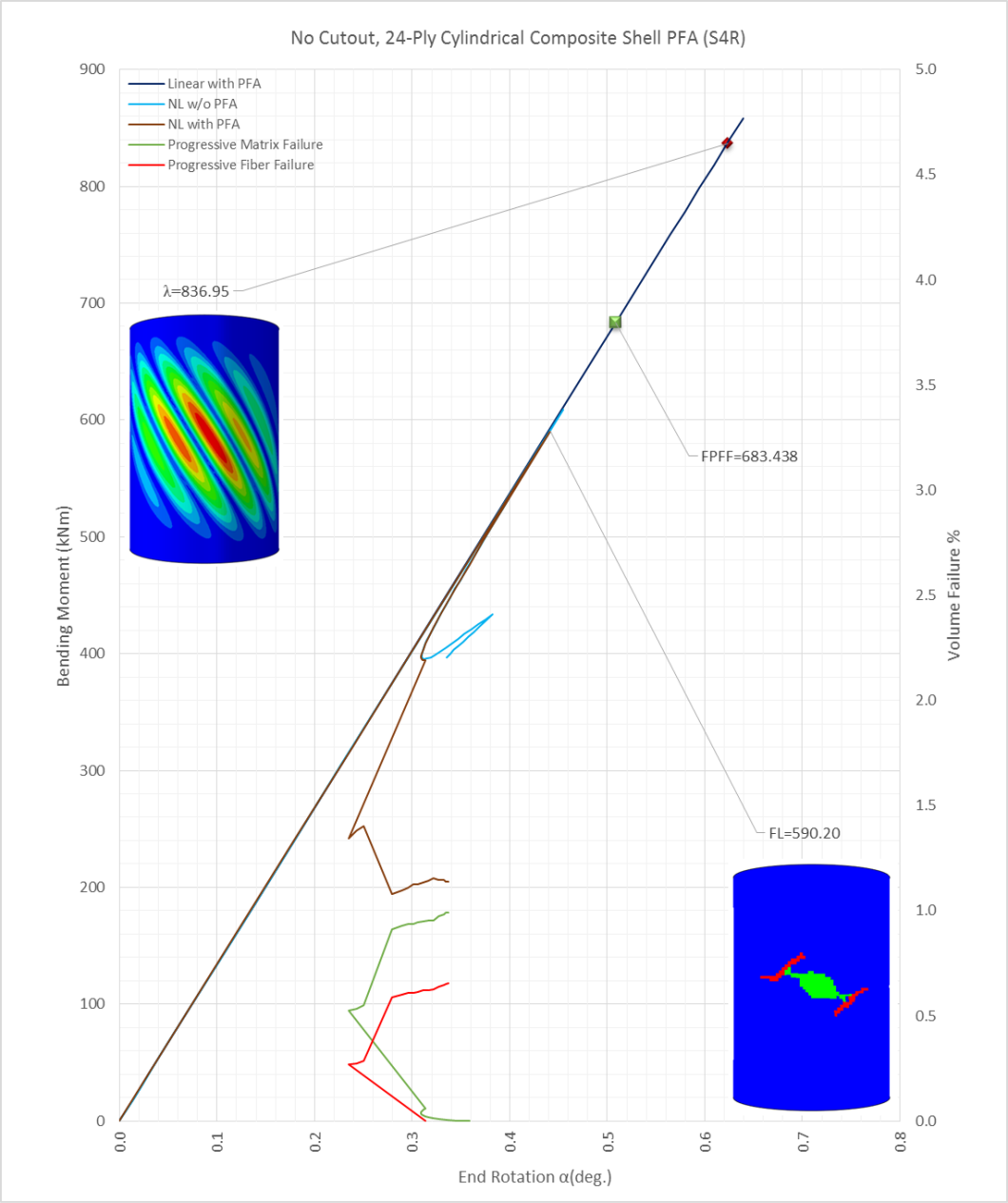


Figure 7.4 : Finite element solutions for VS non-cutout case.

The eigenvalue calculation of 837 kNm corresponds to the IM7/8552 material properties used here and is within the acceptable amount of agreement to the value found by Blom (805 kNm) for slightly different material properties. The first-ply-fiber-failure load calculated from the linear static analysis, designated by FPFF in the figure, is actually calculated to be lower than the critical eigenvalue, however once nonlinearity is considered through the Riks analysis the cylinder's limit moment is dominated by the instability effects. Note that the limit moment (590 kNm) is well above 400 kNm, which is the maximum load that can be applied in the test fixture, so that a significant reduction in load-carrying capability through the

introduction of a cutout must be observed for useful testing. The non-cutout VS cylinder buckles into the traditional mode I (deformation at the bottom of the cylinder where the compressive stresses are the highest) and material failure initiates within the post-buckled region until failure. The inset figures displaying the lower section of the cylinder indicate the mode shape for the first eigenvalue and the material failure initiation from the PFA analysis, respectively, where the green area in the lower right inset represents matrix failure and the red areas indicate the fiber failure. Figure 7.4 represents the principal elements of the response for a given cutout configuration. The appendices contain similar graphs for all configurations considered.

7.4 Variable Stiffness Design Study Results

This section details the design study results by first introducing the possible configurations for the cutout and then providing summaries of the design studies for both eigenvalue analysis and full nonlinear analysis with PFA. Detailed moment-end rotation plots for each configuration are provided in the appendices J, K, L and M.

7.4.1 Cutout configurations

The possible configurations considered in the design study are the same as the ones used for the CS cylinder design study. The major details are repeated here for ease of reference.

The cutout shape is defined as circular and centered longitudinally at the mid-length of the shell. The circumferential location is allowed to vary from the top to the bottom, with any configurations away from the top/bottom also containing a symmetric cutout on the opposite side to maintain left/right symmetry of the shell. The circumferential locations (β, starting from the top of the cylinder) are initially spaced at 15° intervals, with the locations near the top and bottom not utilized due to overlapping from the symmetric cutout on the opposite side. Figure 7.5 demonstrates the possible configurations considered in the initial design study and displays a cutout configuration located at 45°. Cutout size a=iR, represented by the radius of the circular cutout in relation to the radius of the cylindrical shell, is selected to represent small, medium, and large sizes (i=0.1,0.3,0.5, respectively). These sizes are meant to represent typical window or door sizes in an aircraft fuselage. Cutout configurations are represented as

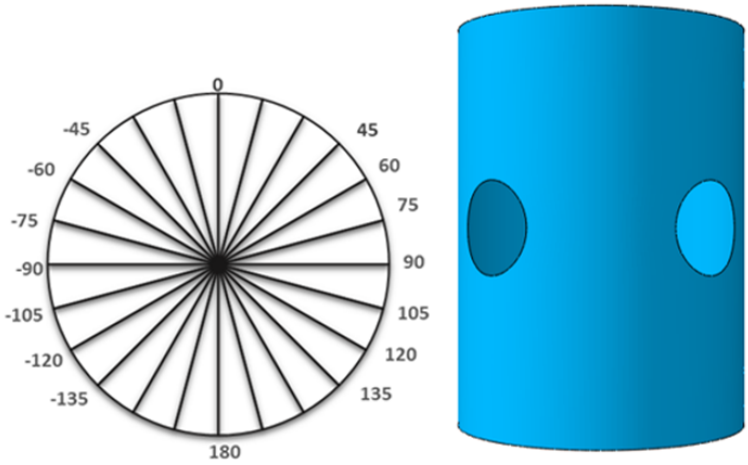


Figure 7.5 : Cutout configuration possibilities and example geometry (0.3R/45).

the size designation followed by the circumferential location in the form iR/β, such as "0.3R/90" for the medium-sized cutout located at the sides of the cylinder.

7.4.2 Eigenvalue analysis

The linear eigenvalue results for the various cutout sizes are useful for several reasons:

(1) They indicate the mode shape for the critical buckling mode, either a global (G) mode, which buckles at the bottom of the cylinder, or a local (L) mode with deformation focused around the cutout,

(2) The linear buckling modes serve as basis for the imperfections introduced into the nonlinear analysis and therefore these shapes guide the post-buckling response,

(3) Design of shell structures often uses linear buckling modes as a performance constraint.

Here the results are presented for the VS case and discussed briefly, with detail and comparisons to nonlinear results postponed until the next section. The raw results for the calculated eigenvalues of the VS cylinder are displayed in Figure 7.6. Each colored line represents a different cutout size as indicated by the legend, and the positions vary around the circumference as denoted by β. Note that 'NC' refers to the non-cutout baseline case. The shaded area represents the allowable loading by the test fixture. The eigenvalues for the non-cutout case and most of the configurations with the cutout located on the top half of the cylinder ($\beta < 90°$) possess the highest eigenvalues. The modes correspond to global deformation with the buckled waves

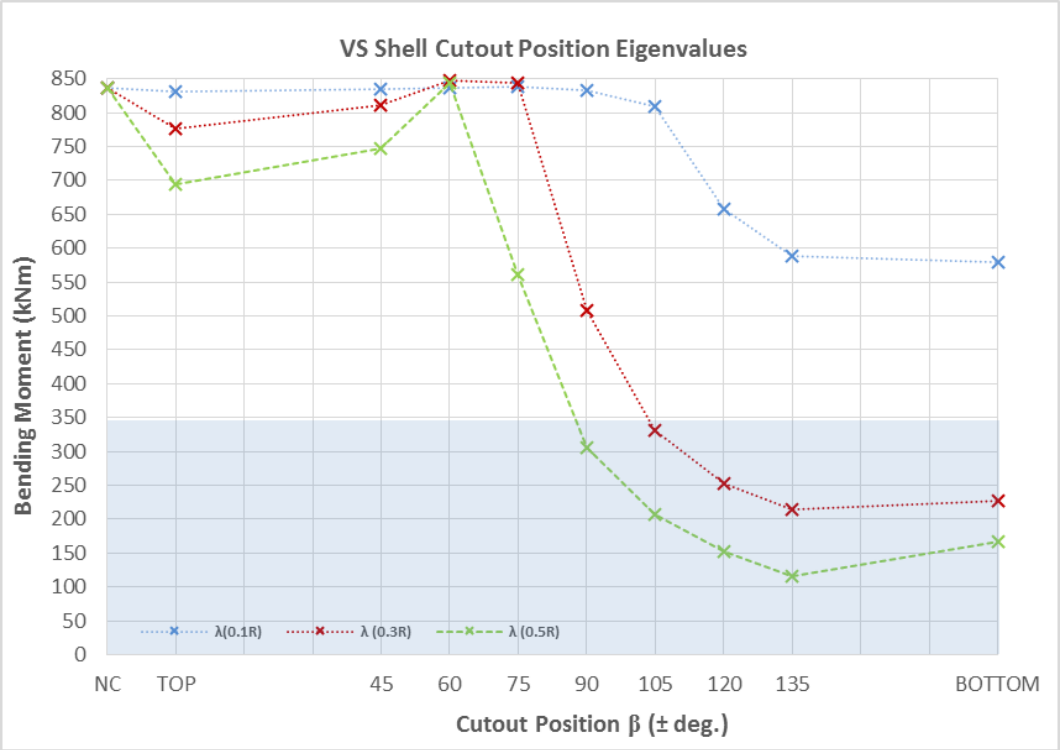


Figure 7.6 : Critical eigenvalues versus cutout position for representative cutout sizes.

occurring at the bottom of the cylinder. Note that the value (837 kNm) is much higher than the CS cylinder baseline case (694 kNm). Slight changes from this baseline value for larger cutout sizes are attributed to the reduced bending stiffnesses of the shell due to the material removed by the cutout. As the cutout size gets larger and moves toward the lower side of the cylinder, the deformation transits into the local mode around the cutout. Significant decrease in the buckling load is observed for these cases, especially for the larger cutout sizes.

A summary of the buckling mode designation, global (G) or local (L), is provided in Table 7.2 for the VS cylinder and corresponds to the observed deformation for the values plotted in Figure 7.6. As a comparison, the corresponding summary for the CS

Table 7.2 : Critical buckling mode summary for VS cutout configurations.

VS LINEAR BUCKLING MODES									
0.0R	G	G	G	G	G	G	G	G	G
0.1R	G	G	G	G	G	L	L	L	L
0.3R	G	G	G	G	L	L	L	L	L
0.5R	G	G	G	L	L	L	L	L	L
$\beta =$	0(T)	45	60	75	90	105	120	135	180(B)

case is provided in Table 7.3. The transition between global and local is similar though

Table 7.3 : Critical buckling mode summary for CS cutout configurations.

CS LINEAR BUCKLING MODES									
0.0R	G	G	G	G	G	G	G	G	G
0.1R	G	G	G	G	G	G	G	L	L
0.3R	G	G	G	G	G	L	L	L	L
0.5R	G	G	G	G	L	L	L	L	L
$\beta =$	0(T)	45	60	75	90	105	120	135	180(B)

shifted to the left for the VS case. This may seem counter-intuitive, indicating that the effect of the cutout is amplified for the VS case, however it must be noted that the critical eigenvalue for the CS global mode is much lower than the value for the VS cylinder, which was designed for a higher buckling mode without any cutout present. Therefore, the possibility of a local critical mode is greater for the VS shell since the global eigenvalue is significantly higher than the local value generated by the presence of the cutout.

7.4.3 Failure limits and mode designations

The principal results for this design study are summarized in a similar fashion as the linear buckling results in Table 7.4 and Figure 7.7, where the designations in Table 7.4 are replaced with the failure mode type and Figure 7.7 includes the ultimate failure load levels as well as the previous eigenvalue results. The failure mode designations and load levels are discerned from the detailed load-displacement curves for each case, which are provided in the appendices.

Table 7.4 : Failure mode summary for VS cylinder cutout configurations.

VS FAILURE MODES									
0.0R	I	I	I	I	I	I	I	I	I
0.1R	I	I	I	I	I	II	II	III	III
0.3R	III	III	I	I	II	II	II	II	II
0.5R	III	III	III	II	II	II	II	II	II
$\beta =$	0(T)	45	60	75	90	105	120	135	180(B)

Closer examination of the results reveals similar trends to the CS case, where mode III failure (material failure without any discernable buckling beforehand, denoted by the red filled symbols) occurs for large cutouts near the top and the small cutout size at the bottom. Mode I failure (classical buckling at the bottom of the cylinder leading to material failure there, represented by green filled symbols) is most apparent for small

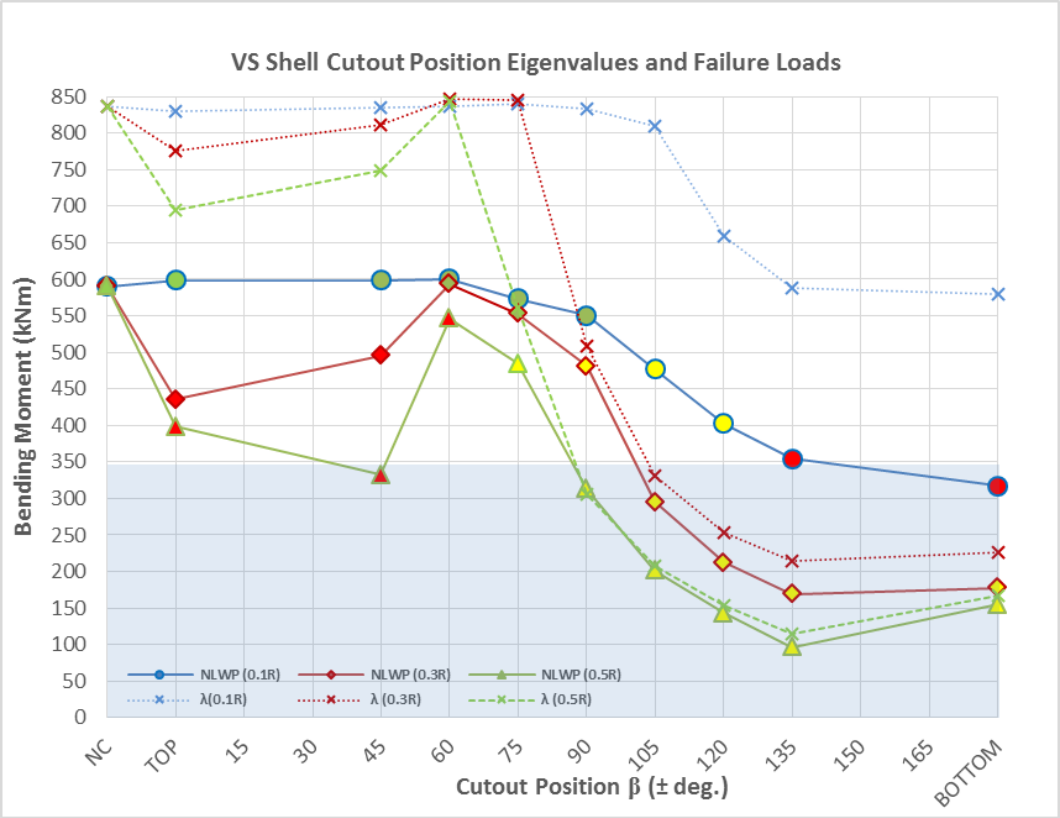


Figure 7.7 : Failure loads versus cutout position β for representative cutout sizes.

cutouts and those located near the tension side of the cylinder. The transition mode II (exhibited by local buckling around the cutout, yellow filled symbols) begins and ends at different locations for each cutout size but represents similar response. The comparisons to the CS results are quite revealing and are therefore presented for each cutout size (Figure 7.8- Figure 7.10) to highlight the difference. Attention is first focused on the 0.1R case displayed in Figure 7.8. The solid lines represent the failure loads and the dotted lines are for the eigenvalues. The 'x' symbol denotes the VS case and the circle is for the CS case, where each symbol has the representative filled color denoting the mode failure type. The trends for the 0.1R case seem similar for both stiffness configurations (though with higher values for the VS case), where the failure limit load is reduced consistently from the linear eigenvalue for the mode I case and the cutouts at the bottom exhibit type III failure. The transition regions are also similar, though the VS case contains one configuration that exhibits mode II failure with local buckling. As discussed previously, the higher global buckling mode for the VS shell allows greater room for the local buckling to occur, which is evidenced here by the yellow shaded value being higher than the corresponding CS configuration. Similar results for the configurations located on the tensile side of the cylinder are apparent for

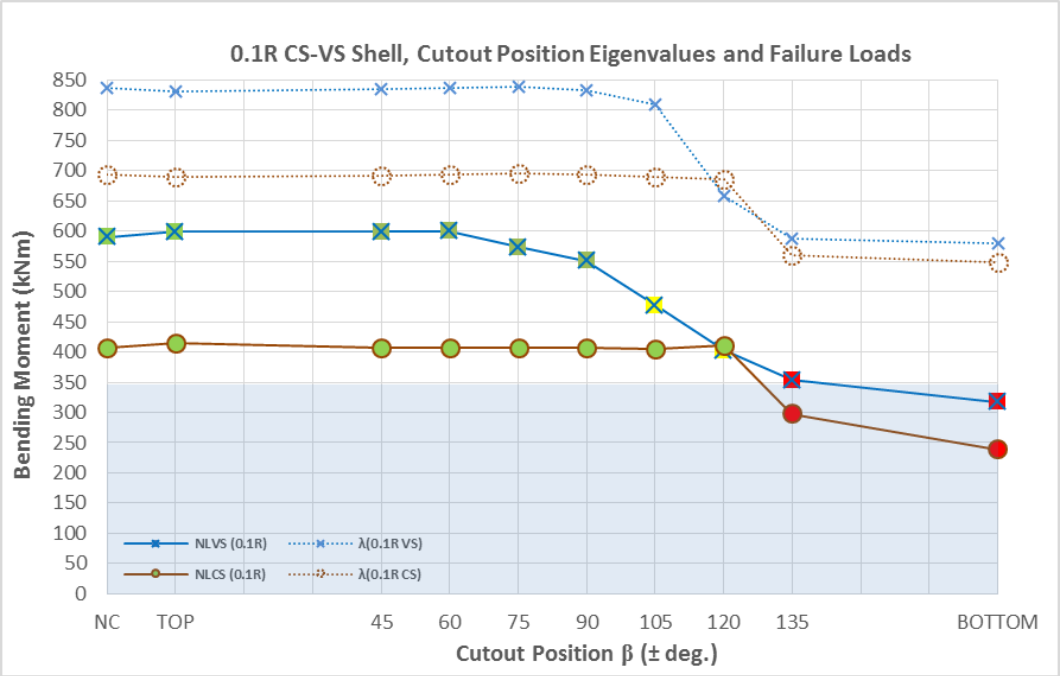


Figure 7.8 : Failure loads versus cutout position β for 0.1R cutout size.

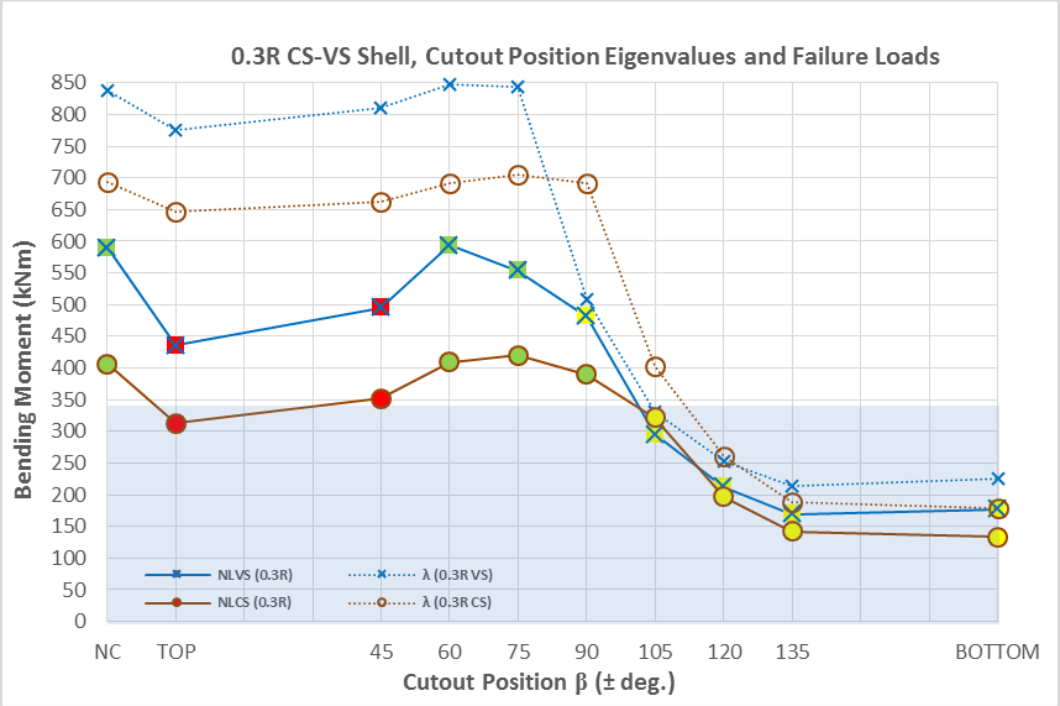


Figure 7.9 : Failure loads versus cutout position β for 0.3R cutout size.

the other two cutout sizes, as evidenced in Figure 7.9 and Figure 7.10. The interesting feature from all three cutout sizes occurs in the transition regions where mode II failure is present. Once the local buckling deformation becomes the critical mode, both stiffness configurations follow similar trajectories in both failure type and failure load level. This indicates that the presence of the cutout is the dominant factor for failure,

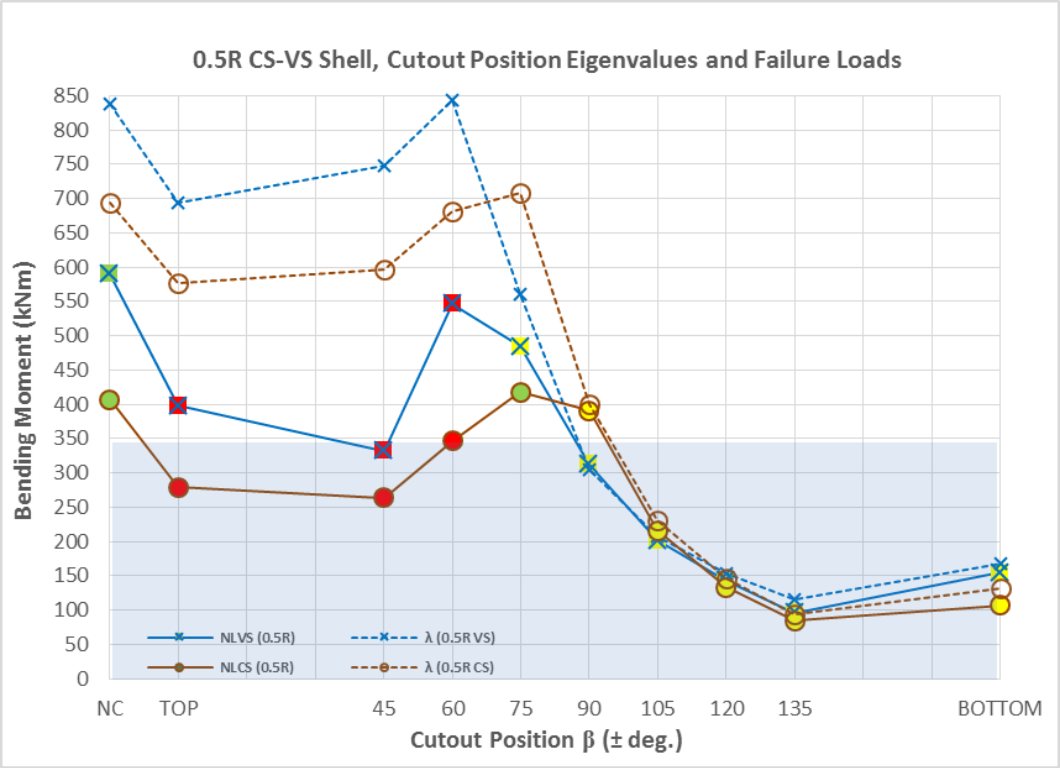


Figure 7.10 : Failure loads versus cutout position β for 0.5R cutout size.

irrespective of the stiffness values in other regions of the shell. This unexpected result reveals that creating a cutout within the compressive side of the cylinder removes the additional load-carrying capability of the optimized fiber orientation design, reducing the failure level to the same as that of the CS shell. This provides an excellent result to be verified through testing.

7.5 Cutout Configuration for Testing

To select a proper cutout configuration for testing, the two major considerations are the mode of failure that is desired to be observed and the limit of the testing fixture. The first consideration was decided for the CS cylinder by selecting the mode II failure, where local buckling occurs first before progressive failure leads to an ultimate load. The cutout configuration chosen for the CS case was 0.3R/120. The design study results here indicate that using the same cutout configuration (0.3R/120) for the VS shell should produce similar testing results. This is further highlighted in Figure 7.11, where the circle focuses on the configurations recommended for machining and testing. The shaded region in Figure 7.11 represents the practical range of the testing fixture that will avoid pull-out within the clamped ends. Both stiffness configurations exhibit

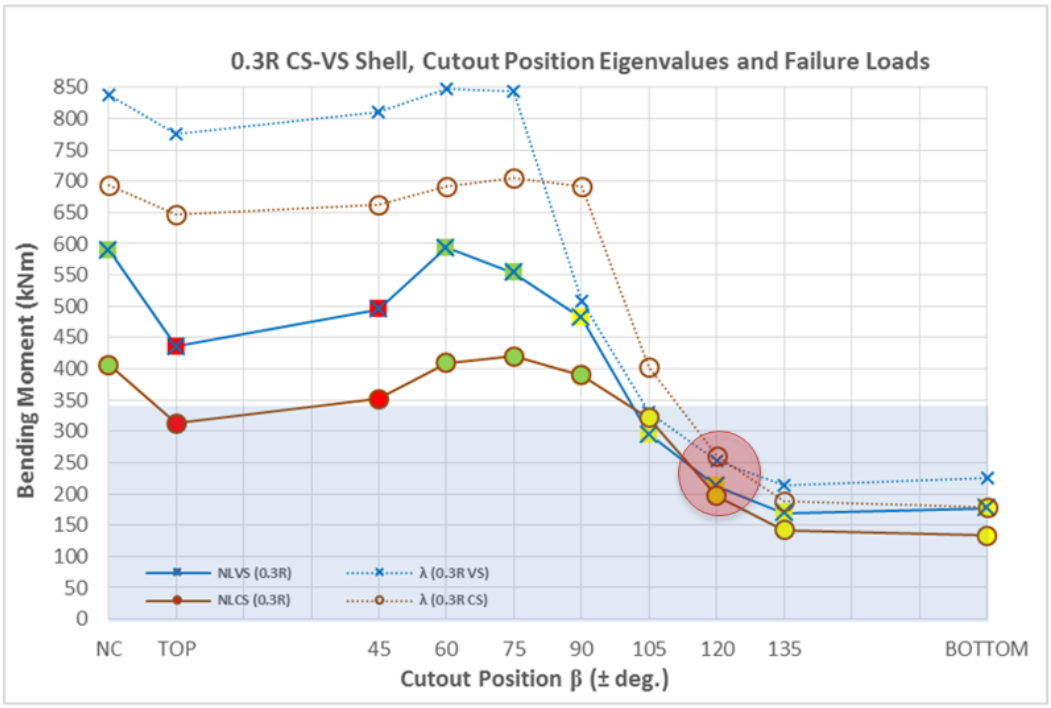
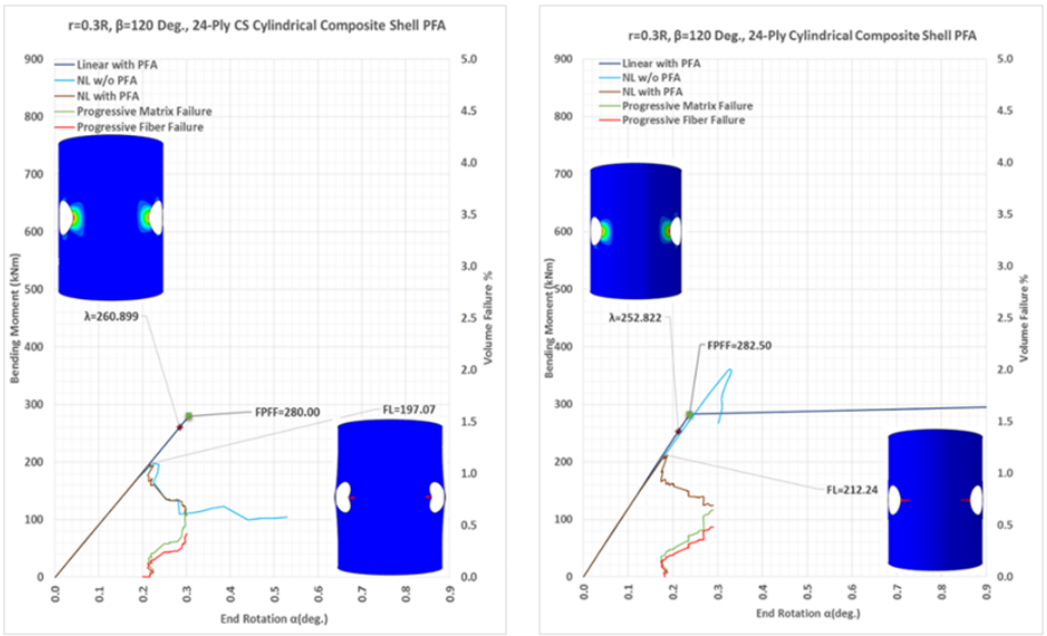


Figure 7.11 : Recommended cutout configuration.

mode II failure there with quite similar behavior and therefore provide an interesting comparison during the testing phase. The tests will determine if the differing stiffness variations will have any effect on the presence of the cutout. For reference, the detailed results for both cases are compared in Figure 7.12 (larger versions can be found in the Appendix). With this general configuration selected, the next step is to



Constant stiffness **Variable stiffness**

Figure 7.12 : Detailed results for 0.3R/120 cutout configurations.

generate a detailed ABAQUS model based on this configuration with the following improvements: actual material properties and layup of the existing part; flexible boundary conditions; and inclusion of the initial shape imperfections. The final model was used to serve as the analytic model for the tests.

8. BUCKLING AND STRENGTH ANALYSIS OF CONSTANT STIFFNESS AND VARIABLE STIFFNESS CYLINDRICAL SHELLS UNDER COMBINED LOADING

The purpose of combined loading study is to evaluate the mechanical response and progressive failure behavior of the CFRP composite laminates with cutouts under combined bending and shear force loading. Since the shell was optimized for pure bending loading only, it was decided to investigate how the shell would behave under combined loading. The geometry of the cylinder and the positions of the cutout for 0.3R cutout size are same as with the previous cutout positions studied in Chapters 6 and 7.

8.1 Loading Conditions

In the combined loading study, in addition to bending moment, vertical shear force applied at one end of the cylinder while applying encastre boundary condition to the other end as shown in Figure 8.1. During the application of the bending moment, the

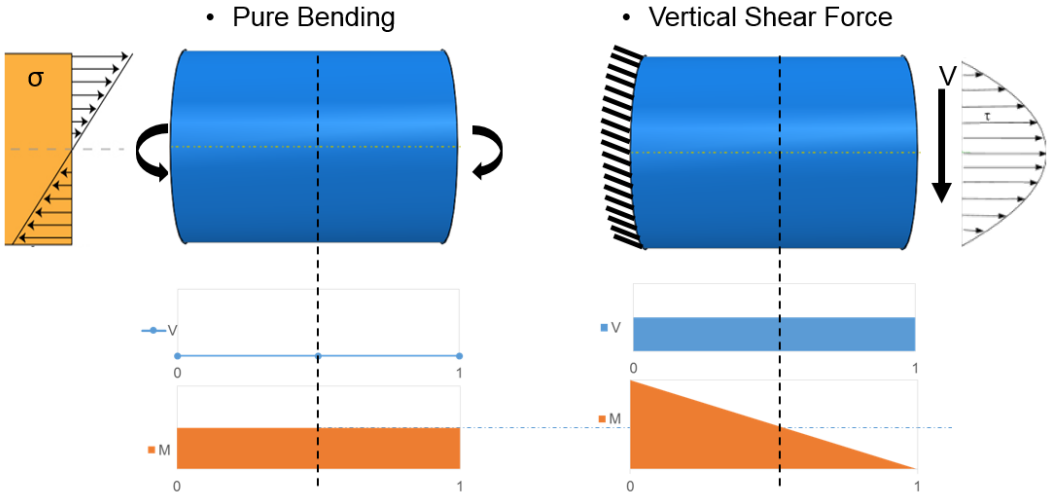


Figure 8.1 : Combined Loading Configuration.

axial stress is maximum at the top and bottom of the cylinder and zero at the neutral axis, which its location is changing depending on the size and position of the cutout as shown in Figure 8.1. On the other hand, the purpose of applying vertical shear force as a second load is to understand the effect of the transverse shear which, its magnitude

varies in vertical direction being zero at top and bottom of the cylinder and maximum at the neutral axis as depicted at the right of the in Figure 8.1. Therefore, it is expected the vertical shear force will be more effective when the cutouts are close to the mid locations. By applying combined bending moment and vertical shear force loading the structure will undergo both axial stress and transverse shear simultaneously. Vertical shear force generates equivalent axial stresses at mid-length (cutout location) plus shear stresses. Vertical end-displacement used (instead of end rotation) for comparison to vertical shear cases as shown in Figure 8.2. The centers of the cylinder at both ends

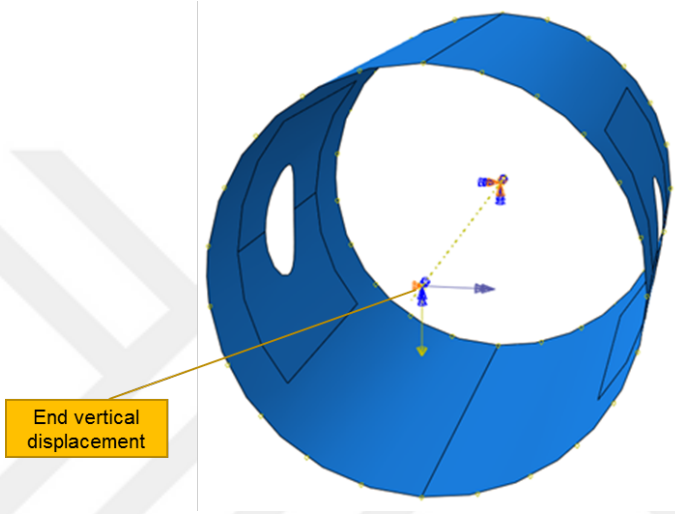


Figure 8.2 : Boundary and Loading Conditions.

are tied to the ends of the cylinder with rigid body constraints. While constraining one end the cylinder with encastre boundary condition, the other end undergoes both bending moment and vertical shear force.

8.1.1 Pure bending moment

To show the effect of combined loading it would be better first to remind the pure bending loading results for both CS and VS cylindrical shells. Under pure bending, as can be seen from Figure 8.3 and Figure 8.4 that the highest failure load levels are reached around 75° cutout position. In addition, when the cutout location is close to the lower section of the cylinder, the failure load level decreases due to the local buckling that occurs around the cutout instead of global buckling.

At cutout positions larger than 90°, the buckling location switches to the cutout edge and failure starts from the cutout edge as shown in Figure 8.3 with yellow color coding for the failure driven by local buckling from the cutout edge. Almost the same trend

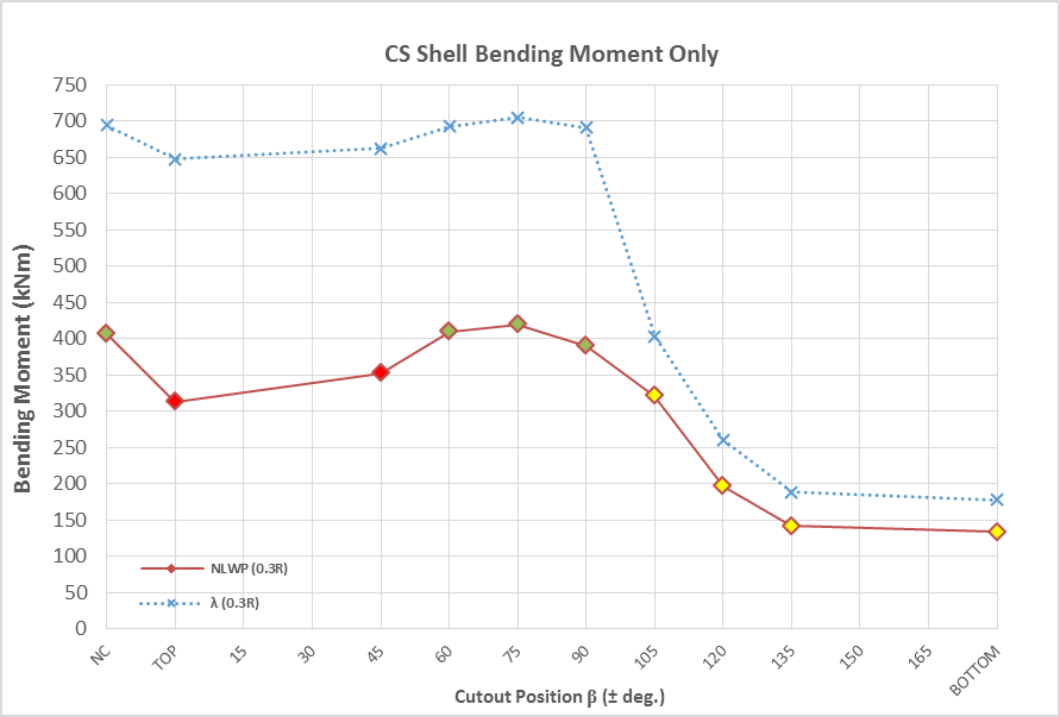


Figure 8.3 : CS shell failure and buckling loads for 0.3R size cutouts under pure bending.

is followed by the VS cylinder except for local buckling starts earlier after 75° cutout location as illustrated in Figure 8.4. Also it is evident that in Failure Mode II, the eigenvalue results are very close to the PFA collapse results by indicating the failure as a result of buckling of the shell.

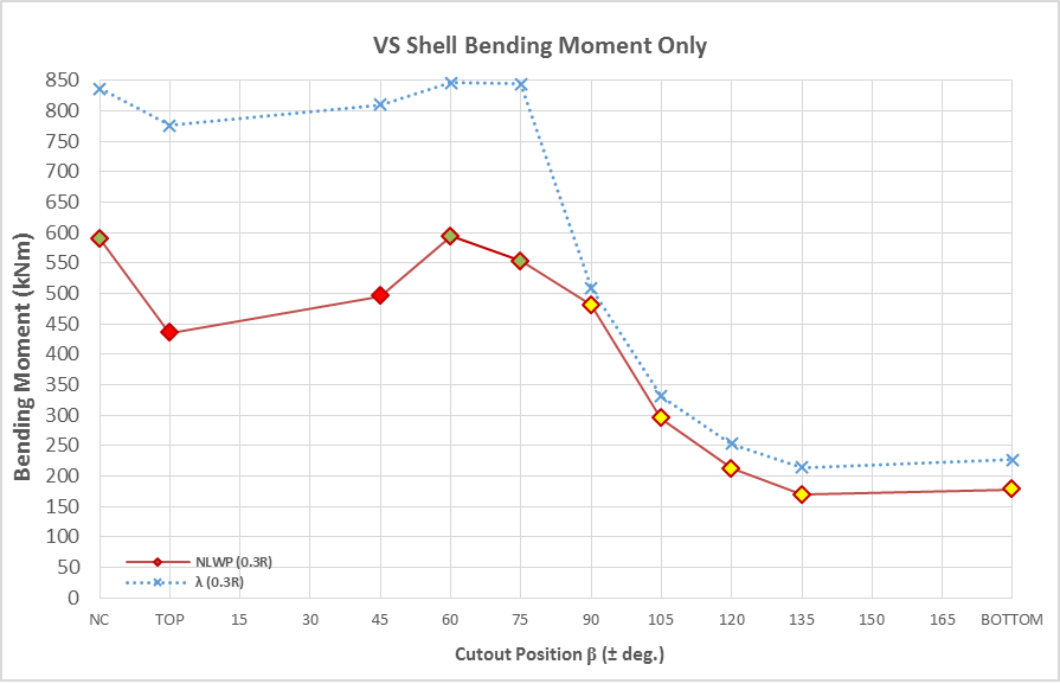


Figure 8.4 : VS shell failure and buckling loads for 0.3R size cutouts under pure bending.

In the 0.3R/90 cutout load/end vertical displacement curve given in Figure 8.5, the fiber and matrix failures start with global buckling and the structure collapses ultimately after certain amount of volume failure generated. When PFA is not included it can be seen from the Figure 8.5 that the failure load level is slightly higher and then collapse starts. This shows that in failure Mode I, the failure is not progressing and immediate collapse initiates. When the failure is caused by global buckling, the cylinder will carry

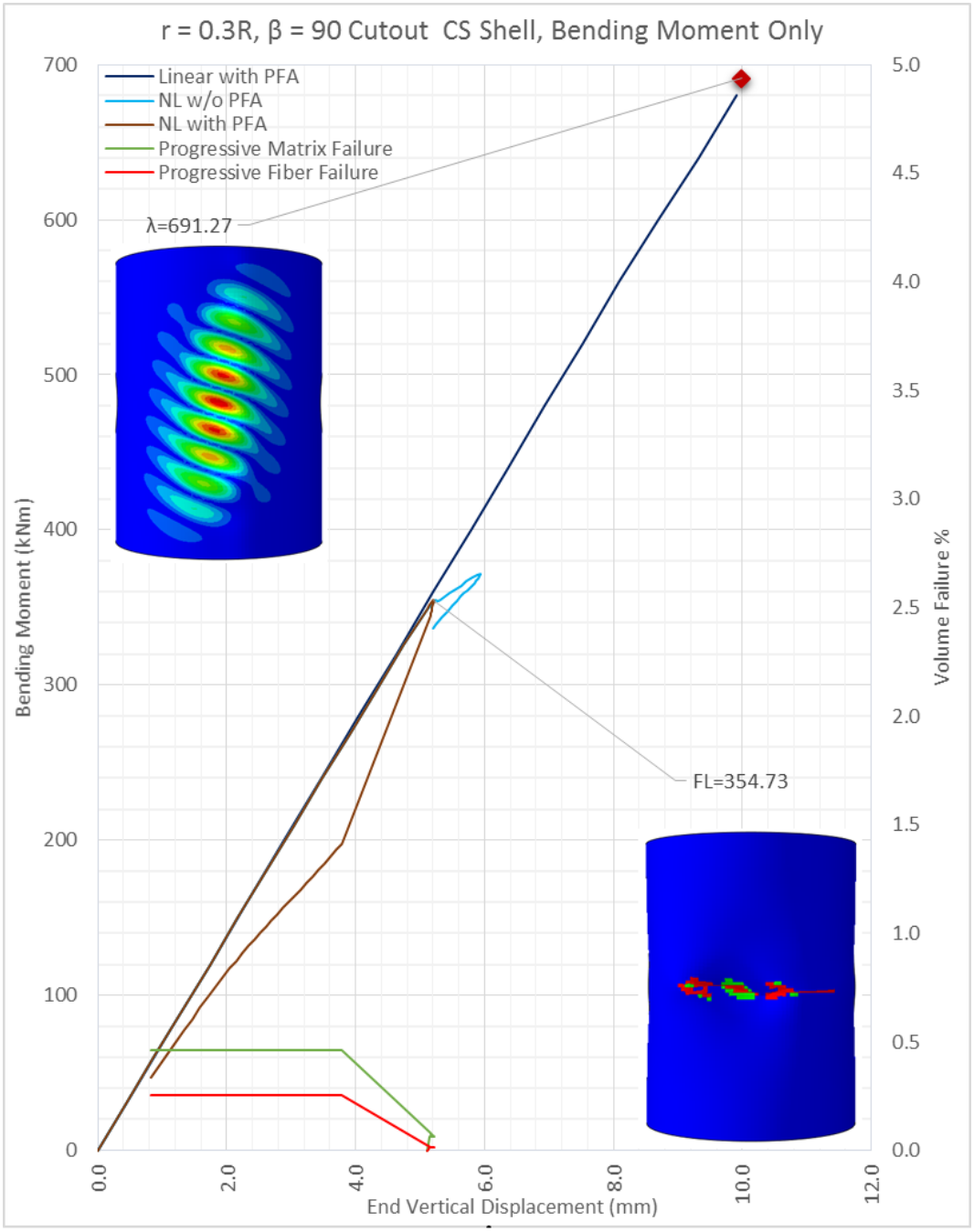


Figure 8.5 : Nonlinear PFA load/end vertical displacement curve.

the bending load until buckling and after that point sudden catastrophic failure occurs.

8.1.2 Vertical shear force

Before applying combined loading, it might be beneficial to see the effect of the vertical shear force individually. Therefore, vertical shear force was applied from one end of the cylinder while constraining the other end in all degrees of freedoms. The failure load in nonlinear analysis and buckling load results for 0.3R cutout at varying positions are given in Figure 8.6 and Figure 8.7. For both CS and VS cylinders only when the

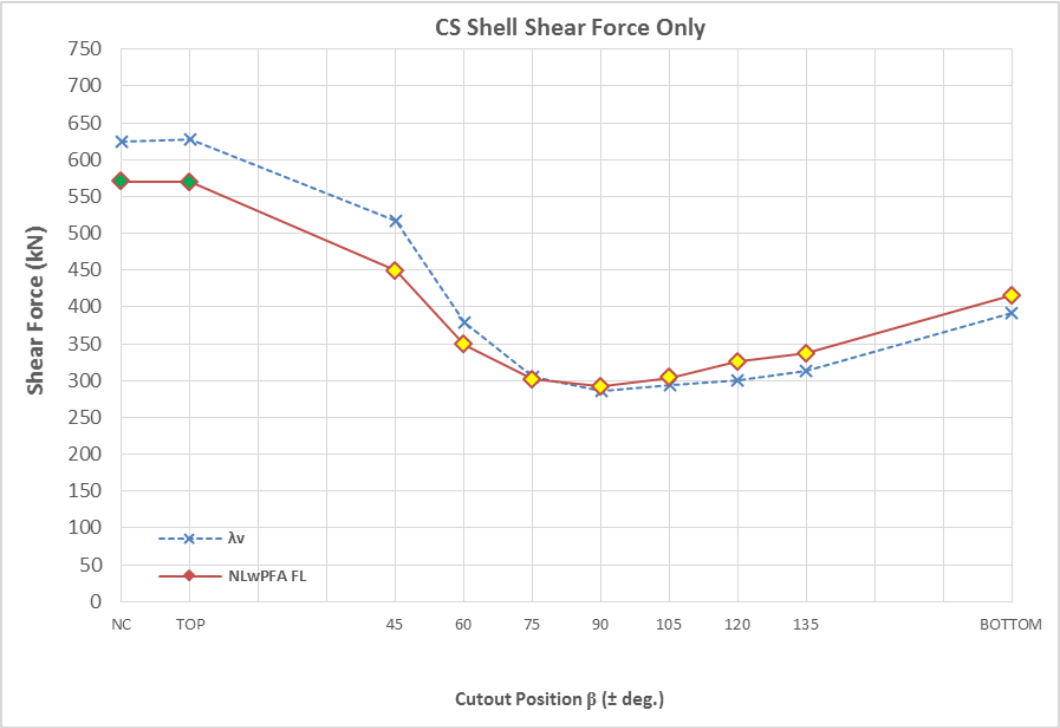


Figure 8.6 : CS shell failure and buckling loads for 0.3R size cutouts under shear force.

cutout is at the top position the cylinders fail as a result of global buckling, while in all other cutout positions failure occurs due to local buckling at the hole edges. In addition to that, an important difference from pure bending moment, in vertical shear force application, although the failure starts due to local buckling, the cylinder is able to carry load further until substantial amount of fiber failures are achieved.

At 75° and 90° cutout locations, the shells have the lowest failure loads, since the transverse shear stress becomes higher at locations close to the neutral axis. At top sections of the cylinders, the failure load is less than the buckling load while it is higher after 75° position, that is because we have tension in top section with lower transverse shear effect and compression in bottom section with the highest transverse shear stress at mid-section of the cylinder. It was also noticed that there is no significant difference

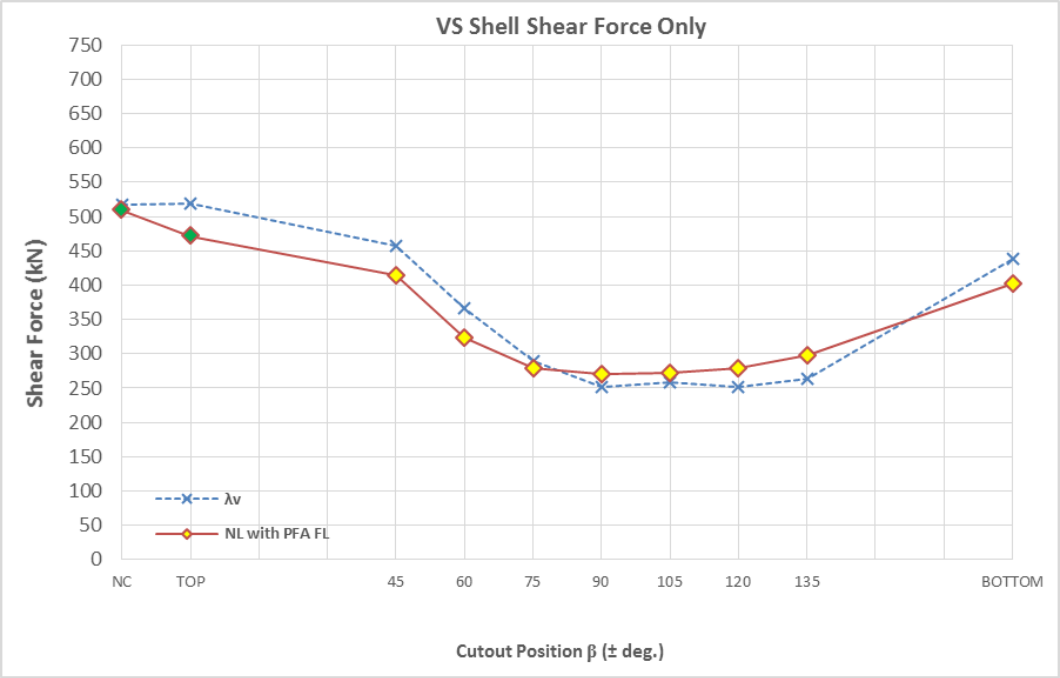


Figure 8.7 : VS shell failure and buckling loads for 0.3R size cutouts under shear force.

between constant stiffness and variable stiffness cylinders when they are compared from their buckling and failure response trend. It can be inferred that, the fact that VS cylinder has lower load level than CS cylinder is due to the design of VS shell to be optimized for the maximizing buckling load level under constant bending moment. The VS shell was designed so that axial stiffness on the tension side of VS cylinder is almost 80% larger than the stiffness of the CS cylinder, while the stiffness on the compression side, near $\beta = 180°$, was slightly smaller than the stiffness of the CS shell. However, under shear force there is no benefit of steered fiber to the failure load, on the contrary there is a slight decrease in the failure load level. Therefore, for the design of the cylinders all possible load combinations for the given mission must be considered during design process.

Since the CS and VS cylinders have similar trends under shear force, only CS shell cases will be further examined. From the shear force figures, it seems non-cutout, 0.3R/45, 0.3R/90 and 0.3R/180 cutout positions needs to be examined more closely, since there are switches between eigenvalue and failure load levels. The load/displacement curves are given below where the displacement is the vertical displacement of the center point of free end of the cylinder. For the non-cutout cylindrical shell, as it can be seen from Figure 8.8, the failure starts from the sides

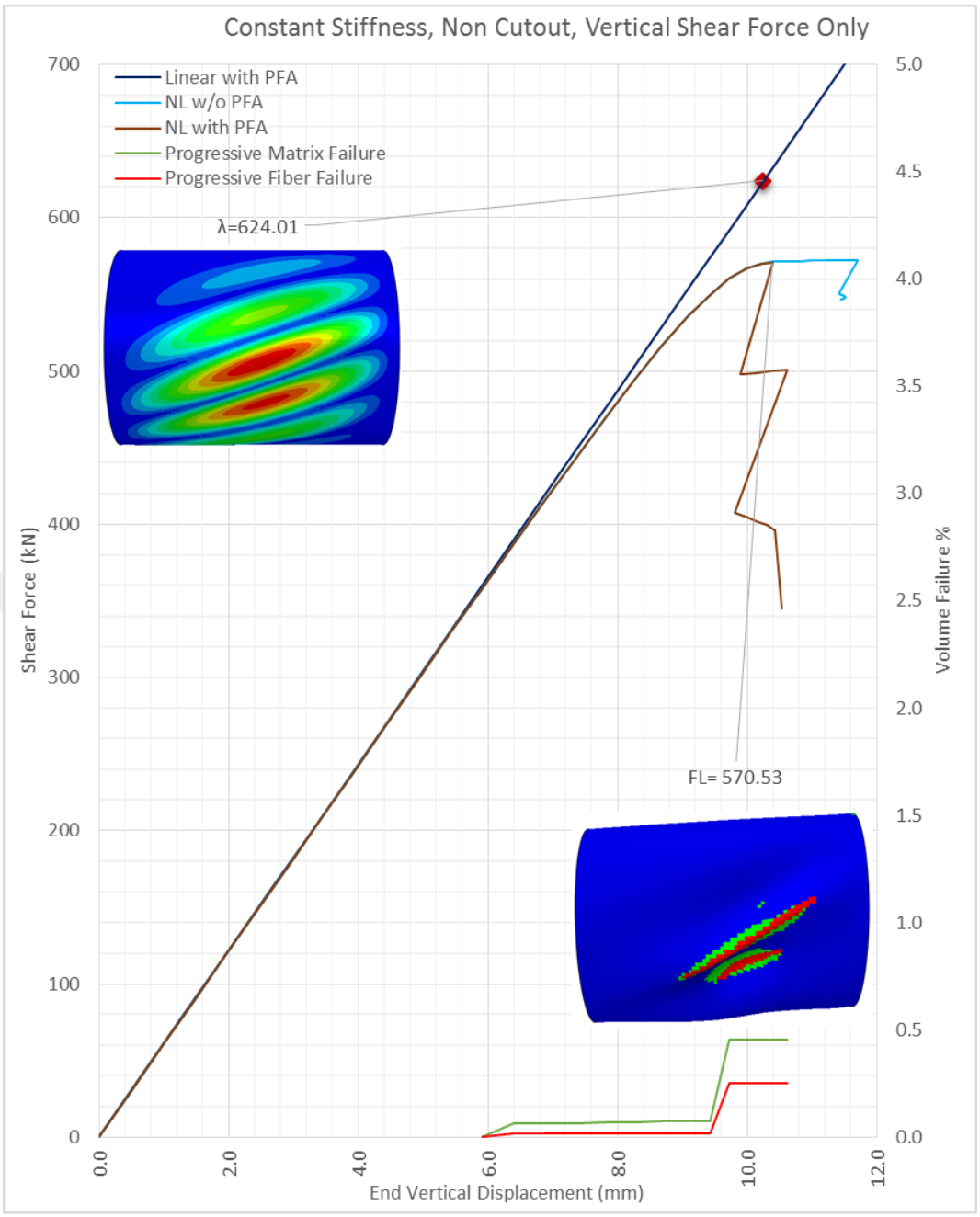


Figure 8.8 : Load/displacement curve for non-cutout CS shell under vertical shear force.

($\beta \approx 90°$) of the cylinder where it is subjected to the highest transverse shear. Under pure bending the shell has failure from the compressive bottom side of the cylinder whereas under vertical shear force the failure occurs due to transverse shear from the sides. However, both failures can be accepted as Mode I failures as result of global buckling.

In 0.3R/45 cutout position, the failure is as a result of local buckling causing Mode II failure as shown in Figure 8.9. The eigenvalue and failure results are very close to each

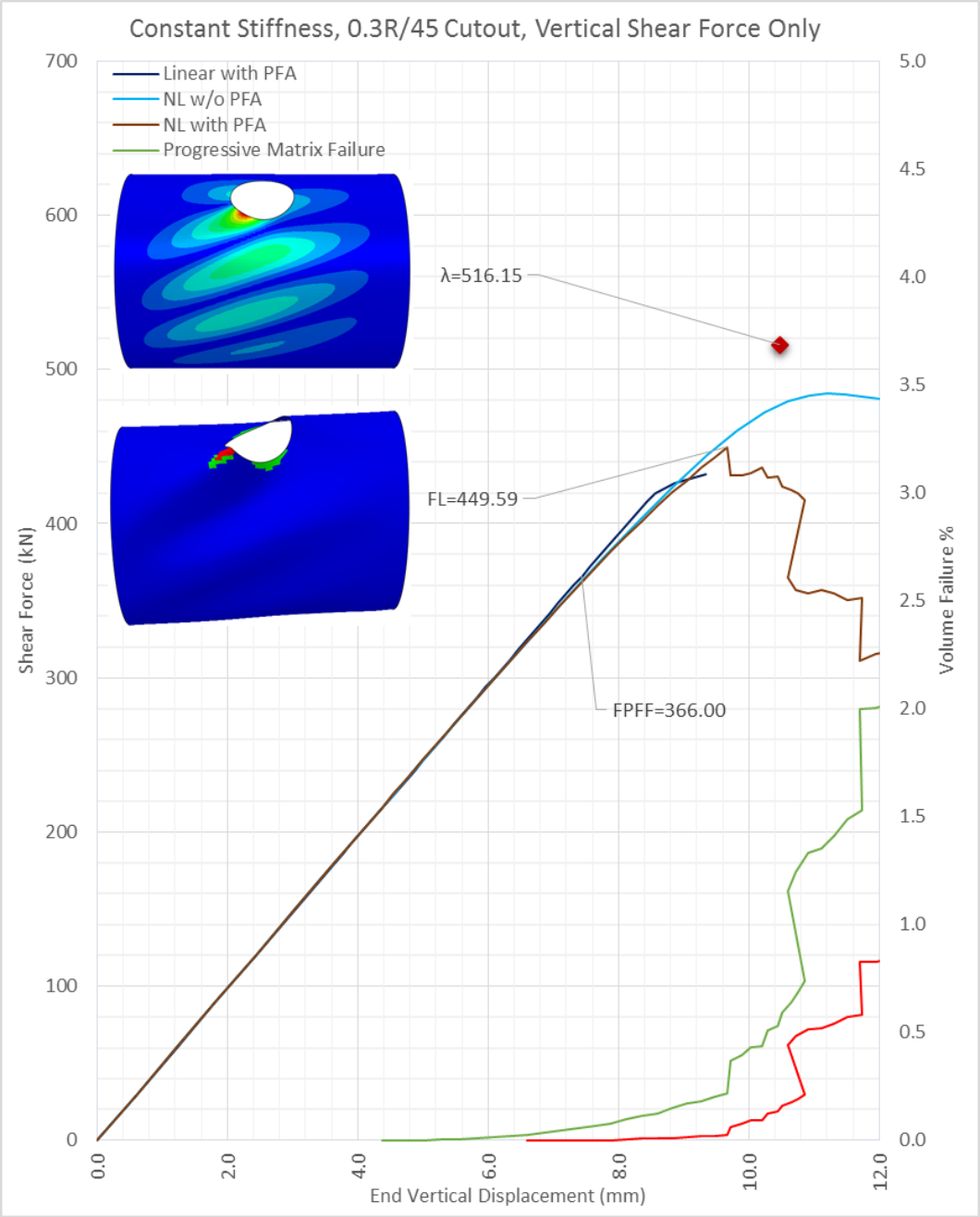


Figure 8.9 : Load/displacement curve for 0.3R/45 cutout, CS shell under vertical shear force.

other which indicates the reason for failure is local buckling. Under pure bending the failure mode is Mode I since there is no transverse shear present at the cutout edge.

As for the cutout at 90° position shown in Figure 8.10, we have the lowest failure load level since the transverse shear becomes maximum at the cutout edge. In addition, the structure continue to carry load until substantial amount of matrix and fiber failures. The linear buckling load is very close to the collapse load. On the other hand, during

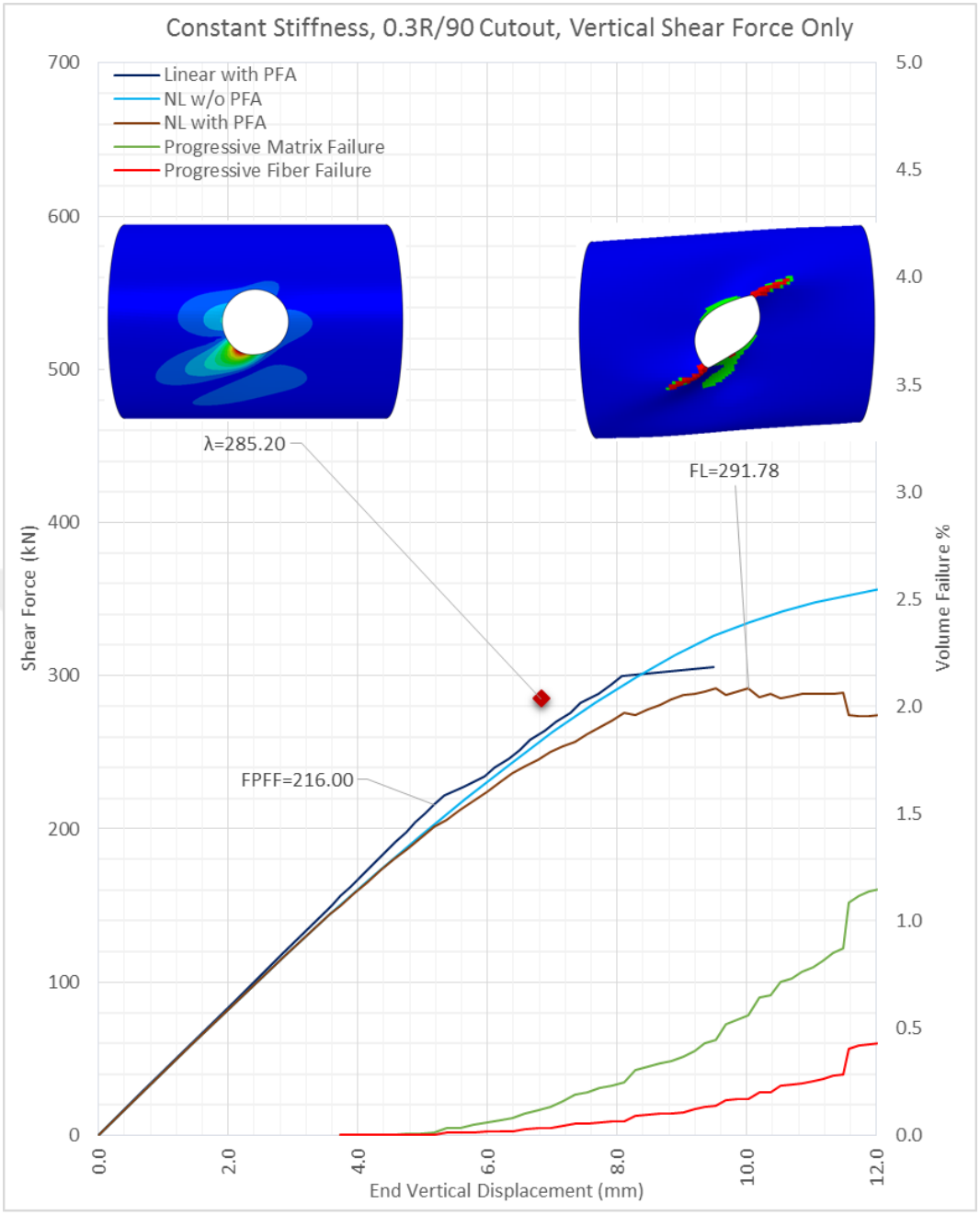


Figure 8.10 : Load/displacement curve for 0.3R/90 cutout, CS shell under vertical shear force.

nonlinear analysis if you do not apply progressive failure, it seems as if the shell will continue to carry load much above the collapse load.

As a final analysis, in 0.3R/180 cutout position, the failure is again as a result of local buckling at the cutout edge as illustrated in Figure 8.11. However, the buckling that occurs in that position is as a result of bending created by vertical shear force since the transverse shear at the bottom of cylinder is almost zero. Therefore, The failure mode is Mode II for both pure bending moment and vertical shear force load cases driven by

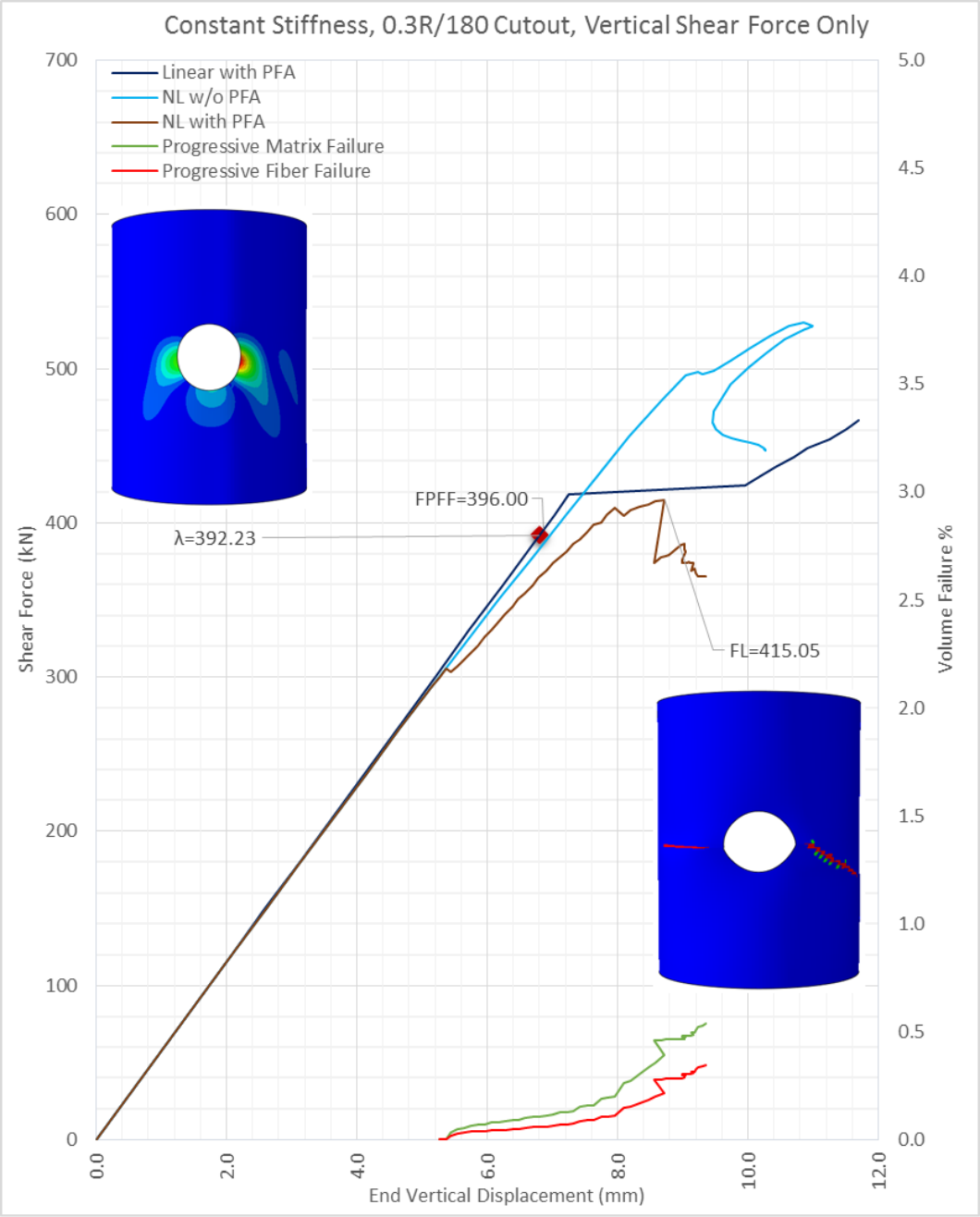


Figure 8.11 : Load/displacement curve for 0.3R/180 cutout, CS shell under vertical shear force.

local buckling due to bending load. Although, the fiber failures starts much earlier than total failure, since accumulation of the fiber failures increases slowly, the cylindrical shell continue to carry the load. After 90° position, since the transverse shear starts to decrease, the collapse load starts to increase respectively. Those results show that, the transverse shear stress is a very effective on the buckling of the cylindrical shells.

Therefore, in the design of the cylindrical shells, vertical shear force must be taken into account very seriously.

8.2 Combined Bending Moment and Vertical Shear Force Loading

In the combined loading analysis in addition to the bending moment, axial shear force also applied from one end of the cylinder while keeping the other end encastre. It was decided to keep the moment created by the shear force at the axial mid-length (L/2) of the cylinder to be proportional to the applied bending moment.

The shear force calculation is given below.

$$R_L = \frac{M_V}{M} \tag{8.1}$$

$$M_V = \frac{V.L}{2} \tag{8.2}$$

where load ratio (R_L) designates the ratio of bending moment (M_V) created by shear force at $x = L/2$ over applied bending moment load (M).

By applying $R_L = (0.05, 0.1, 0.2, 0.5, 1)$ load ratios in addition to pure bending moment and individual vertical shear force cases to the 0.3R/90 cutout position, the calculated buckling eigenvalues and the nonlinear progressive failure load values with illustration of the failure modes are given in Figure 8.12. Note that the results are normalized with respect to individual pure bending moment and vertical shear force results. For lower load ratios, the bending moment dominates the failure response while for higher load ratios, shear force causes failure by initiating buckling around cutouts at 90 degree position. Although the buckling load decreases with the initiation of the vertical shear force, the effect of shear force becomes dominant after $R_L \geq 0.2$. Therefore, $R_L =$ 0.2 load ratio is selected for the investigation of the combined load at various cutout locations.

The bending moment buckling eigenvalue and nonlinear progressive failure analysis results under combined loading for both constant stiffness and variable stiffness cylinders are shown in Figure 8.13 and Figure 8.14. Bending moment contribution from vertical shear force helps failure variation transitions to local modes after 90° position for CS shell and 75° position for VS shell. In both CS and VS shells the linear buckling and nonlinear progressive failure load results are very close to each other in

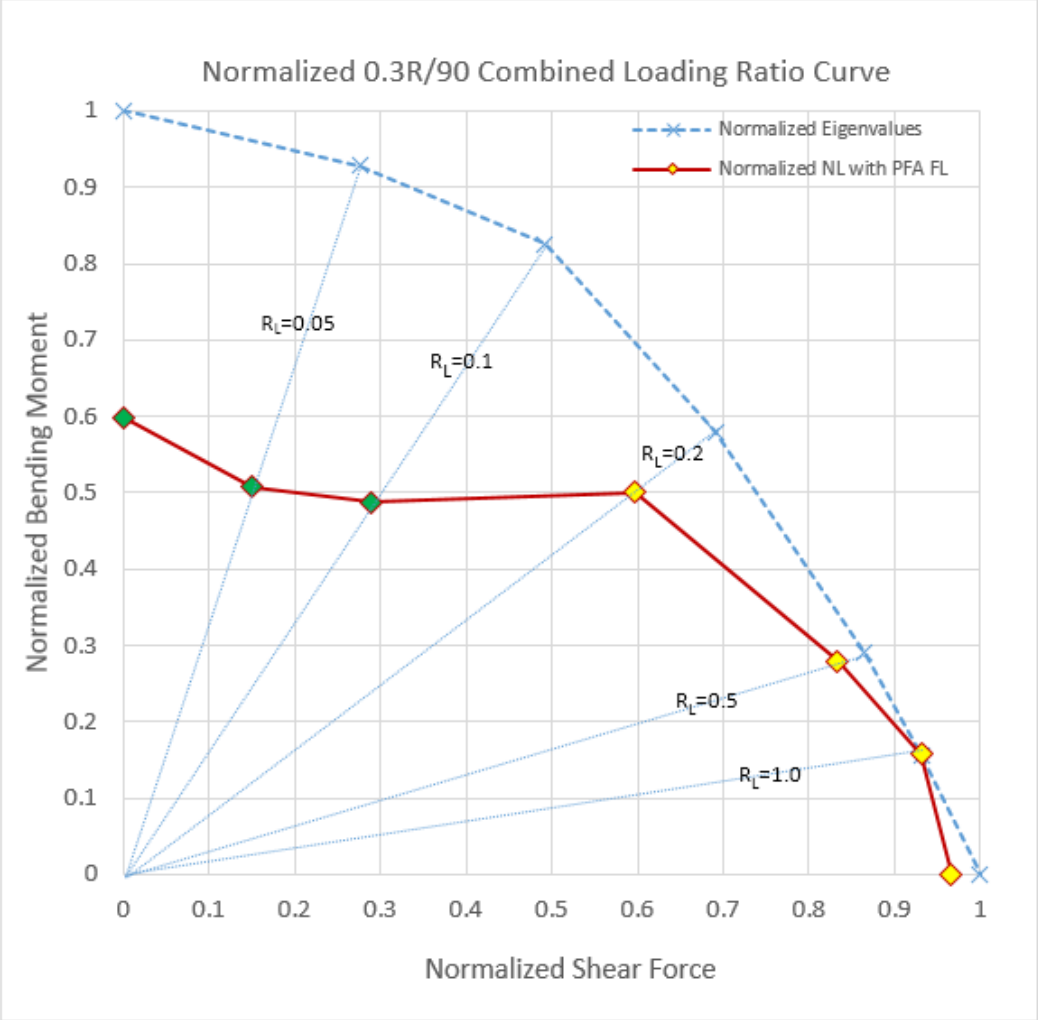


Figure 8.12 : Normalized combined loading results for 0.3R/90 cutout case.

Mode II failures. This shows that local buckling is causing immediate collapse and resulting failure load to decrease.

Figures 8.13 and 8.14 also show that VS load levels are almost the same as CS loads. This is because the VS shell is designed to increase the bending load when it is subjected to pure bending moment. However, with the presence of the vertical shear force, it becomes dominant compare to the bending load. The buckling occurs due to transverse shear effect and causes failure before buckling due to bending moment.

For further investigation, two examples of load/displacement curves selected for CS 0.3R/90 cutout with $R_L = 0.2$ and $R_L = 1.0$ load ratios as shown in Figures 8.15 and 8.16. Both figures show that the linear buckling and FPFF loads are very close to each other indicating that the failure will be as a result of buckling. One important difference is that, the failure load level for $R_L = 0.2$ combined load ratio is much higher

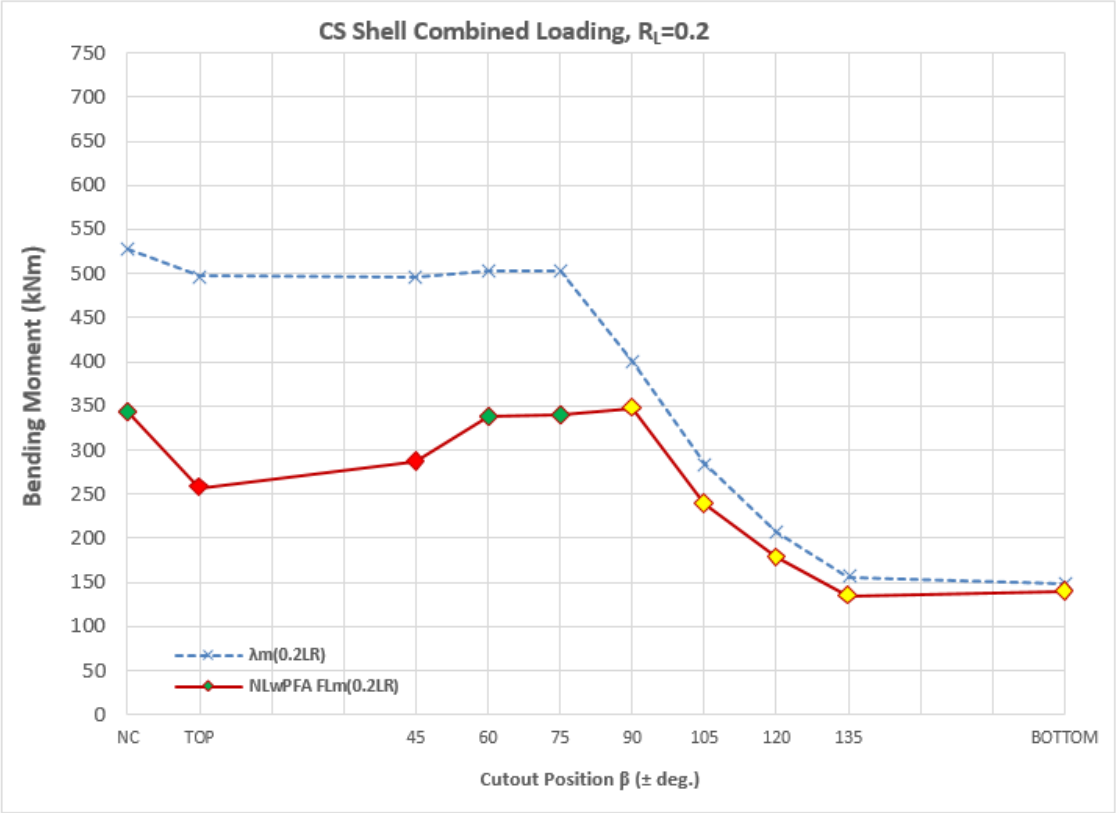


Figure 8.13 : CS shell $R_L = 0.2$ combined load ratio for 0.3R cutout cases.

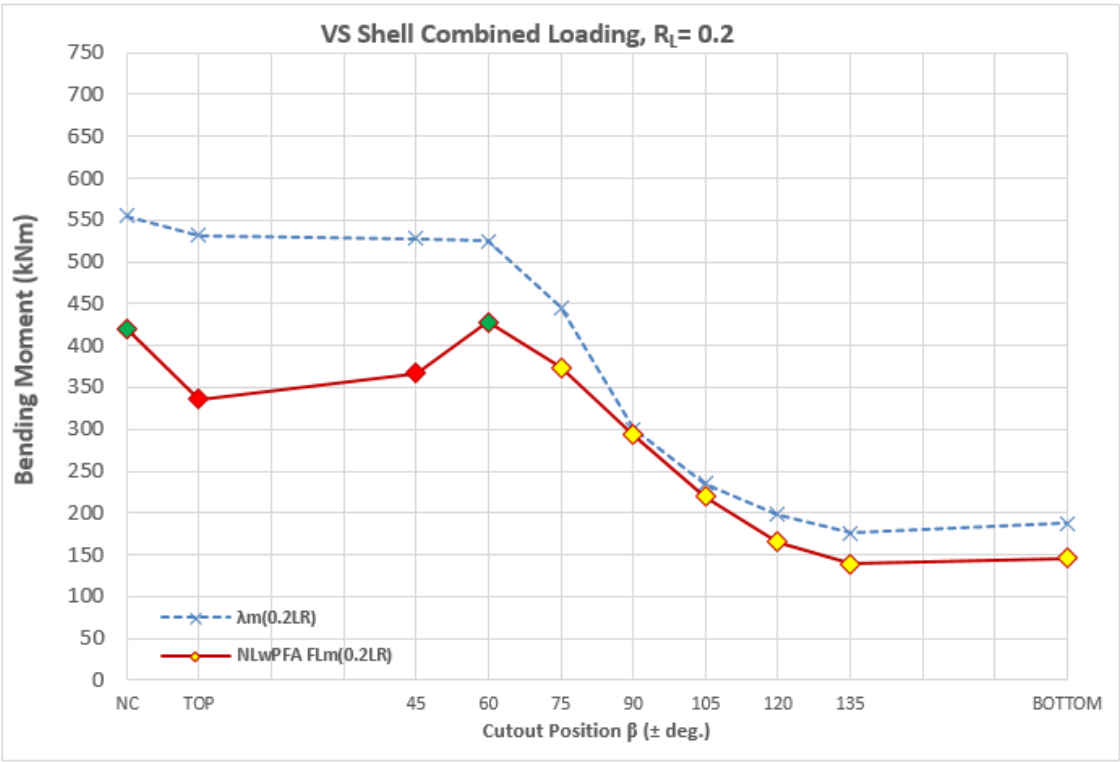


Figure 8.14 : VS shell $R_L = 0.2$ combined load ratio for 0.3R cutout cases.

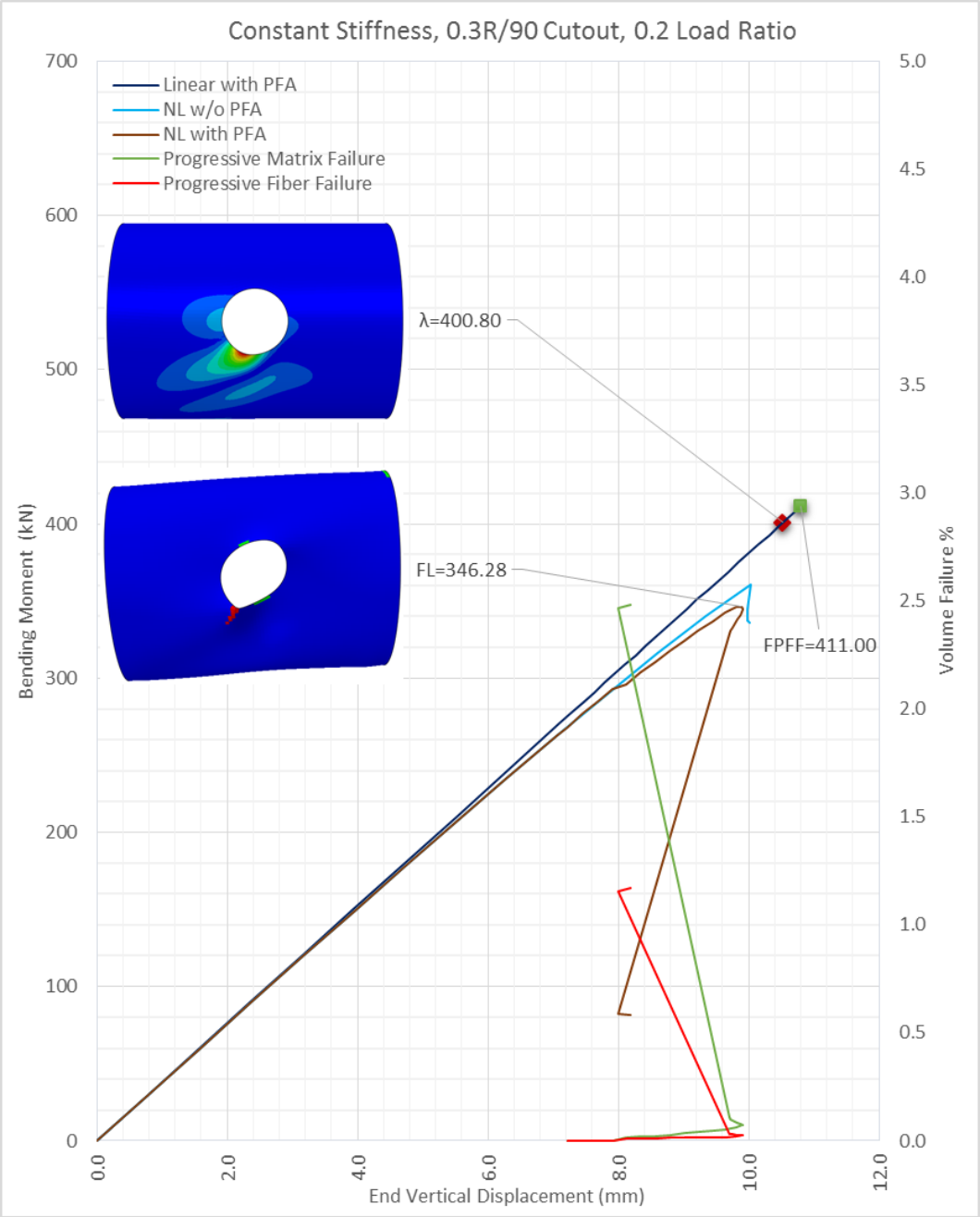


Figure 8.15 : CS shell $R_L = 0.2$ combined load ratio for 0.3R/90 cutout position.

than the $R_L = 1.0$ combined load ratio case. As the effect of the vertical shear force increases, there is a substantial amount of fiber failure that causes the shell collapse at much lower load levels. In addition, since the cutouts are at 90° position, we have maximum transverse shear effect causing the buckling around the cutout edges. When the bending moment is higher (lower load ratio, $R_L = 0.2$), although the failure load is higher, after the failure, the cylinder is not able to further carry the load and catastrophic failure occurs. However, in $R_L = 1.0$ load ratio, despite the lower failure

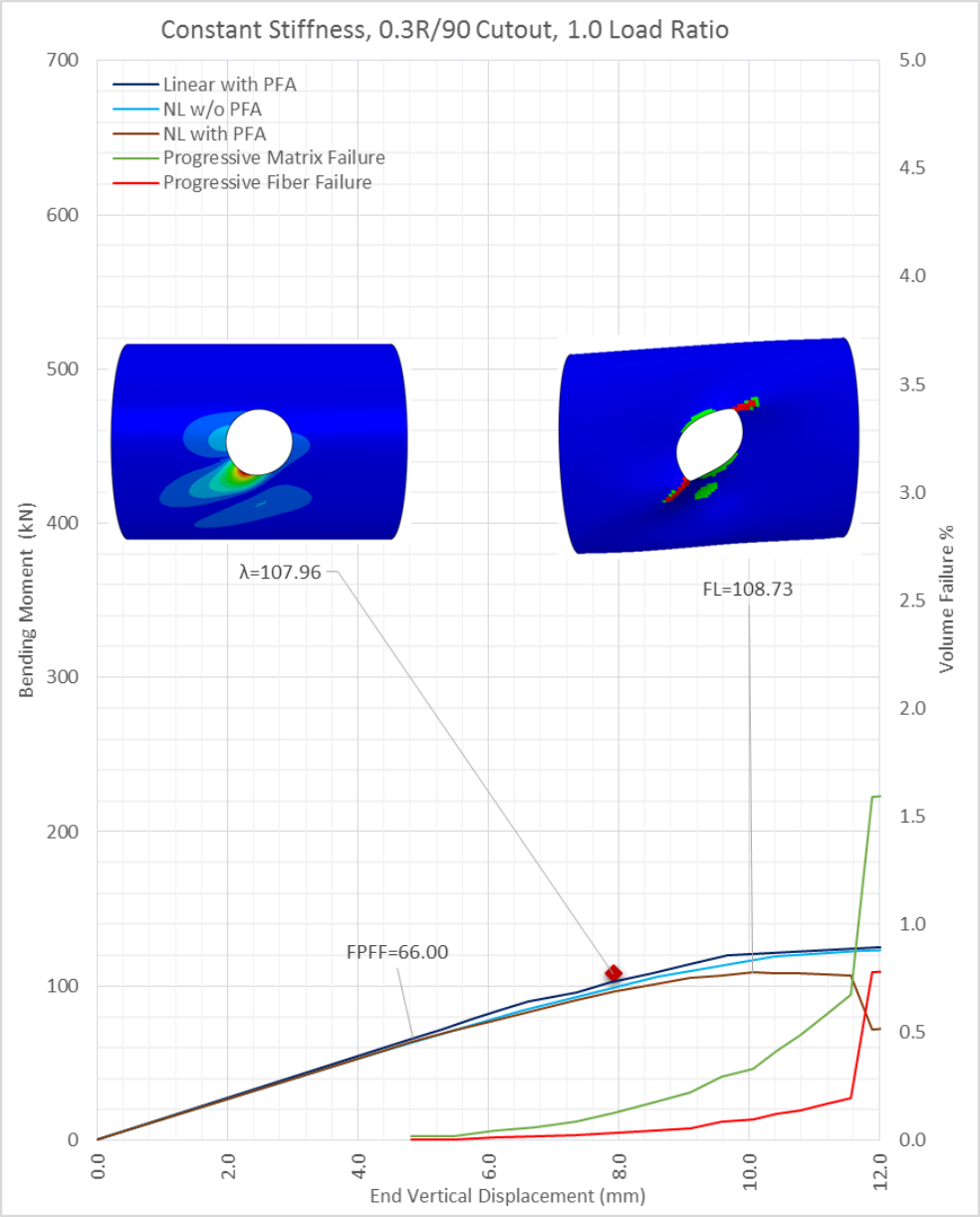


Figure 8.16 : CS shell $R_L = 1.0$ combined load ratio for 0.3R/90 cutout position.

load, the cylinder is able to carry load until almost 20% more vertical displacement is obtained.

Those results show that, the position of the cutouts based on the applied loading becomes very important. One must take into account all the loading conditions before designing the cylindrical shells with door or windows cutouts.

8.2.1 Combined Loading Results

The critical buckling mode and failure mode summaries for both CS and VS cylinders under the effect of vertical shear force only are given in Table 8.1. The table shows that

Table 8.1 : Critical buckling and failure mode summary for 0.3R cutout configurations under constant vertical shear force only.

LINEAR BUCKLING MODES									
0.3R CS	G	L	L	L	L	L	L	L	L
0.3R VS	G	L	L	L	L	L	L	L	L
$\beta =$	0(T)	45	60	75	90	105	120	135	180(B)
NONLINEAR FAILURE MODES									
0.3R CS	I	II	II	II	II	II	II	II	II
0.3R VS	I	II	II	II	II	II	II	II	II
$\beta =$	0(T)	45	60	75	90	105	120	135	180(B)

when the cutout is located at the top position, global buckling results Mode I failure for both CS and VS shells. This is the result of upper side of the cylinder to be under tension while lower side of the cylinder to be under compression. When the cutout is in upper side, there are only two possibilities of the failure. It can fail either due to higher stress level above material strength under tension around the cutout or global buckling from the bottom side of the cylinder. In our case, global buckling causes Mode I failure type. For the rest of the positions, local buckling occurs around the cutout edges which causes Mode II failure type. The critical buckling mode and failure mode summaries for both CS and VS cylinders under the effect of $R_L = 0.2$ load ratio combined loading are given in Table 8.2. The vertical shear force causes the cutout to easily buckle and fail. Both CS and VS shells show almost the same behavior under $R_L = 0.2$ load ratio

Table 8.2 : Critical buckling and failure mode summary for 0.3R cutout configurations under $R_L = 0.2$ load ratio combined loading.

LINEAR BUCKLING MODES									
0.3R CS	G	G	G	G	L	L	L	L	L
0.3R VS	G	G	G	L	L	L	L	L	L
$\beta =$	0(T)	45	60	75	90	105	120	135	180(B)
NONLINEAR FAILURE MODES									
0.3R CS	III	III	I	I	II	II	II	II	II
0.3R VS	III	III	I	II	II	II	II	II	II
$\beta =$	0(T)	45	60	75	90	105	120	135	180(B)

combined loading. When the cutout is close to the top section, there exist material failure resulting Mode III failure. Although, in linear analyses global buckling occur, during nonlinear analyses material failure as a result of shear force causes ultimate failure. The results under shear force show that failures under shear stress generally cause the cylinder buckle locally which is expected. Therefore, re-optimization of

the cylinder in addition to increasing the stiffness around the cutout might be a good solution to increase the failure load.

9. BENDING TEST

After the completion of the numerical analyses of the shells, it is necessary to validate the results with sufficient tests. The objective of the test is to evaluate the accuracy of the finite element prediction for the behavior of a constant-stiffness and a variable-stiffness CFRP composite cylinders under bending. Before testing, to be able to validate the modeling of the structure, the numerical analysis results were compared with the test results of non-cutout cylindrical shell which was performed by A.Blom [3].

9.1 Test Setup

The test setup, which was designed previously by A.Blom [3] was used in testing of CFRP cylindrical shells in TU Delft. The test fixture was specially designed for circular cylinders with a radius of 304.5 mm (12 in) and length of 813 mm (32 in) and the cylinders under consideration have the same geometries. As stated previously in Chapters 6 and 7, the bending tests were performed for the 0.3R/120 cutout configuration in TU Delft. The CS and VS barrels were built at Boeing Seattle Facilities using automated fiber placement machine. The cylindrical shells were manufactured by laying up on a mandrel with AFP machine and curing in an autoclave shown in Figure 9.1. Steel tabs were bonded to the both ends of the cylinder with a paste adhesive to increase the bearing capability of the cylinder at the connection with the loading frame.

The load is conducted on an MTS test bench, model 311.51S, with a maximum load capacity of 3560 kN as shown in Figure 9.2. The load frame was designed exclusively for this test and is shown in Figure 9.3. The load frame is made of S355J2G3 steel. The bending moment loads are applied symmetrically to the both ends of the cylinder by allowing the moment arms to rotate, controlled by the vertical motion of the machine head. The test fixture is loaded in tension, causing a bending moment such that the upper side of the cylinder is in tension and the lower side of the cylinder is in

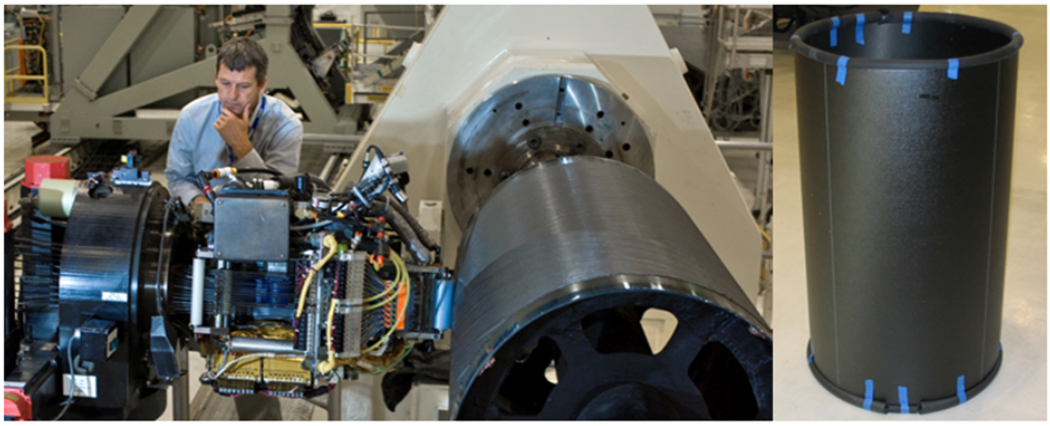
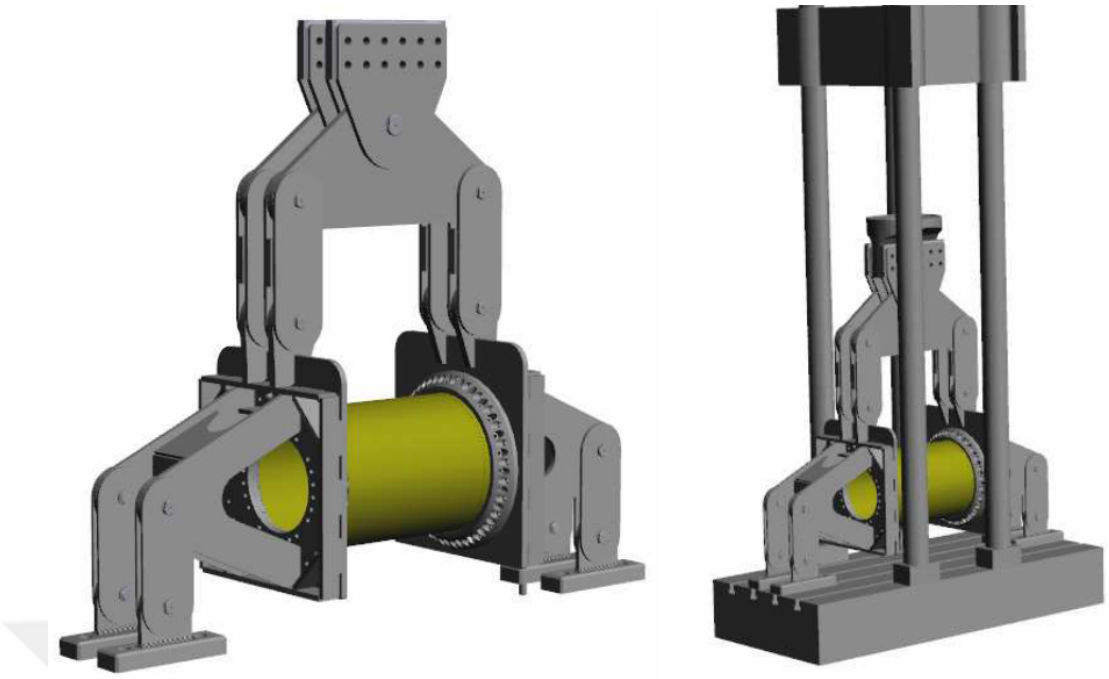


Figure 9.1 : Manufacturing of cylindrical shells (Photo courtesy of A. Blom).



Figure 9.2 : MTS test bench.

compression. The boundary conditions of the cylinder were designed to approach the clamped end conditions as applied in the finite element analysis. Detail information about the test fixture can be obtained from Blom's dissertation [3]. One CS cylinder and one VS cylinder without any cutouts on them were tested previously by Blom [3]. The maximum load that could be applied to the cylinders was limited by the strength of the test fixture's bolt connection. Since the cylinders were built before the detailed design of the test fixture, the cylinders were designed too stiff to be buckled in the test. Therefore, during Blom's testing the cylinders were not able to be loaded beyond the



(a) Load frame designed for introducing the load (b) Complete test configuration

Figure 9.3 : Test fixture.

load that would cause failure in fixture's bearing. In the testing, the end rotation and strains were measured during the testing.

9.2 Machining and Inspection of the Cutouts

To select a proper cutout configuration for testing, the two major considerations were the mode of failure that is desired to be observed and the limit of the testing fixture. As it is highlighted in Figure 9.4, where the circle focuses on the configurations recommended for machining and testing, the first consideration was decided for the CS cylinder by selecting the mode II failure, where local buckling occurs first before progressive failure leads to an ultimate load. The cutout configuration was chosen for the CS case as 0.3R/120. The design study results also indicate that using the same cutout configuration (0.3R/120) for the VS shell should produce similar testing results. The shaded region in Figure 9.4 represents the practical range of the testing fixture that will avoid pullout within the clamped ends. Both CS ans VS configurations exhibit Mode II failure there with quite similar behavior and therefore provide an interesting comparison during the testing phase. The tests will determine if the differing stiffness variations will have any effect on the presence of the cutout.

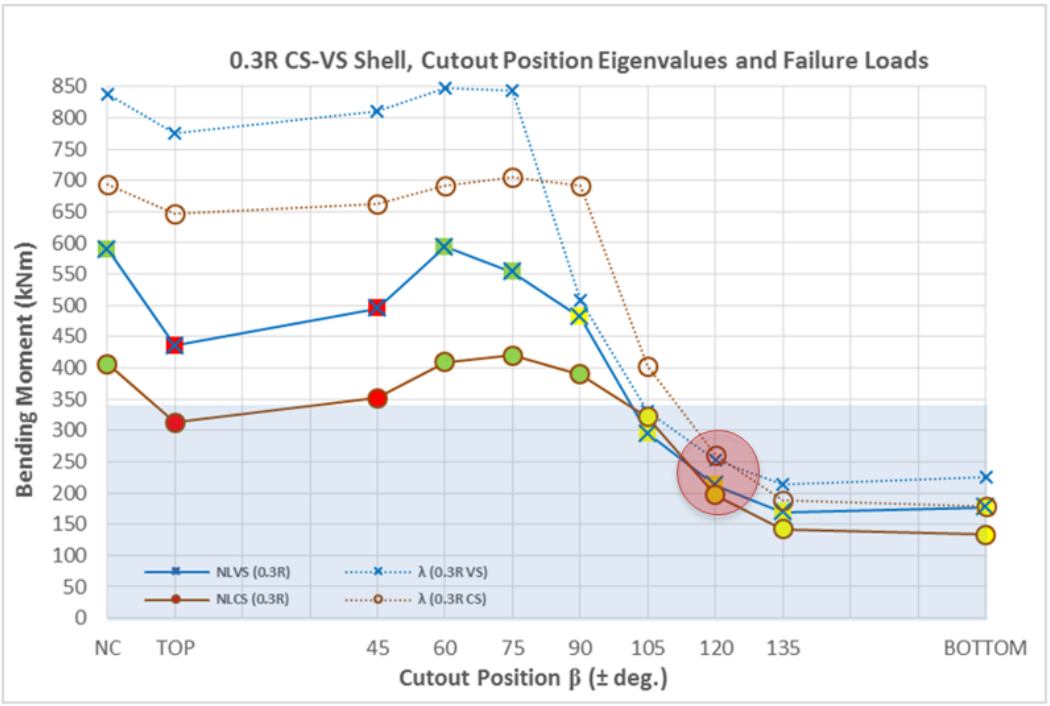


Figure 9.4 : Planned cutout configurations.

The machining of the cutouts into the shells was performed by using the drawing given in the APPENDIX N. After the machining of the cutouts, the visual and Non Destructive Investigation (NDI) of the areas around the cut-outs for two cylindrical CFRP shells were performed. Inspection of the cut-out region for CS cylinder revealed that no visual defects or fibre delamination were observed. Dimensions of the cut-outs, given in Figure 9.5, were measured by the digital caliper to check that they are within defined tolerance level. Cut-out regions for VS cylinder contain visible defects in the

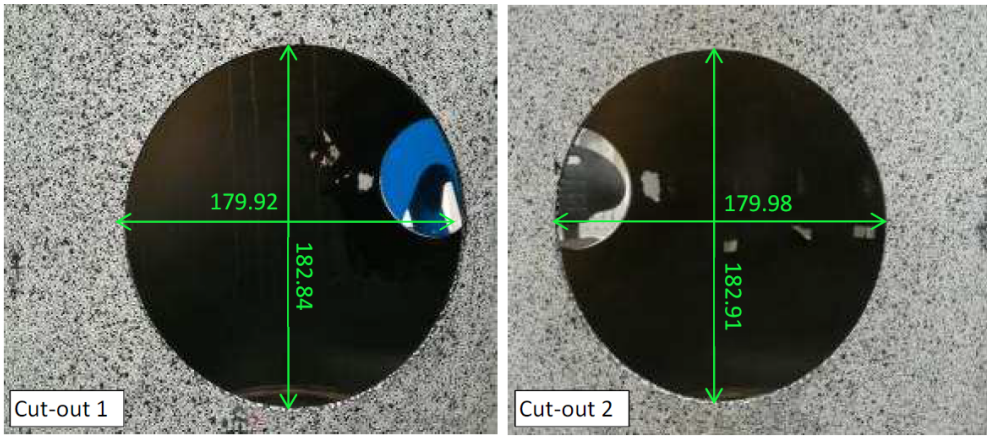


Figure 9.5 : Dimensions of cut-outs of the CS cylinder.

form of pull-out fibres on the outer layer as shown in Figures 9.6 and 9.7. This was due to the fact that higher diameter of the milling drill bit was needed. Indeed, the steel

rings of the steered cylinder did not allow to use fine bit as with the CS cylinder. Inner

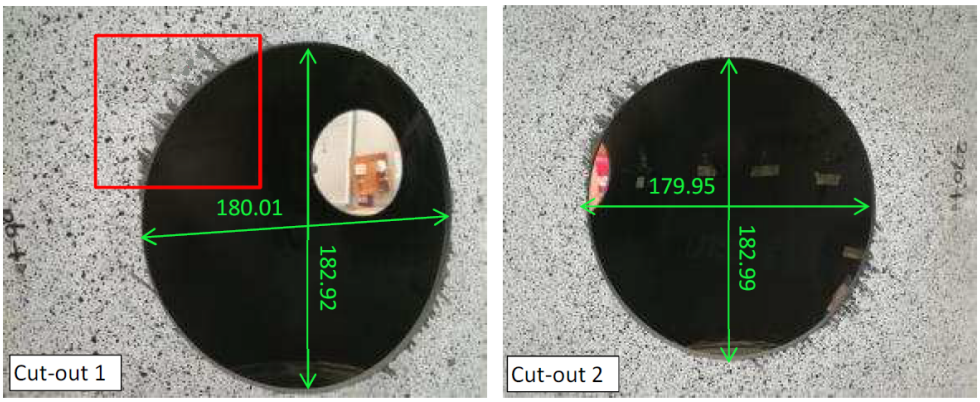


Figure 9.6 : Dimensions of cut-outs of the VS cylinder.



Figure 9.7 : Pulled fibres near the cut-out 1 for VS cylinder.

side of the VS cylinder was generally intact except for a narrow strip of pulled fibres visible in Figure 9.8. Two parallel strips has a width of 4 mm and length of 350 mm in 45 degree angle.

The areas around the cut-outs of both cylinders were examined using portable OLYMPUS OMNISCAN SX workstation with 5 MHz phased array probe containing 16 elements. Scanning was performed manually moving probe along the edge of the cut-out as shown in Figure 9.9. The same operations was also done from inside of the cylinder. The result of the inspection shows that no signs of delamination were found



Figure 9.8 : Inner side of the VS cylinder.



Figure 9.9 : Scanning along the edge of the cutout.

near the cut-outs of CS cylinder. The probe measurement of the area near the edge is almost identical to that one of the intact area away from the opening. In both cases persistent signal from upper and lower surface of the wall were obtained. NDI around the cut-outs of VS cylinder revealed that signs of delamination can be observable on

the outer layer of the areas with pulled-out fibre bundles. Location and dimensions of the damaged areas are marked in Figure 9.10. Although there were several bundles of

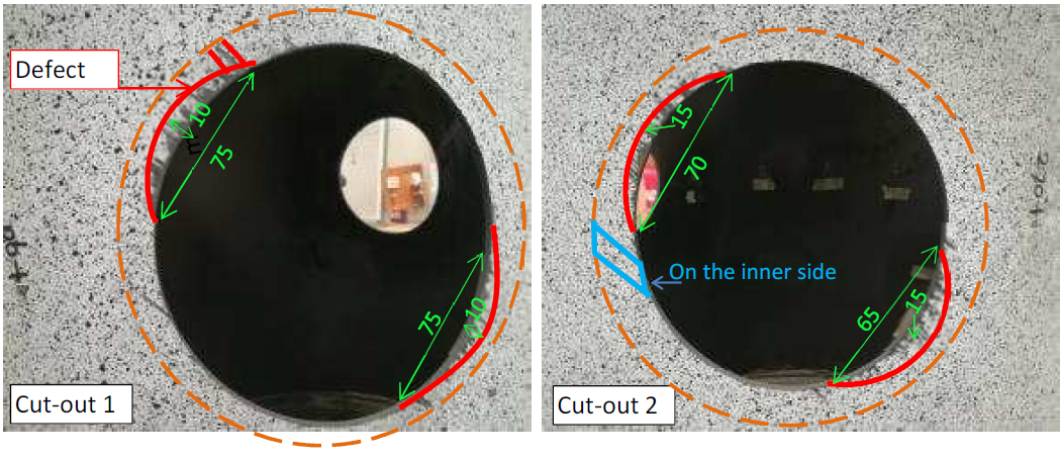


Figure 9.10 : Location of the damaged surfaces in VS cylinder.

pulled out fibers on the surfaces around the cut-outs, no inter-laminar debonding in the middle layers were found. All the defects around cut-outs are localized on the outer layer of the shell.

9.2.1 Specimen Preparation and Installation

The shells cured to specifications were manually trimmed close to their final length of 39 inches. In order to increase the bearing capability of the cylinder at the connection with the loading frame, steel tabs were bonded onto the inner and outer surface on both ends of the cylinder. The dimensions are specified in Figure 9.11. The tabs and

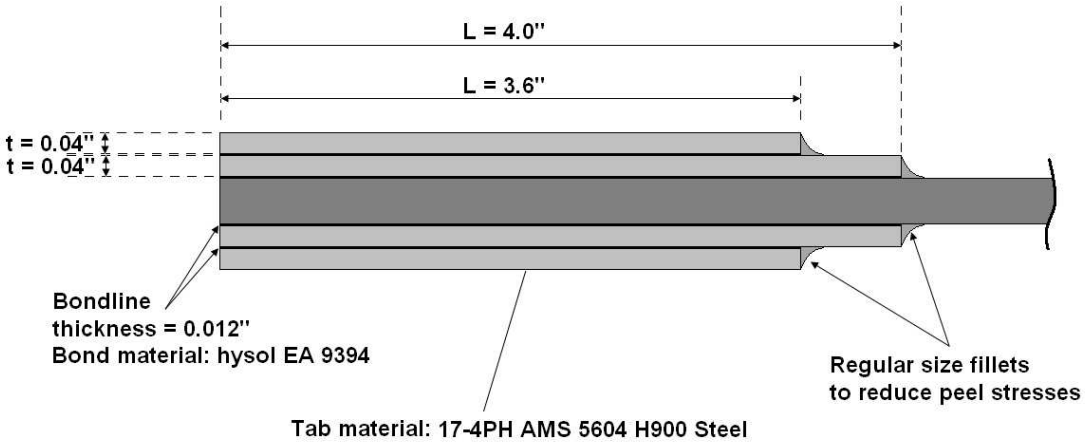


Figure 9.11 : Dimensions of the end tabs.

cylinder surface were then sanded such that the cylinder ends are perpendicular to the

axis of revolution. The cylinder surface is cleaned and strain gauges are bonded at specified locations on the inner and outer surfaces. Then the outer surface is spray painted white and covered with a black speckle pattern.

The shell is vertically placed on one of the support structures and centered between the outer ring and inner ring segments (the rings are shown in Figure 9.12). Then the bolt



Figure 9.12 : End tab view.

holes are match drilled through the shell. Subsequently the second support structure with rings is connected to the first support structure by 2 aluminum plates (shown in Figure 9.13) and fitting bolts. This ensures that the surfaces on which the rings are mounted are exactly parallel and at a distance of 39 inches.

The space between the shell and rings was then filled with paste adhesive which serves as a filler such that the shell can be fully clamped between the rings. The rings were first covered with a remover material to avoid the paste adhesive from sticking to the rings. After the paste adhesive has hardened, the bolts were tightened up to the specified torque. Subsequently the subassembly was moved into the test bench and

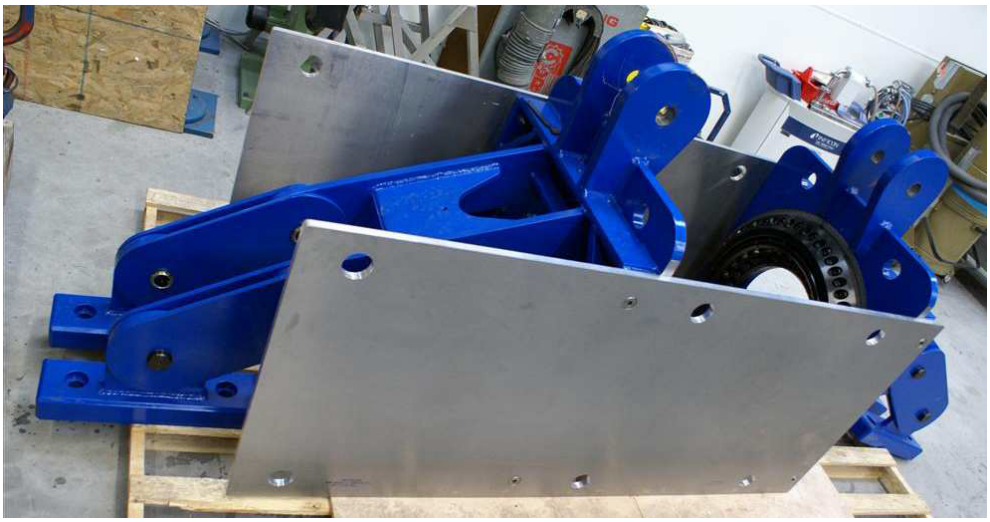


Figure 9.13 : Connection between the two support structures.

assembled to the other components. Finally the aluminum plates were removed from the assembly.

9.2.2 Bending moment calculation

The bending moment can not be measured directly and therefore it is derived from the actuation force, the known weight and configuration of the test fixture. The bending moment applied to the shells was calculated by multiplying the reaction force at each end P/2 (P is the force applied by the machine) with the moment arm d = 711 mm (28 in). In addition, the moment (M_s) caused by the weight of the support structure and rings (colored in yellow in Figure 9.14) were added to calculated moment.

The total moment can be calculated as:

$$M = (P\frac{d}{2}) + M_s \tag{9.1}$$

The displacement of the cylinder and rotations of the test equipment were measured using linear variable differential transformers (LVDT) and lasers. The rotations of the plates about the horizontal and vertical axes were calculated by measuring the displacements of the end-plates at three distinct locations. As a check, the lower struts were instrumented with strain gauges and the struts were calibrated to serve as load cells. First the upper parts of the assembly were installed in the machine (i.e. the upper lugs, upper triangles and upper struts) so that the machine load can be set to zero as indicated in Figure 9.14:

$$F = P - X \tag{9.2}$$

The load F is reacted by the weight of the support structure and rings, and by the

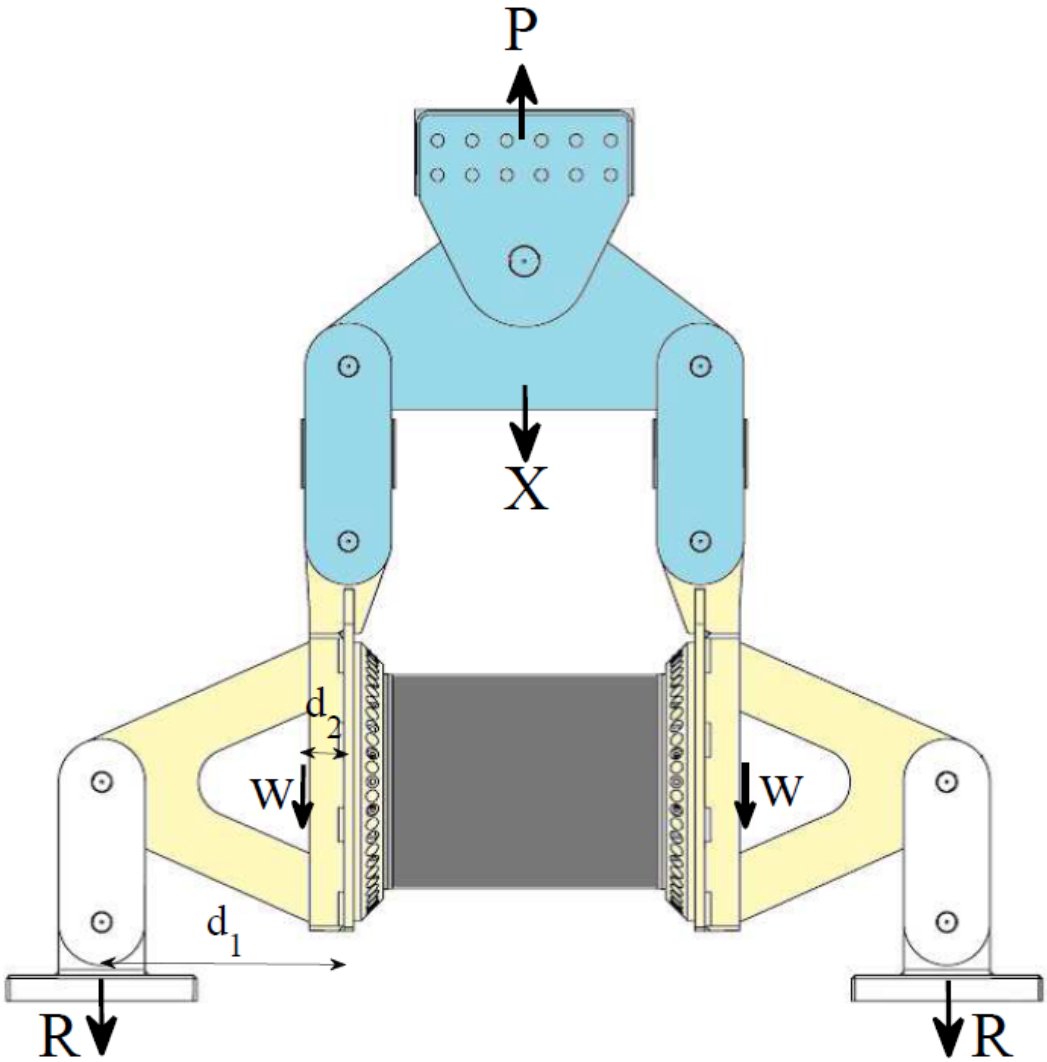


Figure 9.14 : Schematic for the determination of the bending moment.

connections at the lower struts. Together they contribute to the bending moment. From CATIA the weight of one support structure with inner and outer rings was calculated to be w = 1310 lbs, with it's center of gravity at 4.29 inches from the hinge-line of the upper struts. This generates a moment of:

$M_s = w \cdot d_2 = 5620$ in-lbs.

This moment is obtained in order to calculate the necessary axial force that will be applied by the MTS test machine.

9.2.3 Measurement of the displacements

The global displacement of the machine head was measured using the internal mechanism of the MTS test bench. The displacement of the shell and rotations of the

test equipment were measured using LVDT's and lasers. By measuring displacements of the end plates at three distinct locations the rotation of the plate about two axes can be calculated, one of which is the end rotation of the shell. This information is also used to check the symmetry in the loading conditions and to determine if corrections are necessary in the calculation of the bending moment. The vertical deflection of the shell was measured next to the end rings and at x/L = 0.5. As a reference also the vertical displacement of the end rings was measured. All these measurements were done inside the shell so that the field of view of the 3D camera system was not disturbed. Once the displacement at one point is known, the rest of the displacement field can be calculated using the 3D digital image correlation system.

9.2.4 Measurement of the geometric imperfections

Geometric imperfections of the cylinders were measured after the cutouts were machined into the shells. Geometric imperfections of the shell were measured both outside and on the test setup. The data was acquired through the VIC3D stereo digital image correlation system with two digital 1.4 megapixel cameras having 8 mm lenses.

The imperfection measurement for the CS and VS cylinders with cutouts are given in Figures 9.15 and 9.16 in an unwrapped form. In order to obtain this data the

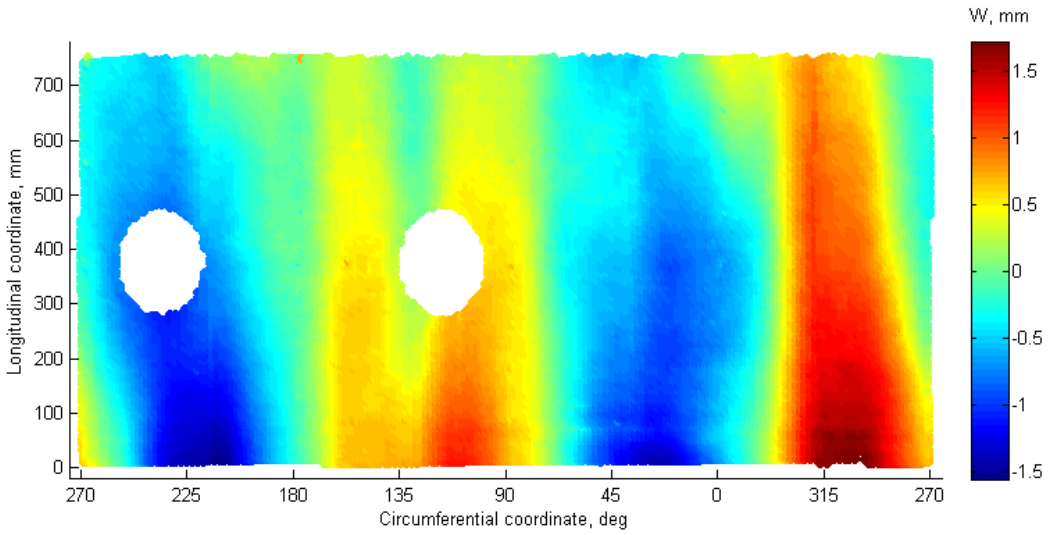


Figure 9.15 : Imperfection data for CS cylinder with cutouts.

specimens were first painted white and then a black speckle pattern was applied, both using acrylic paint. Cameras with 50 mm and 25 mm lenses were used to measure the cylinders outside the test setup and cameras with 8 mm lenses were used to measure

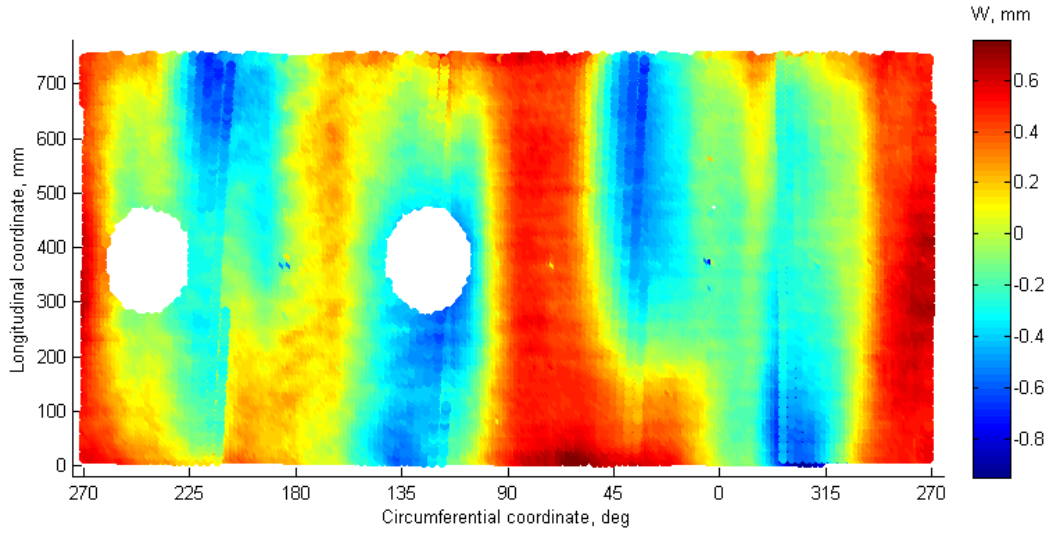


Figure 9.16 : Imperfection data for VS cylinder with cutouts.

the imperfections while the cylinders were assembled in the test setup. The use of a stereo camera system allows for three dimensional correlation, providing information on the initial geometry and on the deformation of the object.

Multiple pictures were taken around the circumference of the cylinder to cover the full surface. The separate images were then combined into one data file covering the whole cylinder during post-processing. Geometric imperfections are generally expressed in terms of a deviation from the perfect cylinder radius. Mathematically the imperfection w is given by,

$$w = r - R \tag{9.3}$$

where r is measured radius and R is the perfect cylinder radius.

The imperfection measurements before opening the cutouts into CS and VS cylinders are given in Figure 9.17 in an unwrapped form. A 3D view of the imperfection data for the CS cylinder is given in Figure 9.18. It can be seen from the figure that there are some ovalizations on the cylinder. Those imperfections may result from the non-perfect manufacturing process or due to its being a thin shell and therefore to be subjected to easy deformation. Since the shells are very sensitive to the imperfections, it is very crucial to measure real imperfection in order to perform a precise numerical analysis.

The theoretical imperfections were obtained numerically from the linear buckling analyses. Those imperfections were in the shape of buckling eigenmodes from the

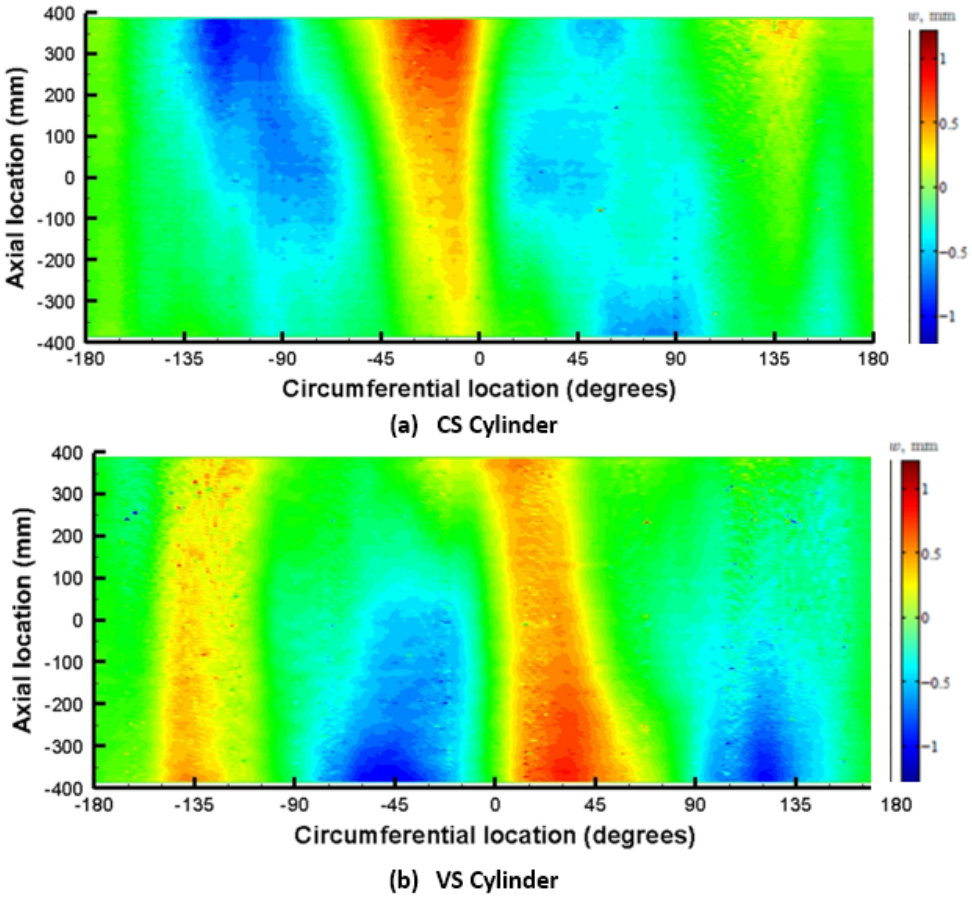


Figure 9.17 : Imperfection data for non-cutout CS and VS cylinders.

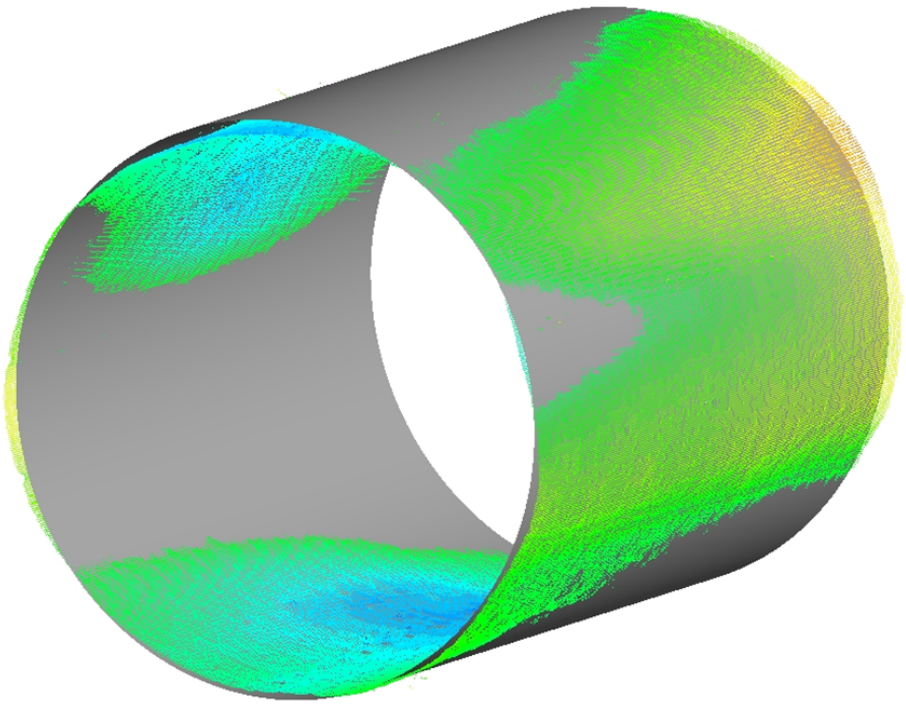


Figure 9.18 : 3D view of imperfection data for non-cutout CS cylinder.

linear buckling analysis in the form of from of first buckling eigenmodes with 10% of the shell thickness were applied during Riks analysis. It was realized that theoretical imperfections also give very close results compare to the real measured imperfections. Therefore, if the manufacturing quality is sufficient enough, one can use theoretical imperfections conveniently.

9.3 Instrumentation and Data Acquisition

Before starting the testing, the test rig containing the cylinder assembly was bolted to the MTS 3500 machine. Tension bolts, connecting end-rings to back-plate, were installed with pre-tension of 200 Nm. Shear bolts, connecting end-rings and cylinder, had a pre-tension of 125 Nm. The base of the machine was used to attach most of the LVDTs and laser displacement sensors. During each test run the following data were recorded:

- DIC images,
- Strains from 36 strain-gauges (KFG-5-350-C1-11),
- Displacements with LVDT‘s and laser distance sensors,
- Axial force, frame displacement and time from MTS 3500 machine,
- Photos and video by regular cameras,
- Visual observations.

The test set-up with connected measurement equipment is shown in Figures 9.19 and 9.20. The positions and directions of the DIC systems are provided in Figure 9.21. Center of the focus for both systems were the lower (compressed) part of the cylinder, including the cut-outs. Each DIC system is synchronized with time and force readings from the MTS 3500 machine.

Strains were measured with general purpose strain axial strain gauges and rosettes at the locations with numbering specified in Figure 9.22. The circumferential location θ=0 corresponds to the tension side of the cylinder, while θ = 180 is the compression side. Since these locations are expected to exhibit the largest strains they are considered most interesting. Many strain gauges were placed along the axial direction at these two locations such that it can be seen where the influence of the boundary disappears. Furthermore a pattern of strain gauges was placed around the circumference in the middle of the shell, because this is where the boundaries have the least influence. One

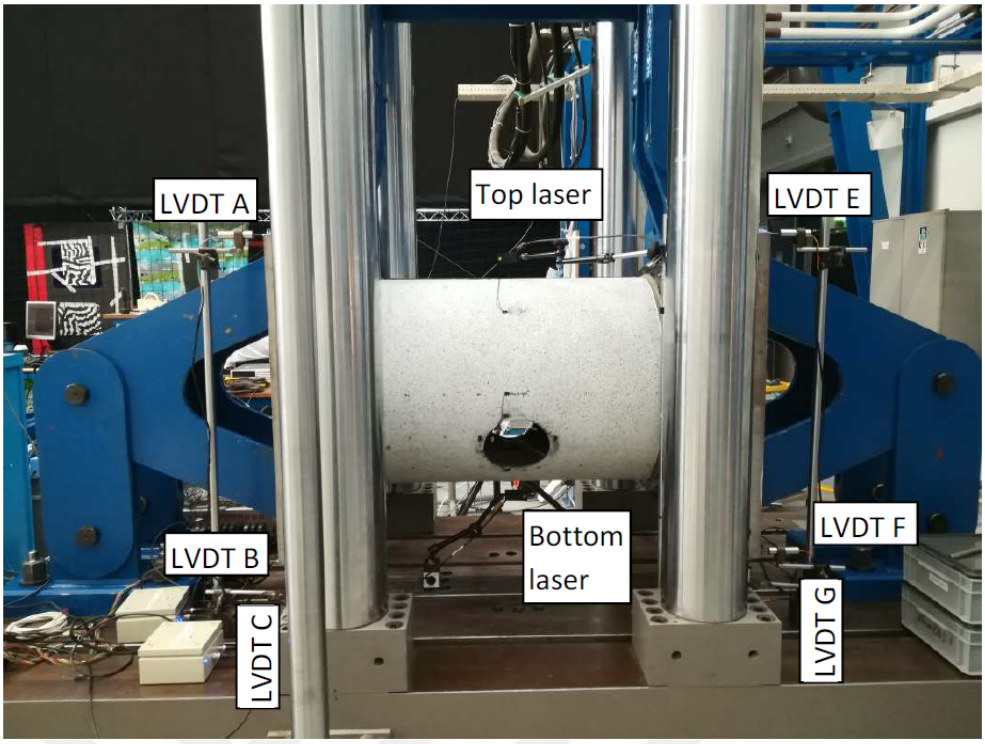


Figure 9.19 : Test set-up on MTS 3500 machine- side 1.

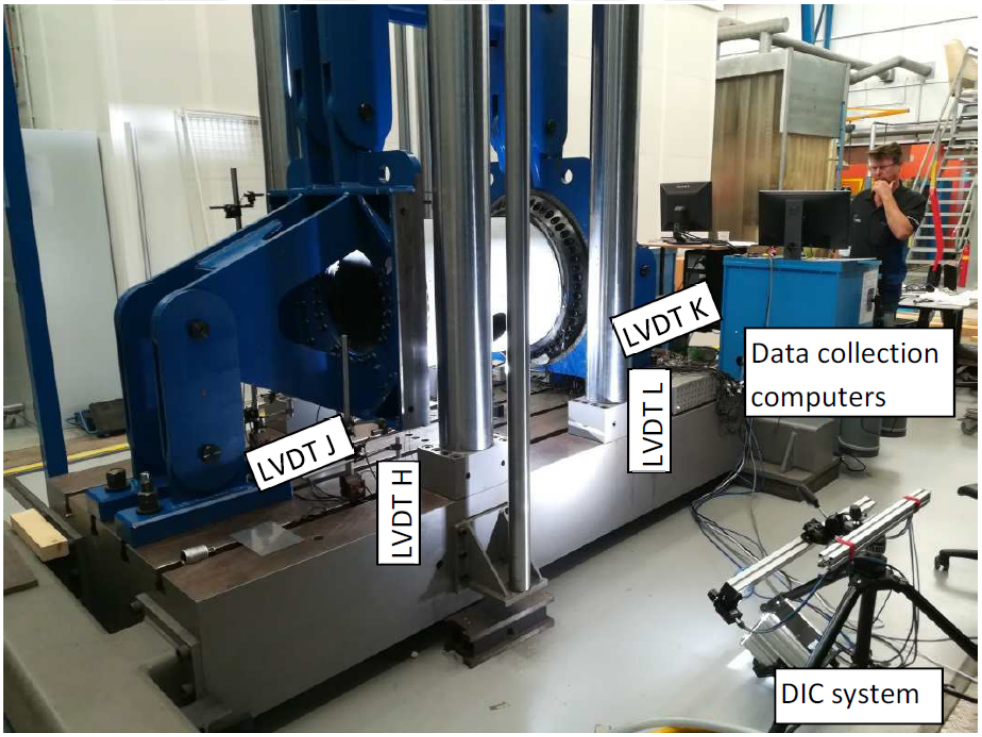


Figure 9.20 : Test set-up on MTS 3500 machine- side 2.

quarter of the shell was covered with a grid in order to see the variation in the strain field. Since the shell was not expected to buckle globally in this test, relatively little strain gauges were attached on the inside of the shell.

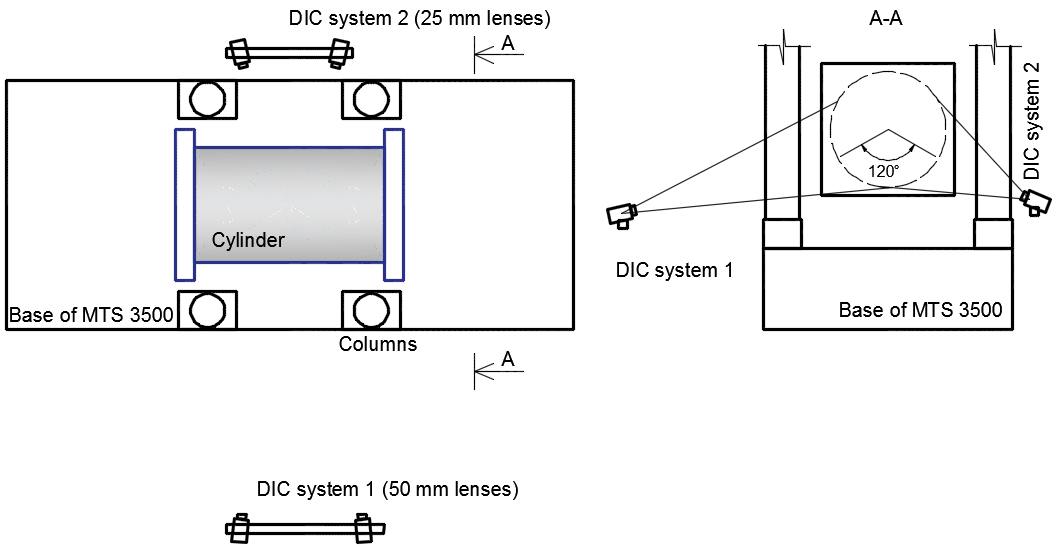


Figure 9.21 : Top and side view of the locations for the DIC systems.

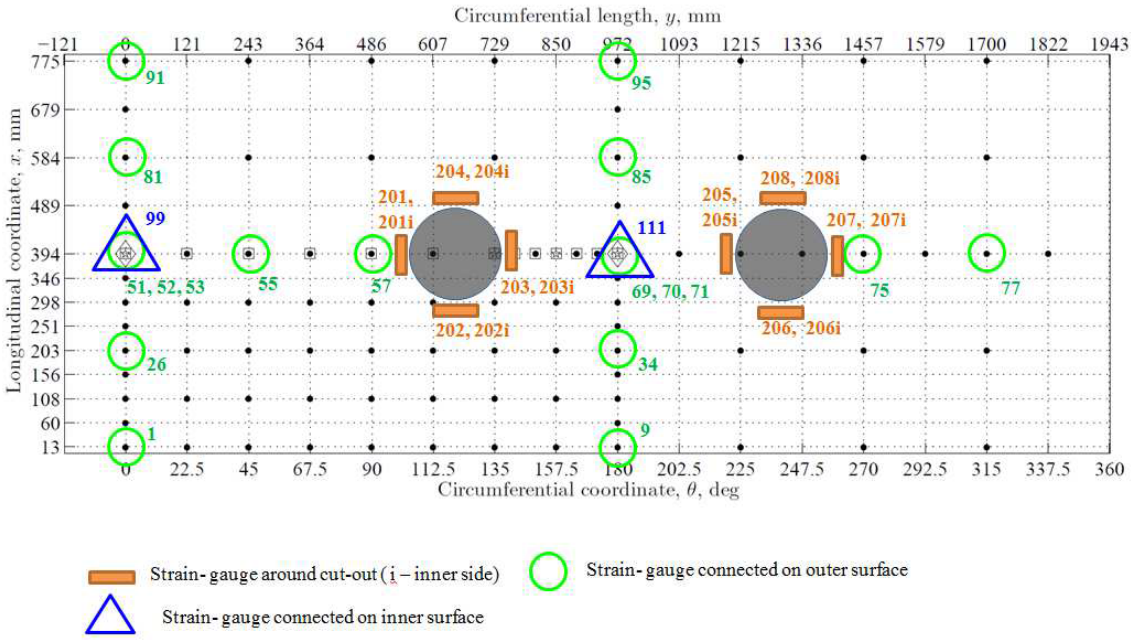


Figure 9.22 : Location of the attached strain-gauges.

Analog signals from the strain-gauges, LVDTs and laser displacement sensors were collected by KEITHLEY data acquisition system together with the load cell and the machine frame displacement values. The data from KEITHLEY and DIC systems were saved at every 5 kN load step. The command to write data was manually triggered from the main computer. During the data saving period, the test was paused for approximately 10 seconds. Bending moment and end rotations were calculated in postprocessing mode using LVDT and axial force readings.

9.4 Test Procedure

The tests was conducted with displacement control applying constant frame vertical movement speed of 0.2 mm/min. Experimental study of each cylinder was performed with the following sequence:

Initial pre-test with load magnitude up to 10 % of the estimated critical load: The test was performed 3 times to assess repeatability. Main purpose of this test is to ensure that data acquisition systems are working properly and the test rig is assembled correctly. Force/end rotation and force/midpoint displacement curves were compared to numerical results to evaluate initial stiffness.

Bending test up to 50 % of the estimated critical load: The test was conducted to ensure that data collection works properly at higher loads magnitudes. In addition to force/end rotation and force/midpoint displacement curves, force/strain curves were compared with numerical model.

Bending test up to 75 % of the estimated critical load: The experimental results were compared with numerical model in the same way as in the previous step.

Bending test until buckling or failure: This is the main test to acquire buckling or failure load of the cylinder. When sudden loss of the load resistance (in the result of buckling or failure) was reached, the test was immediately stopped and the specimen gradually unloaded.

Field inspection with ultrasound scanning probe was performed before the following test in the area between the cut-outs in the compressed part.

9.5 Finite Element Predictions

Although, the end conditions for testing are designed to be fixed boundary conditions, in real case there exist some flexibility between joints of the fixture. Therefore, flexible boundary conditions were generated using spring type elements. Linear axial and rotational springs were added between cylinder ends and the rigid end plates as shown in Figure 9.23. The spring constants were obtained from the A.Blom's study [3]. The springs were added to each end node in the finite element model. The nonlinear progressive failure analysis with real imperfection load/displacement curve for CS cylinder is given in Figure 9.24. As it can be seen from the figure, the theoretical

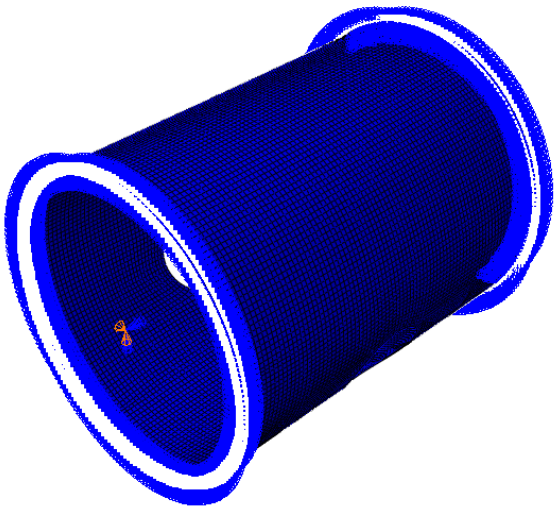


Figure 9.23 : Spring type BCs.

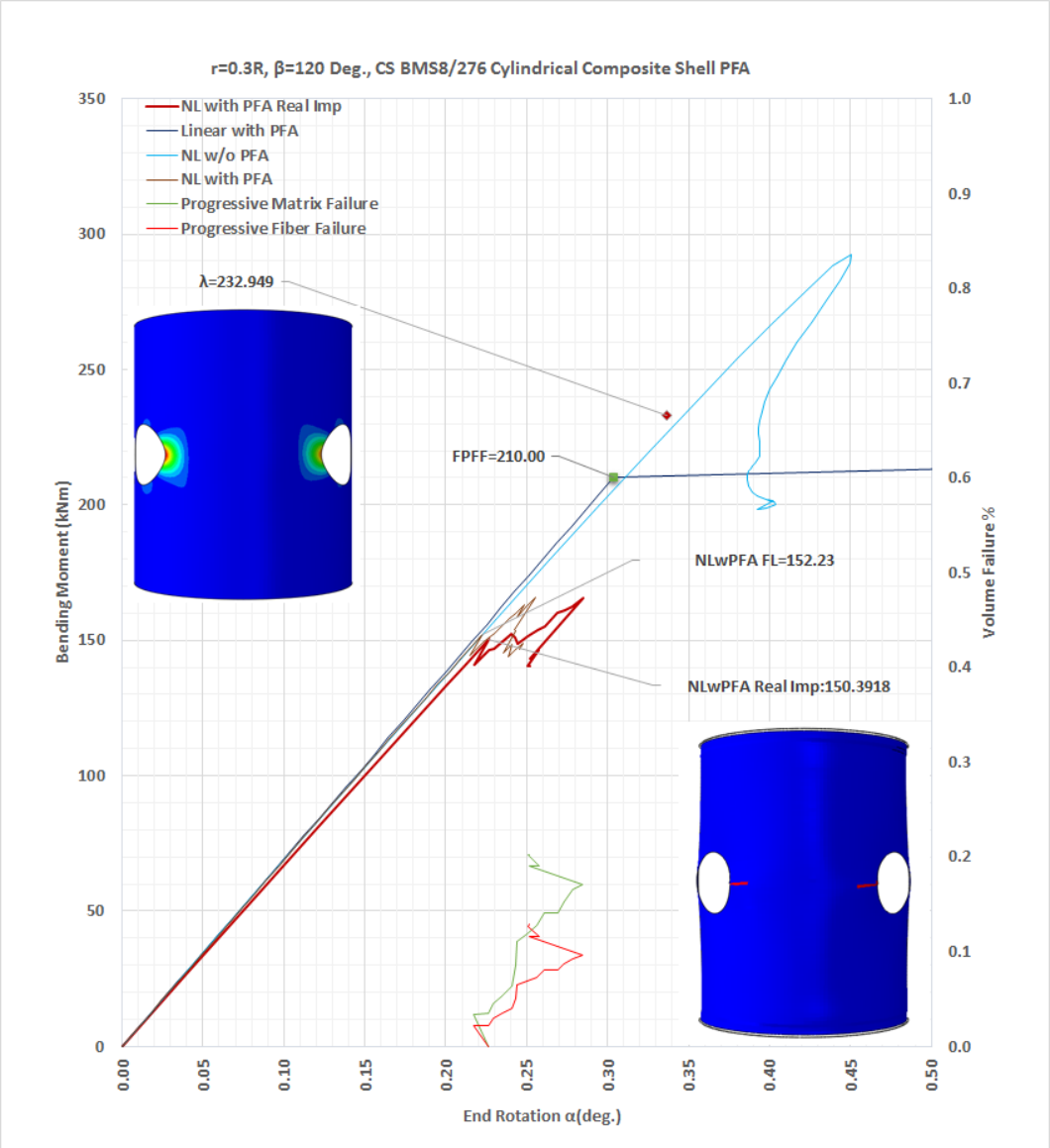


Figure 9.24 : Nonlinear PFA with real imperfection for CS cylinder with cutouts.

imperfection results are very close to the real imperfection results. The failure load is around 150 kNm for CS cylinder with real imperfection, while it is 152 kNm for the theoretical imperfection. On the other hand, for the CS cylinder the ultimate load increases up to 165 kNm.

The nonlinear progressive failure analysis with real imperfection load/displacement curve for VS cylinder is given in Figure 9.25. This figure show that with the real

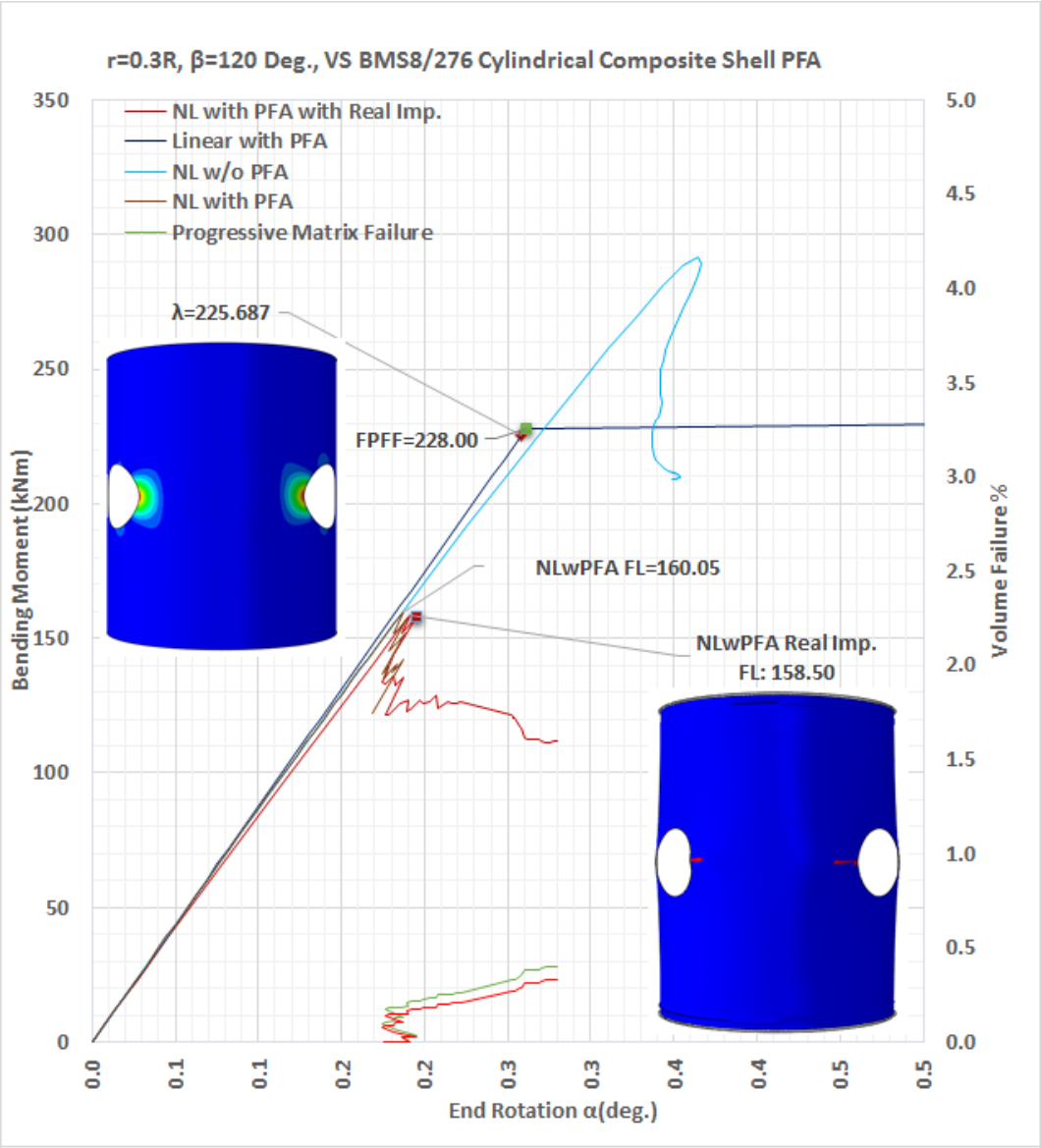


Figure 9.25 : Nonlinear PFA with real imperfection for VS cylinder with cutouts.

imperfections there are not much deviation from the ultimate failure load compare to the theoretical imperfections. The failure load is 158 kNm for VS cylinder with real imperfection, while it is 160 kNm for the theoretical imperfection. From the matrix and fiber failure curves it can be seen that catastrophic failure starts from 146.1 kNm

of the FEM model for the VS cylinder. In both CS and VS cases after the failure the cylinders are able to further carry the loads.

In order further validate the finite element model, the test results of the non-cutout case that were performed previously by A.Blom [3] were compared with the numerical results. As shown in the Figures 9.26 and 9.27, the test were not conducted until failure

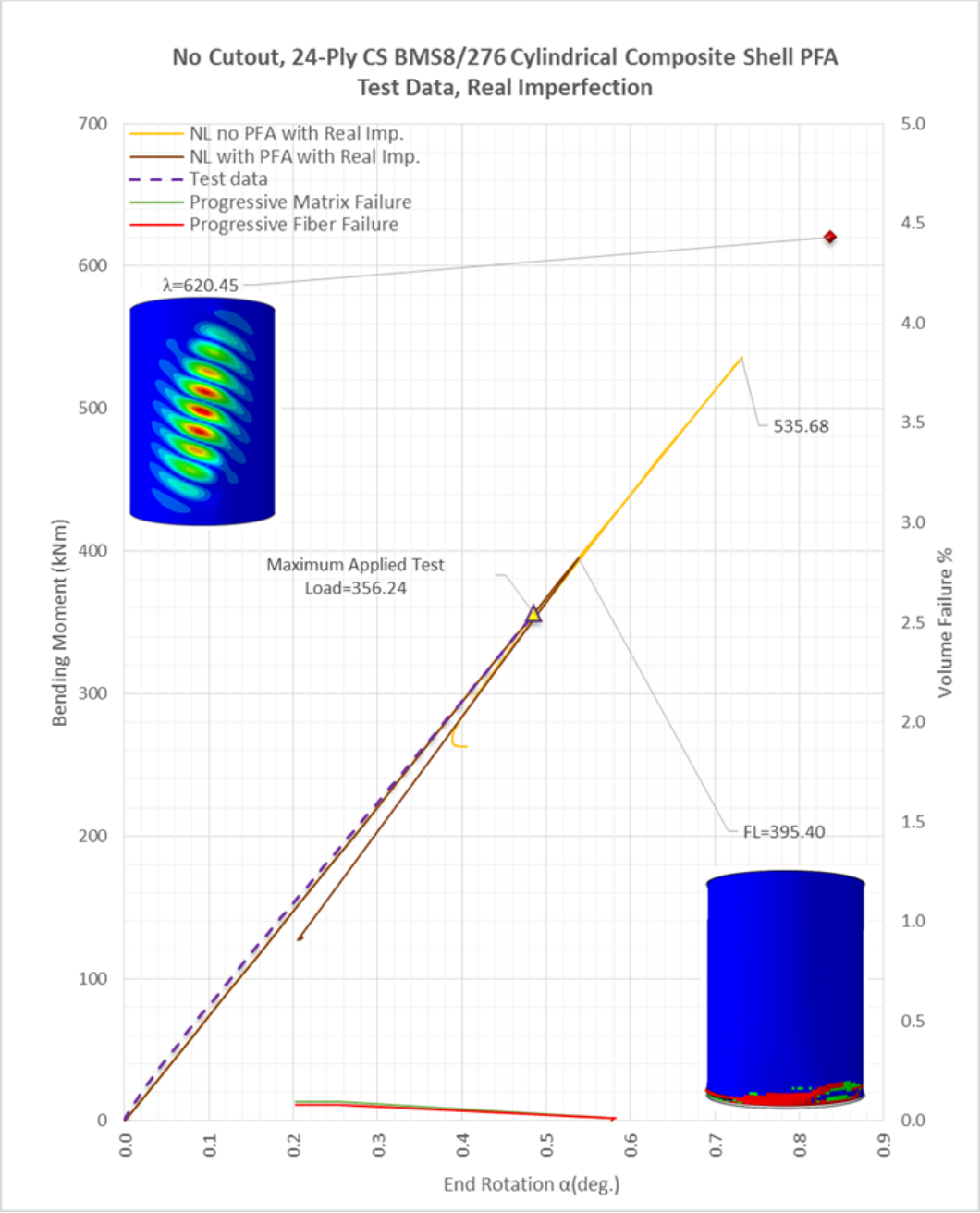


Figure 9.26 : Non-cutout CS test results.

due to the test fixture's bearing load limit and the results have very good correlations with the numerical model.

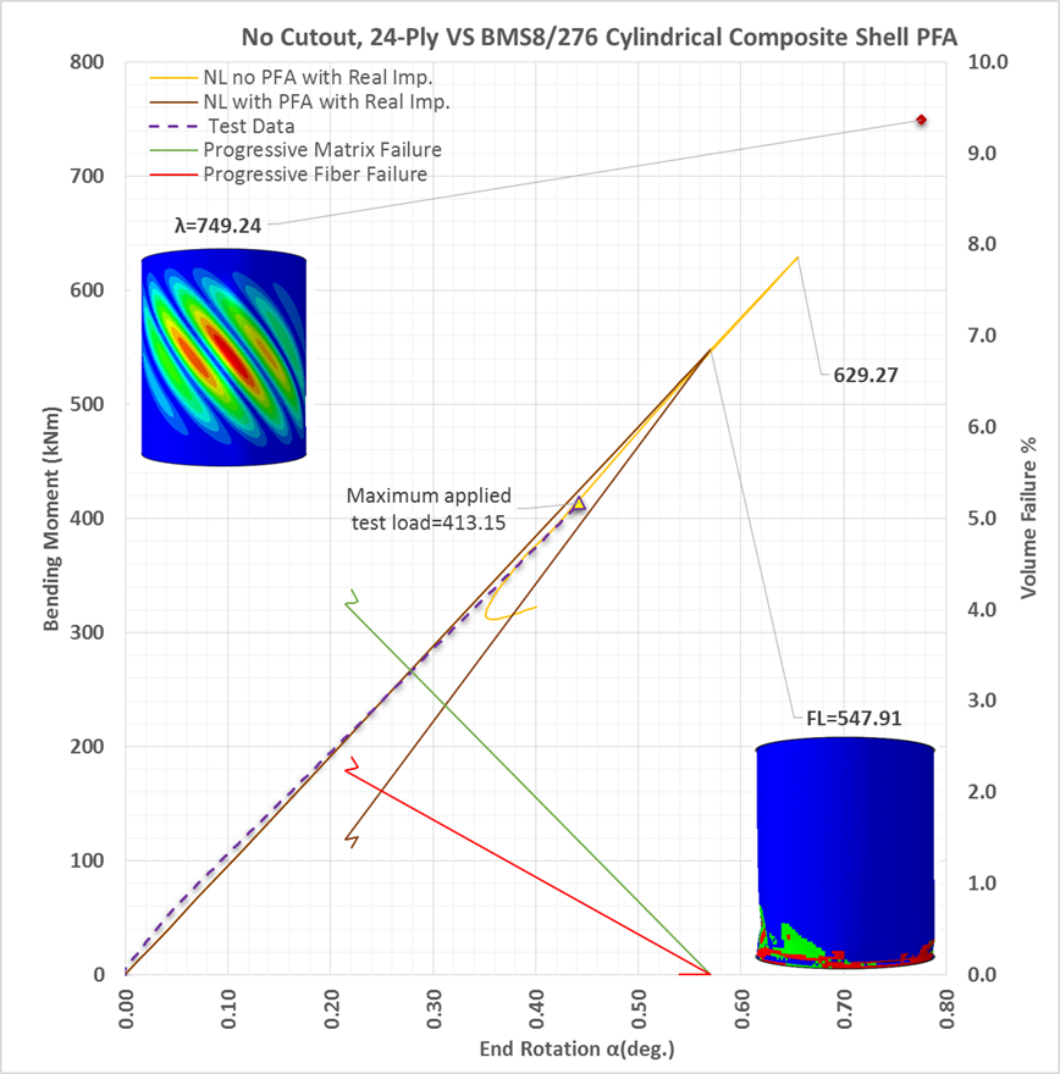


Figure 9.27 : Non-cutout VS test results.

Another result of the numerical analysis is that the failure is expected to start from the edge of the cylinder. Since, the test without cutouts could not have been conducted until failure, it is not possible to compare the failure initiation location. This failure location is as a result of the boundary effect. The grips on the edge of the cylinder cause the failure initiation. On the other hand, during the tests with cutouts, failures started from the cutout edges as a result of local buckling around the cutouts.

9.6 Test Results

The tests were performed up to the failure of the both CS and VS cylinders. The bending moment/end rotation curve for the CS cylinder is given in Figure 9.28. The ultimate load that were recorded during the test of CS cylinder was 175.25 kNM while it is 165.6 kNm for the numerical analysis. However, note that at around 123 kNm

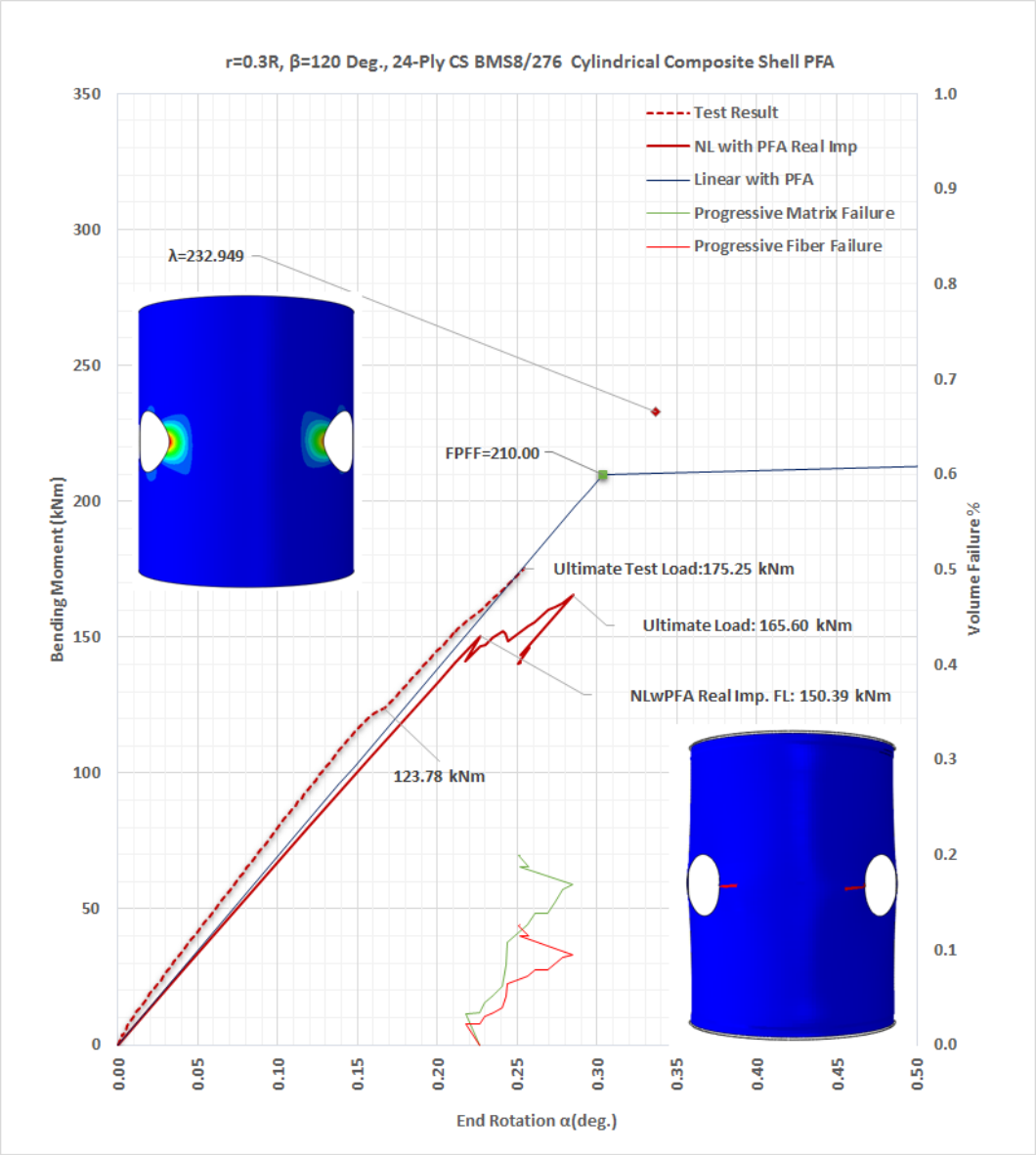


Figure 9.28 : Test result for CS cylinder with cutouts.

there is a change in the slope of the curve of the test result. This incidence can be observed also in the top mid point axial strain curve as shown in Figure 9.33. Since this change in the slope can only be seen in the top axial strain significantly, to find the probable cause the strain results near the boundaries were checked and the similar indication were observed at one of the top edge. This similarity shows that at that boundary edge there is a slight dislocation of the cylinder edge from the test fixture grips. The crack initiation expected to start from the cutout lower edge and propagate towards the bottom of the cylinder. As shown in Figure 9.29 the crack is at the bottom of the cylinder as expected.

The pictures of the failed VS cylinder are given in Figure 9.30 and Figure 9.31. In



Figure 9.29 : The picture of the failed CS cylinder.



Figure 9.30 : The picture of the failed VS cylinder from outside.

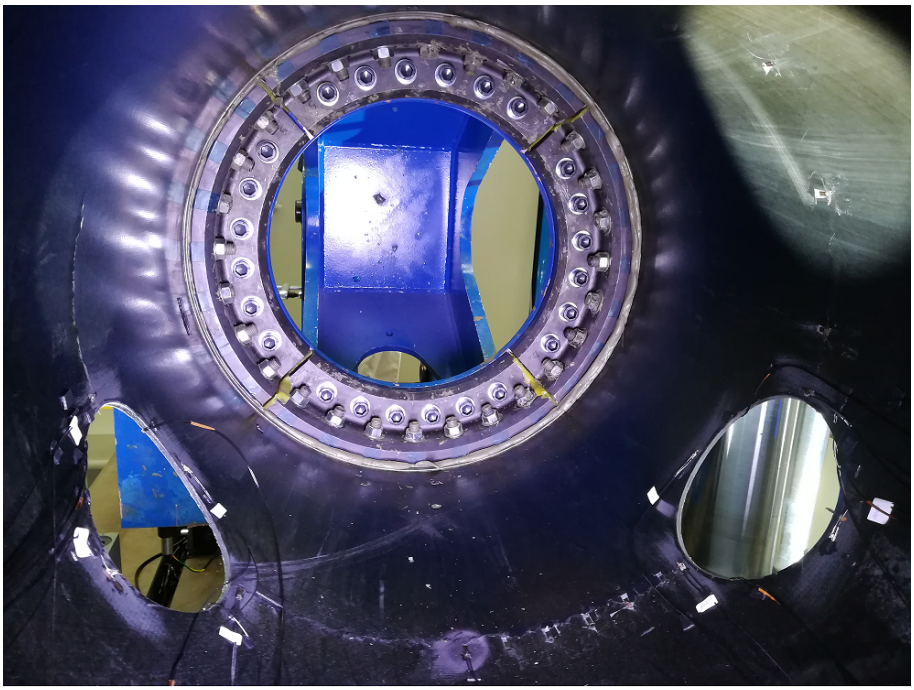


Figure 9.31 : The picture of the failed VS cylinder from inside.

addition, the test result for the VS cylinder is shown in Figure 9.32. The predicted test

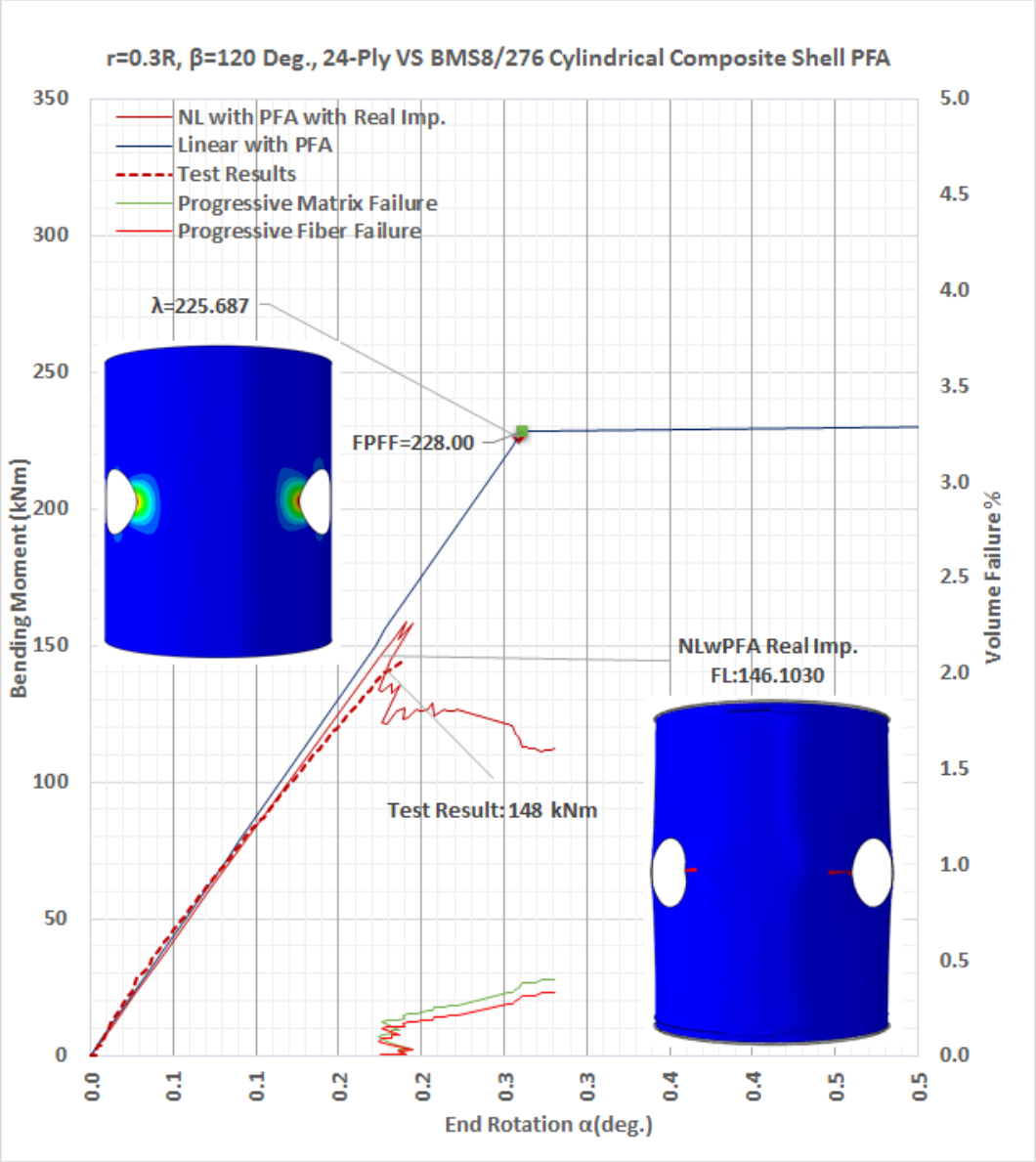


Figure 9.32 : Test result for VS cylinder with cutouts.

result for the VS cylinder was 146 kNm and in the test it was measured as 148 kNm. The load applied by the MTS machine was predicted as 409 kN and it was measured as 416 kN. The failure results show that there is a very close prediction of the failure load between numerical analyses and the test results.

It can be observed both from numerical result and also from the test pictures, failures initiates from the cutout edges as a result of local buckling from the cutout edges. The crack initiation starts first from lower edges of the cutouts and propagates. Once the failure of the bottom part of the cylinder almost completed, the failure also continues

from the upper part of the cylinder. These results are exactly the same as with the non linear progressive failure numerical analyses.

9.6.1 Strain Results

In order to compare the strain results of the numerical model with test results, we can first start with the top and bottom mid points of the both CS and VS cylinders. The axial and circumferential strain results comparison for the CS cylinder is given in the Figure 9.33. The top axial strains have positive values and circumferential strains

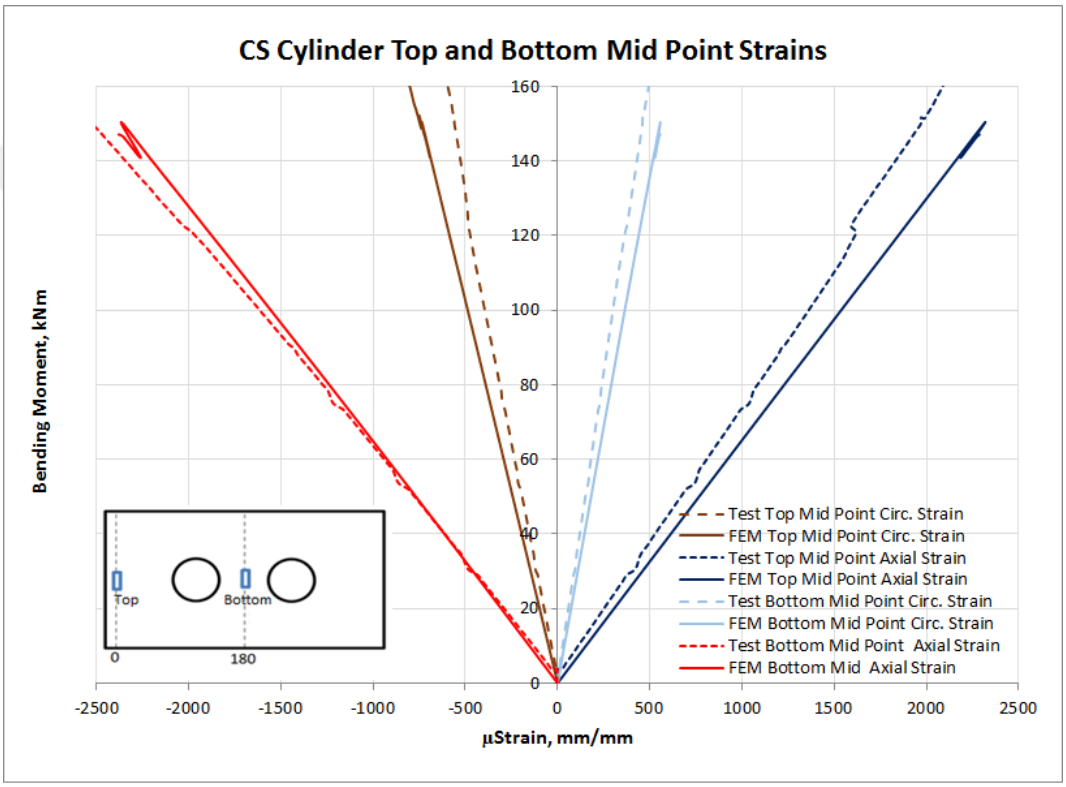


Figure 9.33 : The strain results for CS cylinder for top and bottom mid nodes.

have negative values, while it is the opposite at the bottom side of the cylinder. This proves that upper side of the cylinder is under tension while the bottom side is under compression. At the beginning of the test, the results match each other very closely, however, towards the end of the test there are some deviations. Nevertheless, they are still within the acceptable limits.

The strain results comparison for the VS cylinder is given in the Figure 9.34. Those results are also very similar to the CS cylinder results. Both results show a very good correlation of FEM and testing. The slight difference between the tests and FEM

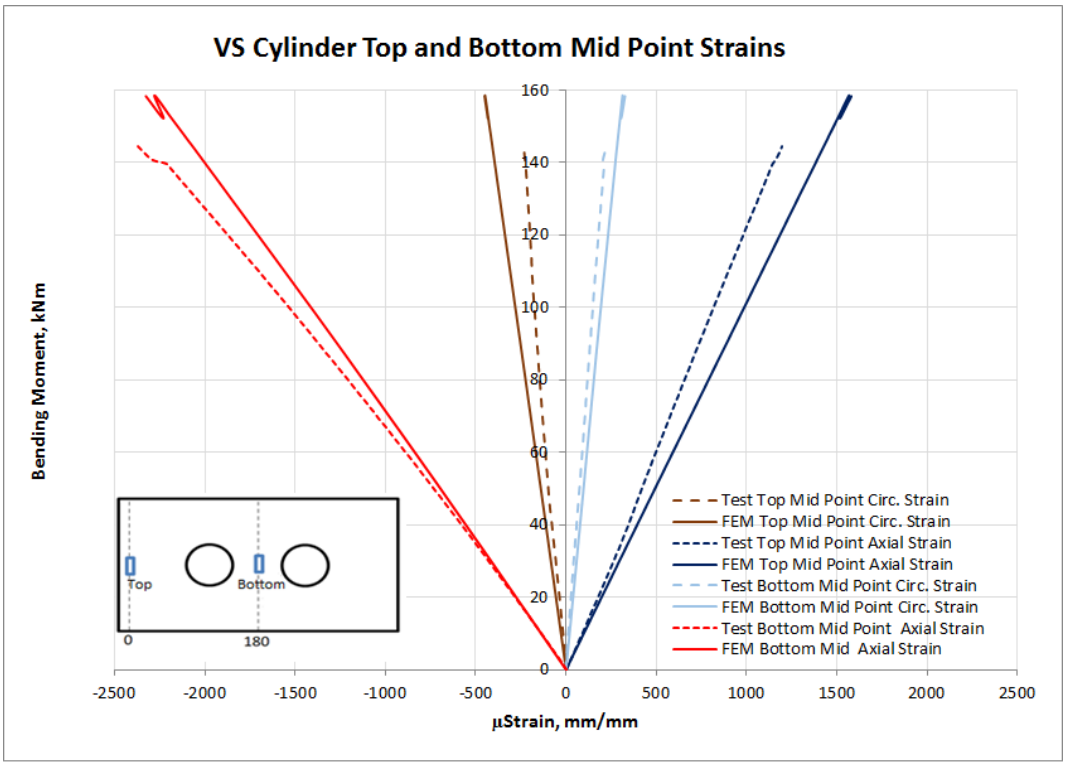


Figure 9.34 : The strain results for VS cylinder for top and bottom mid nodes.

results may occur due to the location of the strain gauge to be slightly different from the location of the numerical model.

Another interesting result is the strains around the cutouts. Around each cutout, four strain gauges were used at the outer surface and four strain gauges were used in the inner surface of the cylinders. The strain results for left and right cutouts for both CS and VS cylinders are given in the Figures 9.35, 9.36, 9.37 and 9.38. Note that, strain orientations, depending on the locations, are either axial or circumferential. Number 201, 203, 205 and 207 strain gauges are the axial strains, while number 202, 204, 206 and 208 are the circumferential strains. The left and right cutout strain results shows very similar behavior. Those results can be also validated with the DIC measurements. The strain results show that initially there is a very good correlation between numerical model and test results. However, after certain load level for the locations under compression there is a slight deviation. It might be due to the location of the strain gauge to be slightly different from the location of the numerical model. On the other hand, for the locations under tension the results are matching sufficiently. For the points in axial locations the strain gauges first undergo compression and then these compression starts to release. These might be the indication of the global buckling

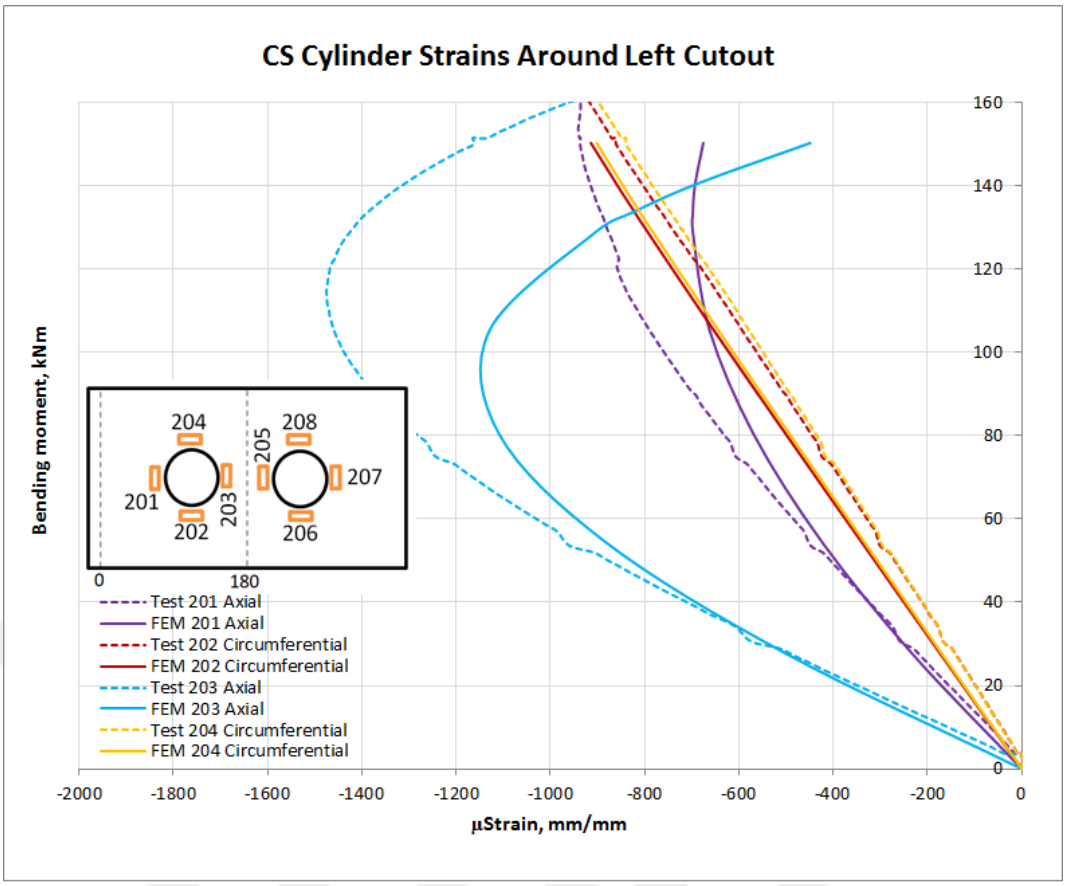


Figure 9.35 : The strain results around left cutout for CS cylinder.

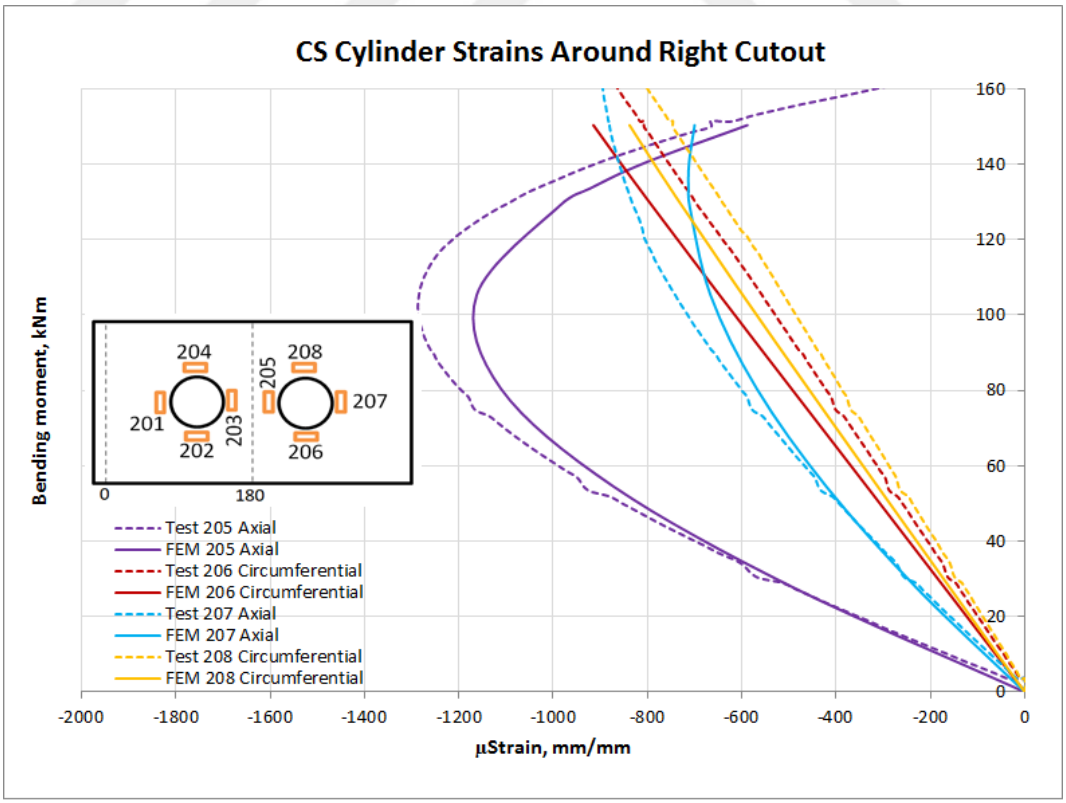


Figure 9.36 : The strain results around right cutout for CS cylinder.

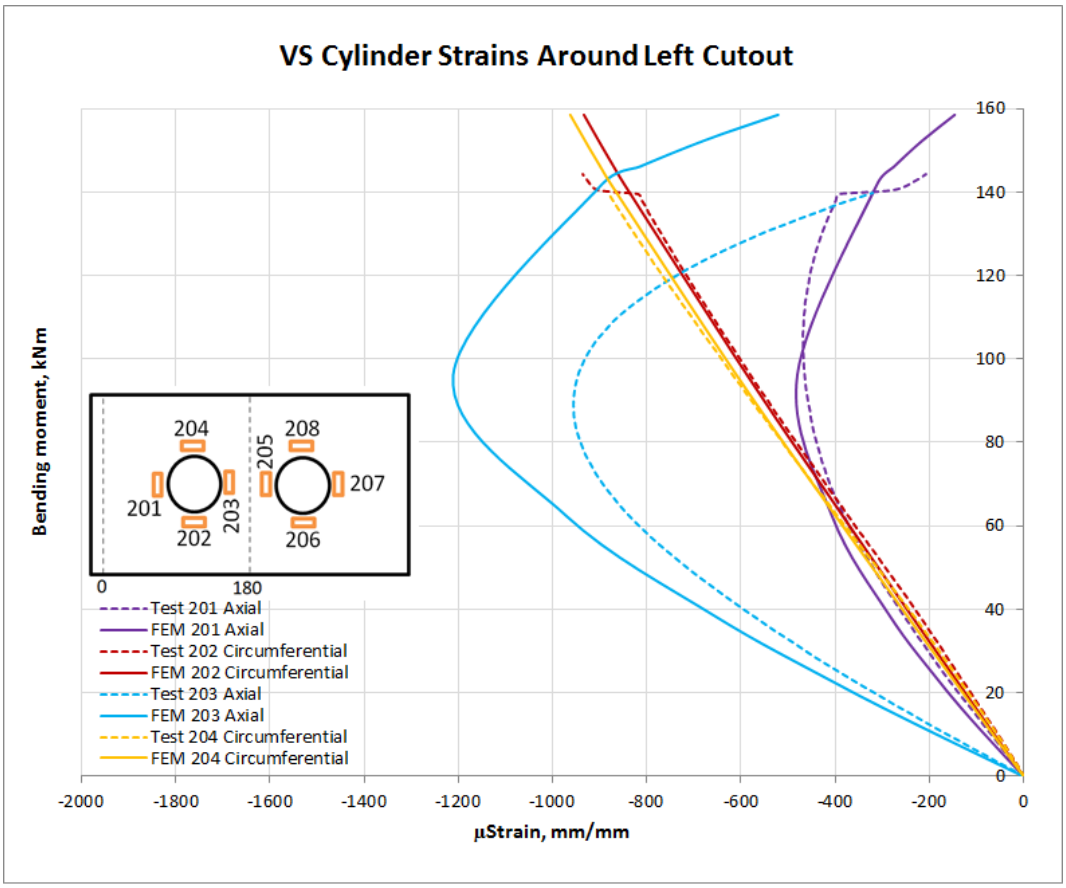


Figure 9.37 : The strain results around left cutout for VS cylinder.

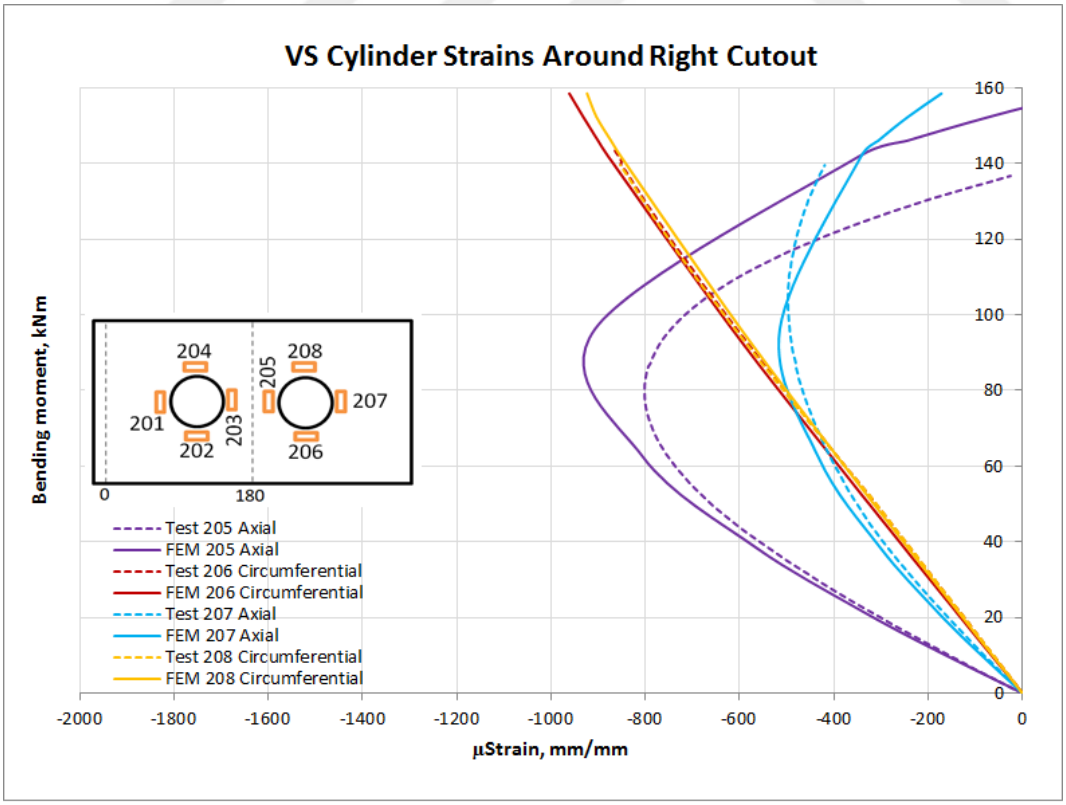


Figure 9.38 : The strain results around right cutout for VS cylinder.

starting point. When a slight global buckling starts may cause the axial compression around the cutouts to release. However, the circumferential compressions continue until failure.

When we compare the DIC measurements with numerical results, as an example, VS axial and circumferential displacement results are shown in Figure 9.39 and Figure 9.40. The images show almost the same results were obtained both in numerical

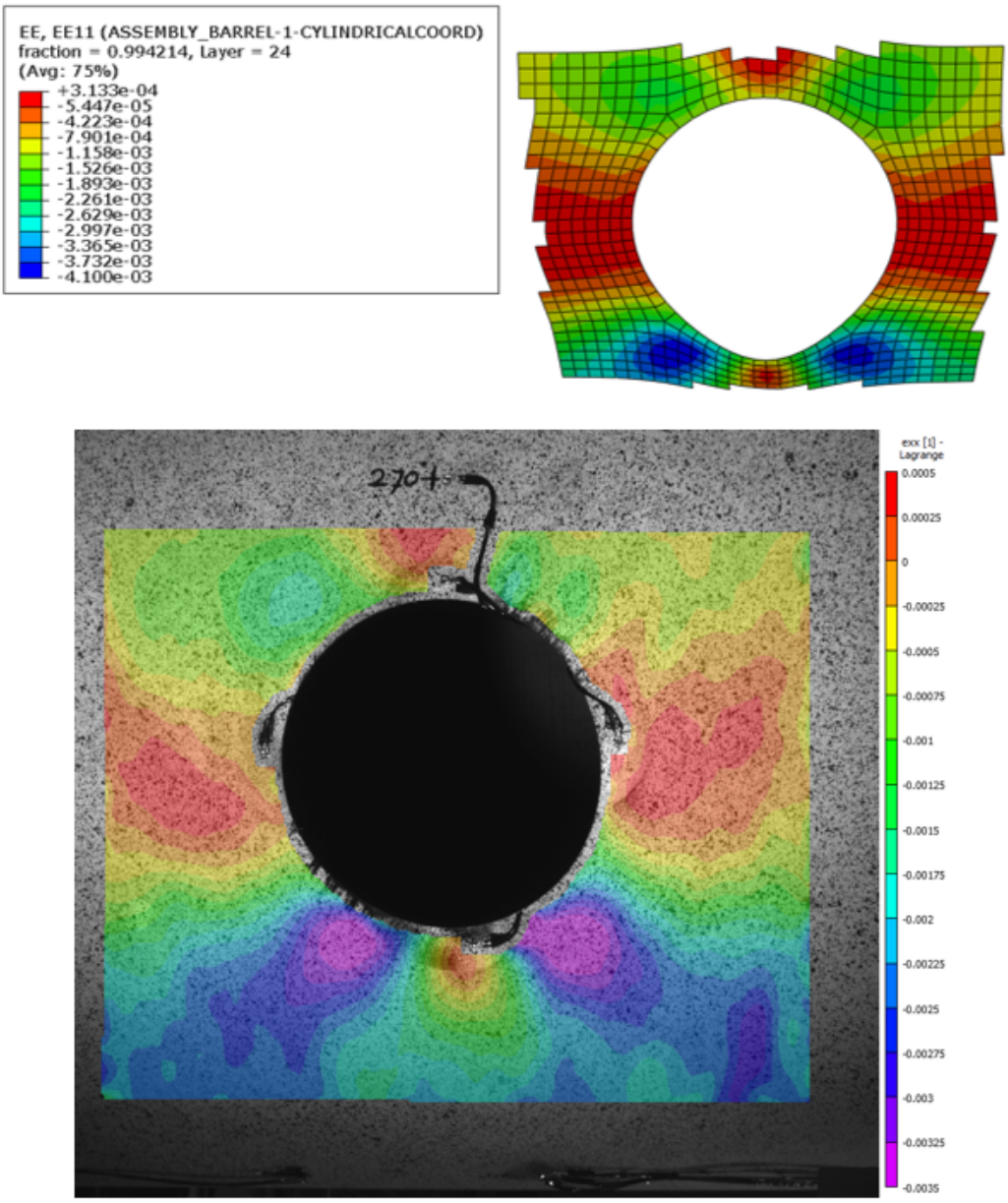


Figure 9.39 : The axial DIC results comparison with FEM results for VS cylinder.

analyses and in the test.

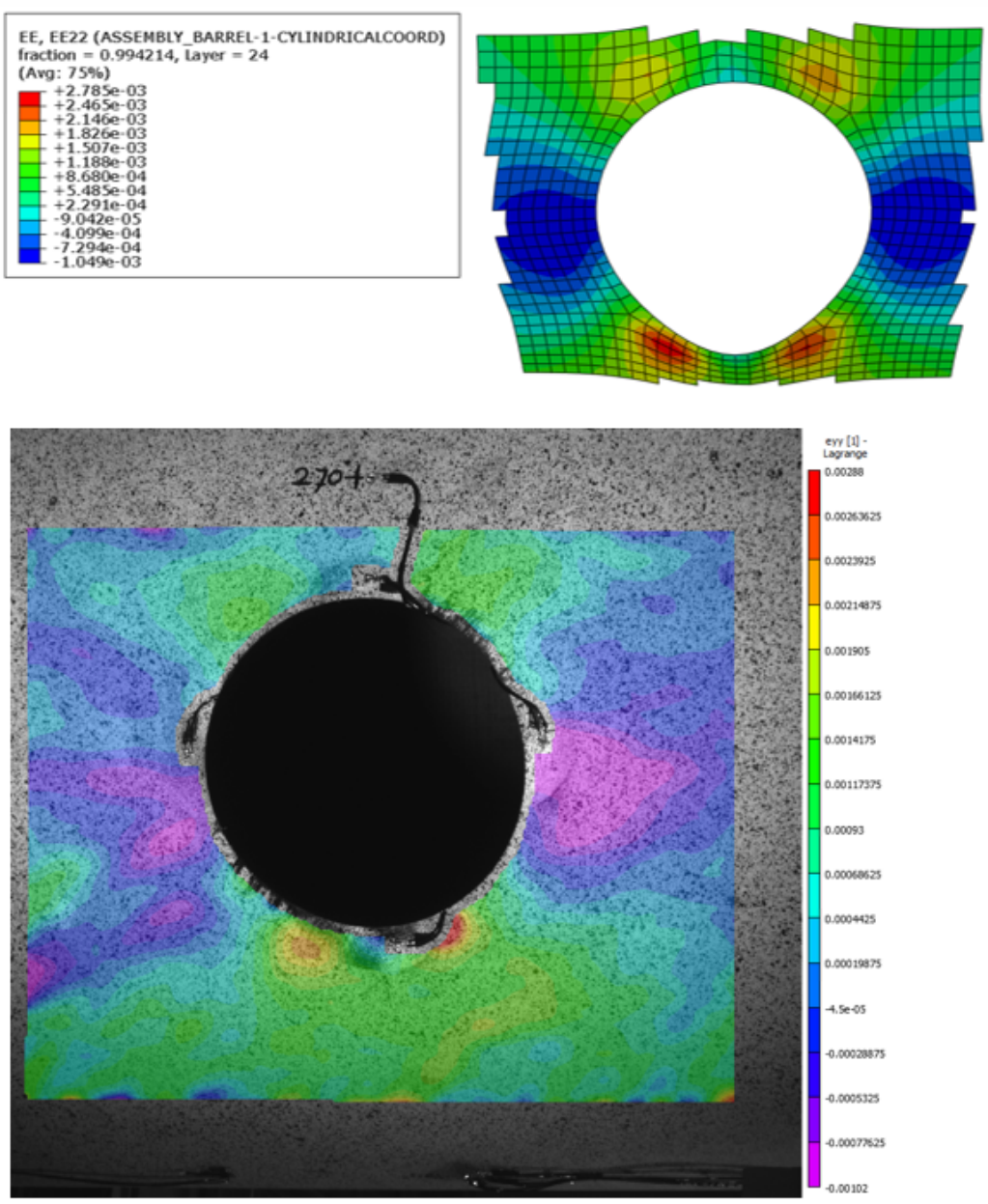


Figure 9.40 : The circumferential DIC results comparison with FEM results for VS cylinder.

10. CONCLUSIONS AND RECOMMENDATIONS

As for the conclusions, the work presented in this dissertation includes the effect of cutouts varying circumferentially and geometrically on both CS and VS cylindrical shells under pure bending and combined loading. During the analyses, nonlinear progressive failure analysis with real imperfections were applied. The numerical results showed that without applying progressive failure, the numerical analysis usually will give higher failure load compare to the one with progressive failure analysis. Therefore, for the reliable numerical results progressive failure analysis must be preferred. Mesh size analysis and element type investigation were performed with different failure criteria.

When the cutouts were introduced into the shell, it was realized that there are actually three distinct failure modes. Failure Mode I may be defined as strength failure driven by global buckling of the cylinder. For these cases, buckling occurs well below the linear estimations for FPFF and buckling loads, and the progressive failure load-displacement curve has the same maximum as the nonlinear case without PFA. Mode shapes and post-buckling deformation is concentrated at the bottom of the cylinder and the drop-off in load-carrying capability after buckling is often severe. Failure Mode II generally can be defined as; strength failure around the cutout driven by local cutout edge buckling. The eigenvalue is below the nonlinear load limit and the associated buckling shape is focused around the cutout as opposed to the classical mode of buckling at the bottom of the cylinder. The FPFF load level and progressive failure for the nonlinear solution greatly demonstrate the stress concentration around the hole, and it is the combination of the material failure and buckling deformation, which leads to the collapse of the cylinder. Failure Mode III was defined as strength failure around the cutout without buckling. It generally occurs with the cutout at the extreme top or bottom of the cylinder and is characterized by catastrophic material failure before any buckling occurs. The linear eigenvalue is well above the FL point, while the FPFF occurs at a much lower level due to the stress concentration around the

cutout. The nonlinear responses demonstrate the dominance of the progressive material failure around the hole, with the failure indicators quickly reaching high levels after initiation. This mode is thus dominated by material failure as opposed to the buckling of Mode I. The design study results indicate that the smaller hole size (0.1R) has little effect on the failure of the cylinder except when it is located at the bottom locations. For the medium and large hole sizes, the configurations with the cutout near the top also exhibit mode III failure due to the stress concentrations around the hole, though this time the region is under high tension instead of compression.

The cutouts within the top half of the cylinder ($\beta < 75^\circ$) do not have an effect on the type of the buckled mode, which remains in the usual global mode, but that the eigenvalues decrease from the non-cutout case load level depending on the size of the cutout. This is due to the fact that the cutouts generally decrease the overall bending stiffness of the shell, thereby producing higher stresses at the compressive region for an equivalent applied bending moment. As the cutout location moves to the side of the shell, the cutout's effect on the bending stiffness is reduced and the critical loads converge back to the non-cutout value. The main exception is for the largest hole size at 90°, where the eigenvalue has dropped considerably as the mode switches to the local one.

During nonlinear analysis of a cylindrical shell under bending moment, while including imperfection, although the first buckling eigenvalue seems critical, the imperfection coming from the remaining distinct mode shapes also becomes very important to predict the failure load. For a cylindrical shell under bending moment the critical failure location is either at compression side of the cylinder or at the cutout edge and the distinct modes at those two locations becomes dominant during the nonlinear analysis and it cannot be decided which one is going to be dominating the failure load. Therefore, during the introduction of geometrical imperfections coming from buckling mode shapes it is vital to include initial distinct mode shapes.

During all the analyses, the only position that always has Mode I failure was at $\pm 75^\circ$ location and has the highest failure load level during both linear and nonlinear progressive failure analysis for all cutout sizes. This result indicates the ability of cylindrical shells to possess cutouts at certain locations without any great effect on the overall failure mode.

While applying combined loading, under shear force there is no benefit of steered fiber to the failure load, on the contrary there is a slight decrease in the failure load level, since the cylinders were optimized for pure bending load case only. In addition, the results under combined loading show that failures under shear stress generally cause the cylinder buckle locally which is expected. Therefore, for the design of the cylinders all possible load combinations for the given mission must be considered during design process and re-optimization of the cylinder in addition to increasing the stiffness around the cutout might be a good solution to increase the failure load.

After the completion of the numerical analyses of the shells, the results were validated with sufficient tests. The objective of the test was to evaluate the accuracy of the finite element prediction for the behavior of a constant-stiffness and a variable-stiffness CFRP composite cylinders under bending.

The test fixture was specially designed for circular cylinders with a radius of 304.5 mm (12 in) and length of 813 mm (32 in) and the cylinders under consideration have the same geometries. The bending tests were performed for the 0.3R/120 cutout configuration in TU Delft. Although, the end conditions for testing are designed to be fixed boundary conditions, in real case there exist some flexibility between joints of the fixture. Therefore, it is important to adjust the boundary conditions of the cylinder in the finite element analysis to be similar to the boundary conditions of the test.

To select a proper cutout configuration for testing, the two major considerations were the mode of failure that is desired to be observed and the limit of the testing fixture. Both CS ans VS configurations exhibit Mode II failure there with quite similar behavior and therefore provide an interesting comparison during the testing phase. The tests showed that stiffness variations did not have much effect with the presence of the cutouts, since the cutout locations reduced the stiffness of the VS cylinder.

Another important factor was the machining of the cutouts into the shells. After the machining of the cutouts, inspection of the cut-out region for CS cylinder revealed that no visual defects or fibre delamination were observed. On the other hand, cut-out regions for VS cylinder contain visible defects in the form of pull-out fibres on the outer layer. This was due to the fact that higher diameter of the milling drill bit was needed since the steel rings of the steered cylinder did not allow to use fine bit as with

the CS cylinder. Therefore it is very crucial to design test fixture and to decide how to machine the composite cylinders.

The installation of the shells in to the fixture is a very crucial step in order to satisfy the symmetry of the specimens. The tabs and cylinder surface must be sanded such that the cylinder ends are perpendicular to the axis of revolution. Two aluminum plates were used to ensure that the surfaces on which the rings are mounted are exactly parallel and at a specified distances.

Since the shells are very sensitive to the imperfections, it is very crucial to measure real imperfection in order to perform a precise numerical analysis. Those imperfections may result from the non-perfect manufacturing process or due to its being a thin shell and therefore to be subjected to easy deformation. It was realized that theoretical imperfections also give very close results compare to the real measured imperfections. Therefore, if the manufacturing quality is sufficient enough, one can use theoretical imperfections conveniently.

During the tests as it was expected from numerical analyses, the failures started from the cutout lower edge and propagate towards the bottom of the cylinder. The failure results show that there is a very close prediction of the failure load. In addition, the strain results obtained from the tests show a very good correlation of the FEM and the testing. The slight difference between the tests and FEM results may occur due to the location of the strain gauge to be slightly different from the location of the numerical model. The left and right cutout strain results shows very similar behavior and those results were also validated with the DIC measurements. For the points in axial locations the strain gauges first undergo compression and then these compression starts to release, which might be an indication of the global buckling starting point.

It can be inferred from the study that, there is a very important effect of cutouts on the collapse load of the cylindrical shells. Since the applied load type was bending, the failure was mostly due to global or local buckling of the cylinder. During local buckling, contrary to global buckling, cylinder was able to carry load further with the strength of fibers located at the top and bottom of the cylinder. However, if you keep increase the cutout size the collapse load will start to decrease.

The results of this study showed that in Mode I failure, we can achieve the highest failure load level, however, it can only be obtained with small size cutouts. When the cutout size is increased, generally the failure mode turns to either Mode II or Mode III depending on the location of the cutout. Therefore, in the design of cylindrical aerospace structures, the window or door cutout size and locations should be adjusted so that the buckling will tend to start from cutout edge to increase the post buckling strength. In addition, it will better to include realistic service combined loading cases with variable size and location of cutouts for the future studies.

10.1 Practical Application of This Study

The results of this study showed that during the design of an airframe structure, if there exist some cutouts, in order to maximize the post buckling strength it is better to have Mode II failure. In Mode II failure, the crack will initiate as a result of buckling around the cutouts by increasing the ultimate failure load compare to global buckling.

In addition to that, cutout size and location is also an important factor in the design of cylindrical structures. One can have larger cutouts in the cylinder if they are oriented in a specific location above the natural axis of cylinder under pure bending without reducing the failure load. The model developed for the cylindrical composite shell were validated by tests and has a very good correlation with the test results. That model can be further developed and used for future applications.

The results of this study can be utilized in the design of new generation aerospace structures with steered fibers and cutouts.

REFERENCES

[1] **Freissinet, S.**, (2011). Worries about new composite made airplane, http://www.1001crash.com/index-page-composite-lg-2.html.

[2] **www.boeing.com**, (2016). Boeing 787, http://www.boeing.com/commercial/787/by-design/{\#}/advanced-composite-use/carbon-laminate.

[3] **Blom, A.W.** (2010). Structural performance of fiber-placed, variable-stiffness composite conical and cylindrical shells, *Ph.D. thesis*.

[4] **B. F.Tatting and Z. Guerdal** (2002). Design and Manufacture of Elastically Tailored Tow Placed Plates, *Nasa Arch.*, (August), http://citeseerx.ist.psu.edu/viewdoc/download?doi=10.1.1.443.7384{\&}rep=rep1{\&}type=pdf{\%}5Cnhttp://www.adoptech.com.

[5] **Gürdal, Z. and Tatting, B.F.** (2005). Tow-Placement Technology and Fabrication Issues for Laminated Composite Structures, *Aerospace*, (April), 23681–23681.

[6] **Gürdal, Z. and Olmedo, R.** (1993). In-Plane Response of Laminates with Spatially Varying Fiber Orientations: Variable Stiffness Concept, *AIAA J.*, *Vol. 31,*(4), 751–758.

[7] **Blom, A.W.**, **Stickler, P.B. and Gürdal, Z.** (2010). Optimization of a composite cylinder under bending by tailoring stiffness properties in circumferential direction, *Compos. Part B Eng.*, *41*(2), 157–165, http://dx.doi.org/10.1016/j.compositesb.2009.10.004.

[8] **Tatting, B.F. and Gürdal, Z.** (2003). Automated Finite Element Analysis of Elastically-Tailored Plates, *Nasa/Cr-2003-212679*.

[9] **AUTODESK**, AUTODESK Helius PFA User's Guide for Abaqus, https://knowledge.autodesk.com/support/helius-pfa/learn-explore/caas/CloudHelp/cloudhelp/2016/ENU/ACMPAN/files/GUID-05546EDB-D1D1-4D0F-B5D6-4C1B9FCB281C-htm.html.

[10] **Dassault Systèmes**, (2015). Abaqus analysis user's guide, Abaqus 2016.

[11] **Blom, A.W.**, **Rassaian, M.**, **Stickler, P.B. and Gürdal, Z.** (2010). Bending test of a variable-stiffness fiber-reinforced composite cylinder, *Collect. Tech. Pap. - AIAA/ASME/ASCE/AHS/ASC Struct. Struct. Dyn. Mater. Conf.*, (April),

12–15, http://www.scopus.com/inward/record.url?eid=2-s2.0-84855624102{\&}partnerID=tZOtx3y1.

[12] **Johnson, T.**, (2013). How composite materials make the most advanced airplane ever., http://composite.about.com/od/applications/a/What-Is-The-787-Dreamliner.htm.

[13] **www.airbus.com**, (2017). Tailored Materials, http://www.airbus.com/aircraftfamilies/passengeraircraft/a350xwbfamily/technology-and-innovation/.

[14] **Jaunky, N.**, **Ambur, D.R.**, **Davila, C.G. and Hilburger, M.** (2001). Progressive Failure Studies of Composite Panels with and without Cutouts, *NASA/CR-2001-211223 Rep.*

[15] **Lopes, C.S.**, **Camanho, P.P.**, **Gürdal, Z. and Tatting, B.F.** (2007). Progressive failure analysis of tow-placed, variable-stiffness composite panels, *Int. J. Solids Struct.*, *44*(25-26), 8493–8516.

[16] **Khani, A.**, **Ijsselmuiden, S.T.**, **Abdalla, M.M. and Gürdal, Z.** (2011). Design of variable stiffness panels for maximum strength using lamination parameters, *Compos. Part B Eng.*, *42*(3), 546–552, http://www.sciencedirect.com/science/article/pii/S1359836810002131.

[17] **Khani, A.**, **Abdalla, M.M. and Gürdal, Z.** (2012). Circumferential stiffness tailoring of general cross section cylinders for maximum buckling load with strength constraints, *Compos. Struct.*, *94*(9), 2851–2860, http://dx.doi.org/10.1016/j.compstruct.2012.04.018.

[18] **Ismail, M.**, **Baharudin, B.T.H.T.**, **Yahya, S.A. and Kahar, H.A.** (2013). Finite Element Analysis of Composite Cylinder with Centre Cutout under Axial Load and Internal Pressure, *Adv. Mater. Res.*, *701*(October), 425–429, http://www.scientific.net/AMR.701.425.

[19] **Shi, S.**, **Sun, Z.**, **Ren, M.**, **Chen, H. and Hu, X.** (2013). Buckling response of advanced grid stiffened carbon-fiber composite cylindrical shells with reinforced cutouts, *Compos. Part B Eng.*, *44*(1), 26–33, http://linkinghub.elsevier.com/retrieve/pii/S1359836812004982.

[20] **Tatting, B.F.**, **Setoodeh, S. and Gürdal, Z.** (2005). Enhancements of Tow-Steering Design Techniques: Design of Rectangular Panel Under Combined Loads, *Nasa/Cr-2005-000000*.

[21] **Kim, B.C.**, **Weaver, P.M. and Potter, K.** (2015). Computer aided modelling of variable angle tow composites manufactured by continuous tow shearing, *Compos. Struct.*, *129*, 256–267, http://dx.doi.org/10.1016/j.compstruct.2015.04.012.

[22] **Soremekun, G.**, **Gürdal, Z.**, **Kassapoglou, C. and Toni, D.** (2002). Stacking sequence blending of multiple composite laminates

using genetic algorithms, *Compos. Struct.*, *56*(1), 53–62, http://www.sciencedirect.com/science/article/pii/S0263822301001854.

[23] **IJsselmuiden, S.T.**, **Abdalla, M.M.**, **Seresta, O. and Gürdal, Z.** (2009). Multi-step blended stacking sequence design of panel assemblies with buckling constraints, *Compos. Part B Eng.*, *40*(4), 329–336, http://dx.doi.org/10.1016/j.compositesb.2008.12.002.

[24] **Blom, A.W.**, **Setoodeh, S.**, **Hol, J.M.A.M. and Gürdal, Z.** (2008). Design of variable-stiffness conical shells for maximum fundamental eigenfrequency, *Comput. Struct.*, *86*(9), 870–878.

[25] **Blom, A.W.**, **Tatting, B.F.**, **Hol, J.M.A.M. and Gürdal, Z.** (2009). Fiber path definitions for elastically tailored conical shells, *Compos. Part B Eng.*, *40*(1), 77–84, http://dx.doi.org/10.1016/j.compositesb.2008.03.011.

[26] **Blom, a.W.**, **Lopes, C.S.**, **Kromwijk, P.J.**, **Gurdal, Z. and Camanho, P.** (2009). A Theoretical Model to Study the Influence of Tow-drop Areas on the Stiffness and Strength of Variable-stiffness Laminates, *J. Compos. Mater.*, *43*(5), 403–425.

[27] **Blom, A.W.**, **Abdalla, M.M. and Gürdal, Z.** (2010). Optimization of course locations in fiber-placed panels for general fiber angle distributions, *Compos. Sci. Technol.*, *70*(4), 564–570, http://dx.doi.org/10.1016/j.compscitech.2009.12.003.

[28] **Marouene, A.**, **Boukhili, R.**, **Chen, J. and Yousefpour, A.** (2016). Buckling behavior of variable-stiffness composite laminates manufactured by the tow-drop method, *Compos. Struct.*, *139*, 243–253, http://dx.doi.org/10.1016/j.compstruct.2015.12.025.

[29] **White, S.C.**, **Weaver, P.M. and Wu, K.C.** (2014). Post-buckling analyses of variable-stiffness composite cylinders in axial compression, *Compos. Struct.*, (December), http://dx.doi.org/10.1016/j.compstruct.2014.12.013.

[30] **Senocak, E. and Waas, A.M.** (1996). Optimally reinforced cutouts in laminated circular cylindrical shells, *Int. J. Mech. Sci.*, *38*(2), 121–140.

[31] **Van Tooren, M.J.L.**, **Van Stijn, I.P.M. and Beukers, A.** (2002). Curvature effects on the stress distribution in sandwich cylinders with a circular cut-out, *Compos. Part A Appl. Sci. Manuf.*, *33*(11), 1557–1572.

[32] **Makeev, A.**, **Seon, G. and Lee, E.** (2010). Failure Predictions for Carbon/Epoxy Tape Laminates with Wavy Plies, *J. Compos. Mater.*, *44*(1), 95–112, http://jcm.sagepub.com/cgi/doi/10.1177/0021998309345352.

[33] **Chen, J.F.**, **Morozov, E.V. and Shankar, K.** (2014). Simulating progressive failure of composite laminates including in-ply and delamination damage effects,

Compos. Part A Appl. Sci. Manuf., *61*, 185–200, http://dx.doi.org/10.1016/j.compositesa.2014.02.013.

[34] **Angélico, R.A.**, **Ribeiro, M.L.**, **Tita, V.**, **Engenharia, E.D.**, **Carlos, D.S.**, **São, U.D.**, **São-carlense, A.T.**, **Schmidt, P.A. and Sp, C.** (2010). Investigation of the Composite Progressive Failure Model Parameters, *11th Pan-American Congr. Appl. Mech.*, volume 66, pp.0–5.

[35] **Lapczyk, I. and Hurtado, J.A.** (2007). Progressive damage modeling in fiber-reinforced materials, *Compos. Part A Appl. Sci. Manuf.*, *38*(11), 2333–2341.

[36] **Oterkus, E.**, **Erdogan, M. and Nemeth, M.P.** (2007). Stress Analysis of Composite Cylindrical Shells With an Elliptical Cutout, *J. Mech. Mater. Struct.*, *2*(April), 695–727.

[37] **Poore, A.L.**, **Barut, A. and Madenci, E.** (2008). Free vibration of laminated cylindrical shells with a circular cutout, *J. Sound Vib.*, *312*(1-2), 55–73, http://linkinghub.elsevier.com/retrieve/pii/S0022460X07008292.

[38] **Camanho, P.P.**, **Tow-placement, A. and Panels, V.s.** (2009). Variable-Stiffness Composite Panels : Effects of Stiffness Variation on the Buckling and Failure, *Technology*, (September), 7–11.

[39] **Ambur, D.**, **Jaunky, N. and Davila, C.** (2004). Progressive Failure of Composite Laminates Using LaRC02 Criteria, *45th AIAA/ASME/ASCE/AHS/ASC Struct. Struct. Dyn. & Mater. Conf.*, (January), http://arc.aiaa.org/doi/abs/10.2514/6.2004-1595.

[40] **Puck, A.**, **Schu, H.**, **Schürmann, H. and Schu, H.** (2002). Failure Analysis of FRP Lamninates by Means of Physically Based Phenomenological Models.pdf, *Compos. Sci. Technol.*, *62*(7), 1633–1662.

[41] **Davila, C.G.**, **Camanho, P.P. and Rose, C.A.** (2005). Failure Criteria for FRP Laminates, *J. Compos. Mater.*, *39*(4), 323 – 345.

[42] **Davila, C.G.**, **Camanho, P.P. and Rose, C.A.** (2005). Failure Criteria for FRP Laminates, *J. Compos. Mater.*, *39*(4), 323 – 345.

[43] **Hashin, Z.** (1980). Failure Criteria for Unidirectional Fiber Composites, *J. Appl. Mech.*, *47*(2), 329.

[44] **Maimí, P.**, **Camanho, P.P.**, **Mayugo, J.A. and Dávila, C.G.** (2007). A continuum damage model for composite laminates: Part I - Constitutive model, *Mech. Mater.*, *39*(10), 897–908.

[45] **Camanho, P.P.**, **Sanders, W.**, **Davila, C. and Mayugo, J.** (2009). Progressive failure analysis of advanced composites, *Univ. Porto FA8655-06-1-3072 Rep.*, *44*(0704).

[46] **Knight, N.** (2008). Factors Influencing Progressive Failure Analysis Predictions for Laminated Composite Structures, *49th AIAA/ASME/ASCE/AHS/ASC Struct. Struct. Dyn. Mater. Conf.*, 092047, http://arc.aiaa.org/doi/pdf/10.2514/6.2008-2108.

[47] **Cárdenas, D.**, **Elizalde, H.**, **Marzocca, P.**, **Abdi, F.**, **Minnetyan, L. and Probst, O.** (2013). Progressive failure analysis of thin-walled composite structures, *Compos. Struct.*, *95*, 53–62.

[48] **Liu, P.F. and Zheng, J.Y.** (2008). Progressive failure analysis of carbon fiber/epoxy composite laminates using continuum damage mechanics, *Mater. Sci. Eng. A*, *485*(1-2), 711–717.

[49] **Hansen, A.C. and Garnich, M.R.** (1995). A multicontinuum theory for structural analysis of composite material systems, *Compos. Eng.*, *5*(9), 1091–1103.

[50] **Mayes, J.S. and Hansen, A.C.** (2004). Composite laminate failure analysis using multicontinuum theory, *Fail. Criteria Fibre-Reinforced-Polymer Compos.*, *64*, 490–517.

[51] **Mayes, J.S. and Hansen, A.C.** (2004). A comparison of multicontinuum theory based failure simulation with experimental results, *Fail. Criteria Fibre-Reinforced-Polymer Compos.*, *64*, 1026–1044.

[52] **Levi, H.**, **Ishai, O.**, **Altus, E. and Sheinman, I.** (1995). Mechanical performance of thin-walled tubular composite elements under uniaxial loading part 1: Tensile behaviour.", *Compos. Struct.*, *31*(2), 163–170.

[53] **Benamira, M.**, **Hochard, C. and Haiahem, a.** (2011). Behaviour to failure of fibre mat reinforced composite under combined loading conditions, *Compos. Part B Eng.*, *42*(6), 1412–1419, http://linkinghub.elsevier.com/retrieve/pii/S1359836811002356.

[54] **Fam, A.**, **Kim, Y.J. and Son, J.K.** (2010). A numerical investigation into the response of free end tubular composite poles subjected to axial and lateral loads, *Thin-Walled Struct.*, *48*(8), 650–659, http://linkinghub.elsevier.com/retrieve/pii/S0263823110000649.

[55] **a.L. Martins, L.**, **Bastian, F.L. and Netto, T.a.** (2012). Structural and functional failure pressure of filament wound composite tubes, *Mater. Des.*, *36*, 779–787, http://linkinghub.elsevier.com/retrieve/pii/S0261306911007898.

[56] **Autodesk** (2017). Overcoming Challenges in Progressive Failure Analysis of Composite Materials.

[57] **Riks, E.** (1979). An incremental approach to the solution of snapping and buckling problems, *International Journal of Solids and Structures*, *15*(7), 529 – 551, http://www.sciencedirect.com/science/article/pii/0020768379900817.

[58] **Marlett, K.** (2011). Hexcel 8552 IM7 Unidirectional Prepreg 190 gsm & 35%RC Qualification Material Property Data Report, 238.

[59] **Çelebi, M. and Türkmen, H.S.**(2017). Buckling Analysis of CFRP Composite Cylindrical Shell with Cutouts in Bending, *Journal of Aeronautics and Space Technologies*, 1–9.

[60] **Çelebi, M.**, **Zafer, G.**, **Tatting, B.F.**, **Blom, A.W.**, **Rassaian, M. and Wanthal, S.** (2017). Effects of Size and Location of a Circular Cutout on Buckling and Failure of a Cylindrical Shell in Bending, (January), 1–18.

APPENDICES

APPENDIX A : CS Cylinder Linear Buckling Results for Cutout Configurations
APPENDIX B : CS, 0.1R Cutout Analysis Results
APPENDIX C : CS, 0.3R Cutout Analysis Results
APPENDIX D : CS, 0.5R Cutout Analysis Results
APPENDIX E : CS, 0.3R Cutout Detail Analysis Results
APPENDIX F : CS, 0.4R Cutout Detail Analysis Results
APPENDIX G : CS, 0.5R Cutout Detail Analysis Results
APPENDIX H : CS, 0.6R Cutout Detail Analysis Results
APPENDIX I : Centroid Calculation of the Elements
APPENDIX J : VS Cylinder Linear Buckling Results for Cutout Configurations
APPENDIX K : VS, 0.1R Cutout Detailed Analysis Results
APPENDIX L : VS, 0.3R Cutout Detailed Analysis Results
APPENDIX M : VS, 0.5R Cutout Detailed Analysis Results
APPENDIX N : Drawing for Machining of Planned Cutout Configurations

APPENDIX A: CS Cylinder Linear Buckling Results for Cutout Configurations

Table A.1 and A.2 lists the lowest eigenvalue and displays the corresponding mode shape for each cutout configuration in the initial design study.

Table A.1 : Eigenvalue and mode shapes according to cutout positions.

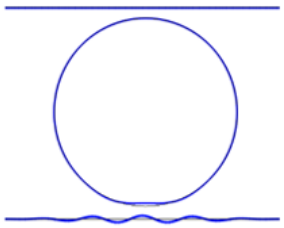
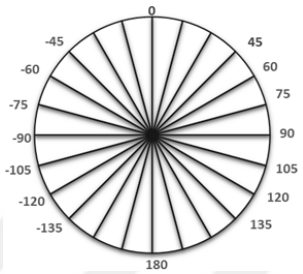
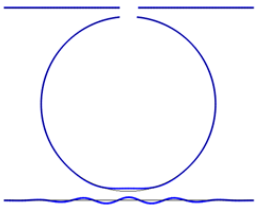
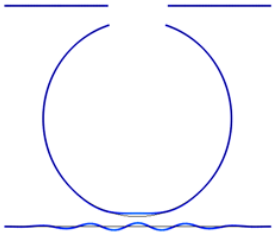
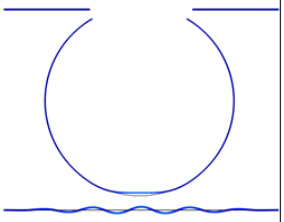
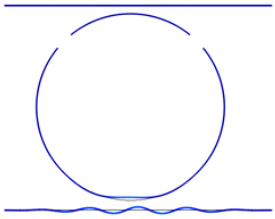
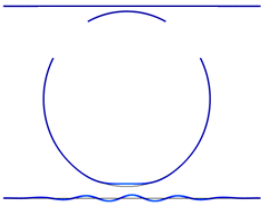
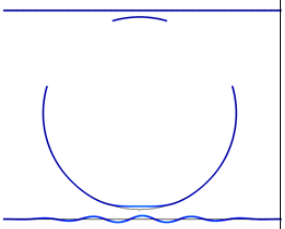
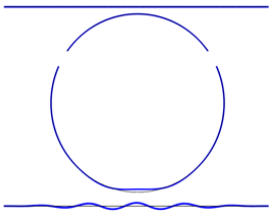
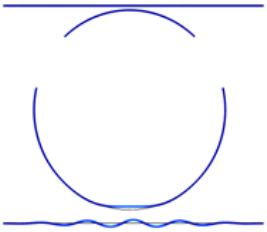
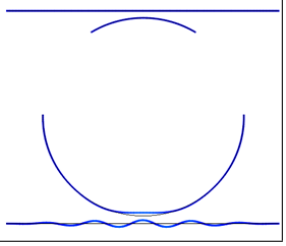
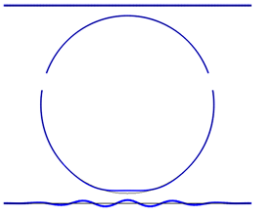
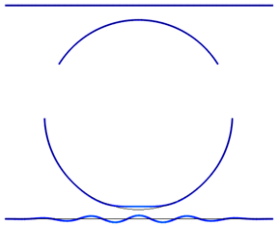
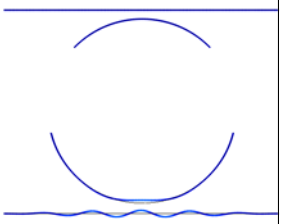
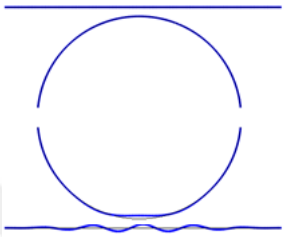
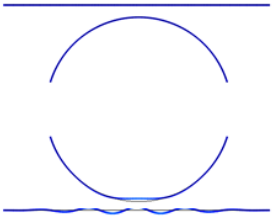
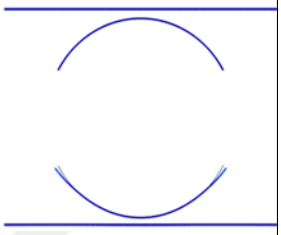
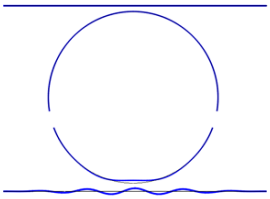
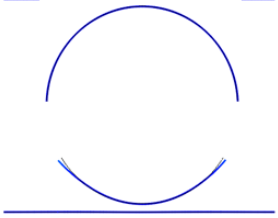
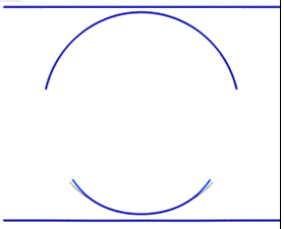
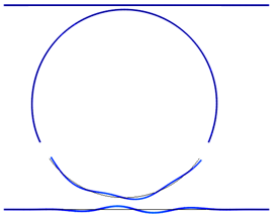
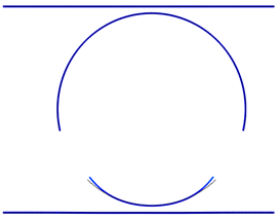
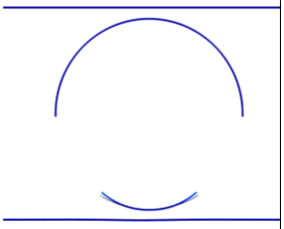
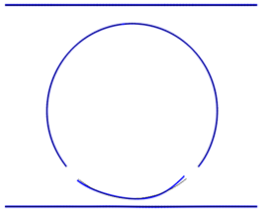
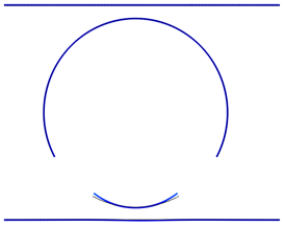
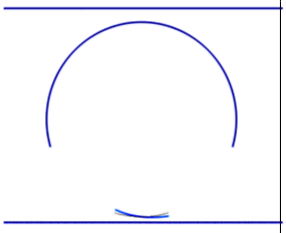
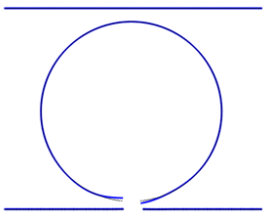
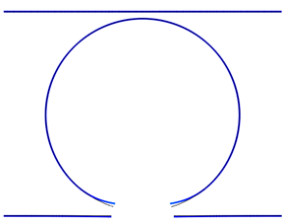
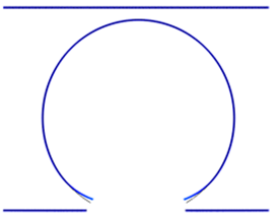
No Cutout	(λ /FL) kNm	693.80/406.71	
			
β	0.1R:λ/FL (kNm)	0.3R:λ/FL (kNm)	0.5R:λ/FL (kNm)
0°	689.72/414.82	647.55/313.39	576.25/279.50
			
±45°	690.98/406.89	662.35/352.36	595.62/264.20
			
±60°	693.78/406.28	692.50/409.56	681.63/346.54
			

Table A.2 : Eigenvalue and mode shapes according to cutout positions (cont.).

β	0.1R:λ/FL (kNm)	0.3R:λ/FL (kNm)	0.5R:λ/FL (kNm)
$\pm 75^\circ$	695.34/406.75	705.18/420.05	709.02/418.22
			
$\pm 90^\circ$	693.79/406.76	691.27/414.00	399.76/391.07
			
$\pm 105^\circ$	690.10/404.89	403.40/312.79	230.52/215.77
			
$\pm 120^\circ$	685.53/411.60	260.90/197.07	146.50/133.53
			
$\pm 135^\circ$	560.64/297.81	189.12/141.78	94.71/84.14
			
180°	458.91/238.55	178.22/133.47	131.61/106.87
			

APPENDIX B: CS, 0.1R Cutout Analysis Results

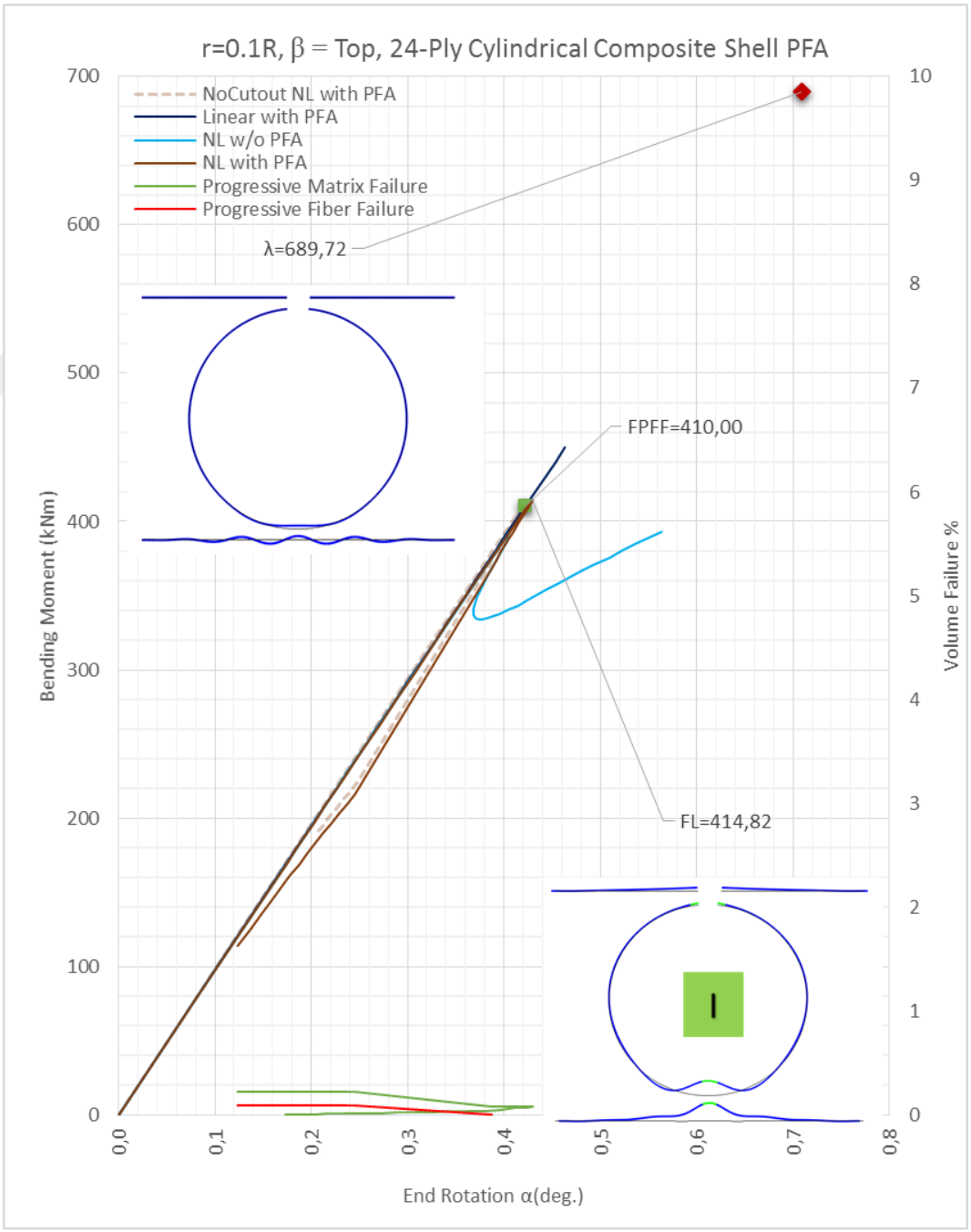


Figure B.1 : 0.1R/0 analysis result.

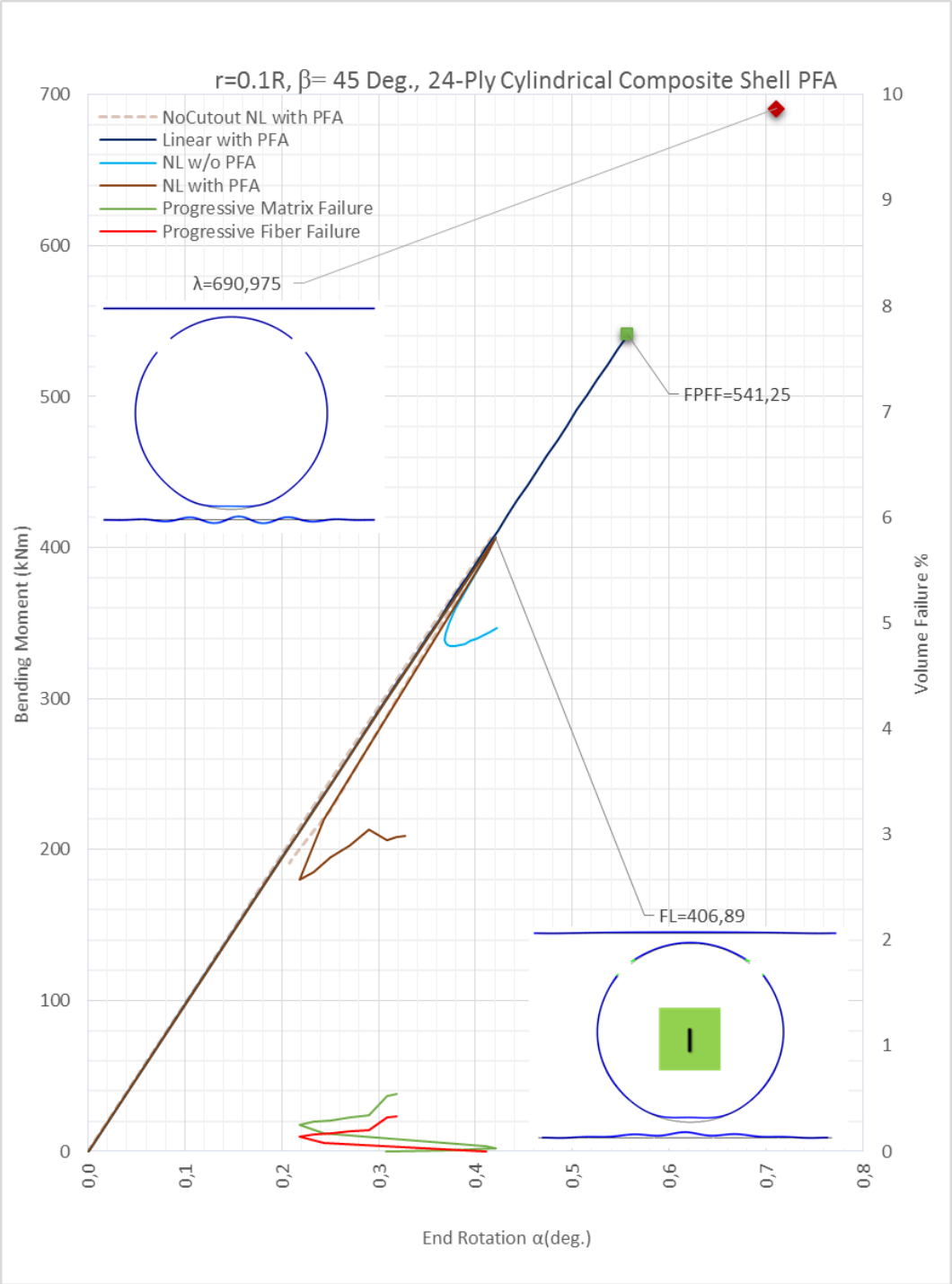


Figure B.2 : 0.1R/45 analysis result.

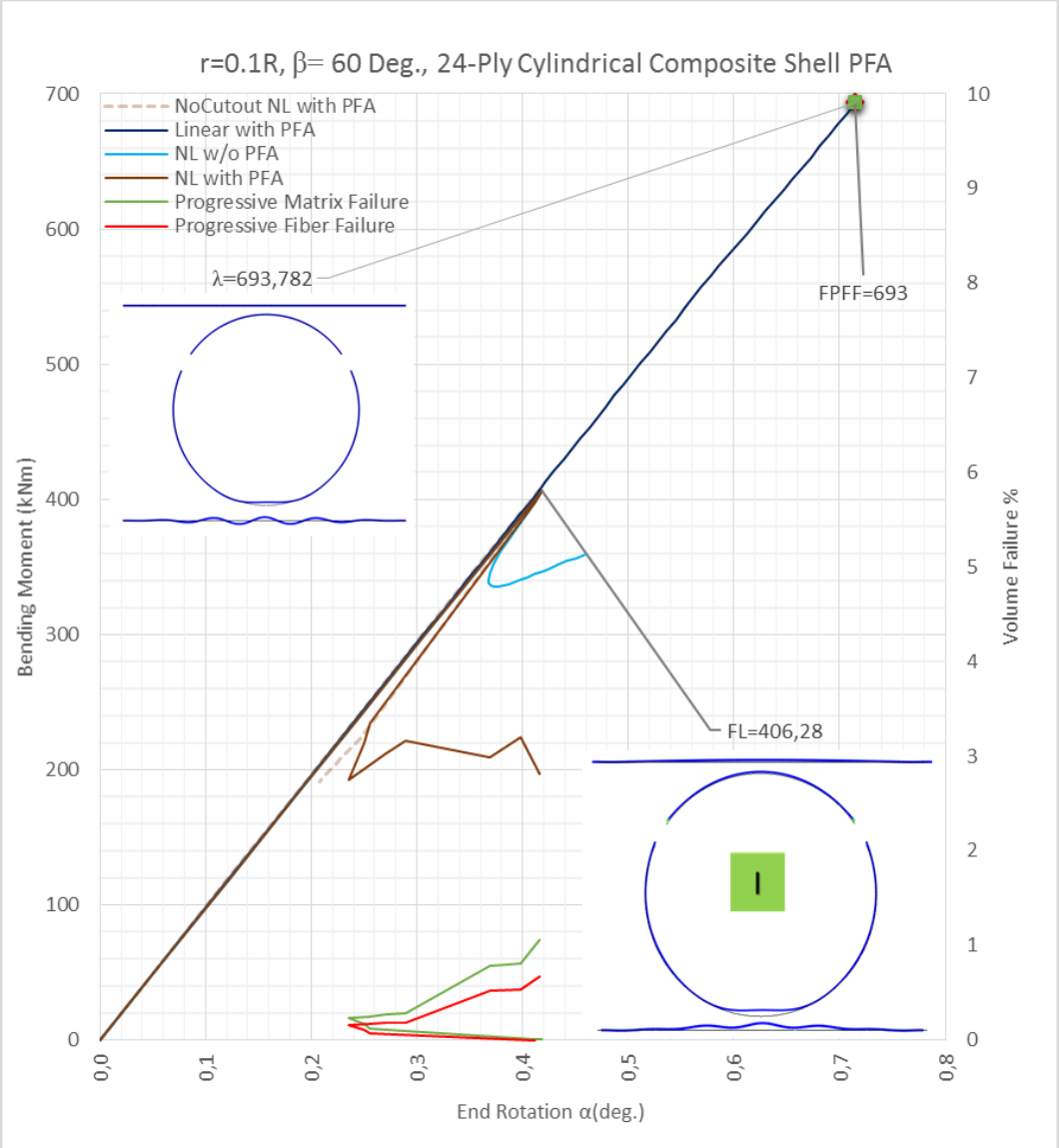


Figure B.3 : 0.1R/60 analysis result.

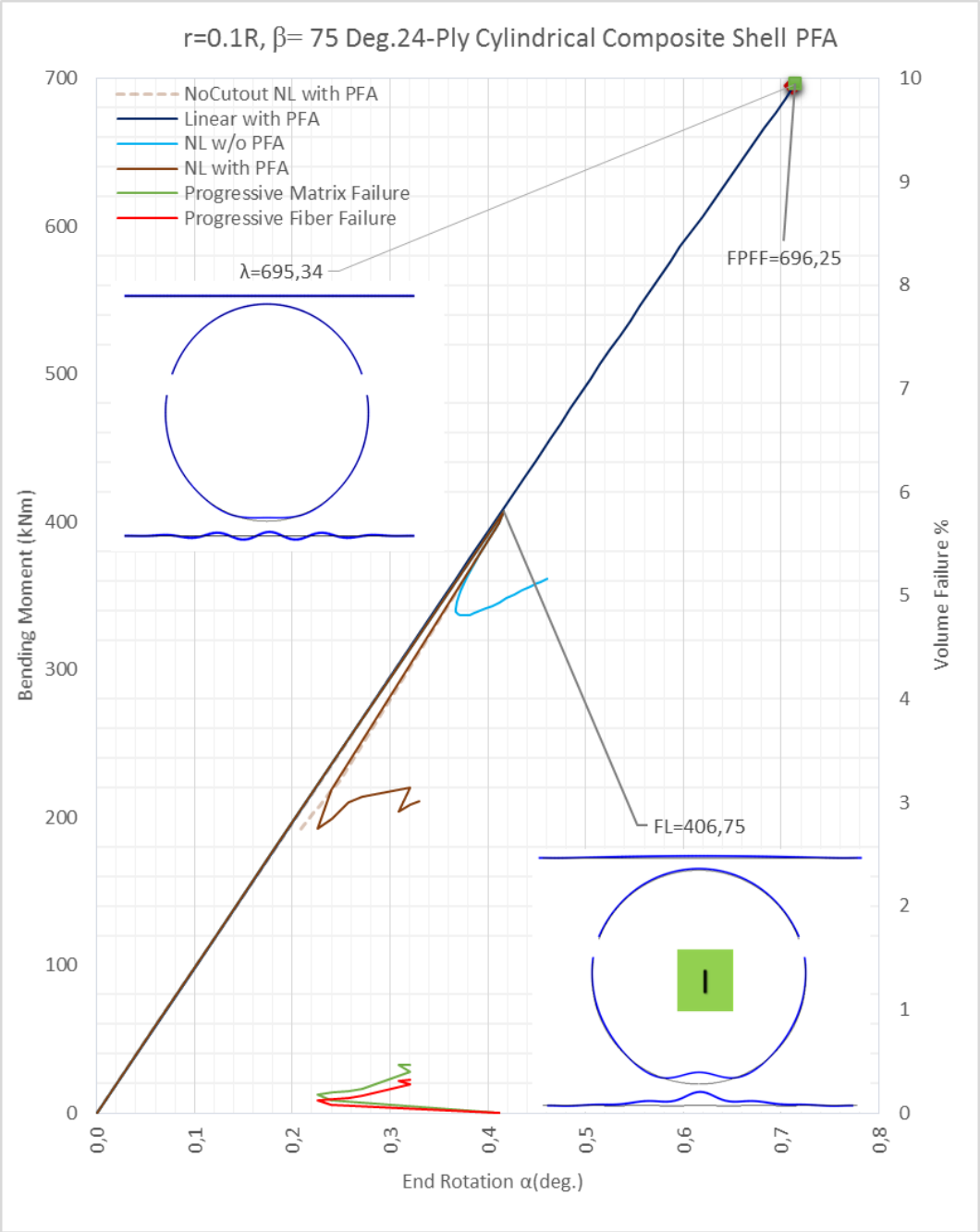


Figure B.4 : 0.1R/75 analysis result.

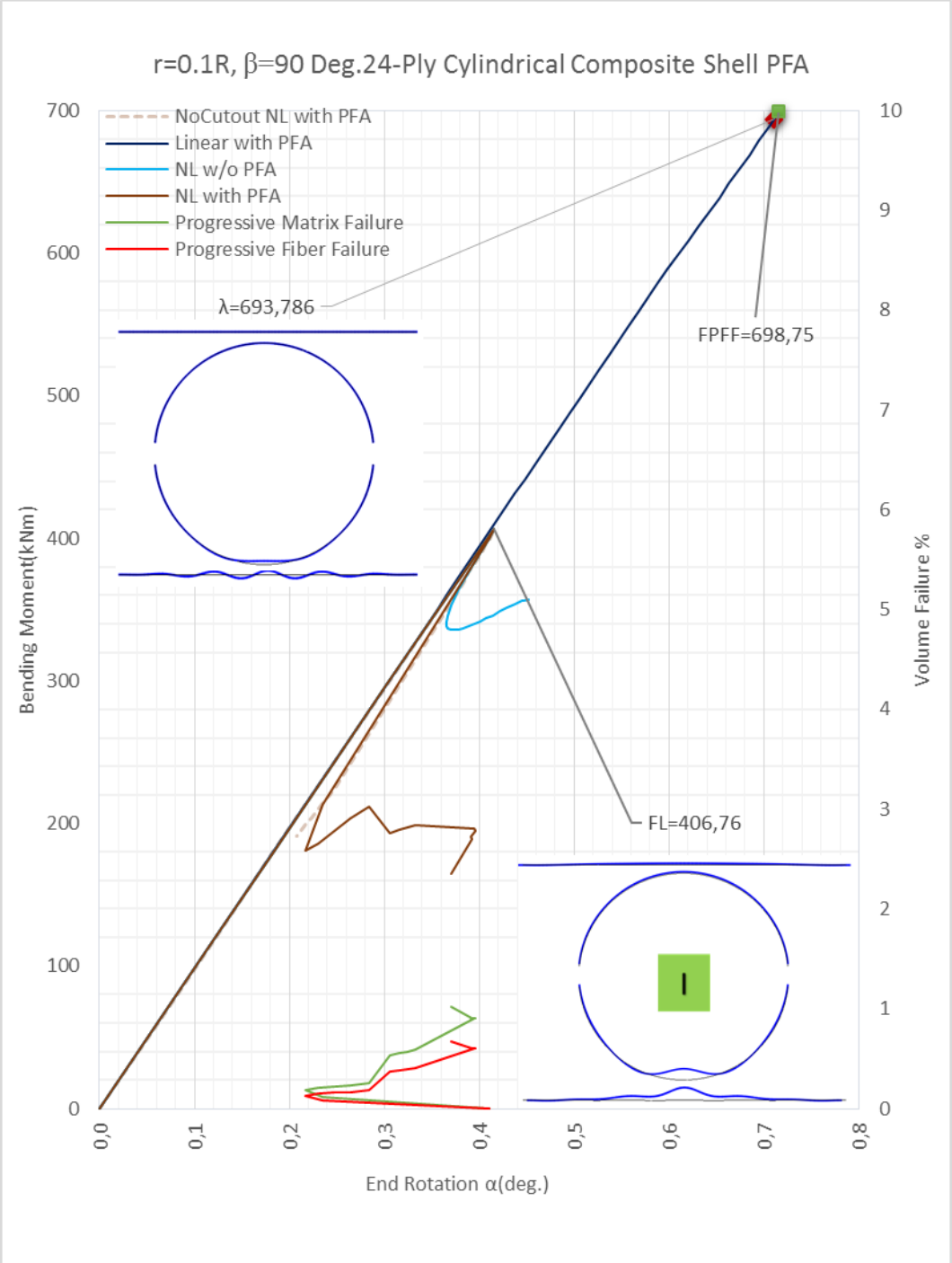


Figure B.5 : 0.1R/90 analysis result.

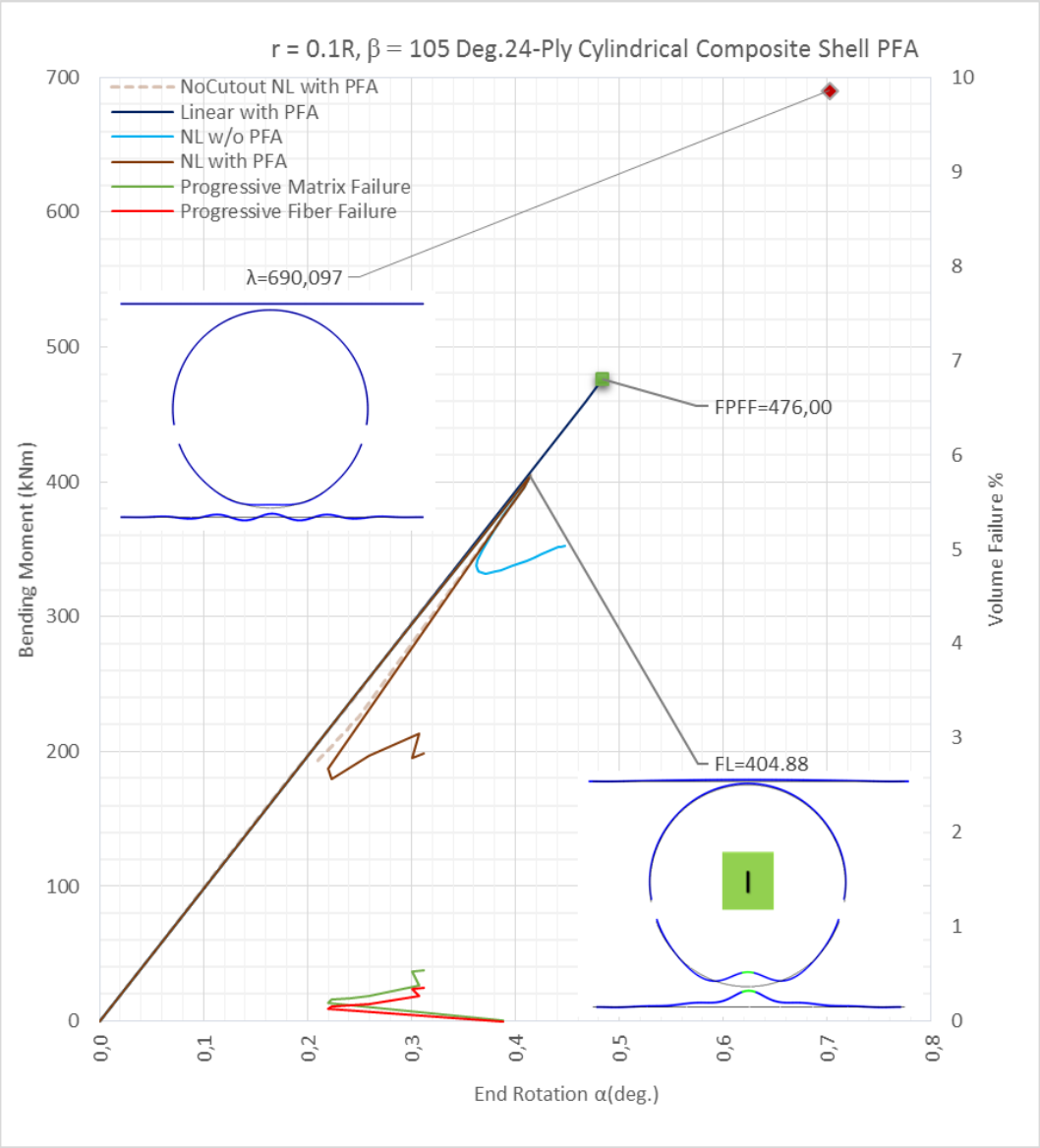


Figure B.6 : 0.1R/105 analysis result.

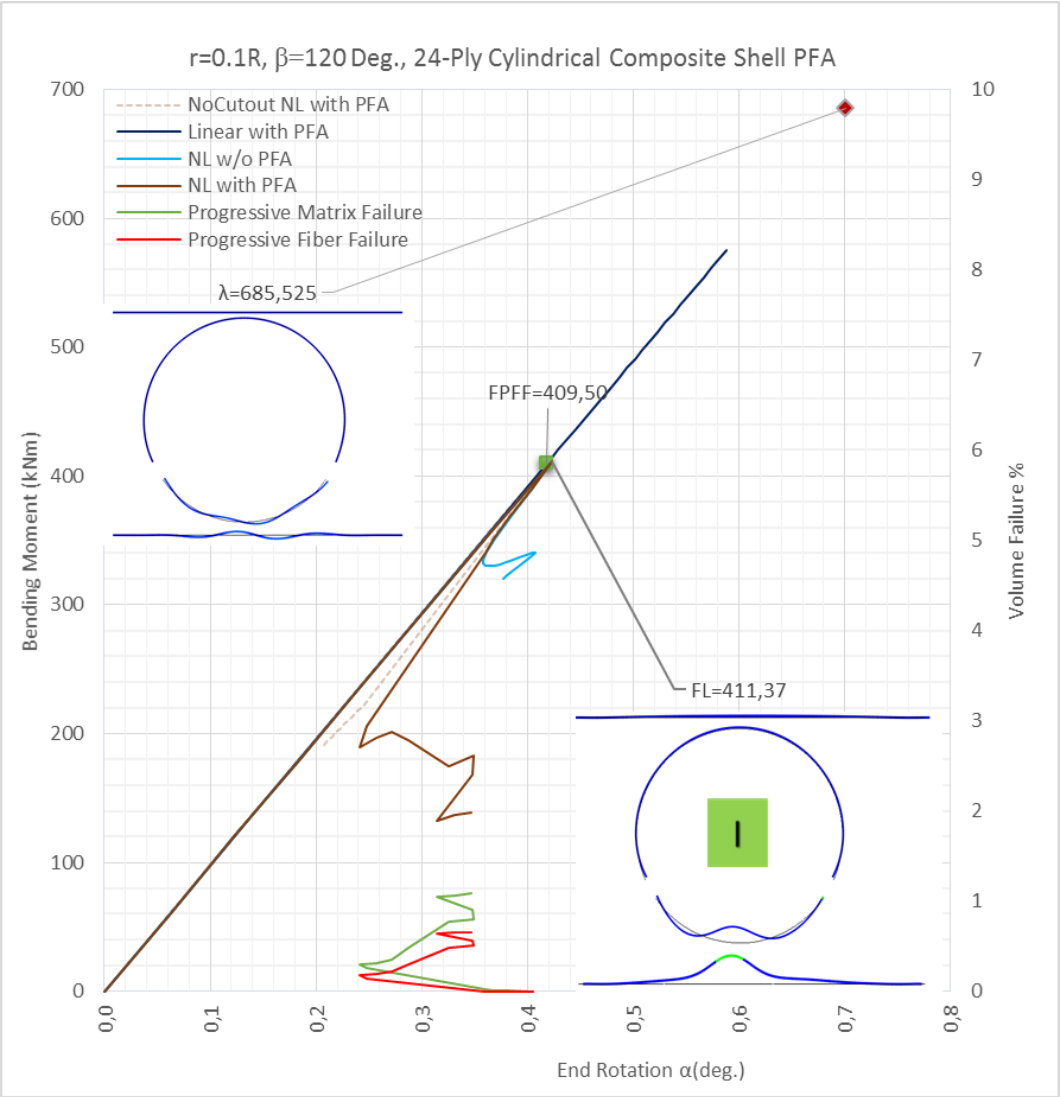


Figure B.7 : 0.1R/120 analysis result.

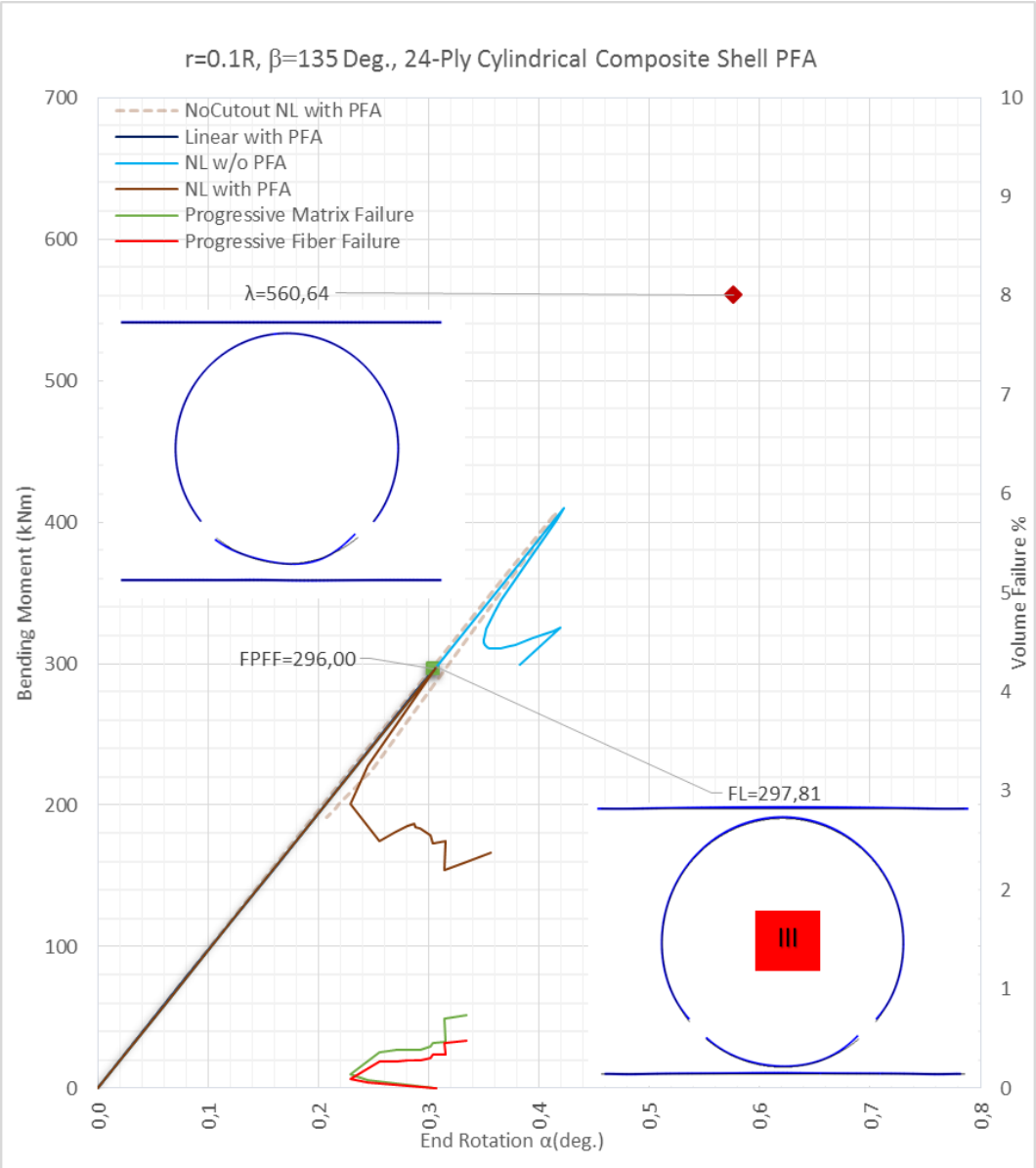


Figure B.8 : 0.1R/135 analysis result.

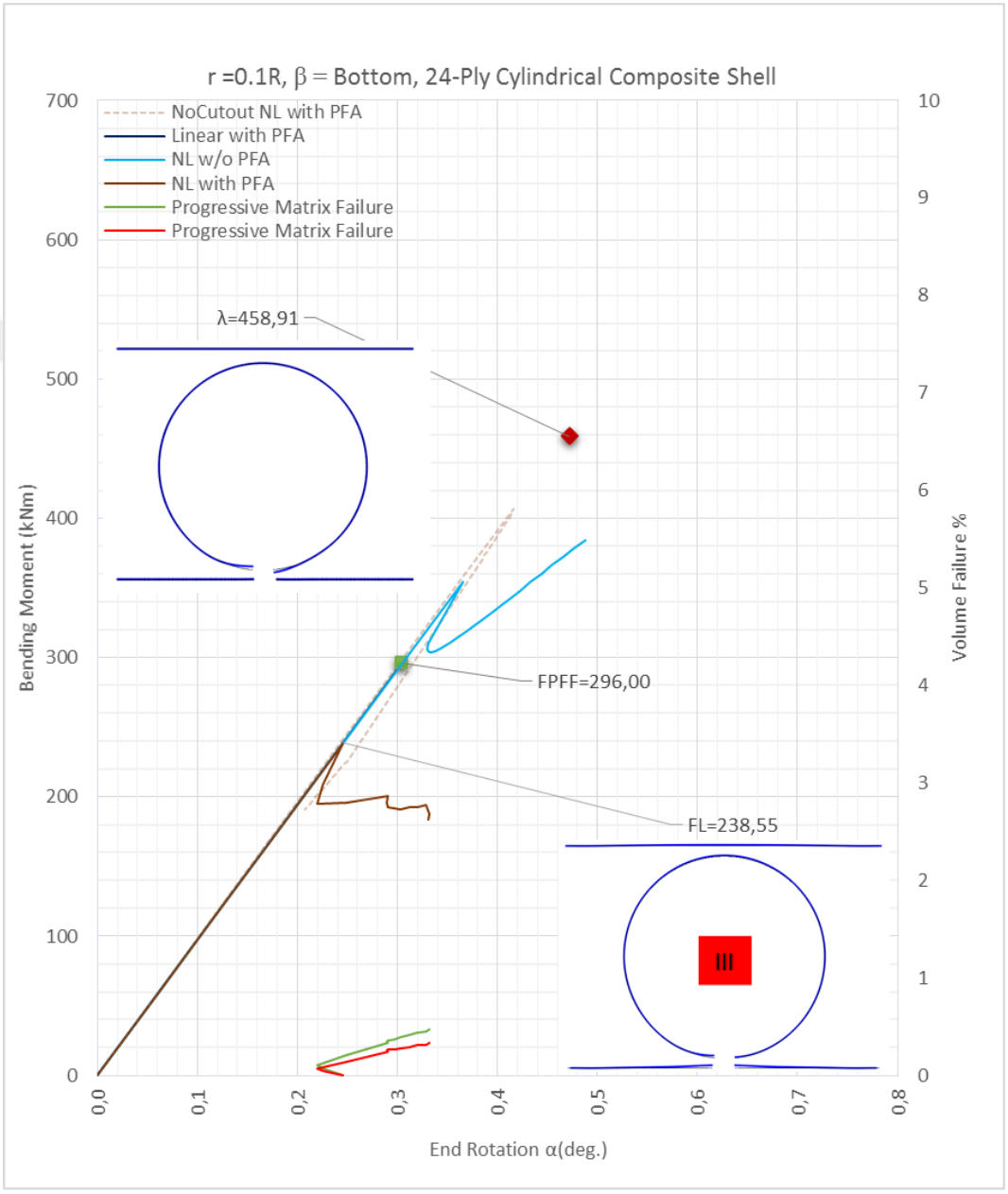


Figure B.9 : 0.1R/180 analysis result.

APPENDIX C: CS, 0.3R Cutout Analysis Results

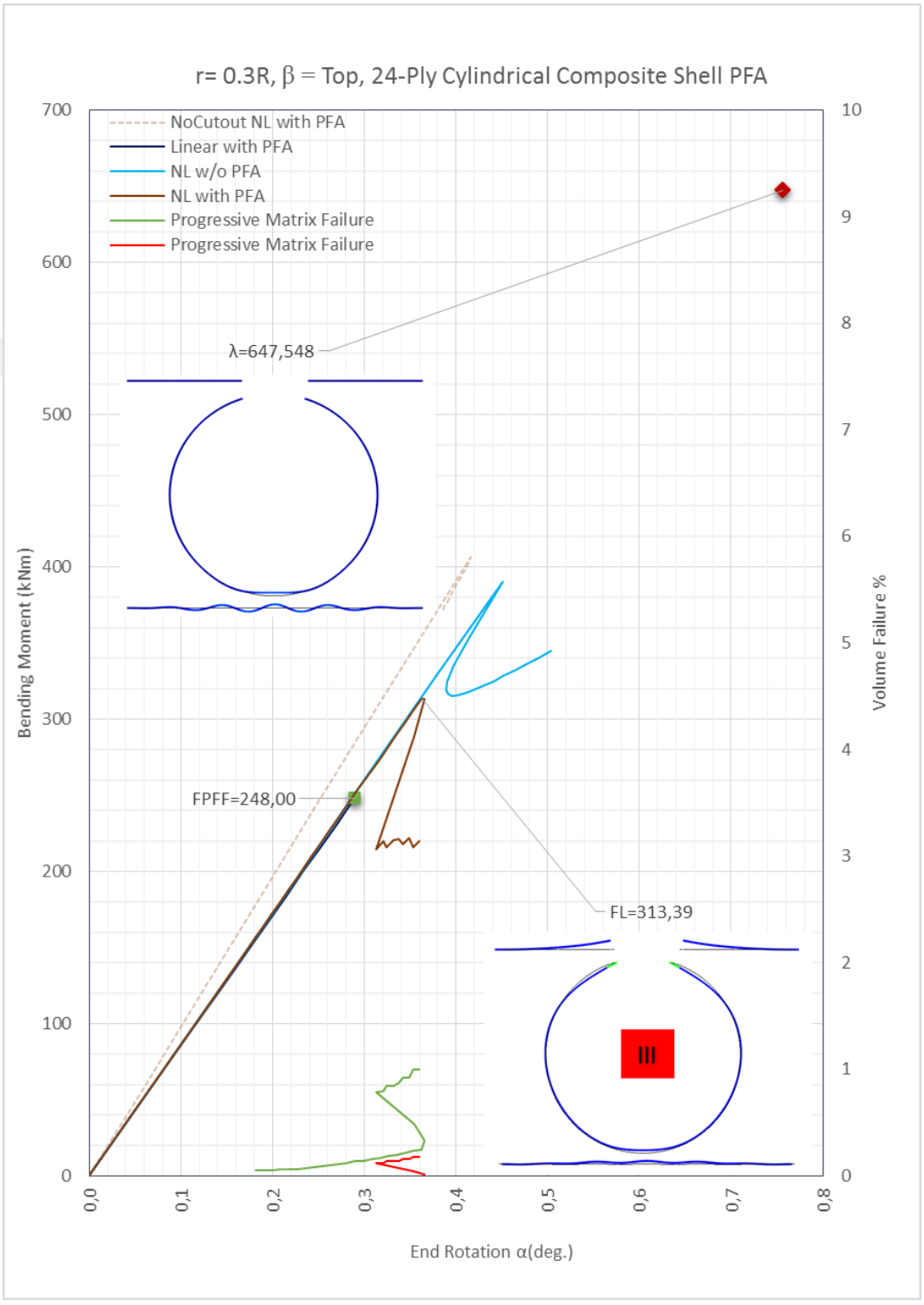


Figure C.1 : 0.3R/0 analysis result.

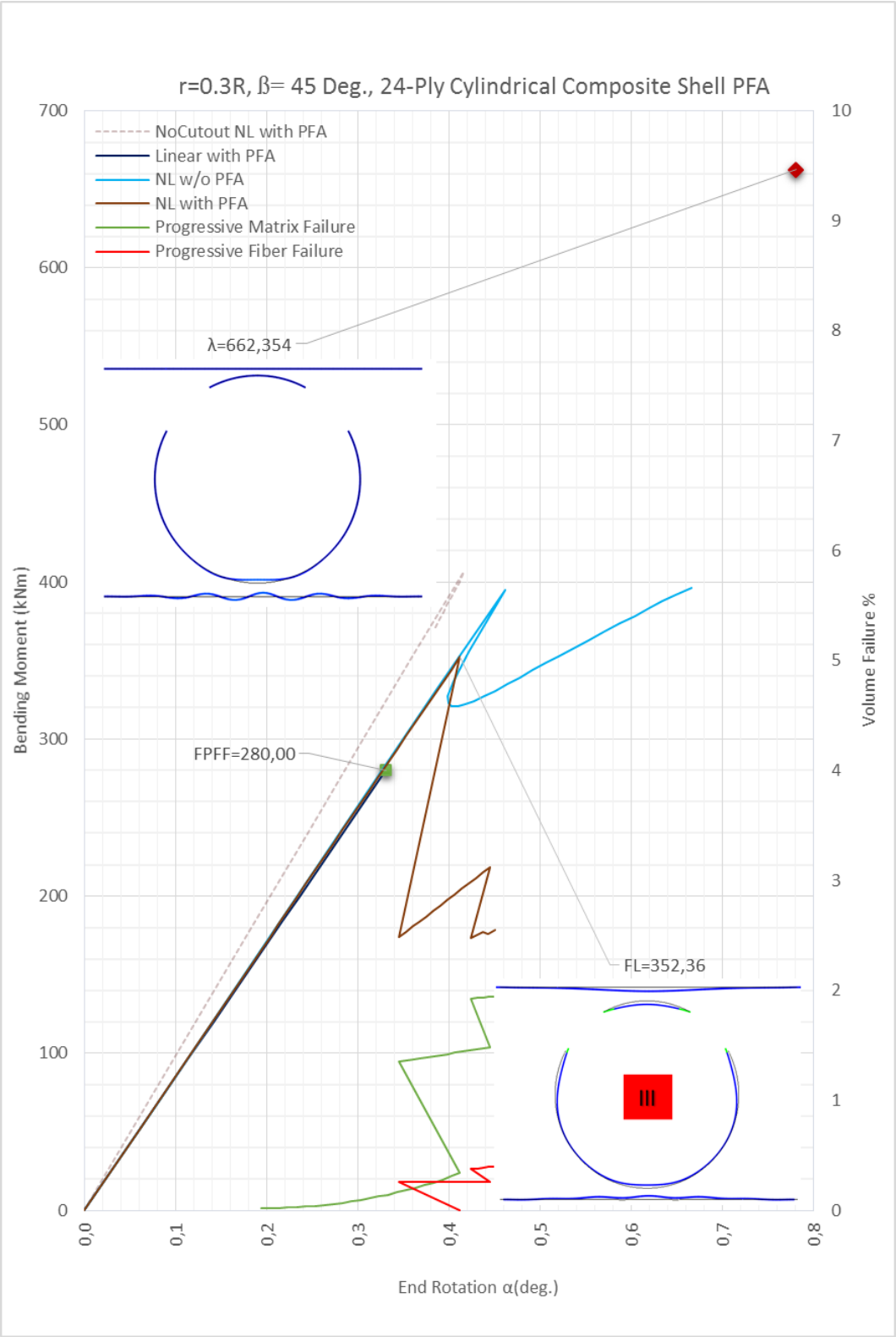


Figure C.2 : 0.3R/45 analysis result.

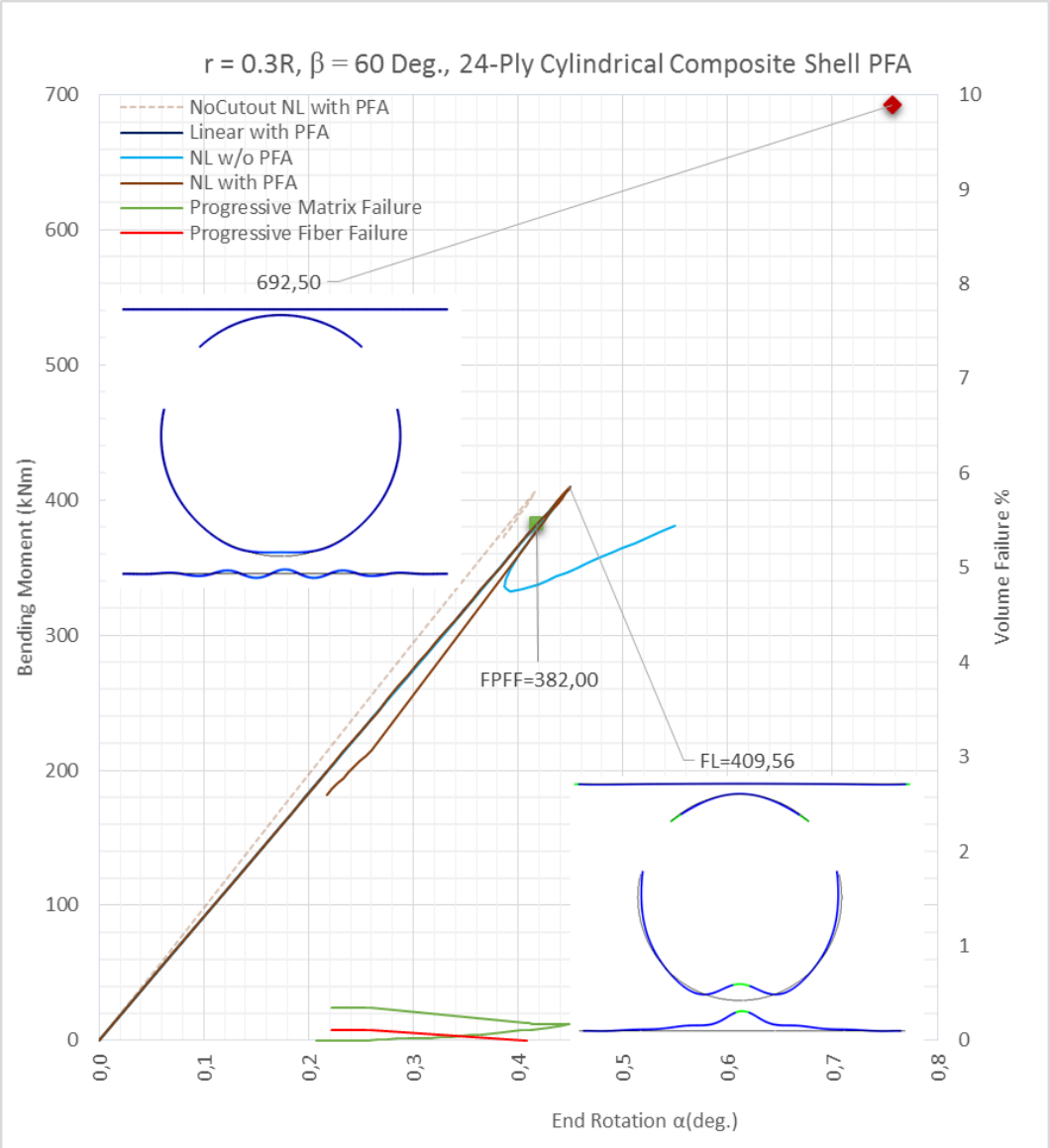


Figure C.3 : 0.3R/60 analysis result.

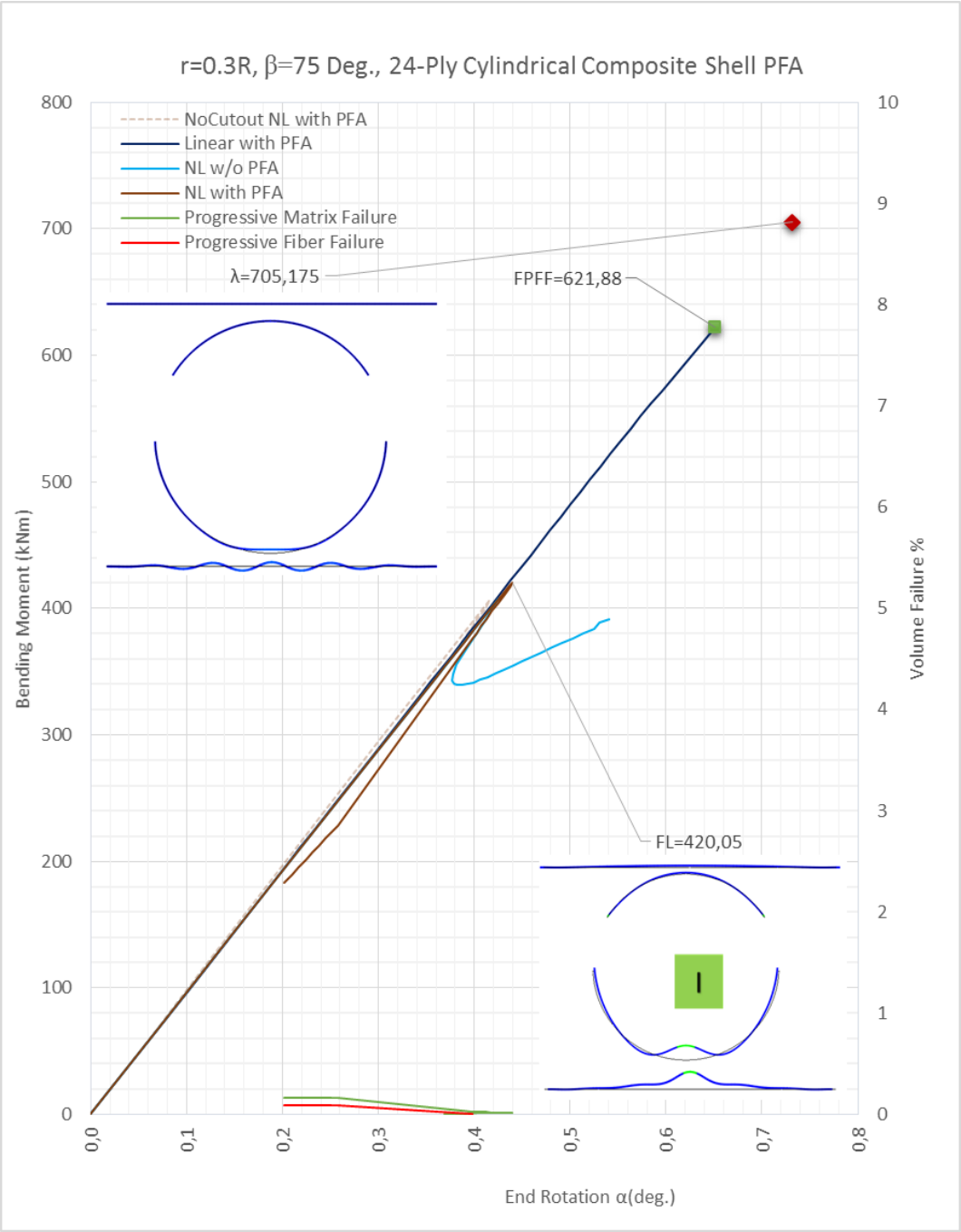


Figure C.4 : 0.3R/75 analysis result.

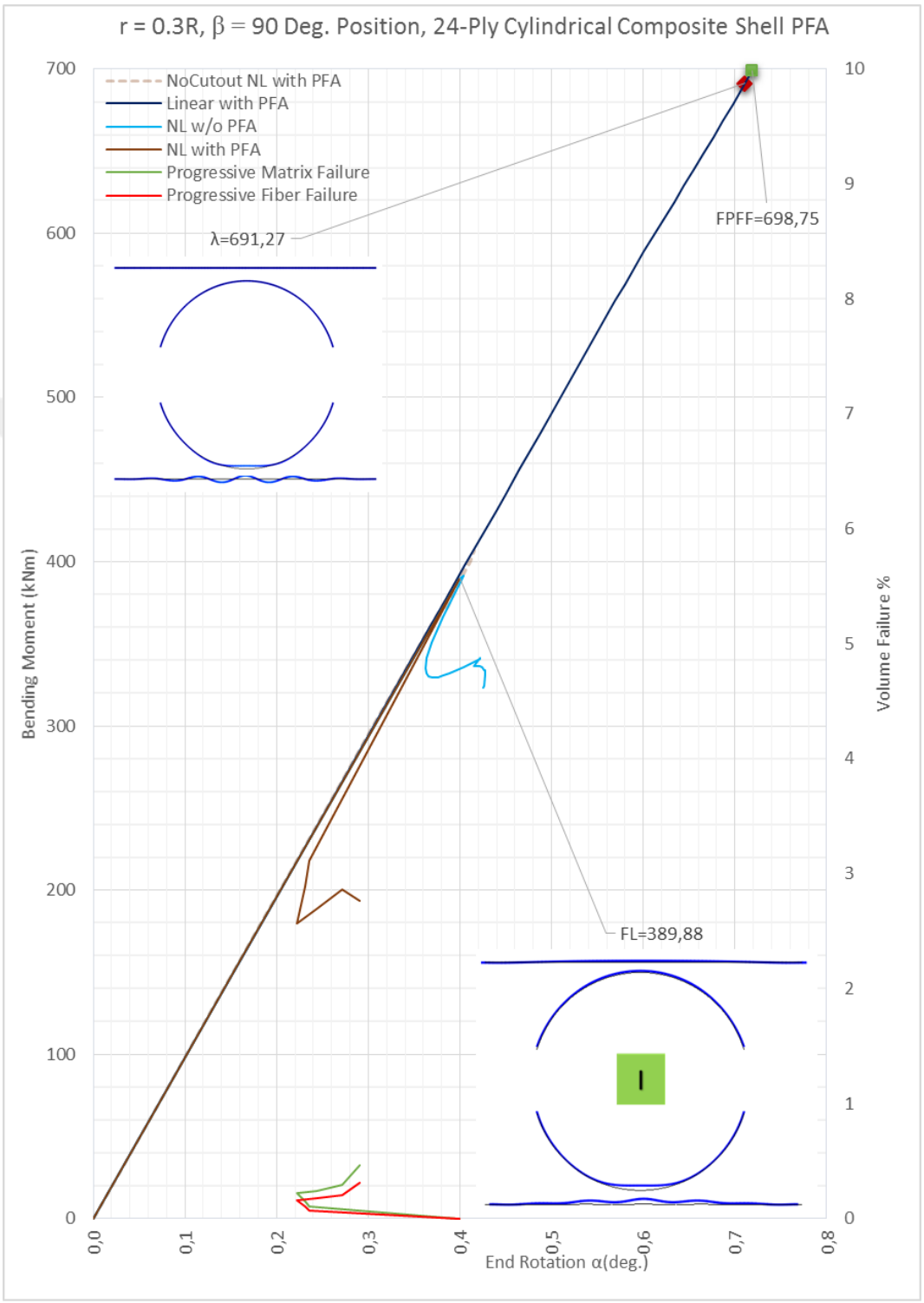


Figure C.5 : 0.3R/90 analysis result.

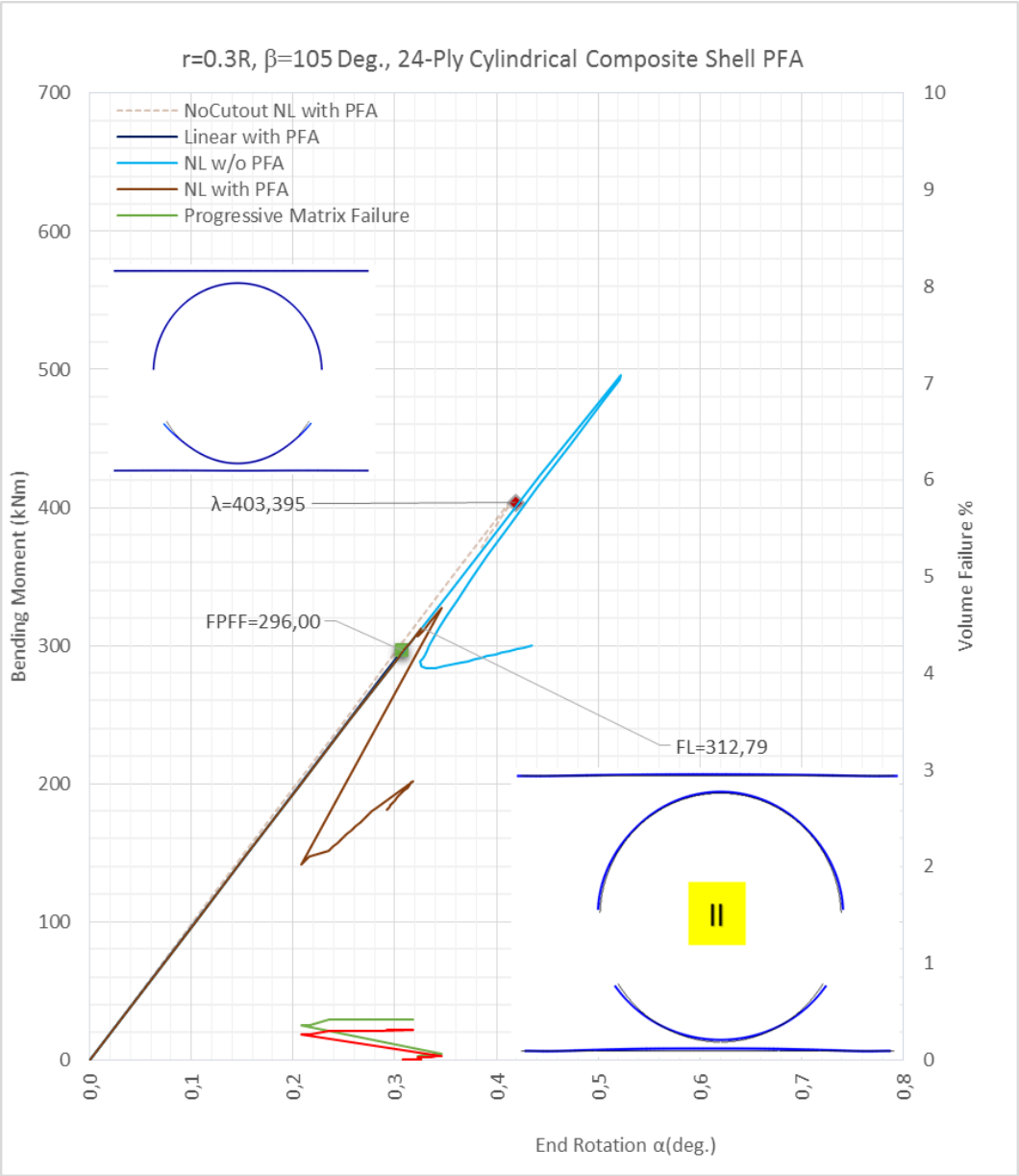


Figure C.6 : 0.3R/105 analysis result.

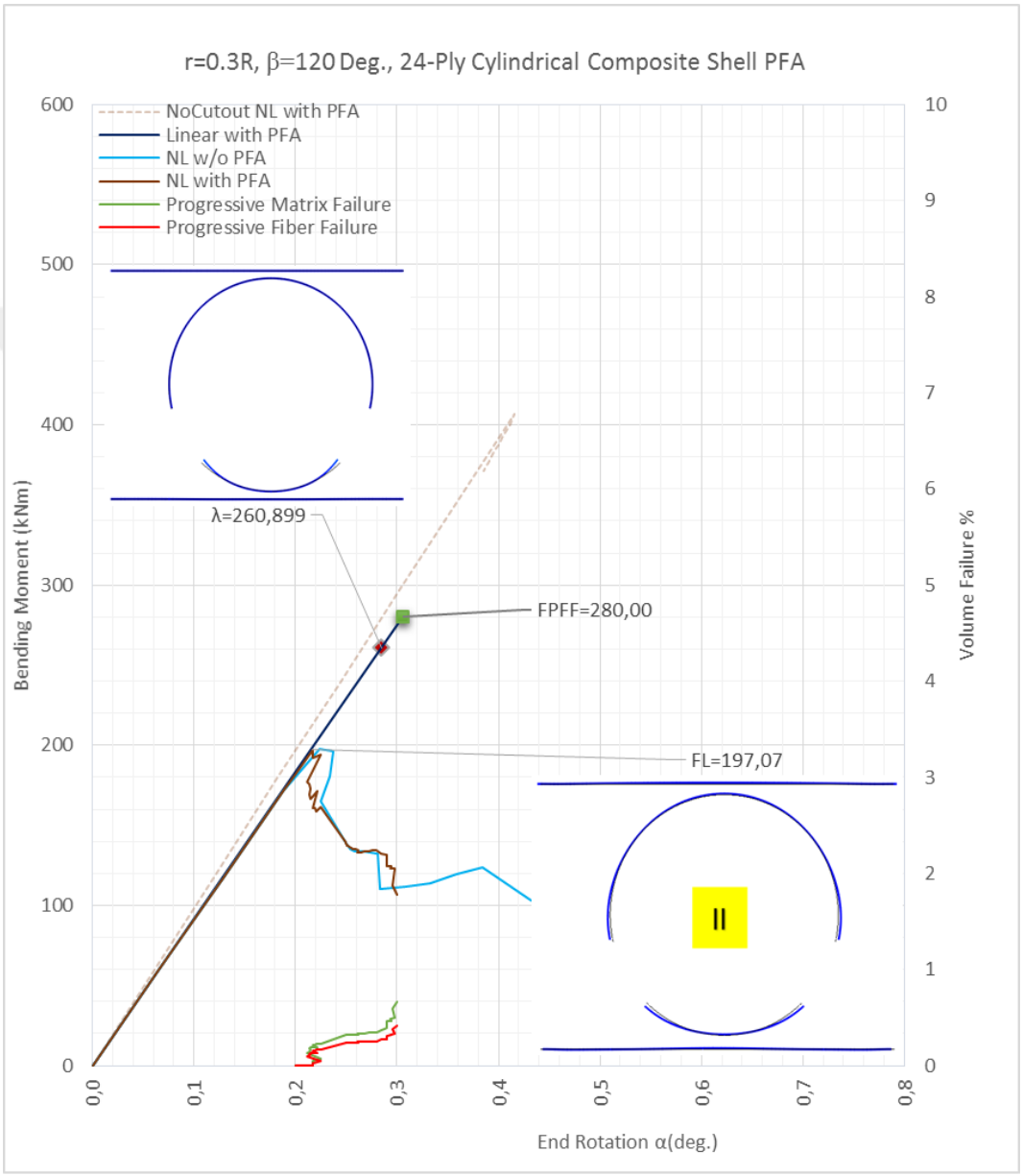


Figure C.7 : 0.3R/120 analysis result.

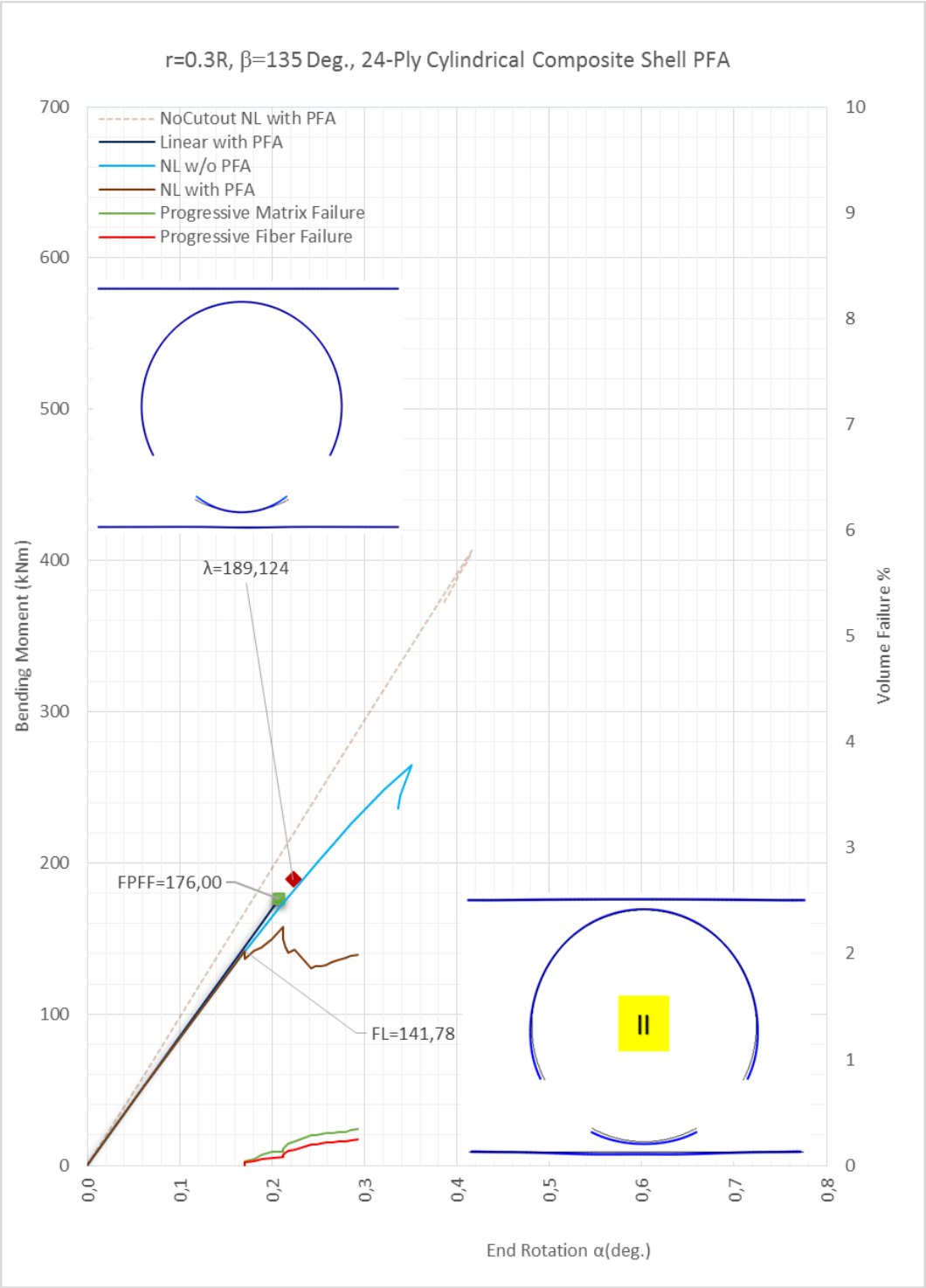


Figure C.8 : 0.3R/135 analysis result.

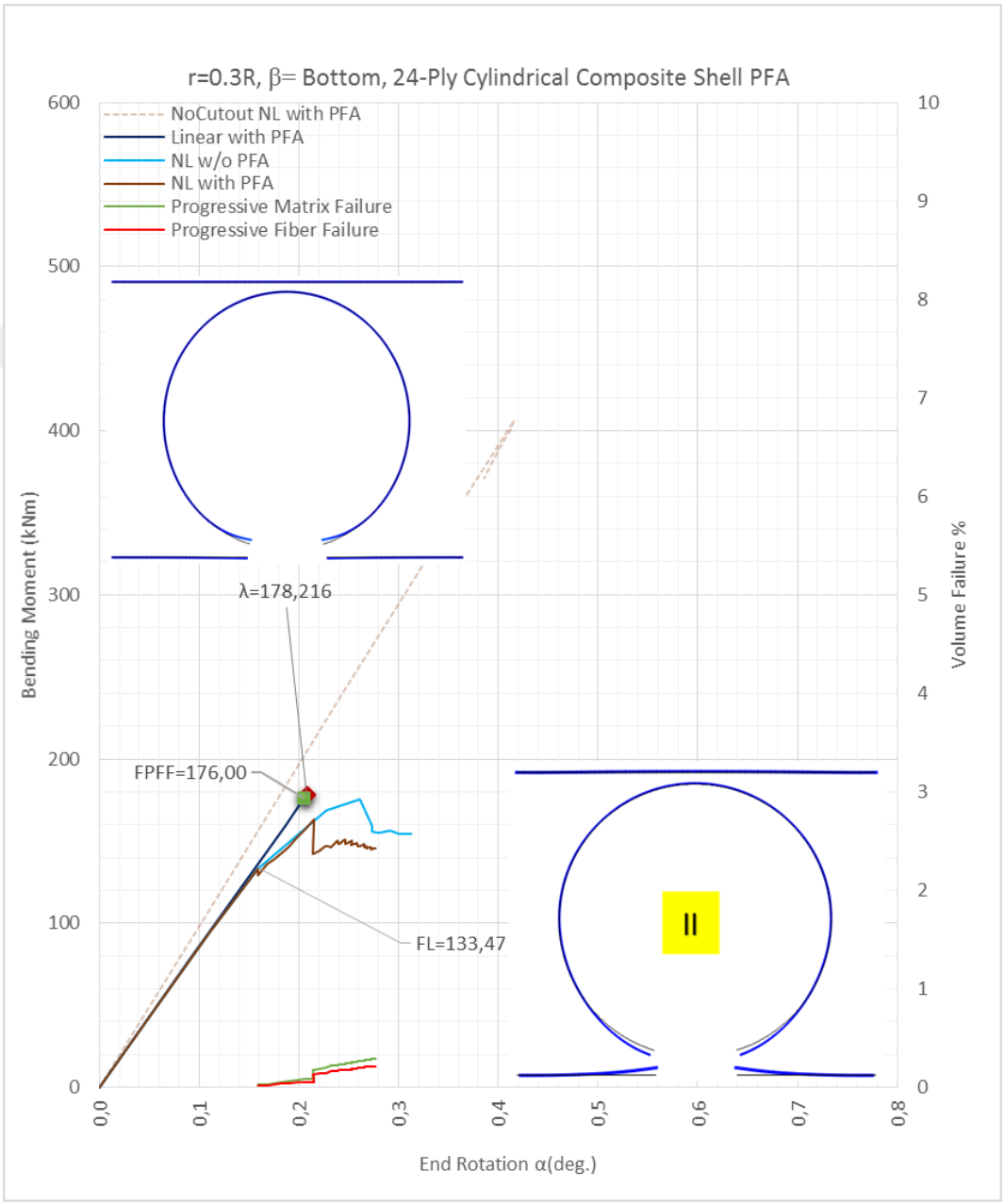


Figure C.9 : 0.3R/180 analysis result.

APPENDIX D: CS, 0.5R Cutout Analysis Results

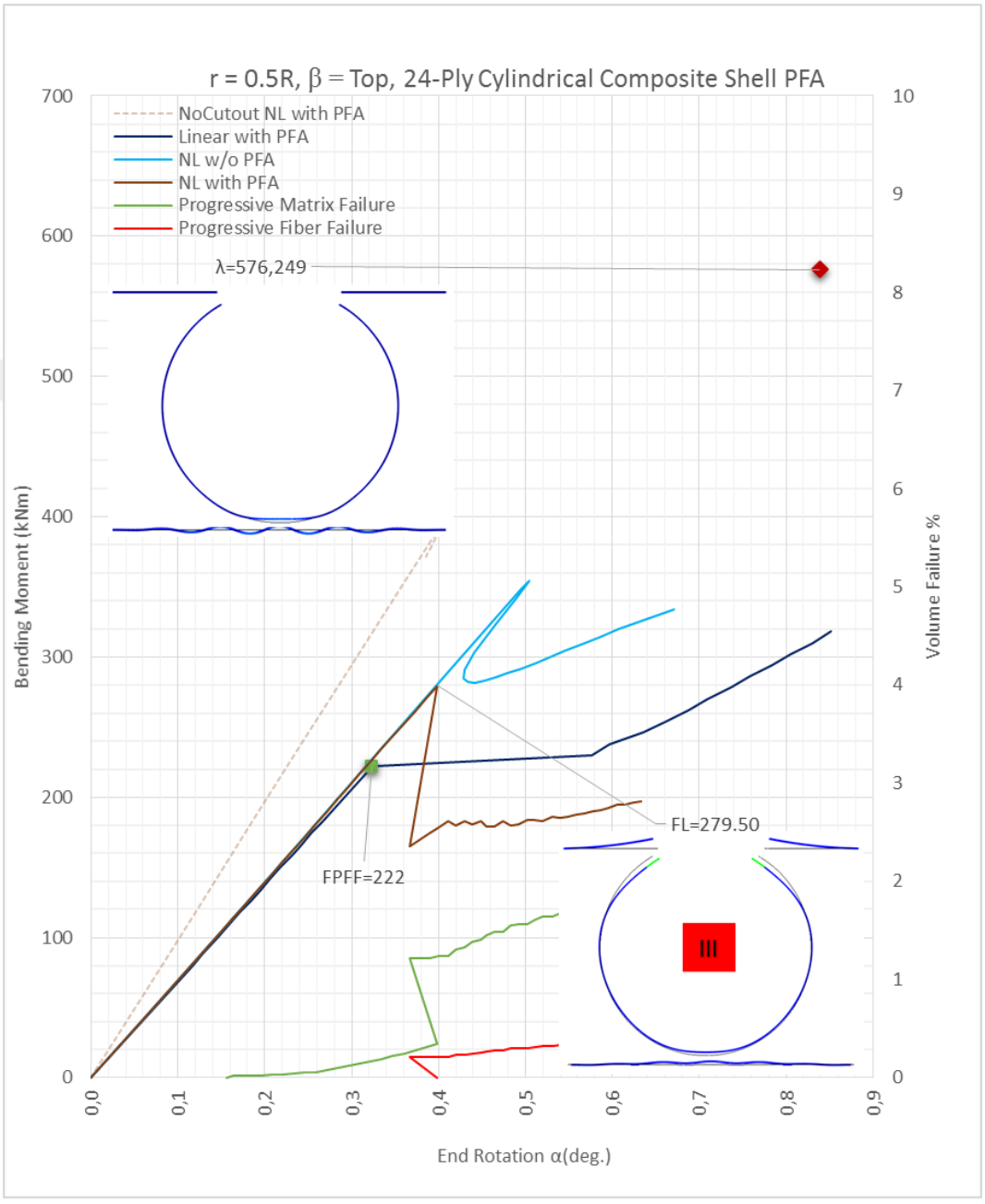


Figure D.1 : 0.5R/0 analysis result.

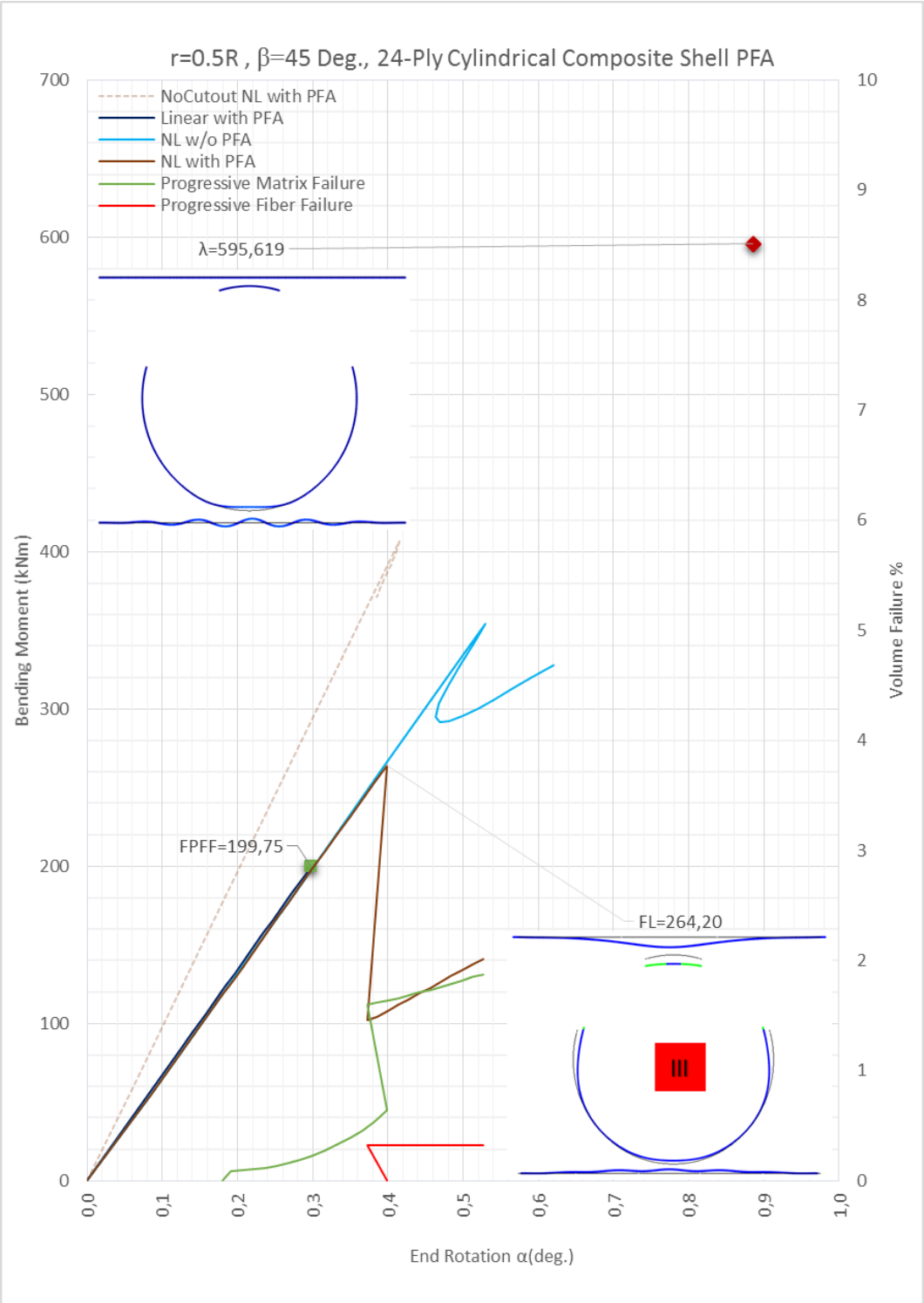


Figure D.2 : 0.5R/45 analysis result.

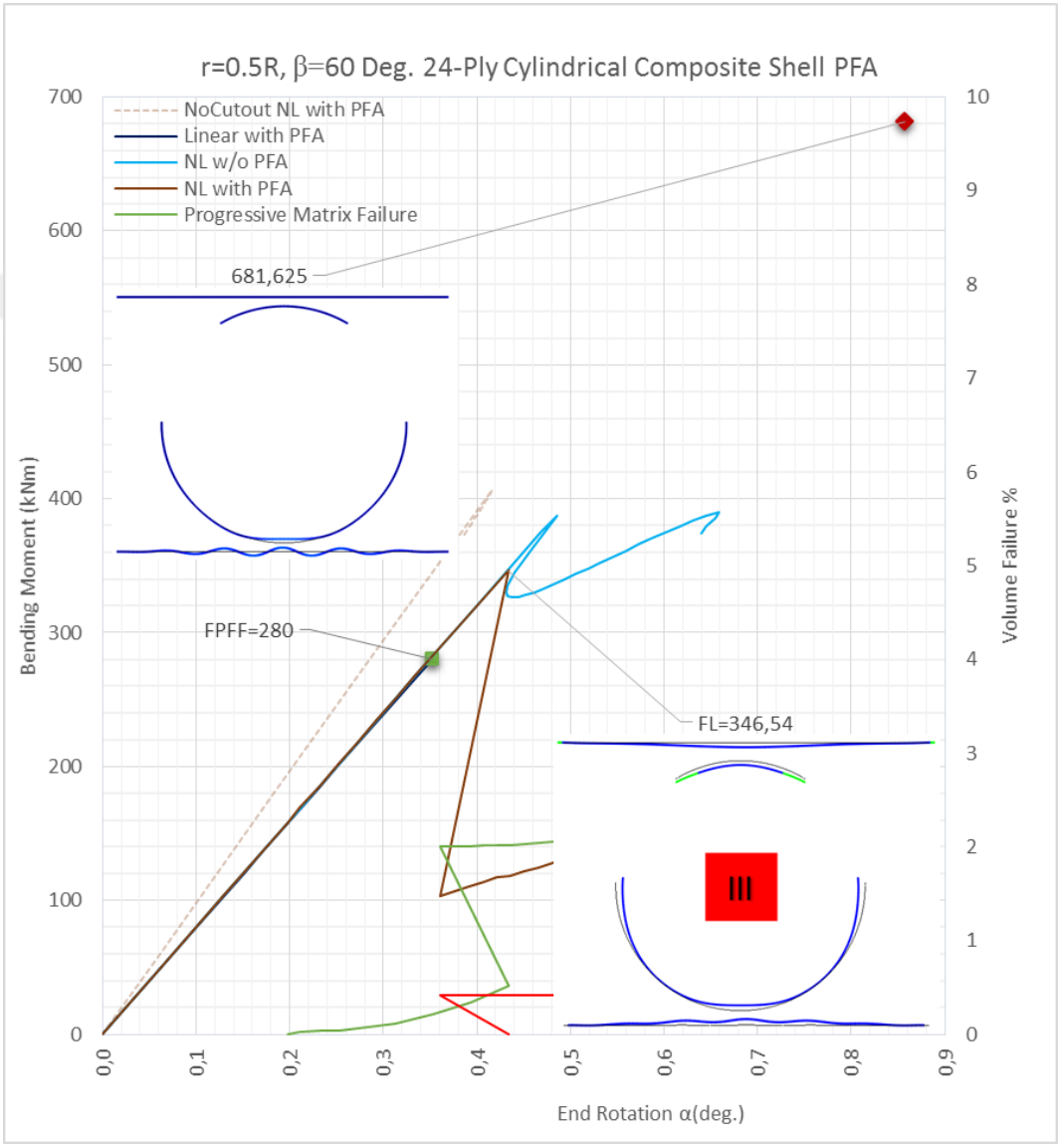


Figure D.3 : 0.5R/60 analysis result.

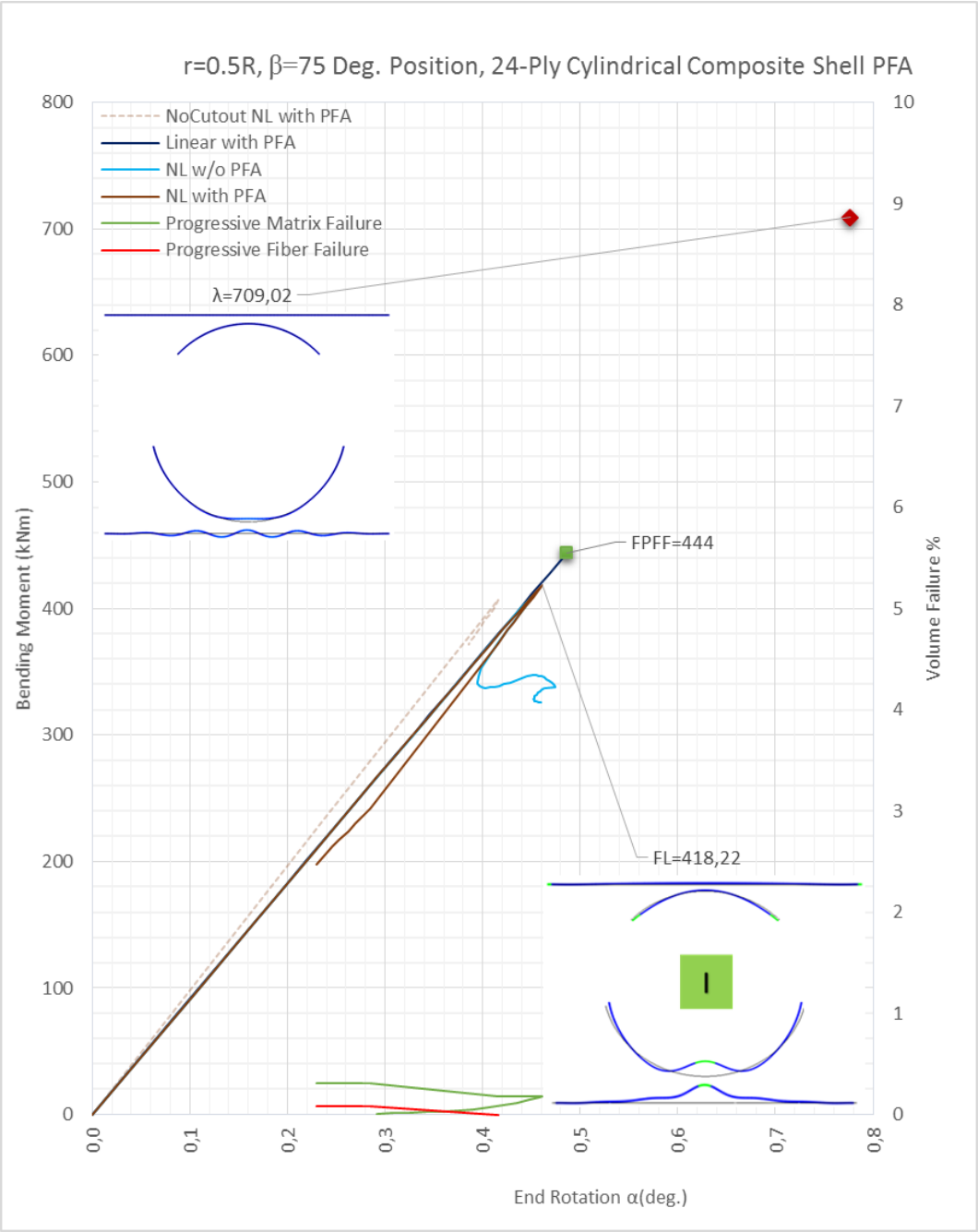


Figure D.4 : 0.5R/75 analysis result.

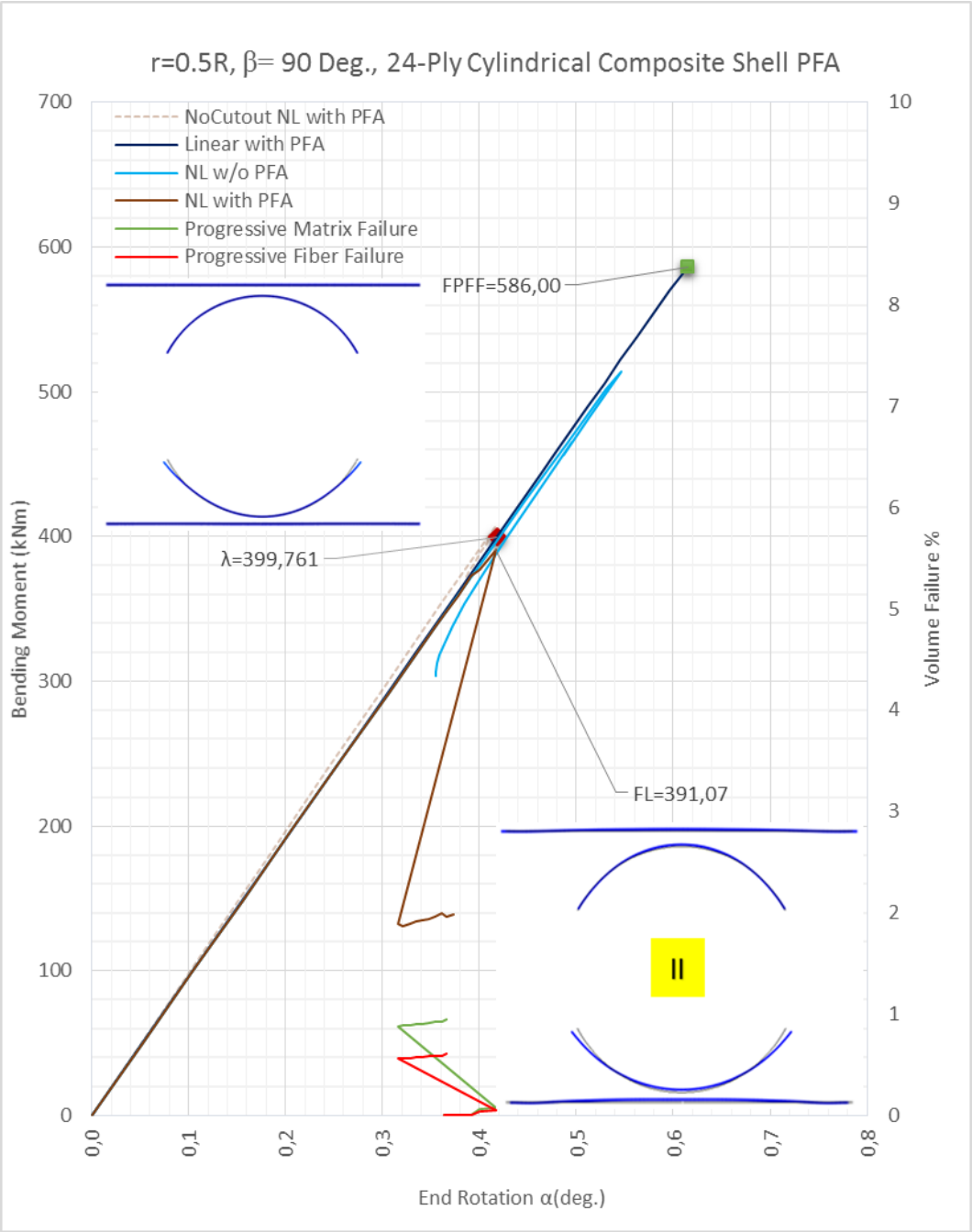


Figure D.5 : 0.5R/90 analysis result.

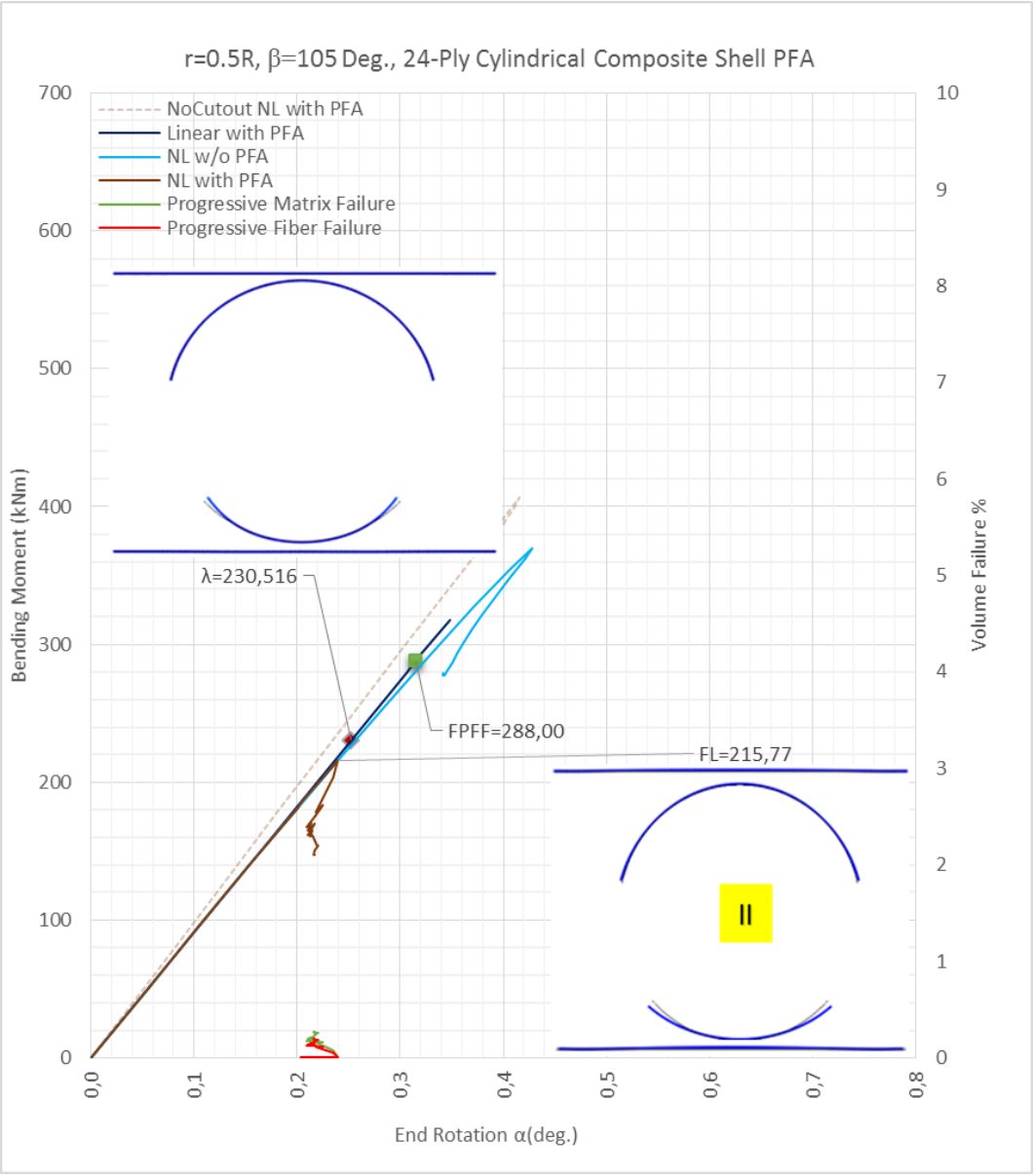


Figure D.6 : 0.5R/105 analysis result.

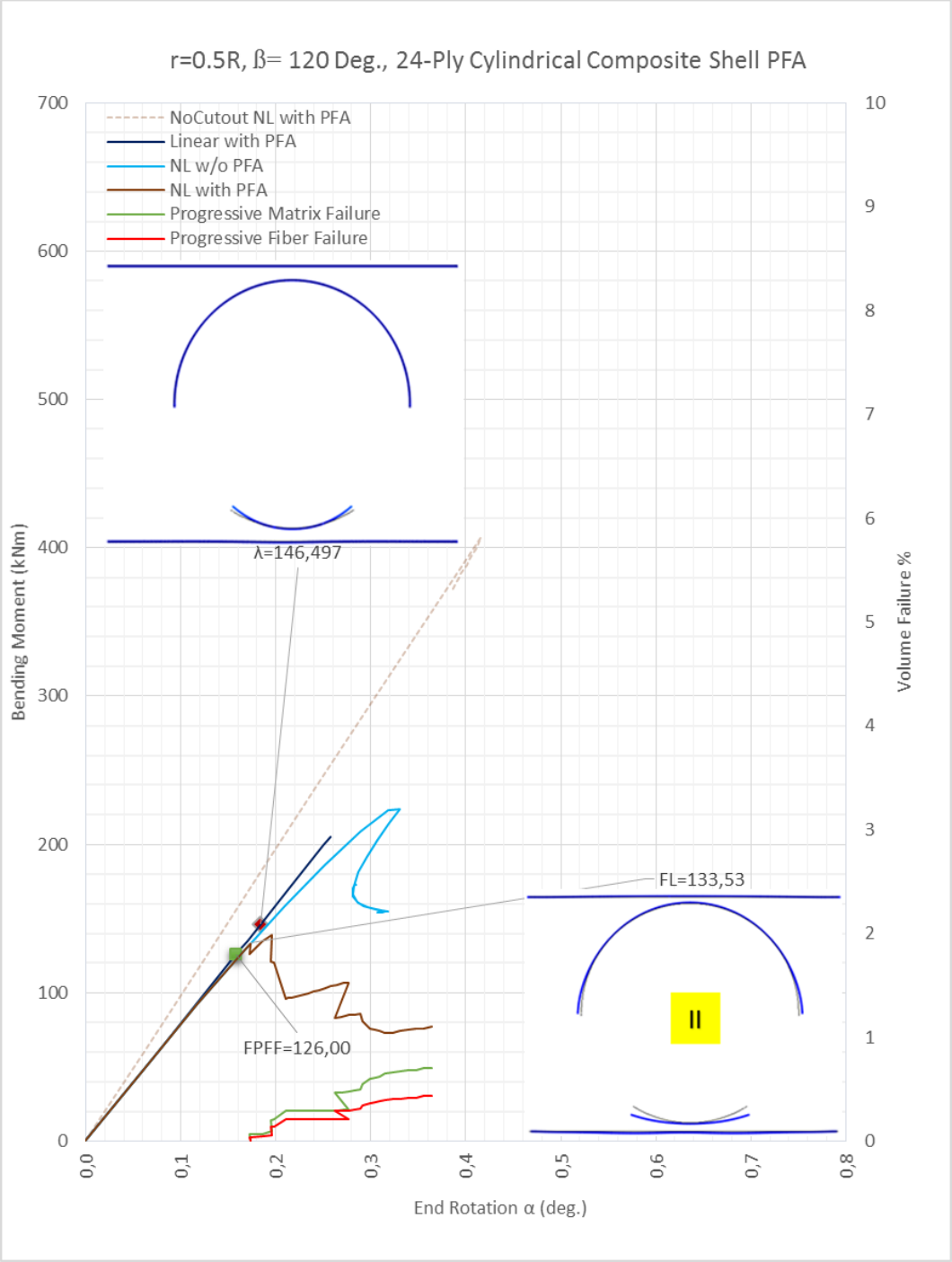


Figure D.7 : 0.5R/120 analysis result.

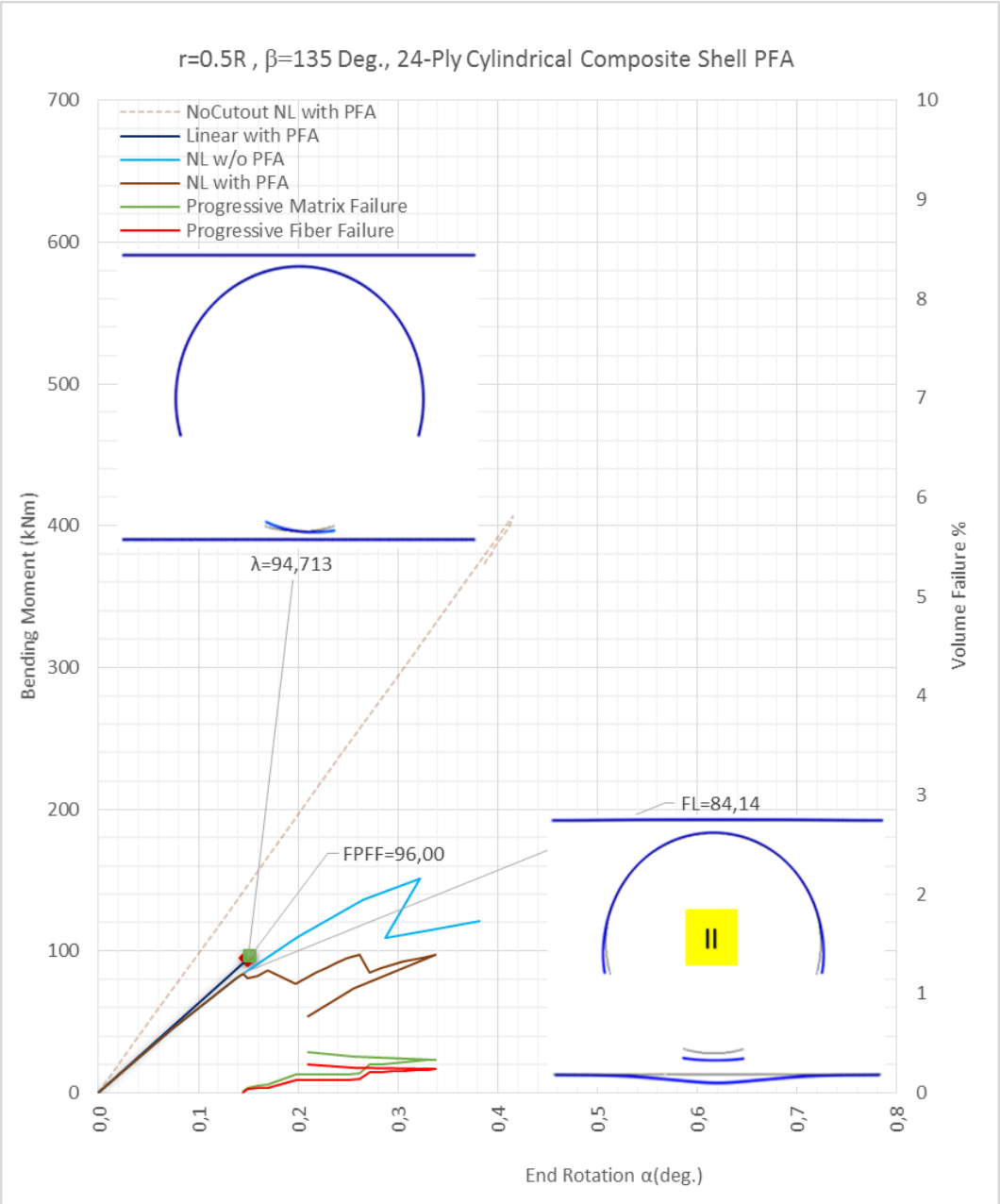


Figure D.8 : 0.5R/135 analysis result.

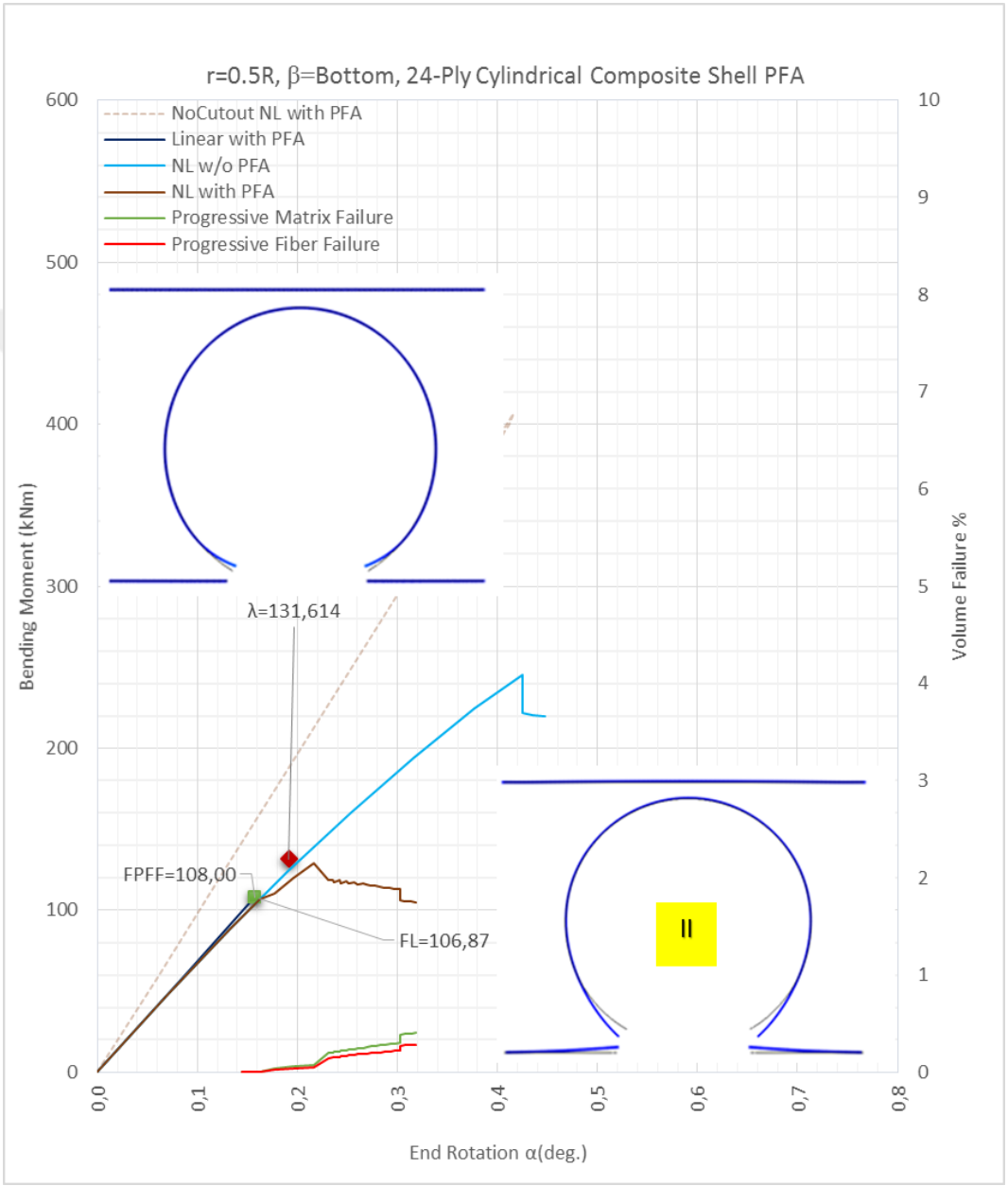


Figure D.9 : 0.5R/180 analysis result.

APPENDIX E: CS, 0.3R Cutout Detail Analysis Results

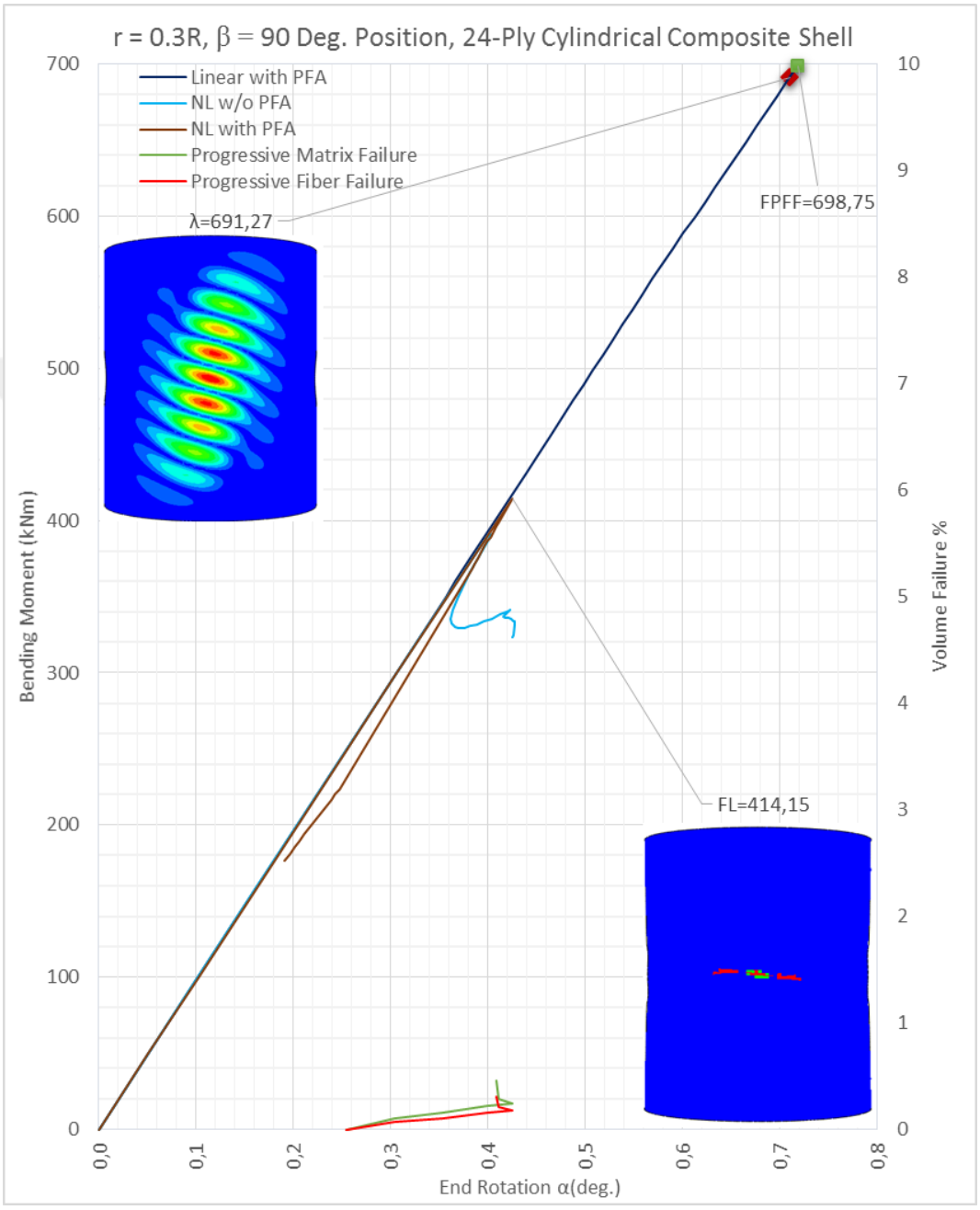


Figure E.1 : 0.3R/90 analysis result.

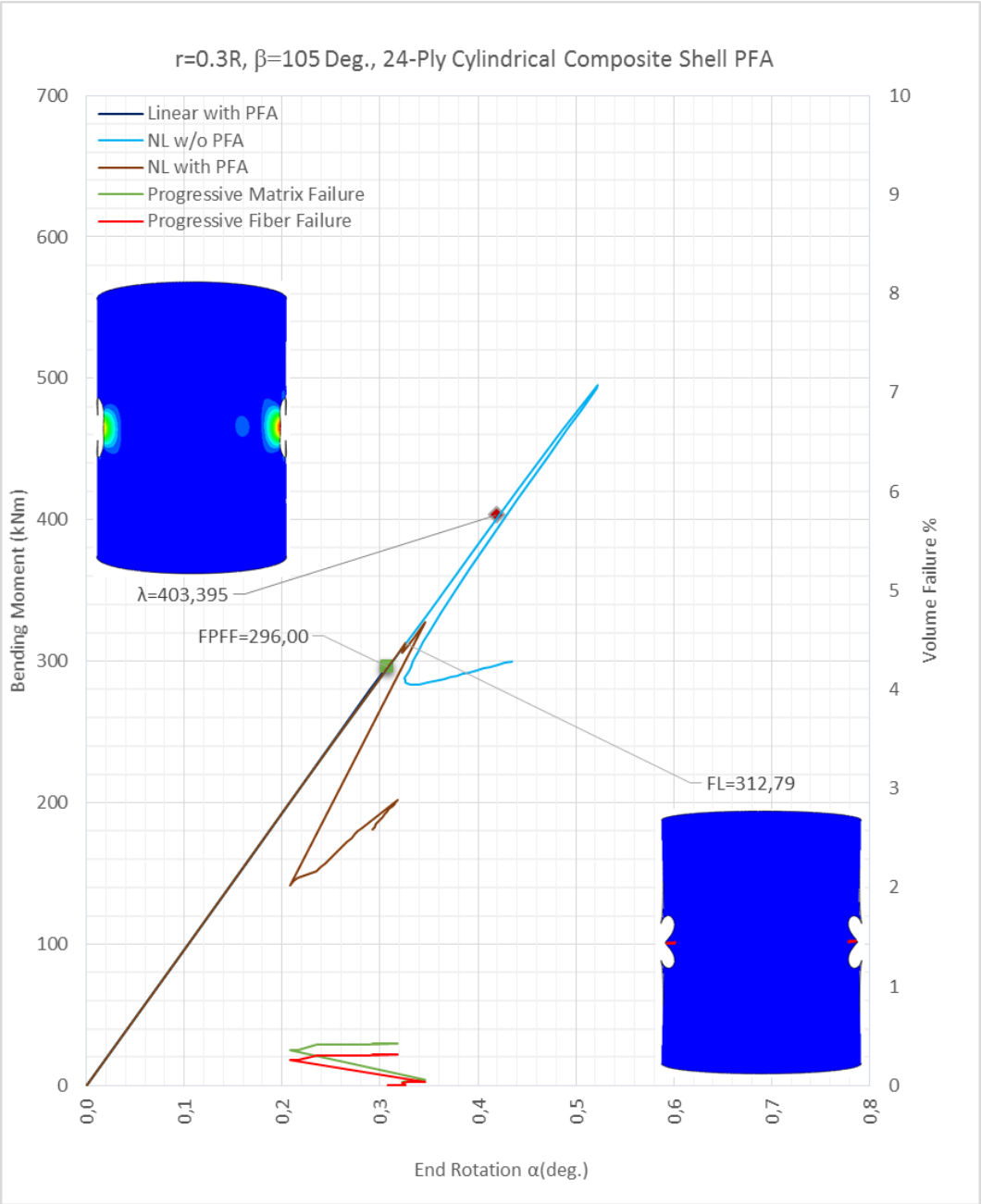


Figure E.2 : 0.3R/105 analysis result.

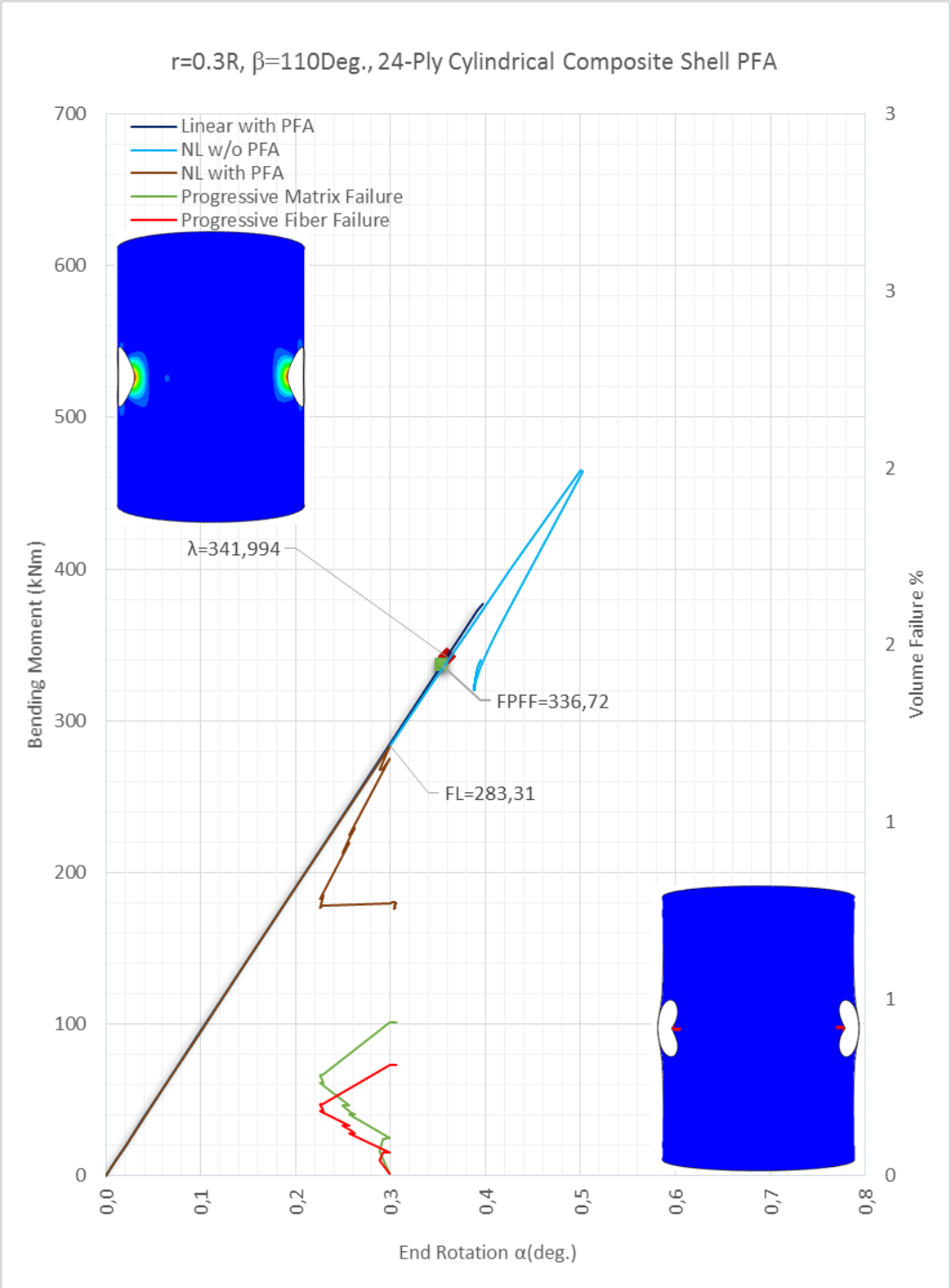


Figure E.3 : 0.3R/110 analysis result.

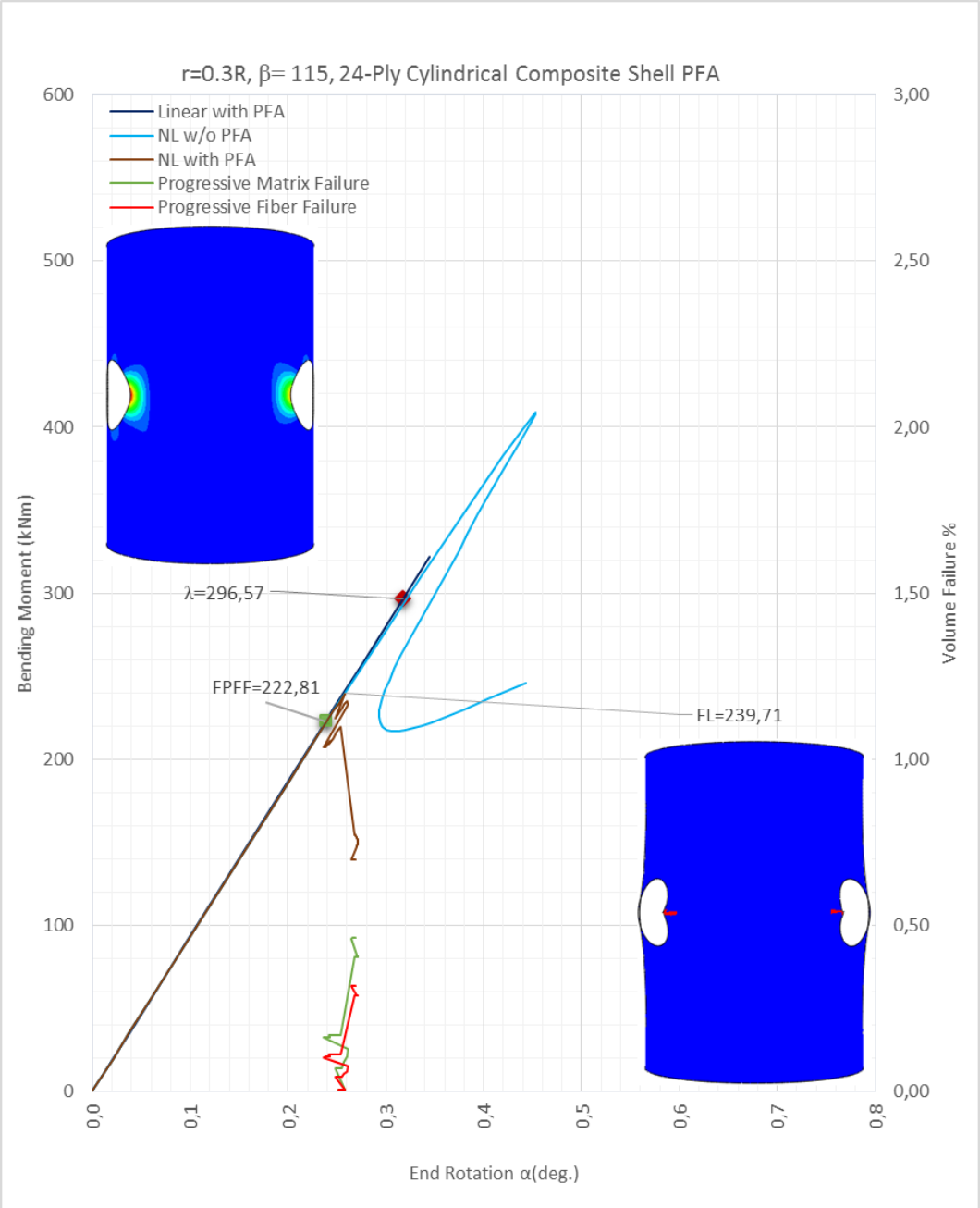


Figure E.4 : 0.3R/115 analysis result.

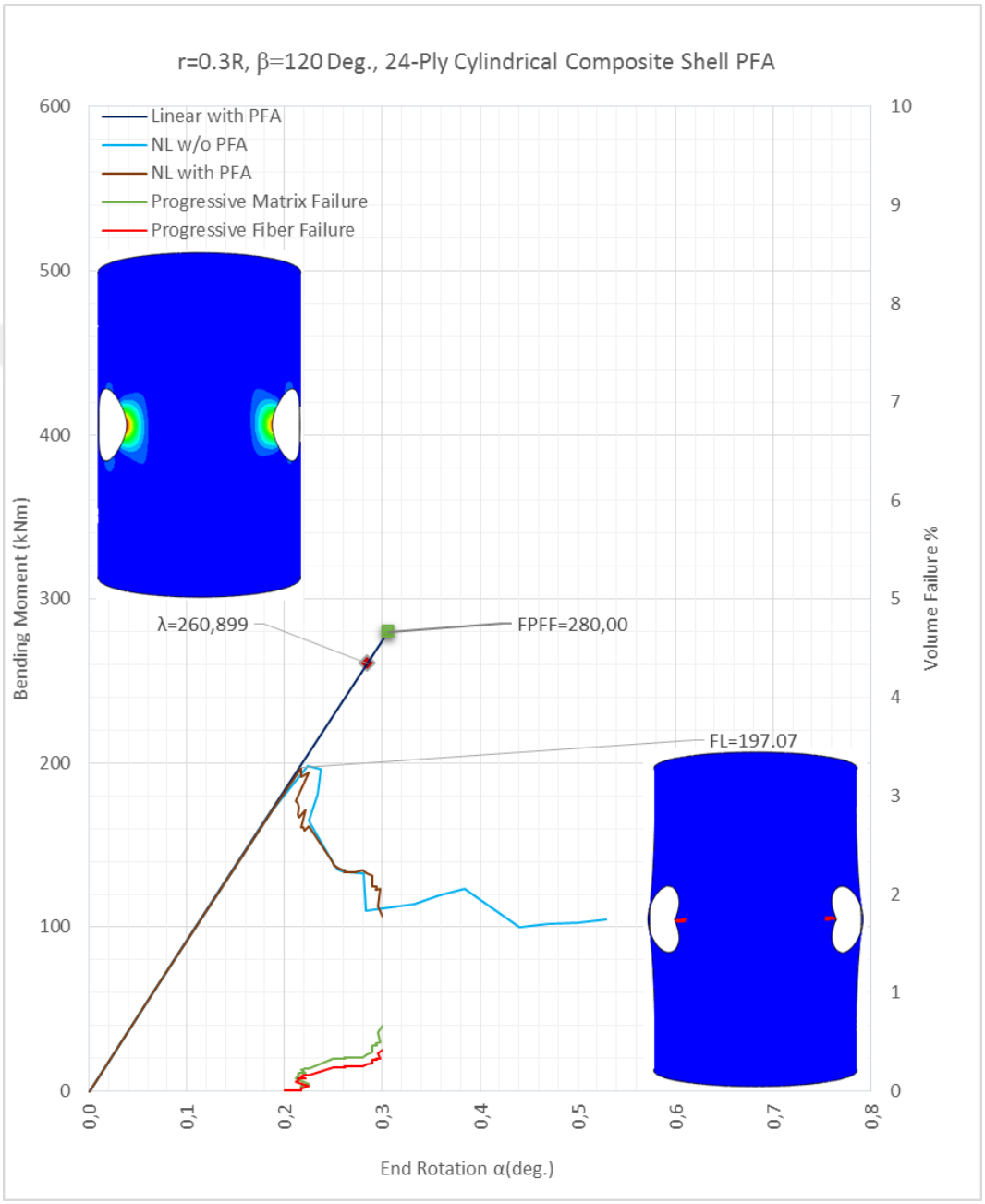


Figure E.5 : 0.3R/120 analysis result.

APPENDIX F: CS, 0.4R Cutout Detail Analysis Results

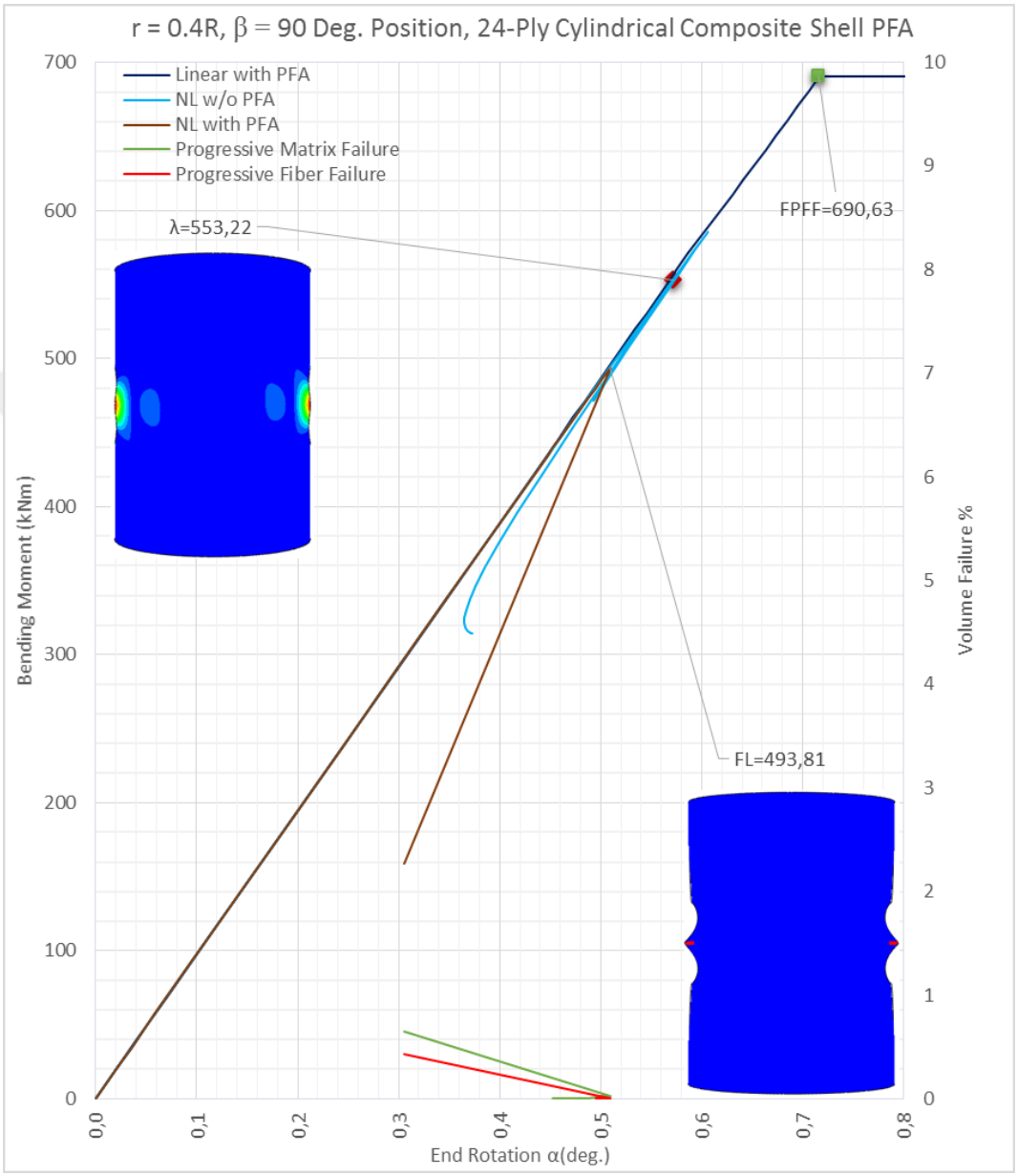


Figure F.1 : 0.4R/90 analysis result.

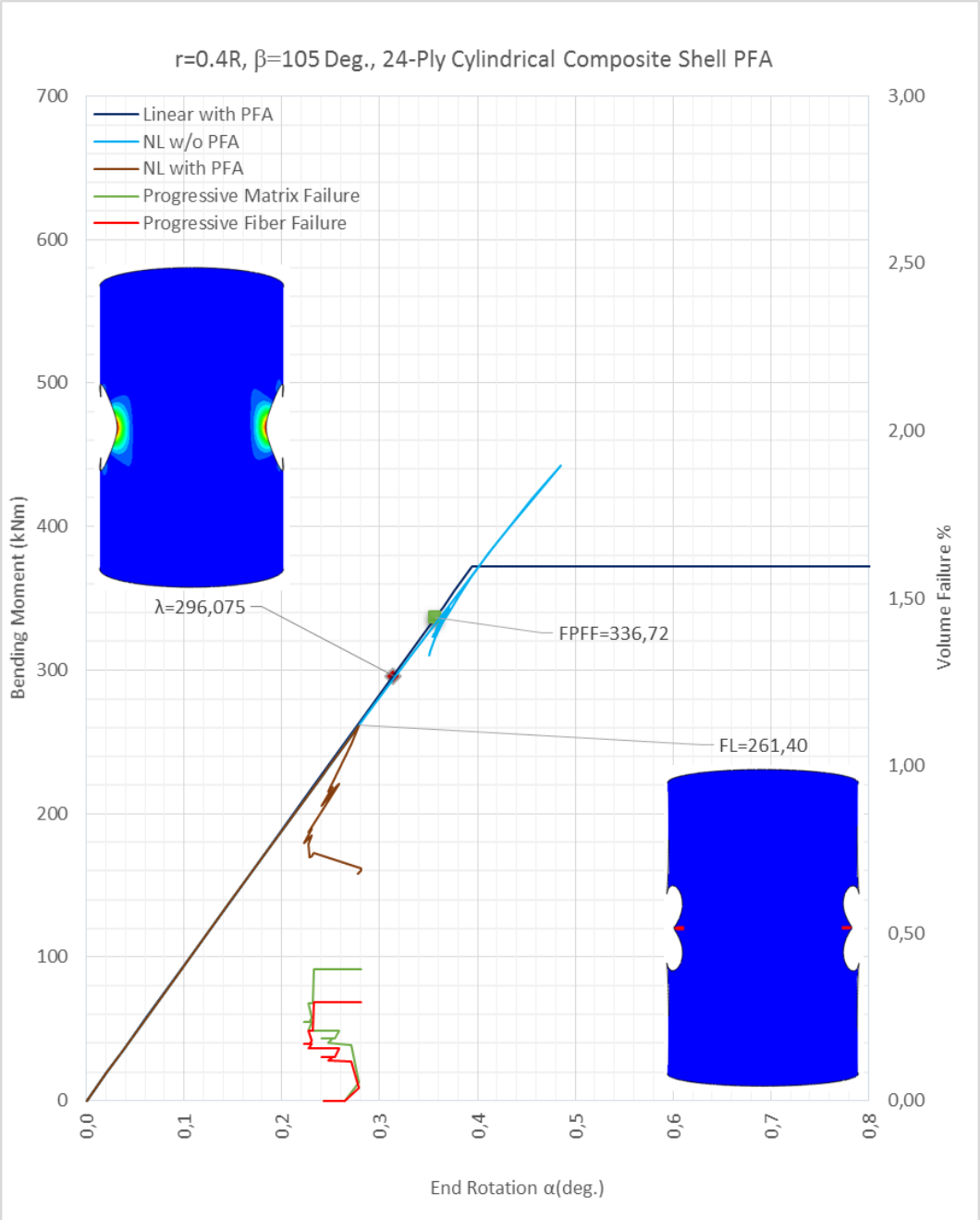


Figure F.2 : 0.4R/105 analysis result.

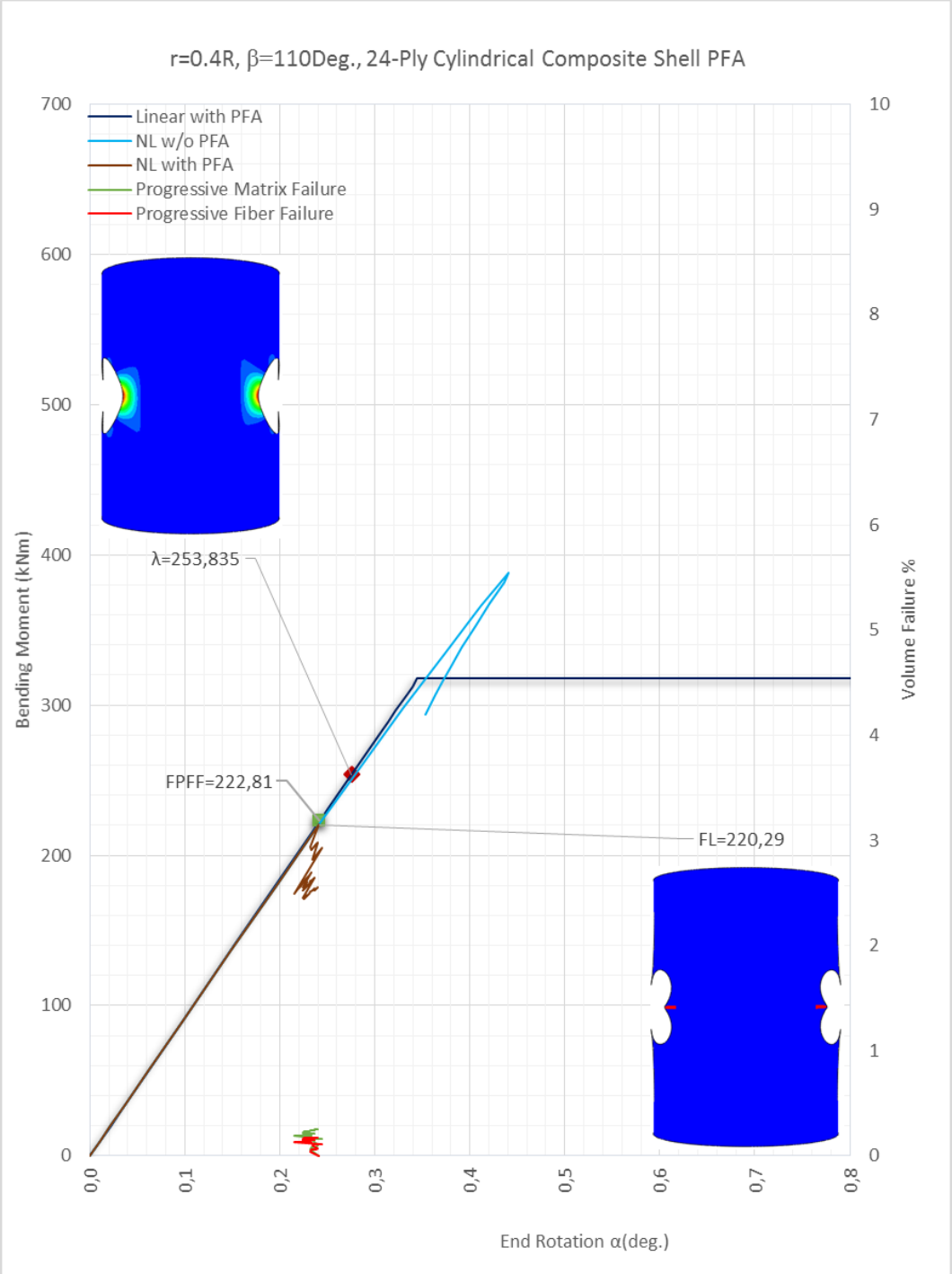


Figure F.3 : 0.4R/110 analysis result.

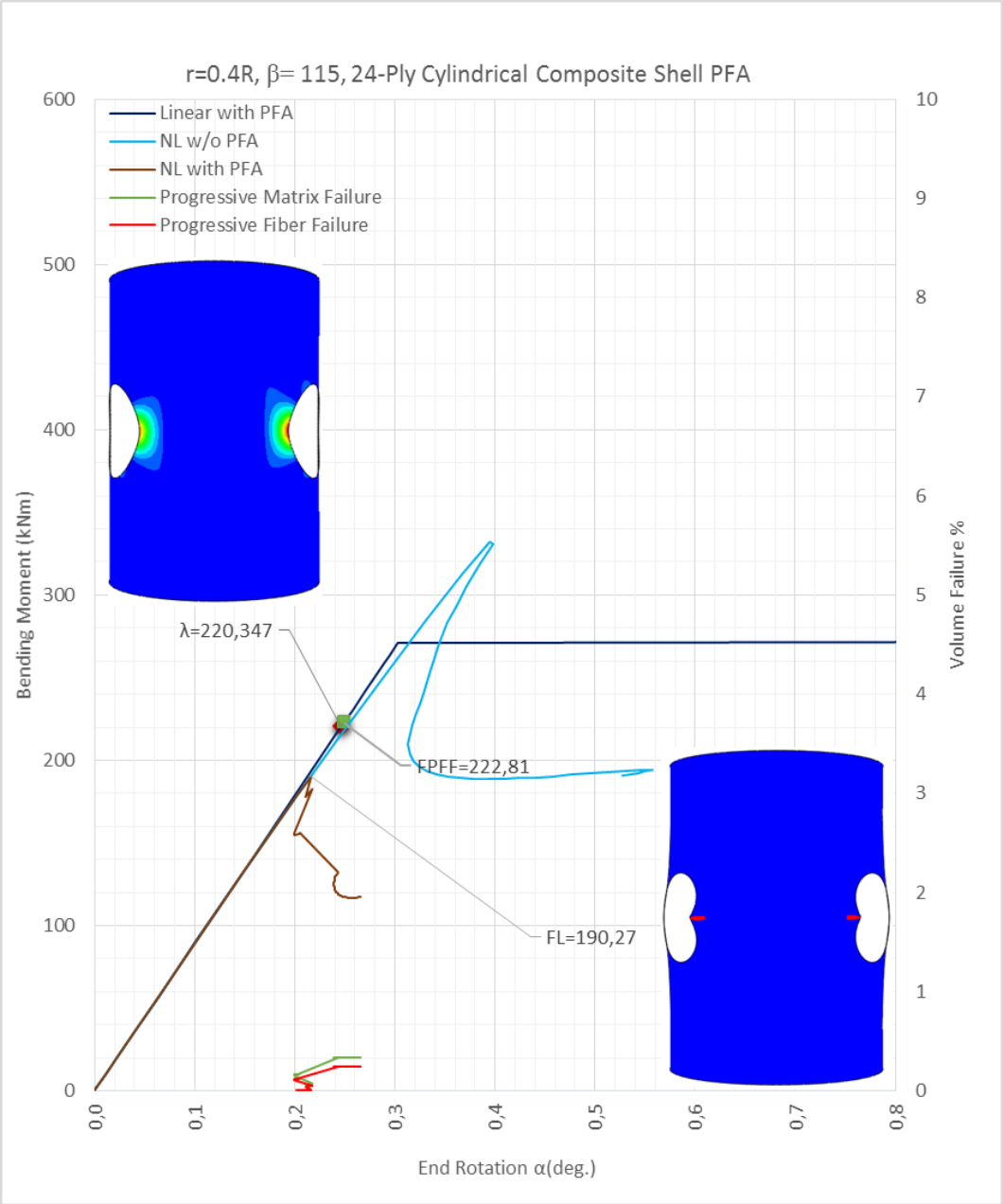


Figure F.4 : 0.4R/115 analysis result.

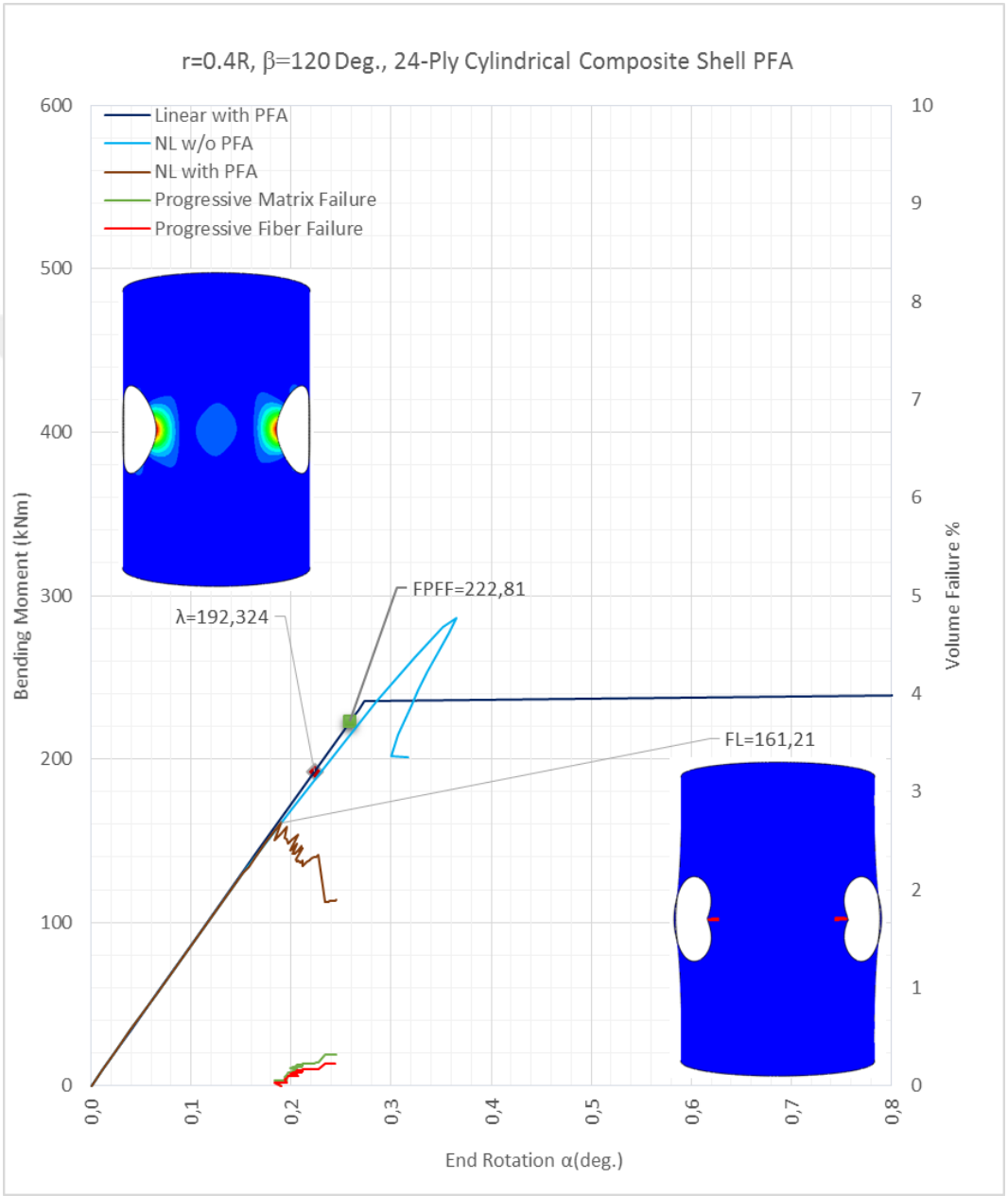


Figure F.5 : 0.4R/120 analysis result.

APPENDIX G: CS, 0.5R Cutout Detail Analysis Results

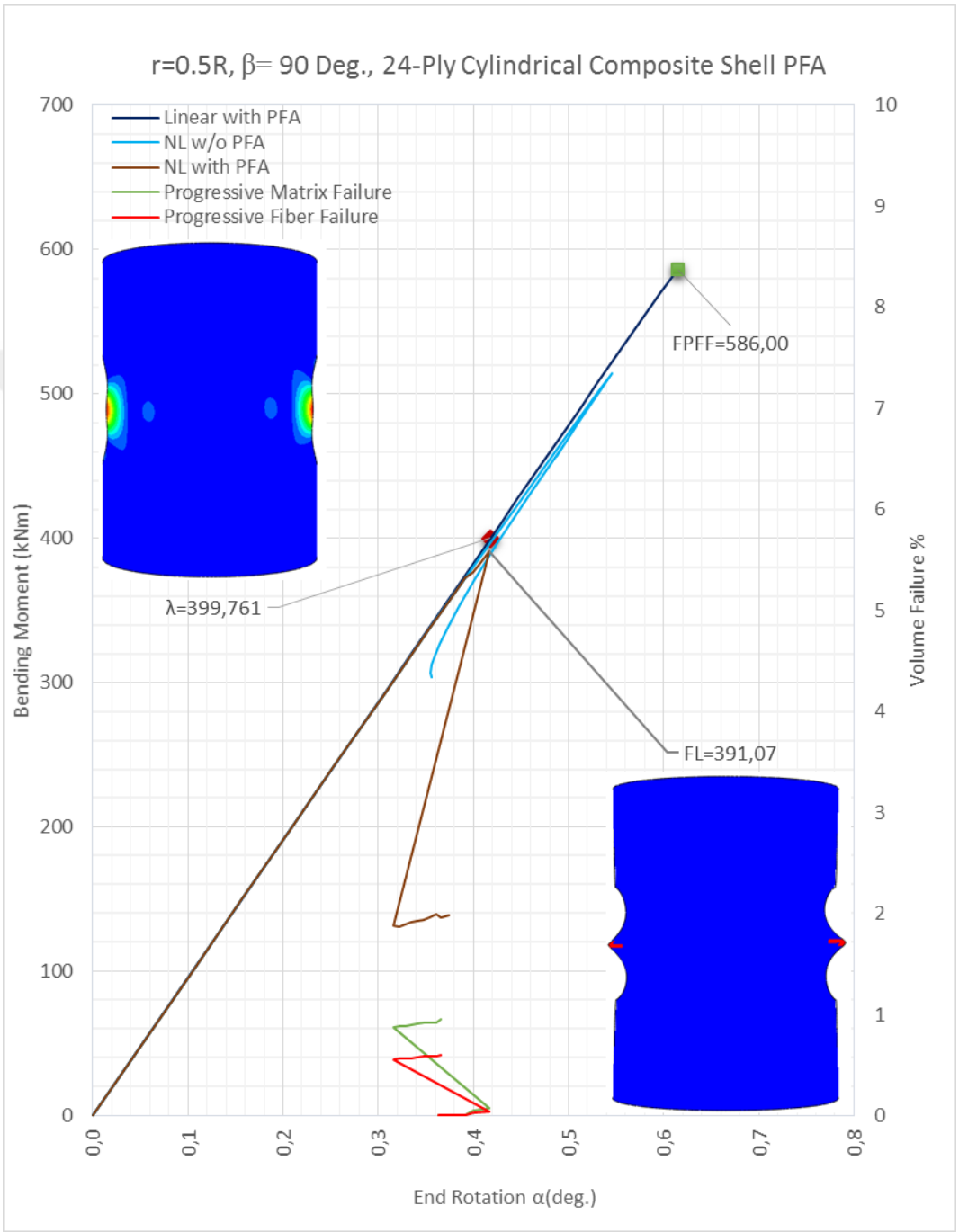


Figure G.1 : 0.5R/90 analysis result.

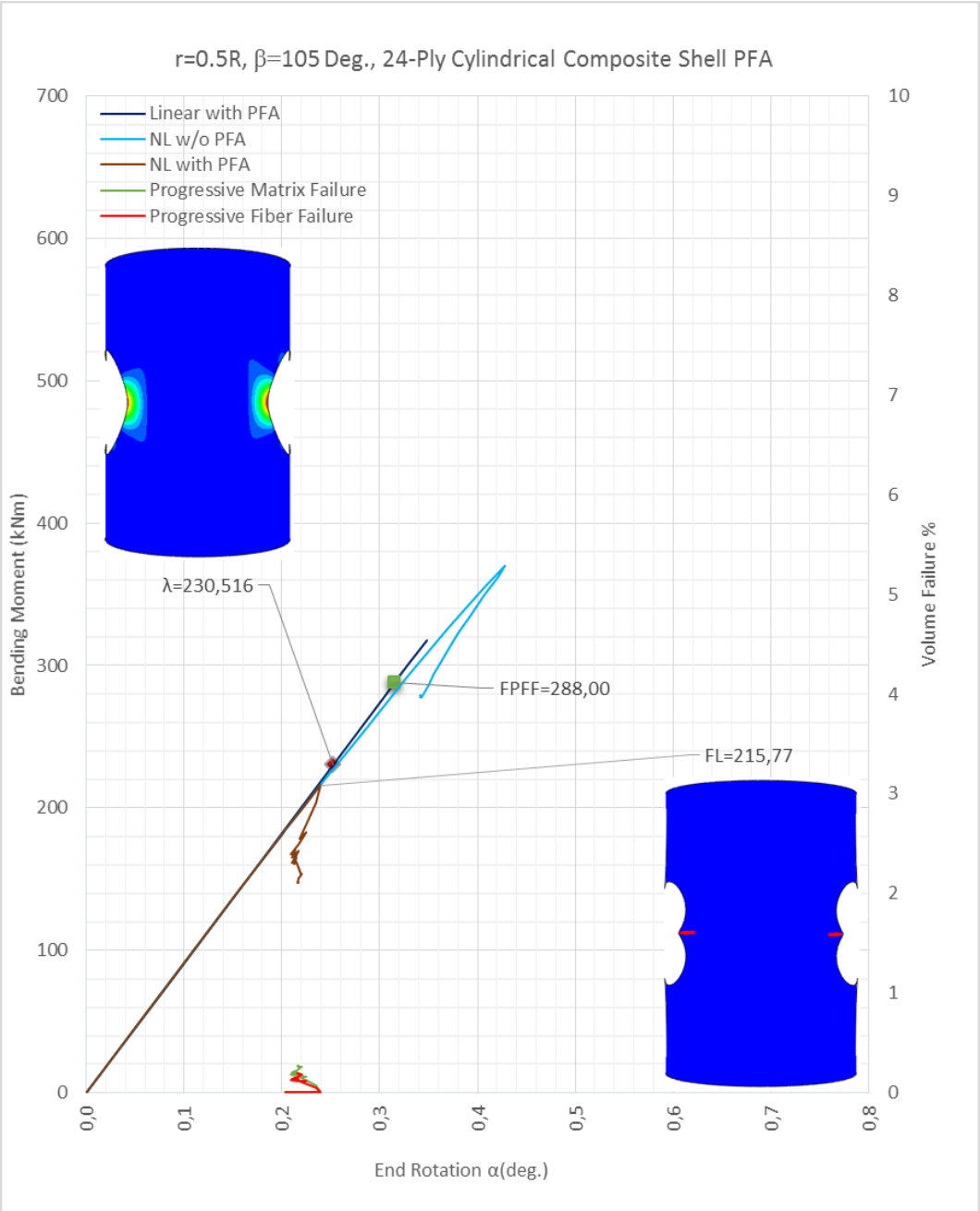


Figure G.2 : 0.5R/105 analysis result.

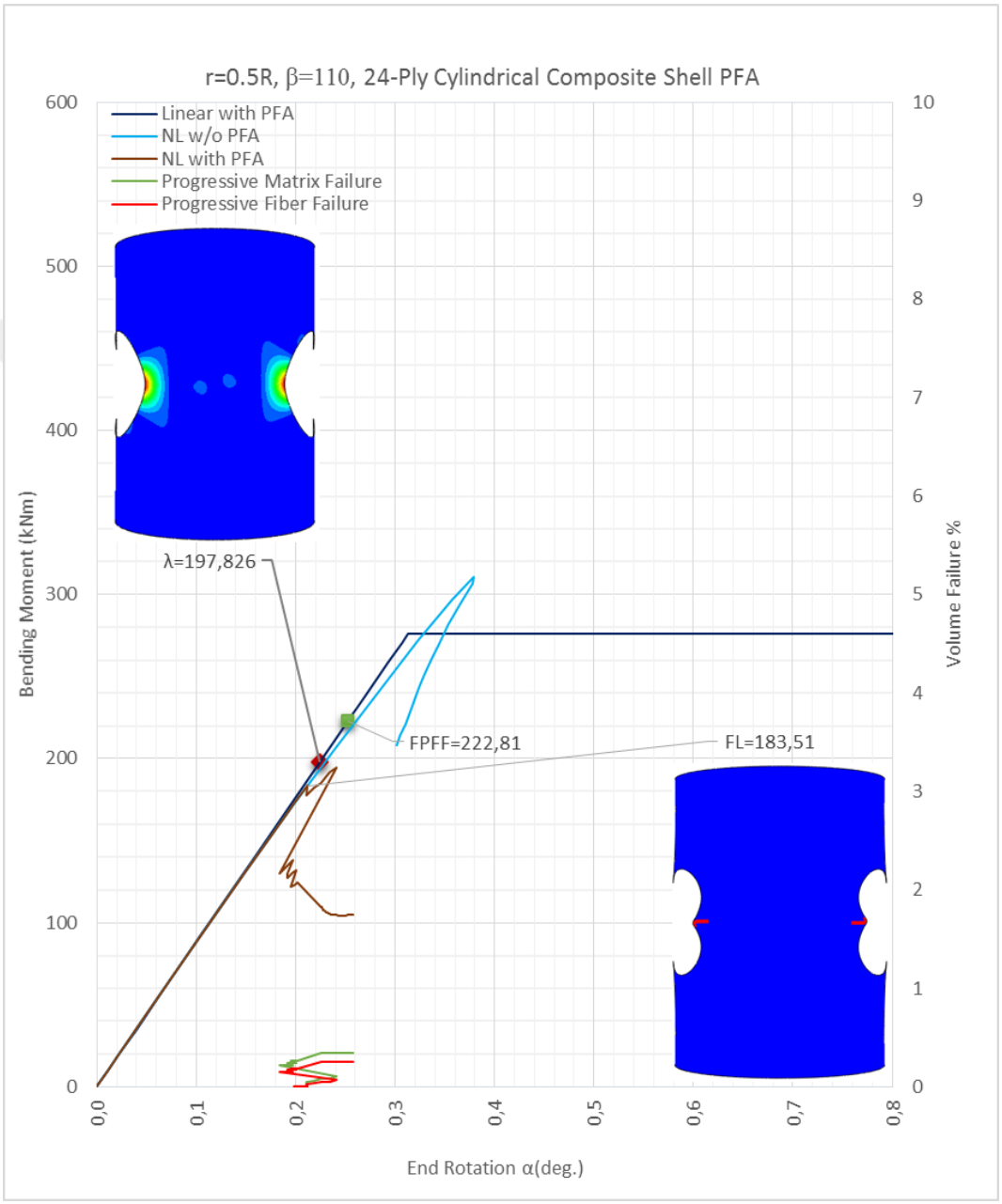


Figure G.3 : 0.5R/110 analysis result.

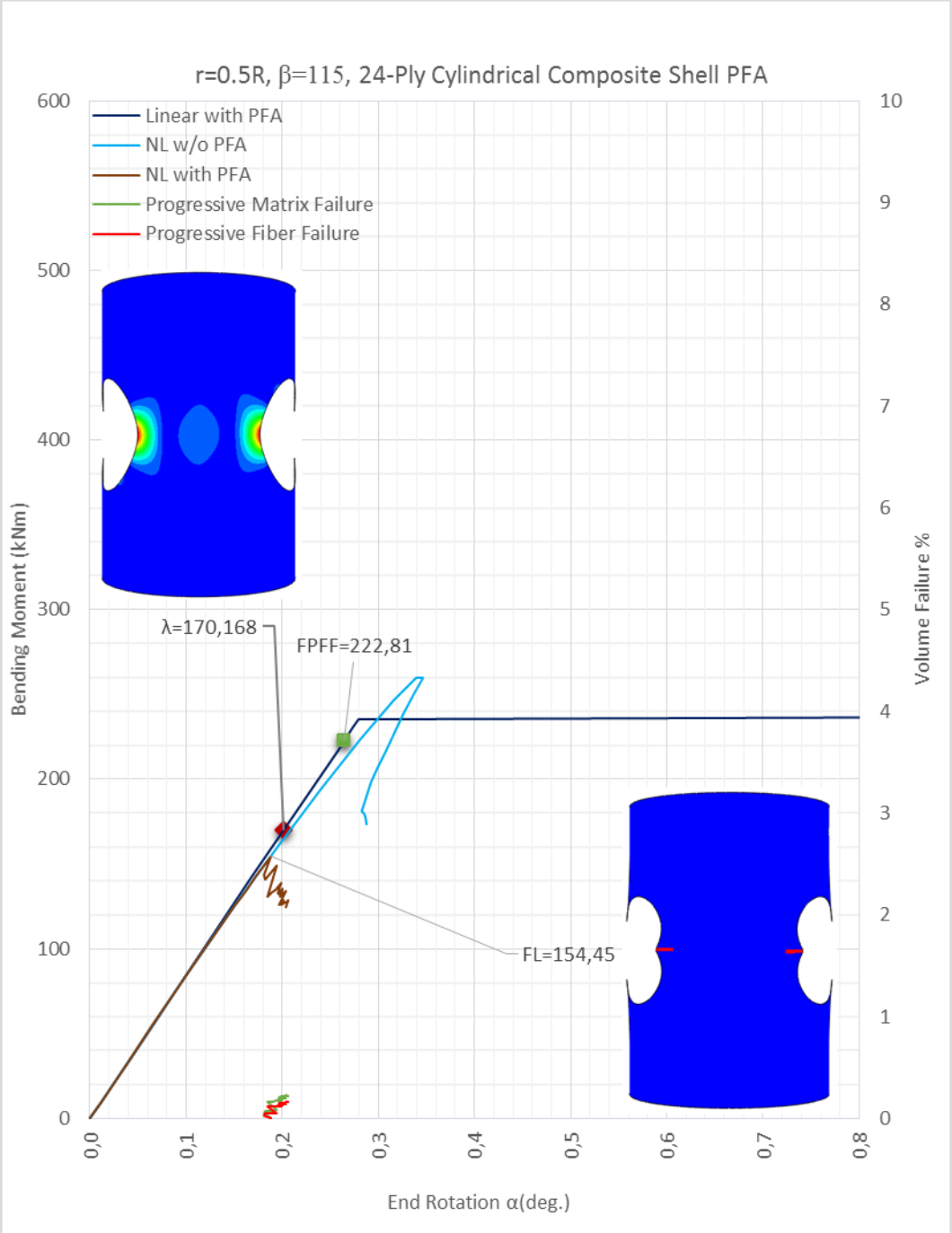


Figure G.4 : 0.5R/115 analysis result.

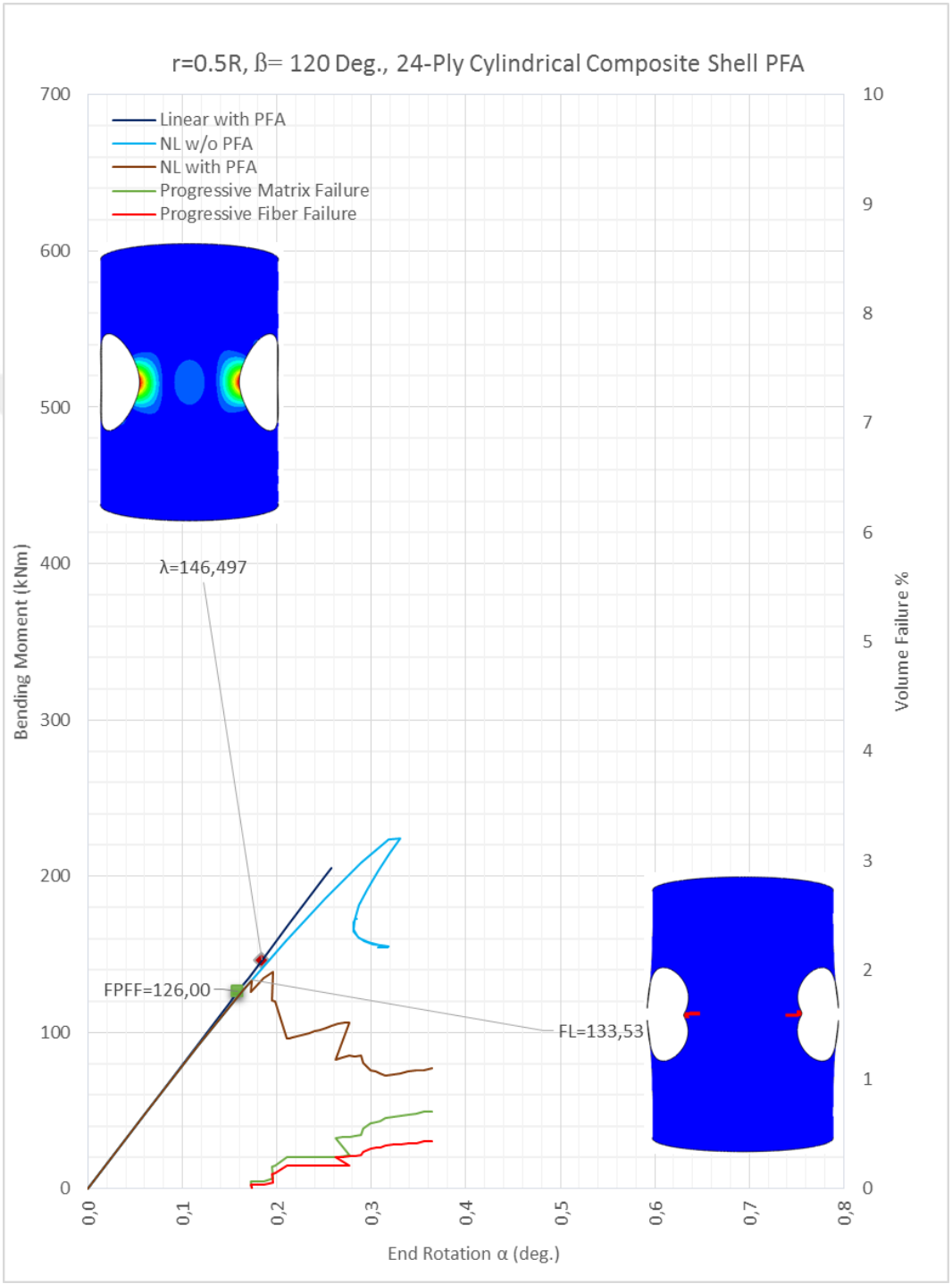


Figure G.5 : 0.5R/120 analysis result.

APPENDIX H: CS, 0.6R Cutout Detail Analysis Results

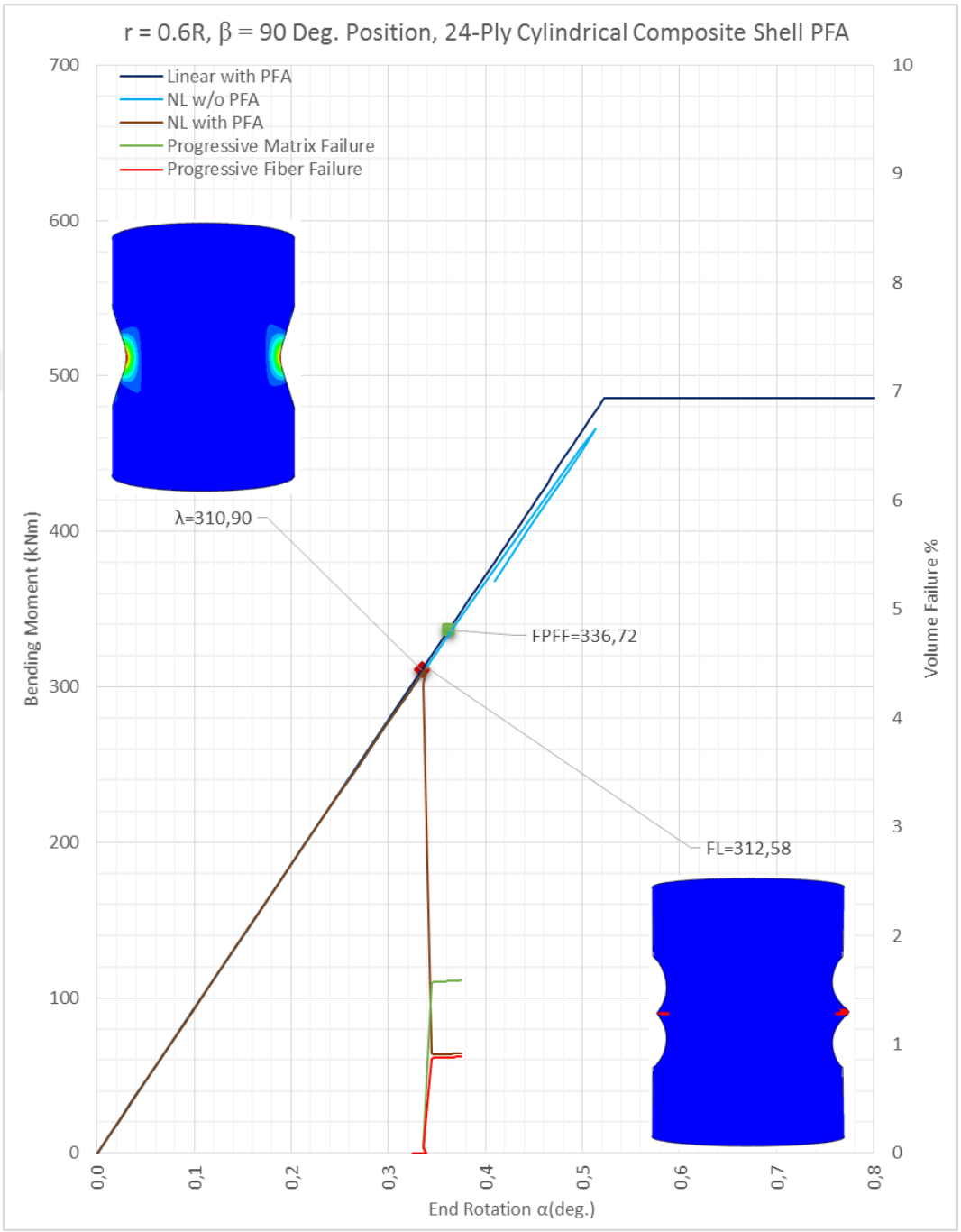


Figure H.1 : 0.6R/90 analysis result.

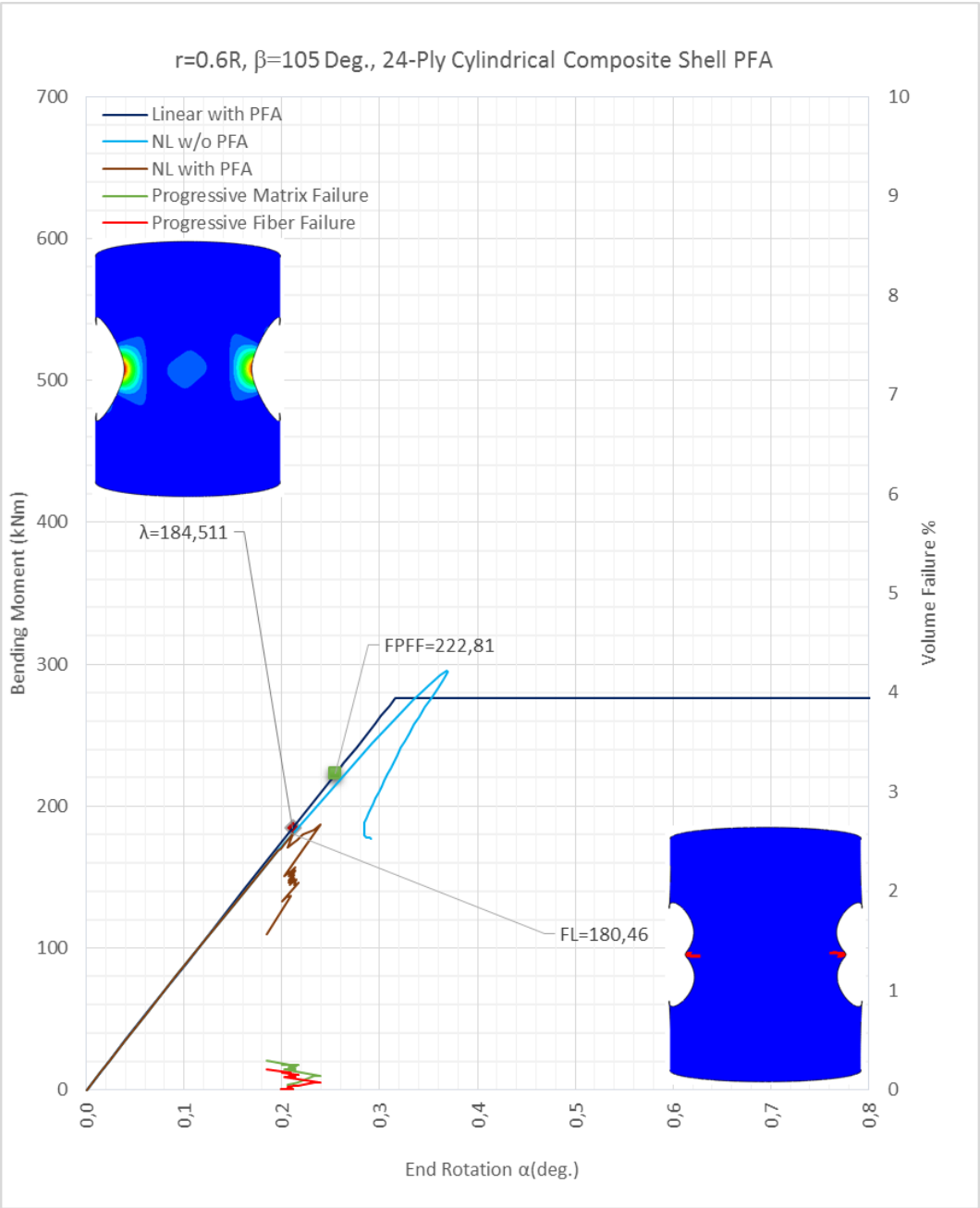


Figure H.2 : 0.6R/105 analysis result.

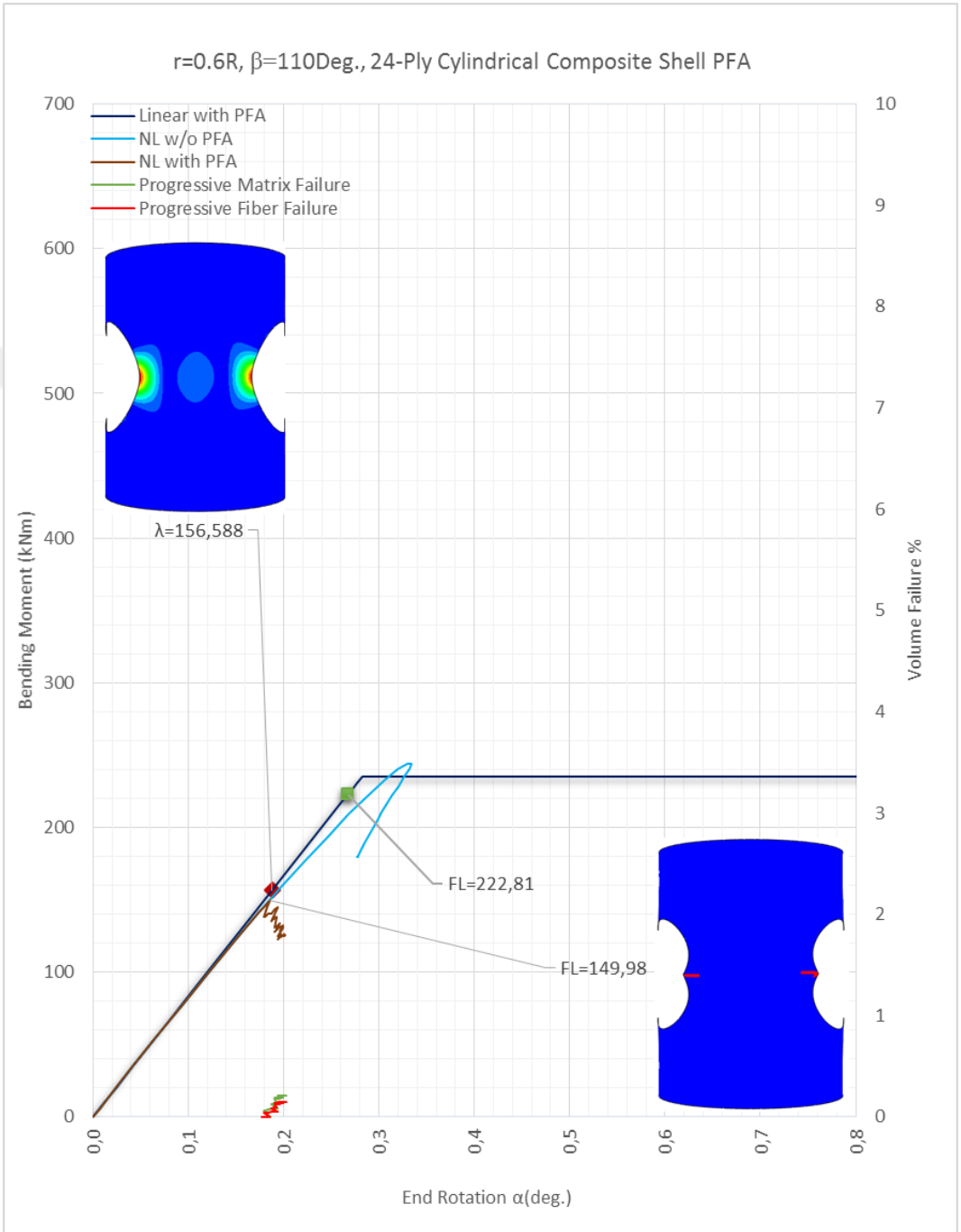


Figure H.3 : 0.6R/110 analysis result.

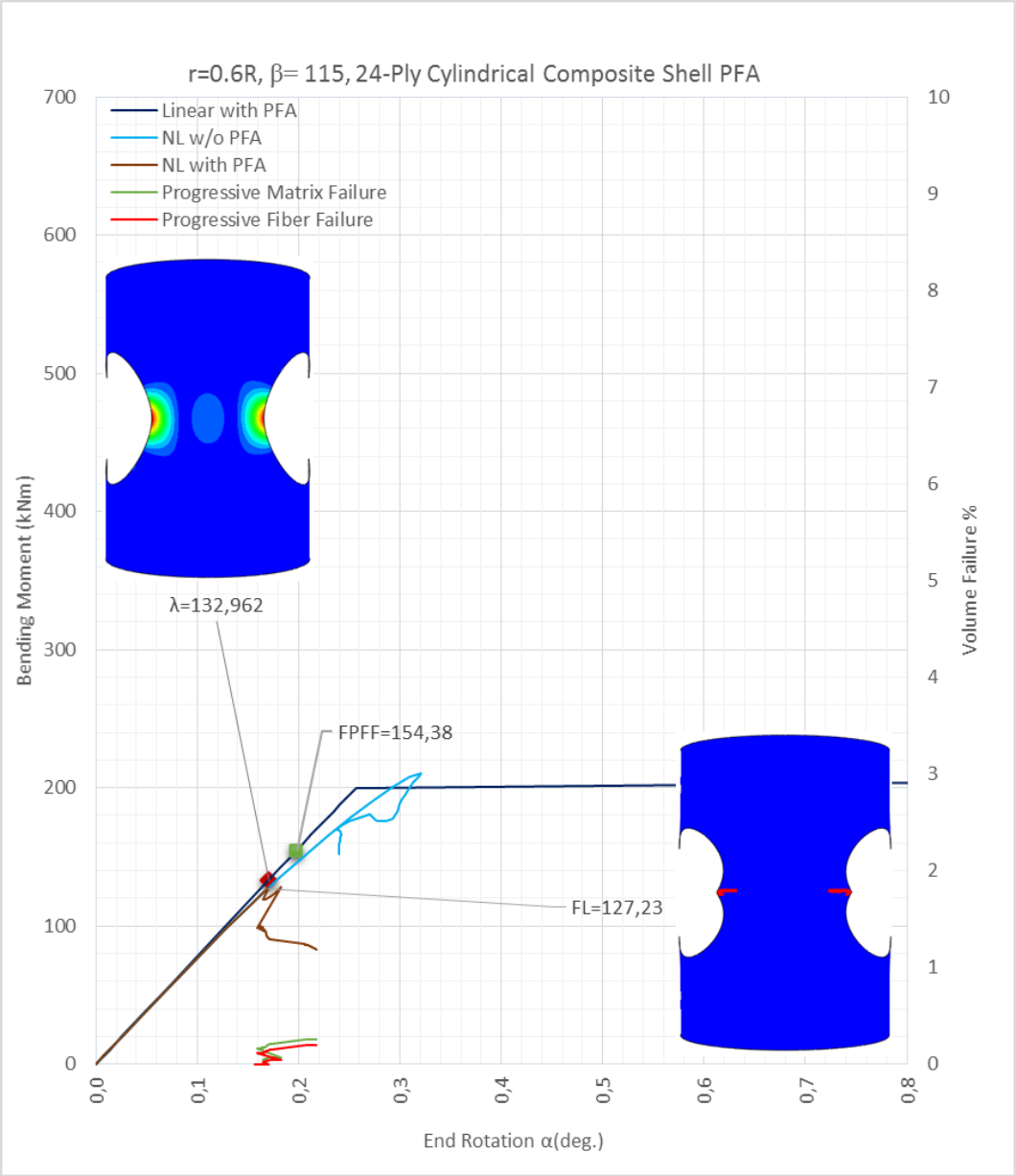


Figure H.4 : 0.6R/115 analysis result.

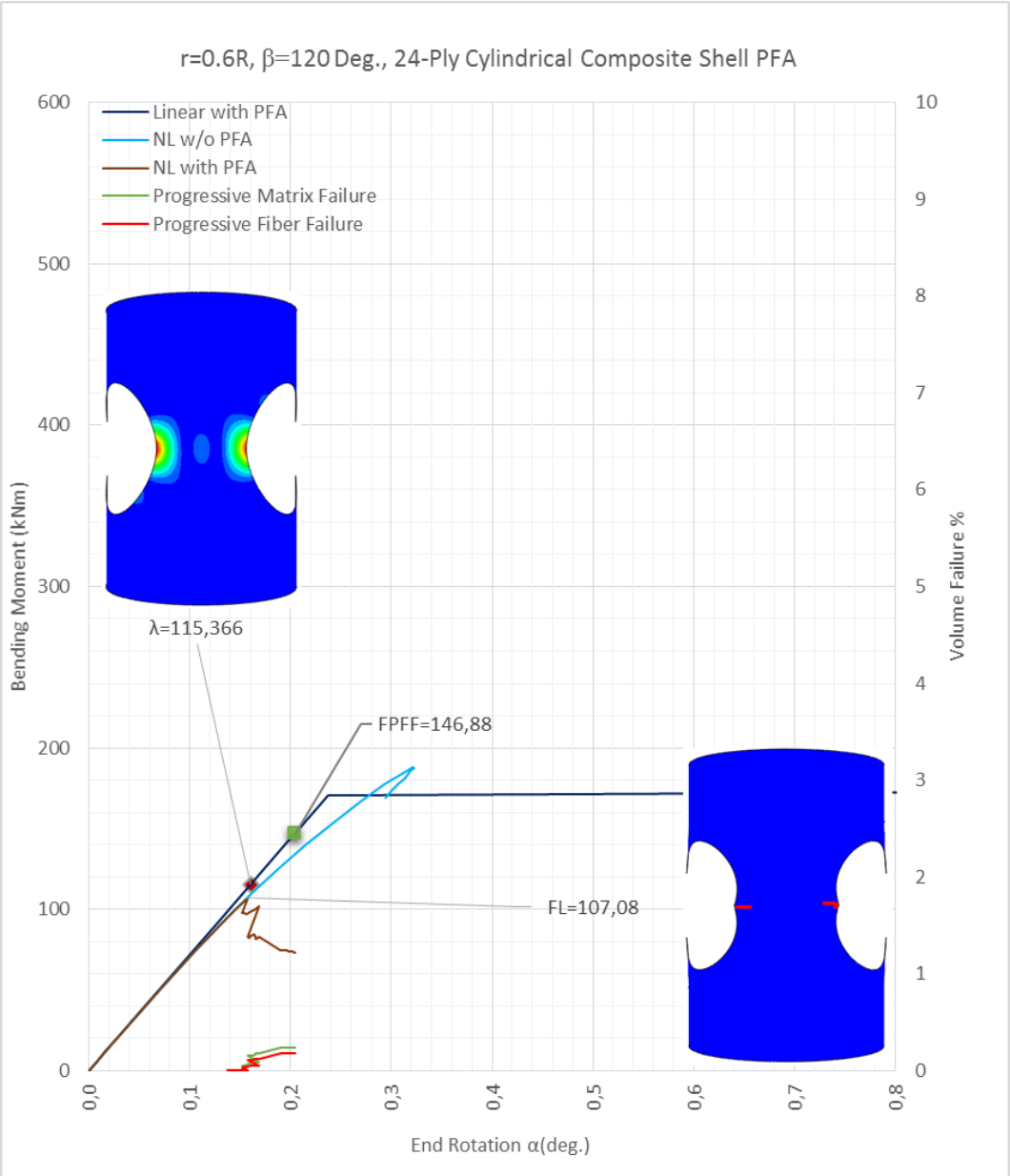


Figure H.5 : 0.6R/120 analysis result.

APPENDIX I: The Centroid Calculation of the Elements

In order to define VS fiber orientation angle it is required to find the coordinates of the centroid of the elements. The centroid of the numerical model elements were calculated from the four connected nodes of each element. Therefore, transformation of the curved surface into planar surface and then back to curved surface is needed. This is done by transformation between Cylindrical coordinate system and Cartesian coordinate system shown in Figure I.1. To perform the transformation in Python coding from cylindrical coordinate to cartesian coordinate system, following calculations were applied.

$$\theta_i = arctan(y,x) \tag{I.1}$$

$$S_i = R.\theta_i \tag{I.2}$$

$$Z_i = z_i, (i = 0,3) \tag{I.3}$$

where x, y and z are the coordinates of the nodes in curved surface.

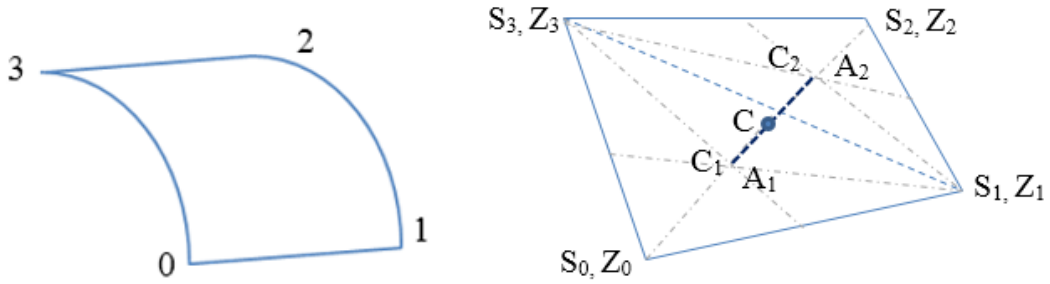


Figure I.1 : Cylindrical and Cartesian coordinate representations.

$$C_1 = (\frac{S_0+S_1+S_3}{3}, \frac{Z_0+Z_1+Z_3}{3}) \tag{I.4}$$

$$C_2 = (\frac{S_1+S_2+S_3}{3}, \frac{Z_1+Z_2+Z_3}{3}) \tag{I.5}$$

$$A_1 = \frac{1}{2}abs[(S_1-S_0).(Z_3-Z_1)-(S_1-S_3).(Z_0-Z_1)] \tag{I.6}$$

$$A_2 = \frac{1}{2}abs[(S_1-S_3).(Z_2-Z_1)-(S_1-S_2).(Z_3-Z_1)] \tag{I.7}$$

$$C = (\frac{A_1.C_{1s}+A_2.C_{2s}}{A_1+A_2}, \frac{A_1.C_{1z}+A_2.C_{2z}}{A_1+A_2}) \tag{I.8}$$

$$C = (S,Z), \theta = \frac{S}{R} \tag{I.9}$$

Coordinates of nodes in curved surface:

$$x = R.\sin\theta, y = R.\cos\theta, z = Z \tag{I.10}$$

APPENDIX J: VS Cylinder Linear Buckling Results for Cutout Configurations

Table J.1 : VS cylinder eigenvalue and mode shapes for cutout positions.

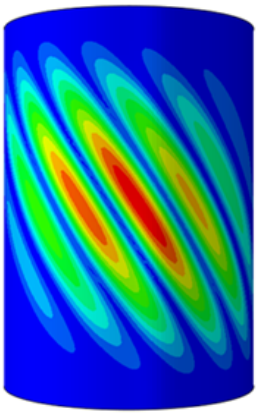
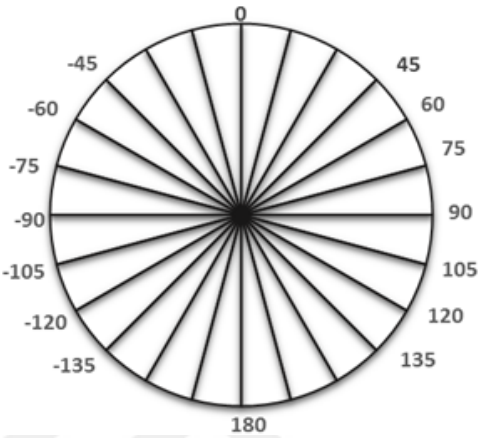
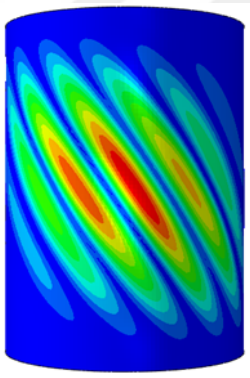
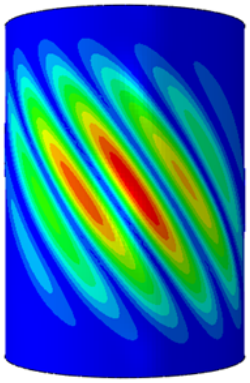
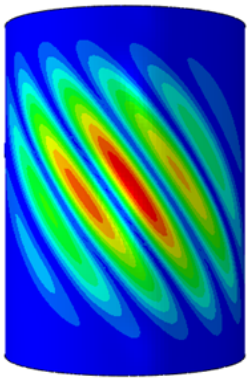
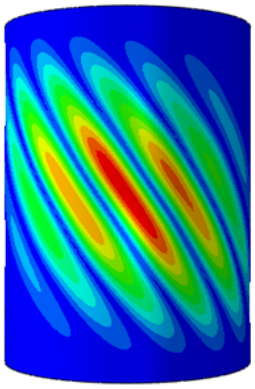
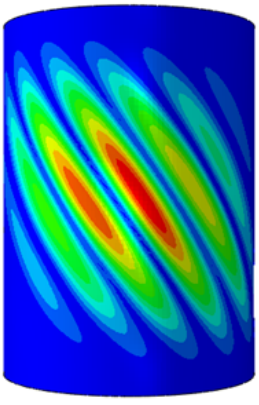
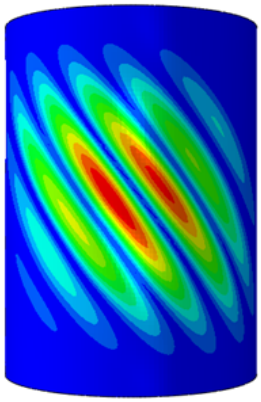
No Cutout	(λ /FL) kNm	836.95/590.20	
			
β	0.1R:λ/FL (kNm)	0.3R:λ/FL (kNm)	0.5R:λ/FL (kNm)
0°	830.61/598.87	776.21/435.46	694.44/398.34
			
±45°	834.77/598.74	810.71/495.57	747.89/332.39
			

Table J.2 : VS cylinder eigenvalue and mode shapes for cutout positions (cont.).

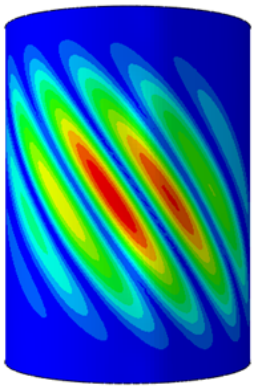
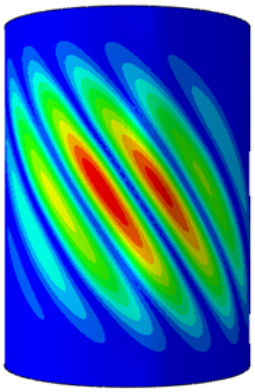
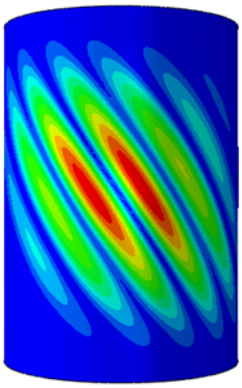
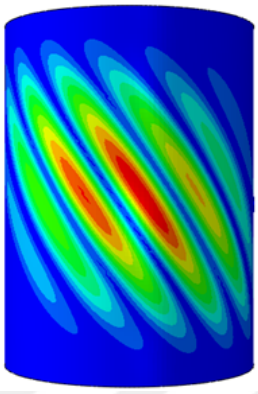
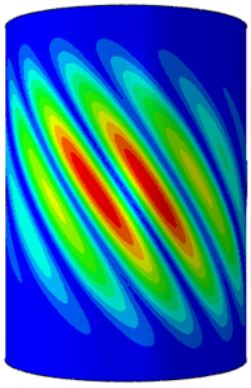
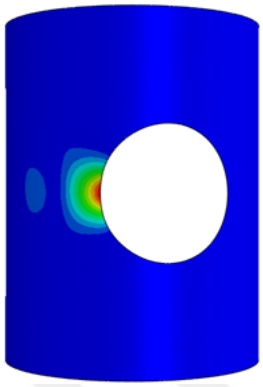
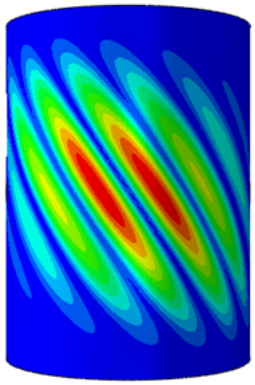
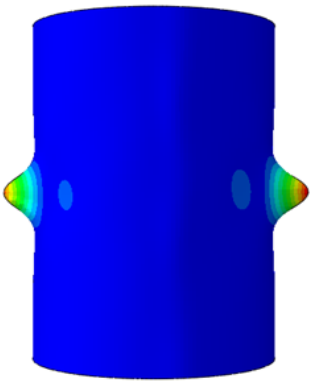
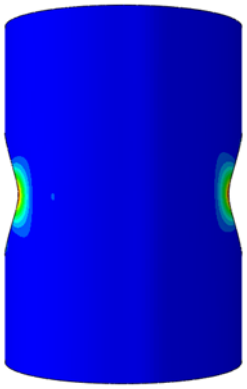
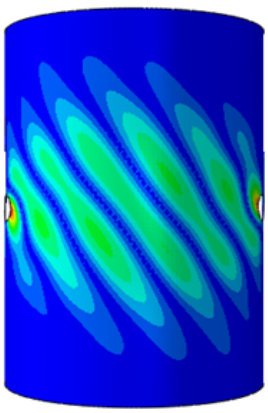
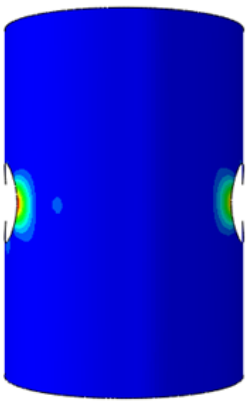
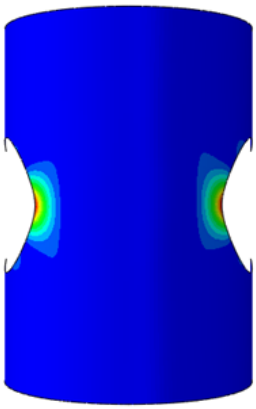
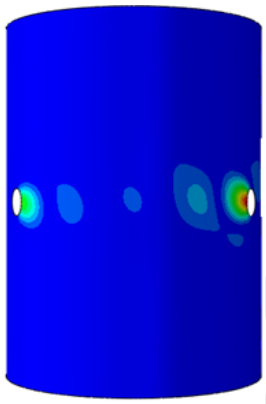
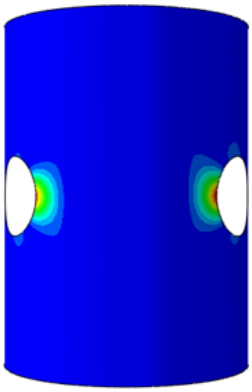
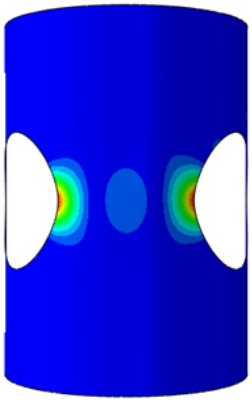
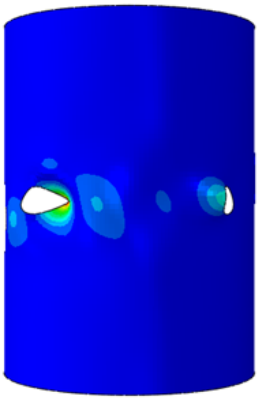
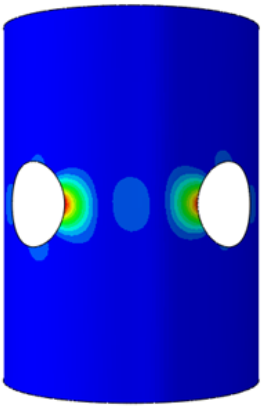
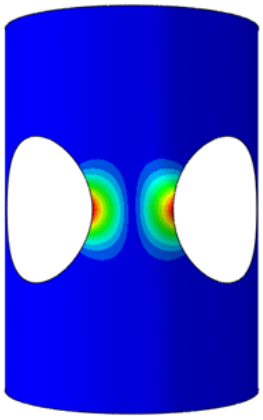
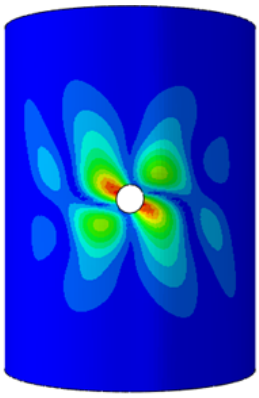
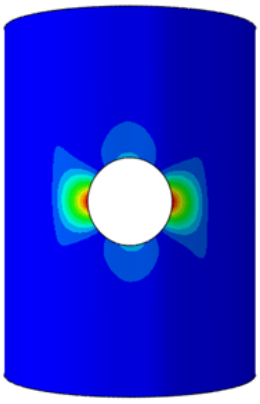
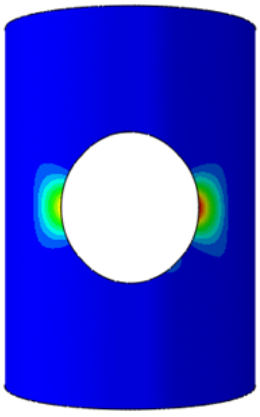
β	0.1R:λ/FL (kNm)	0.3R:λ/FL (kNm)	0.5R:λ/FL (kNm)
$\pm 60^\circ$	837.06/600.18	846.75/593.94	843.24/546.48
			
$\pm 75^\circ$	839.20/573.39	844.32/553.39	560.58/484.44
			
$\pm 90^\circ$	833.25/550.58	507.87/481.10	305.26/312.86
			
$\pm 105^\circ$	809.11/585.78	330.85/294.79	207.01/201.22
			

Table J.3 : VS cylinder eigenvalue and mode shapes for cutout positions (cont.).

β	0.1R:λ/FL (kNm)	0.3R:λ/FL (kNm)	0.5R:λ/FL (kNm)
$\pm 120^\circ$	658.49/402.59	252.82/212.24	152.96/143.40
			
$\pm 135^\circ$	587.49/353.98	214.14/169.30	115.34/96.73
			
180°	578.82/317.34	226.31/177.54	167.65/154.93
			

APPENDIX K: VS, 0.1R Cutout Analysis Results

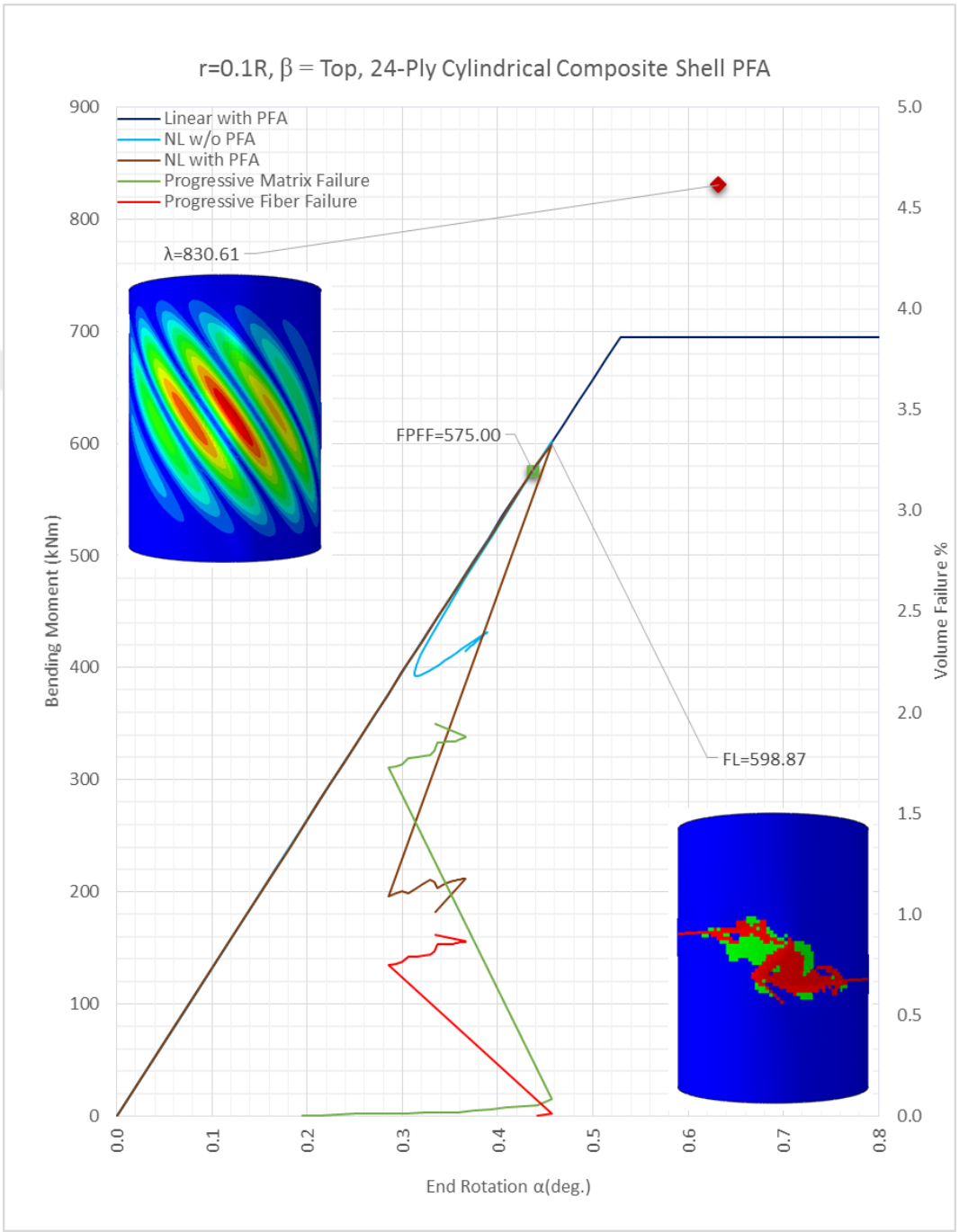


Figure K.1 : 0.1R/0 analysis result.

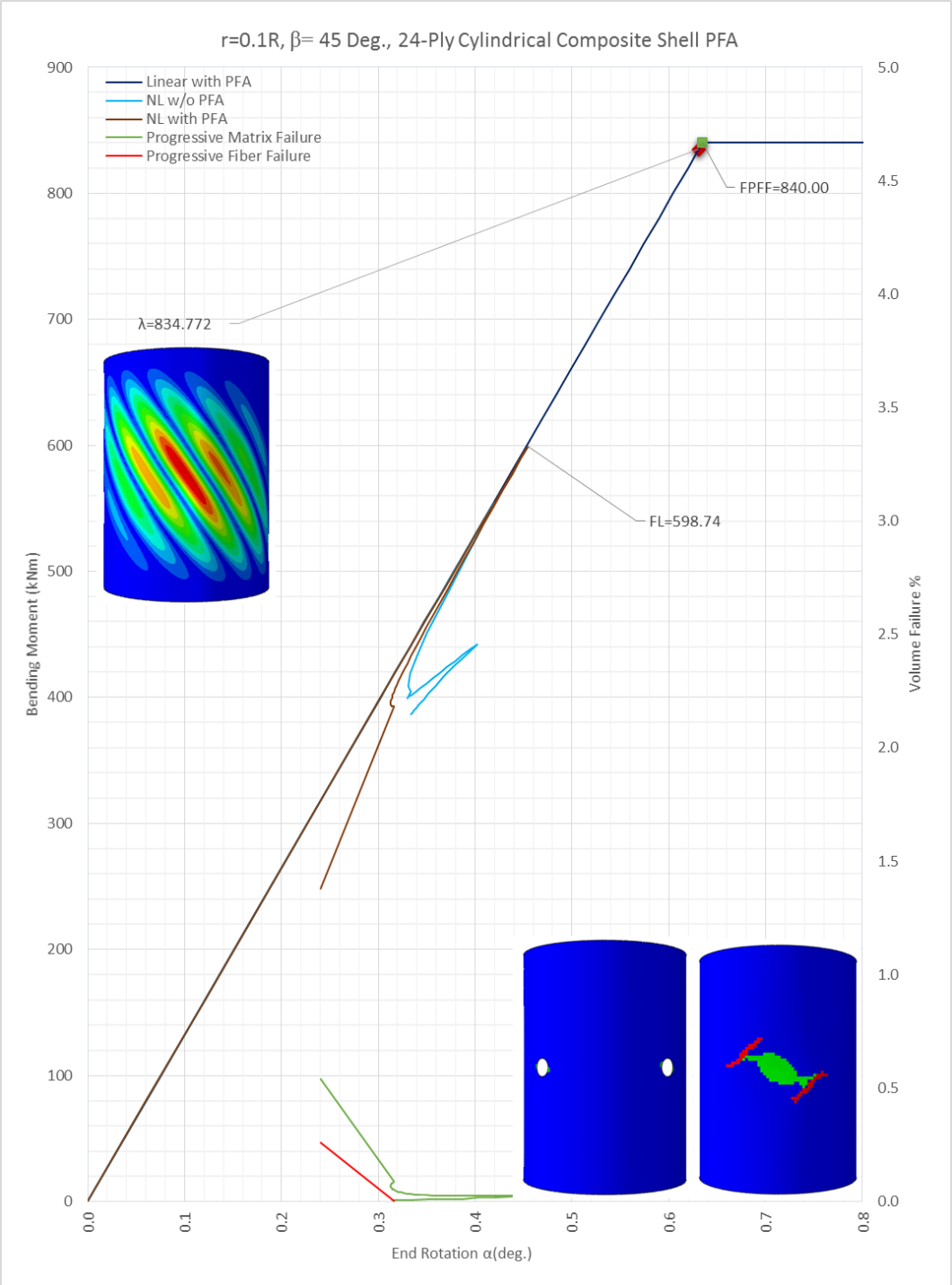


Figure K.2 : 0.1R/45 analysis result.

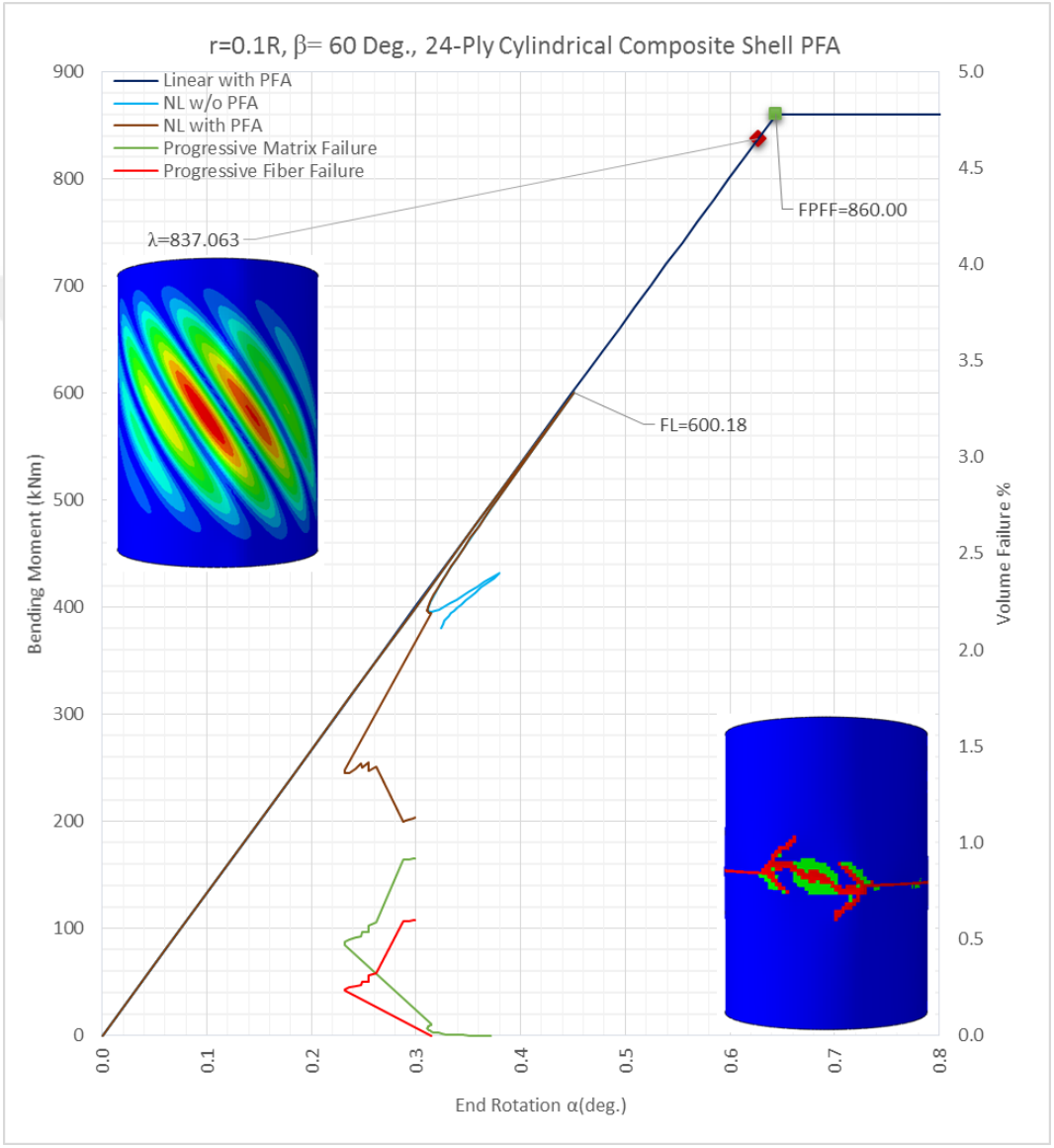


Figure K.3 : 0.1R/60 analysis result.

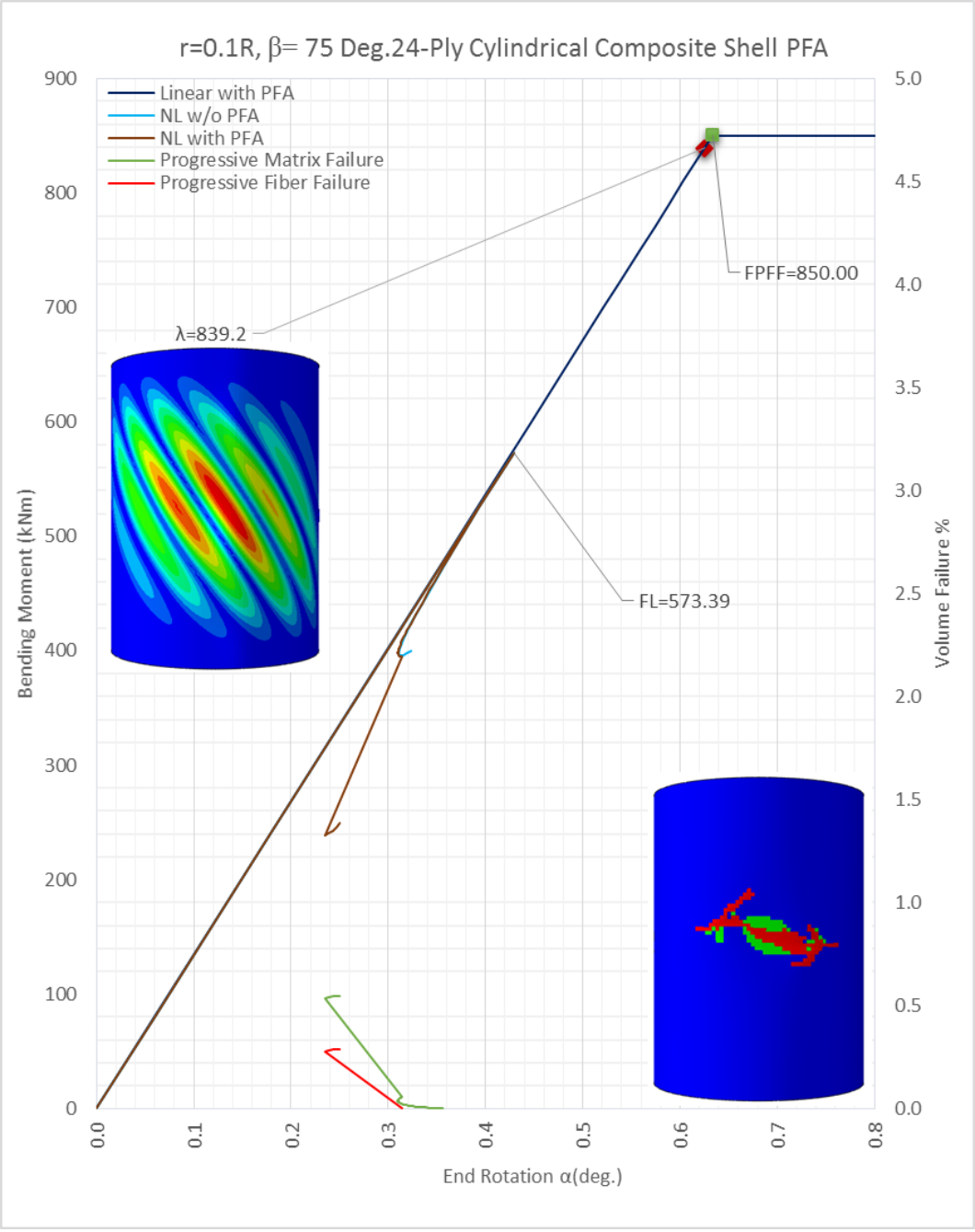


Figure K.4 : 0.1R/75 analysis result.

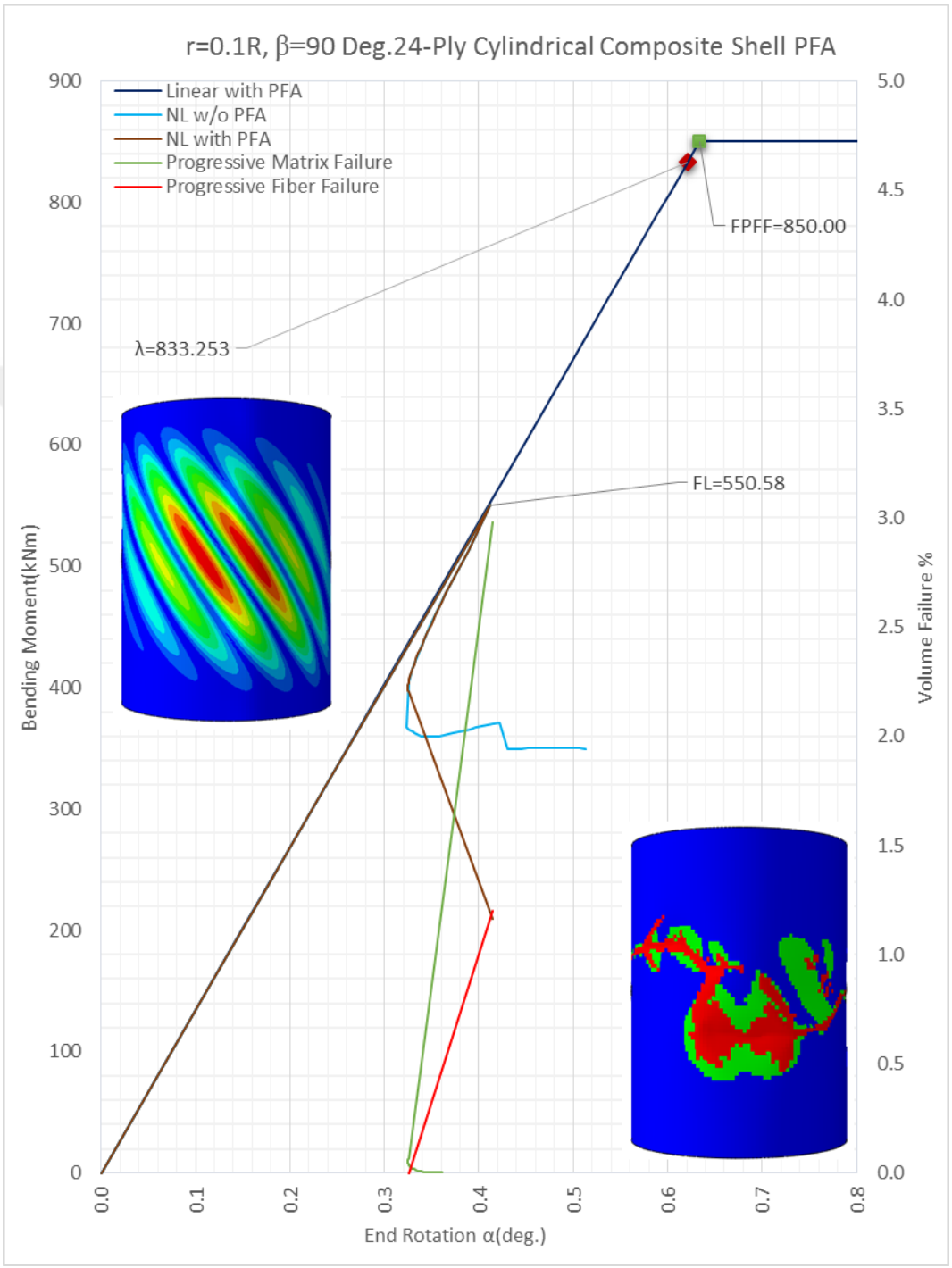


Figure K.5 : 0.1R/90 analysis result.

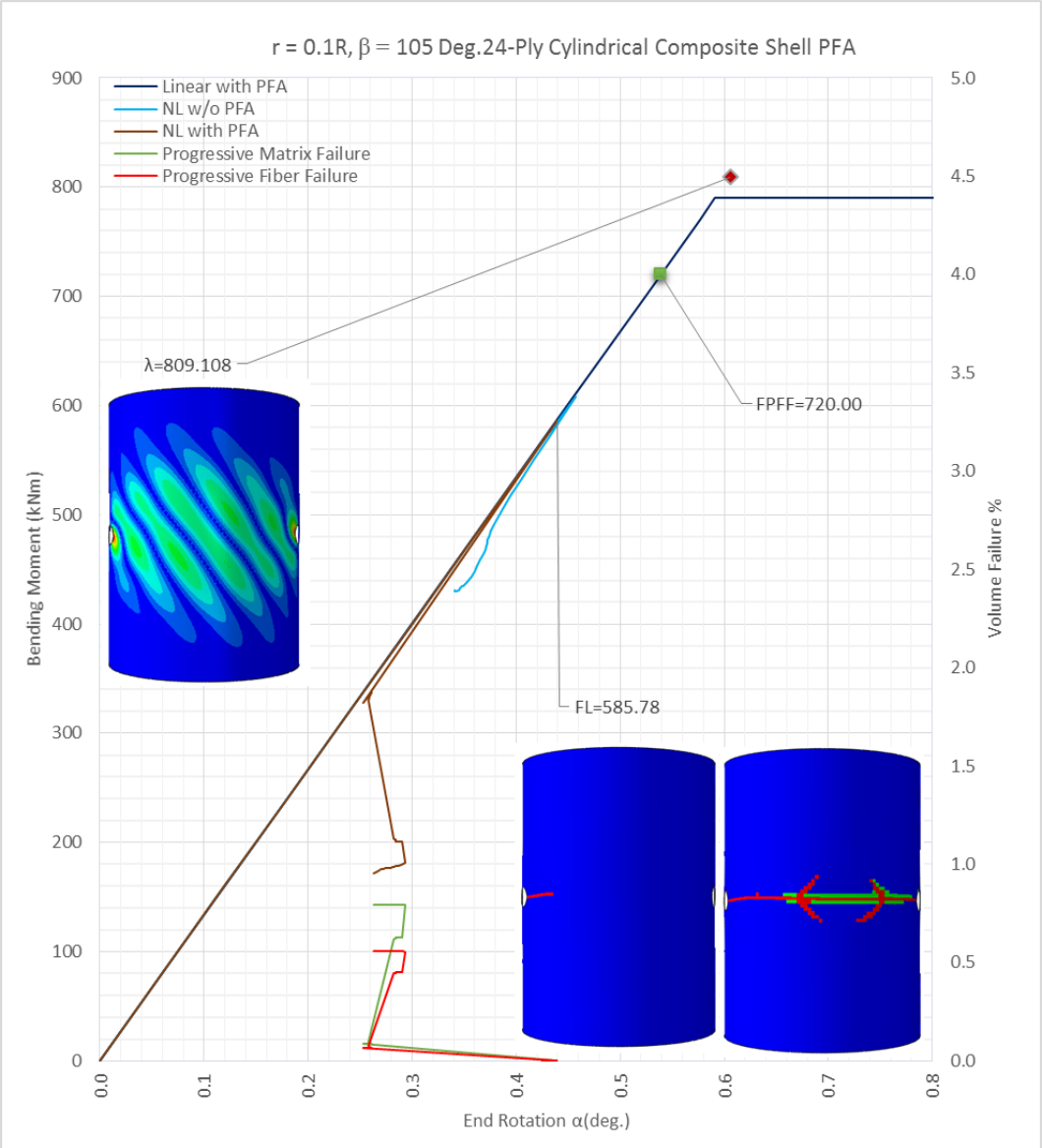


Figure K.6 : 0.1R/105 analysis result.

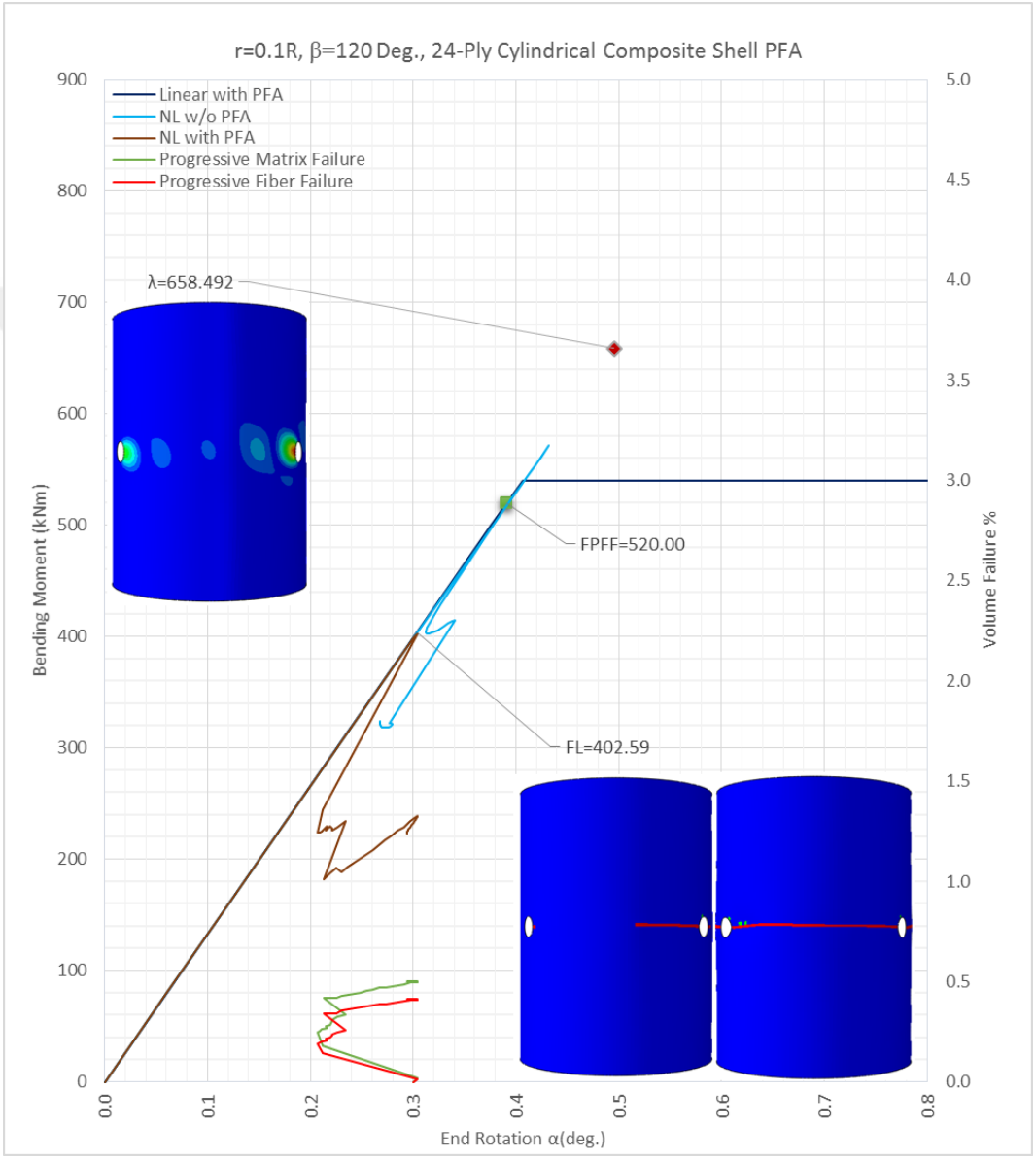


Figure K.7 : 0.1R/120 analysis result.

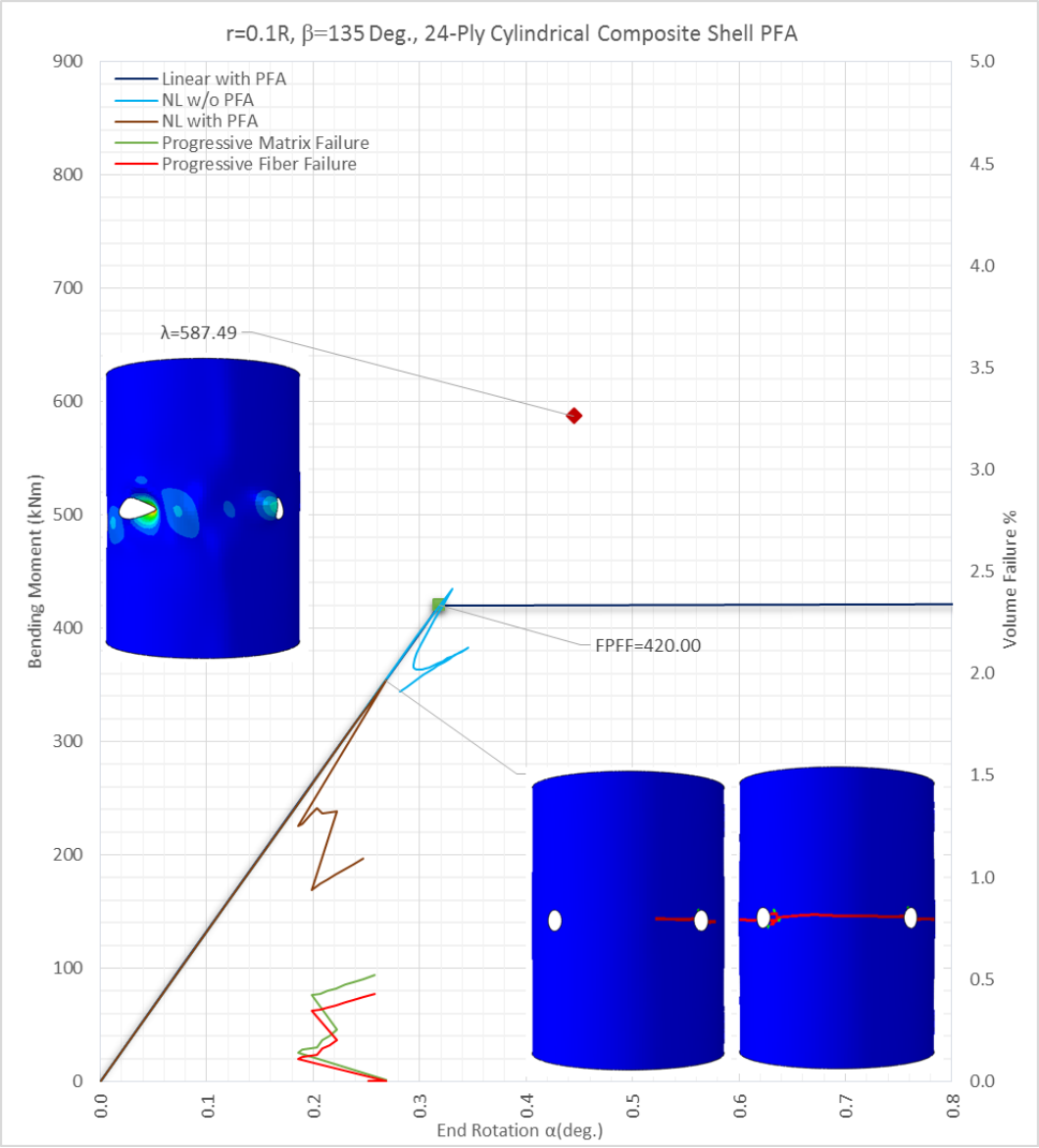


Figure K.8 : 0.1R/135 analysis result.

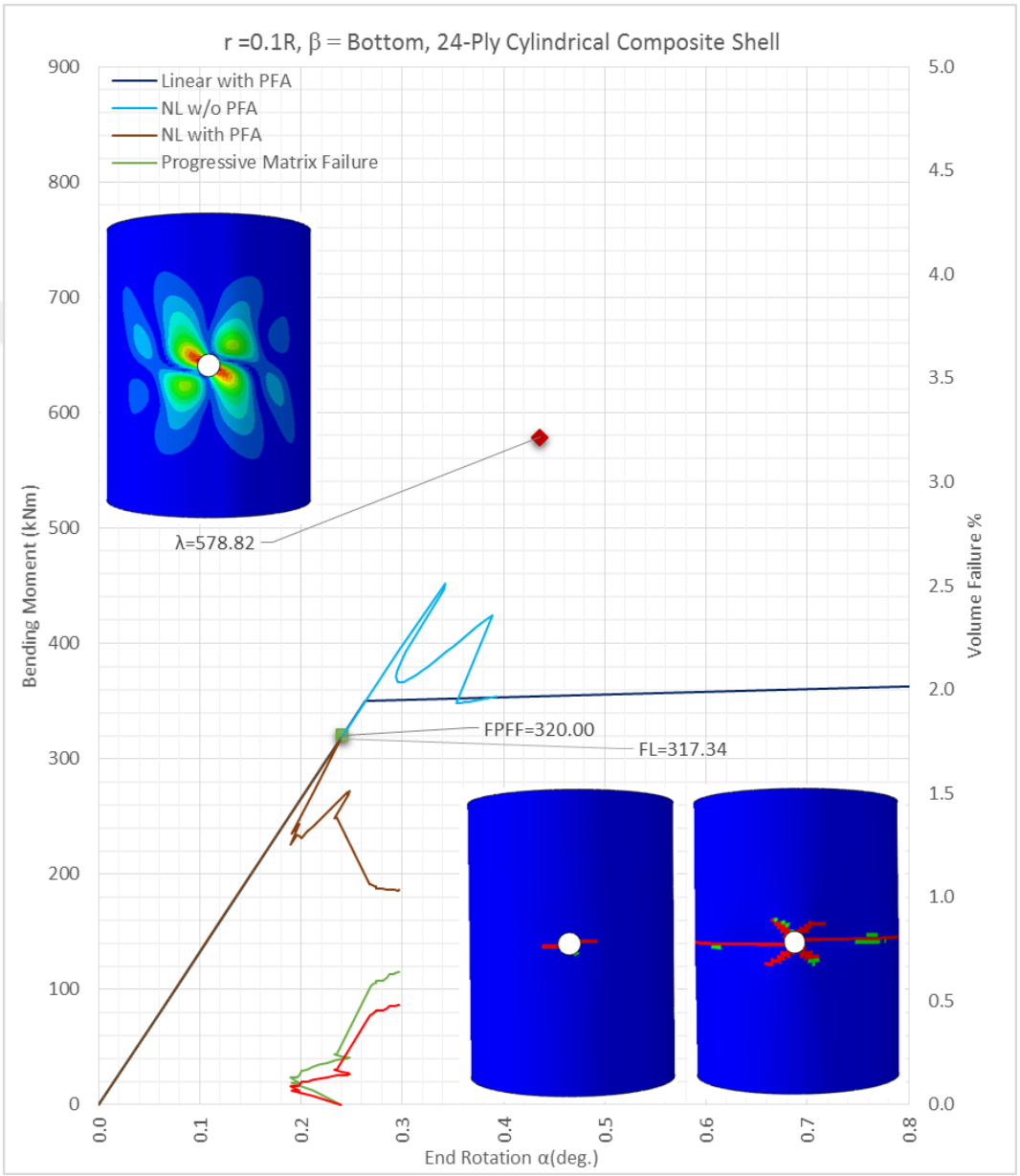


Figure K.9 : 0.1R/180 analysis result.

APPENDIX L: VS, 0.3R Cutout Analysis Results

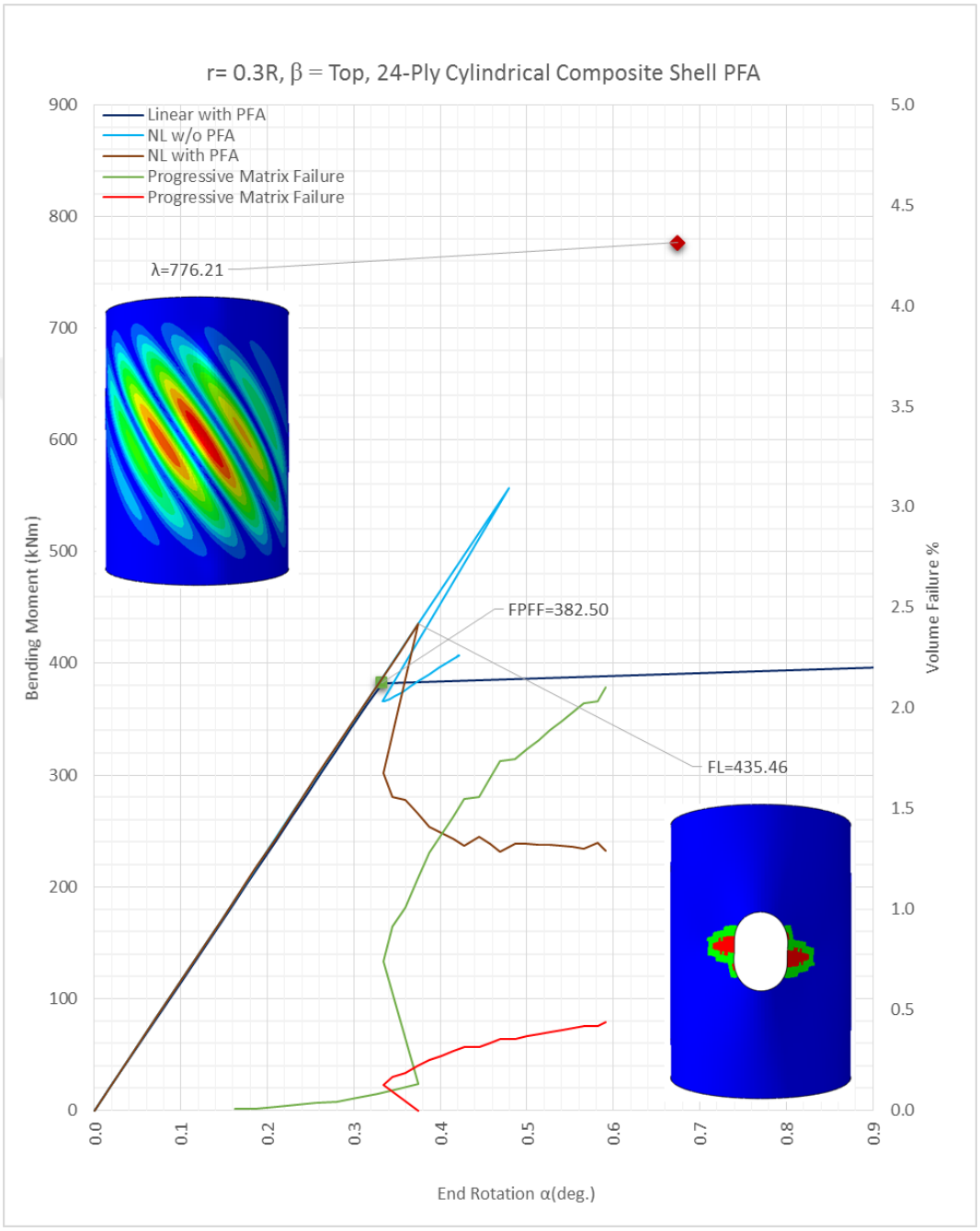


Figure L.1 : 0.3R/0 analysis result.

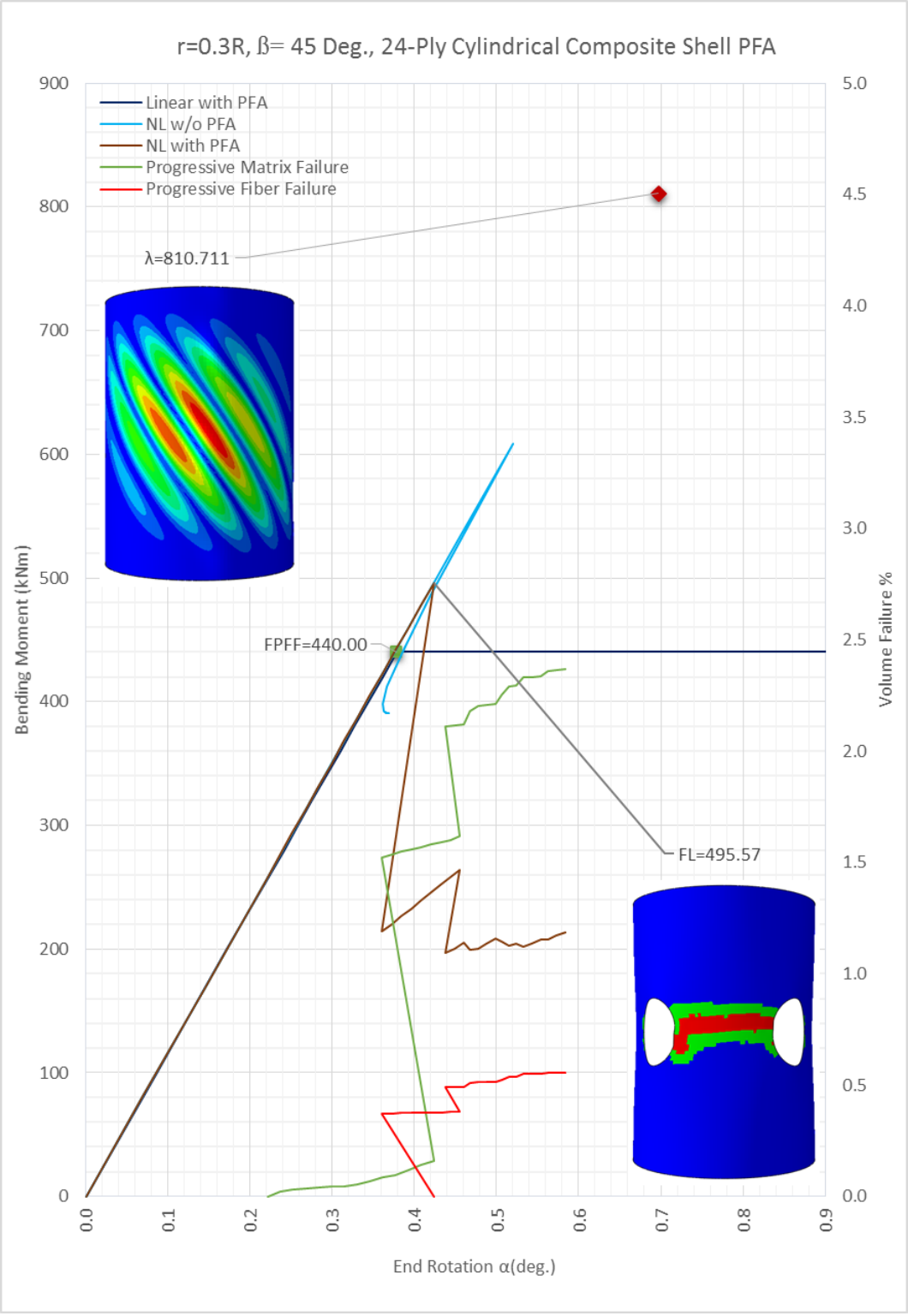


Figure L.2 : 0.3R/45 analysis result.

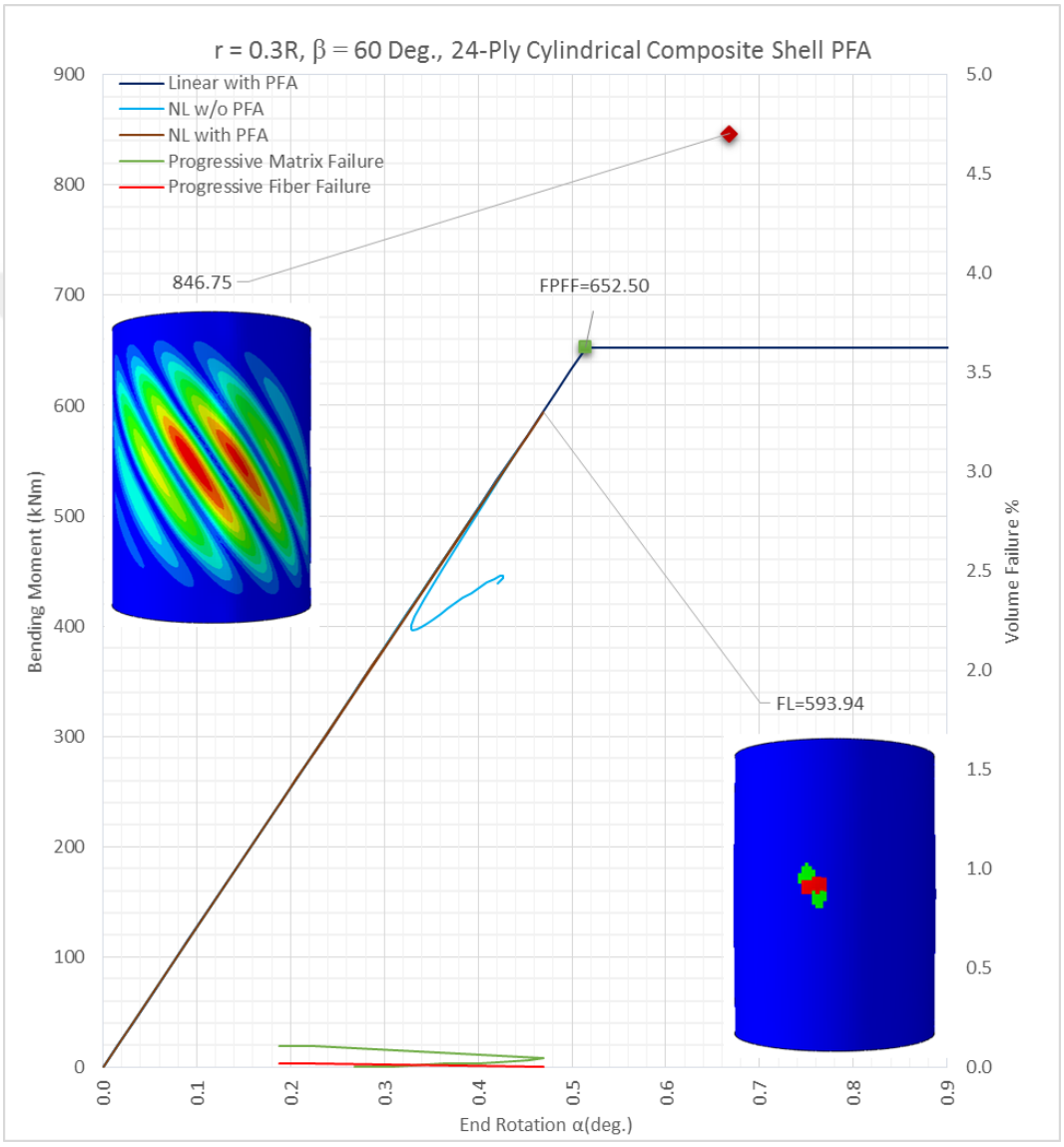


Figure L.3 : 0.3R/60 analysis result.

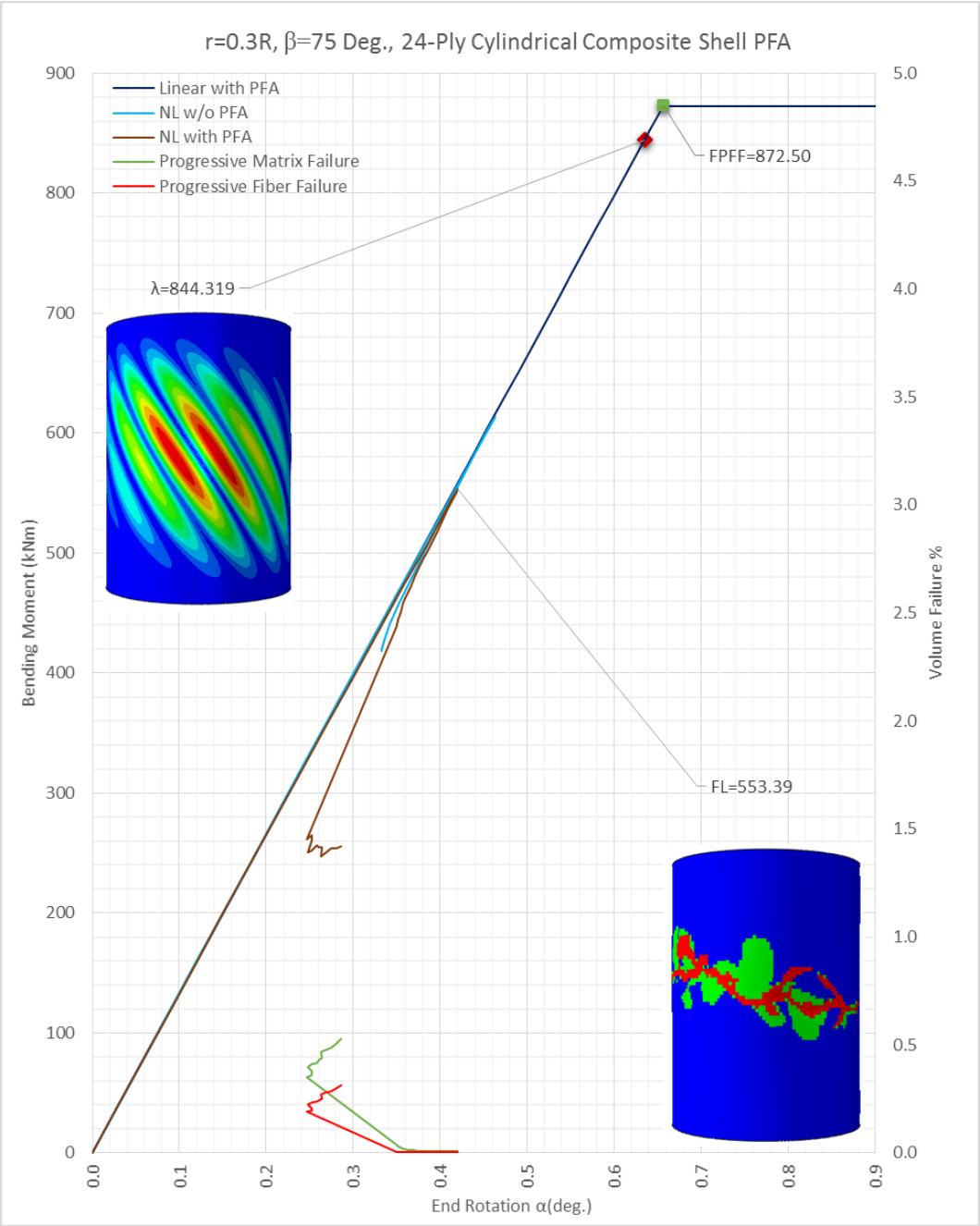


Figure L.4 : 0.3R/75 analysis result.

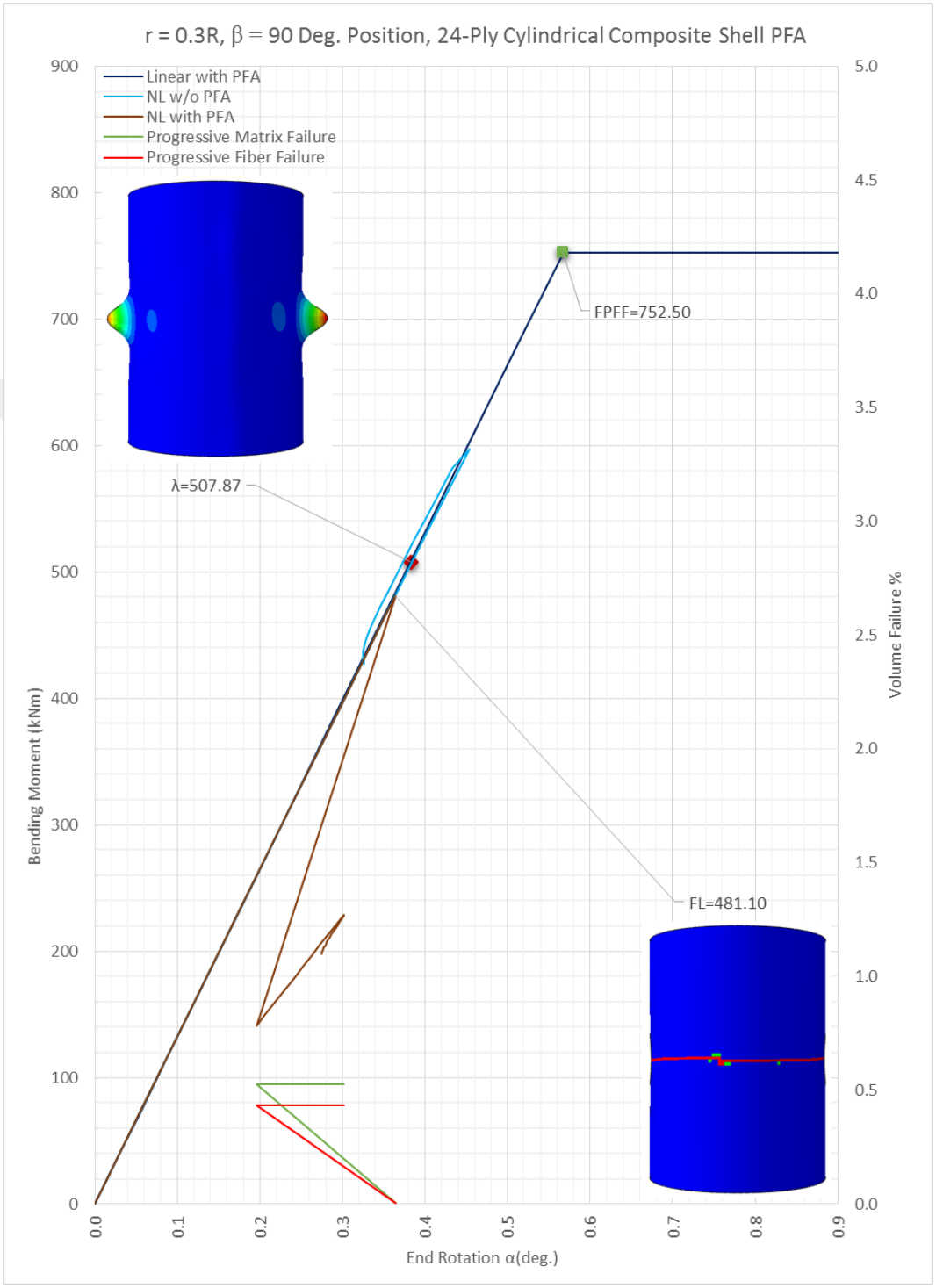


Figure L.5 : 0.3R/90 analysis result.

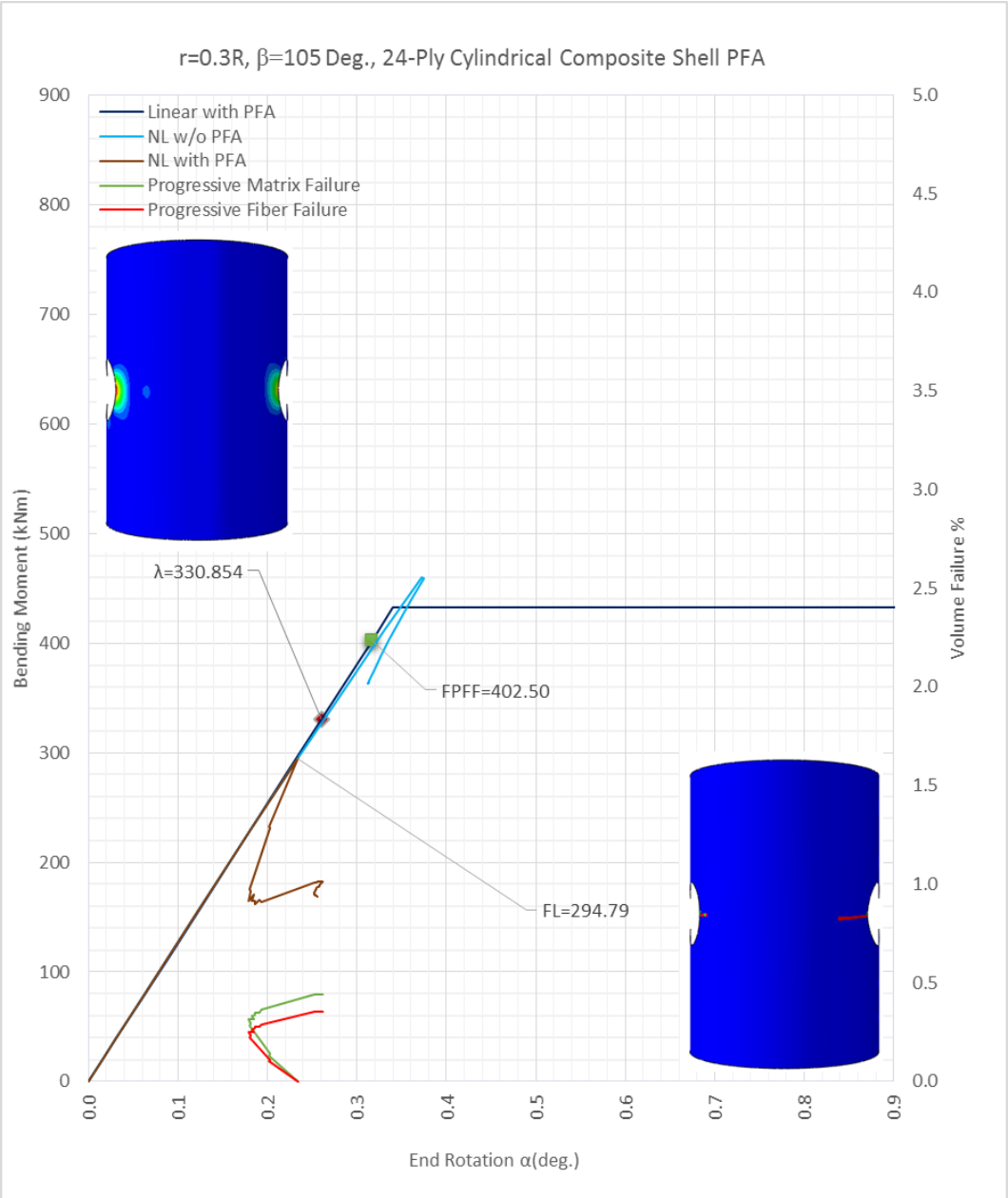


Figure L.6 : 0.3R/105 analysis result.

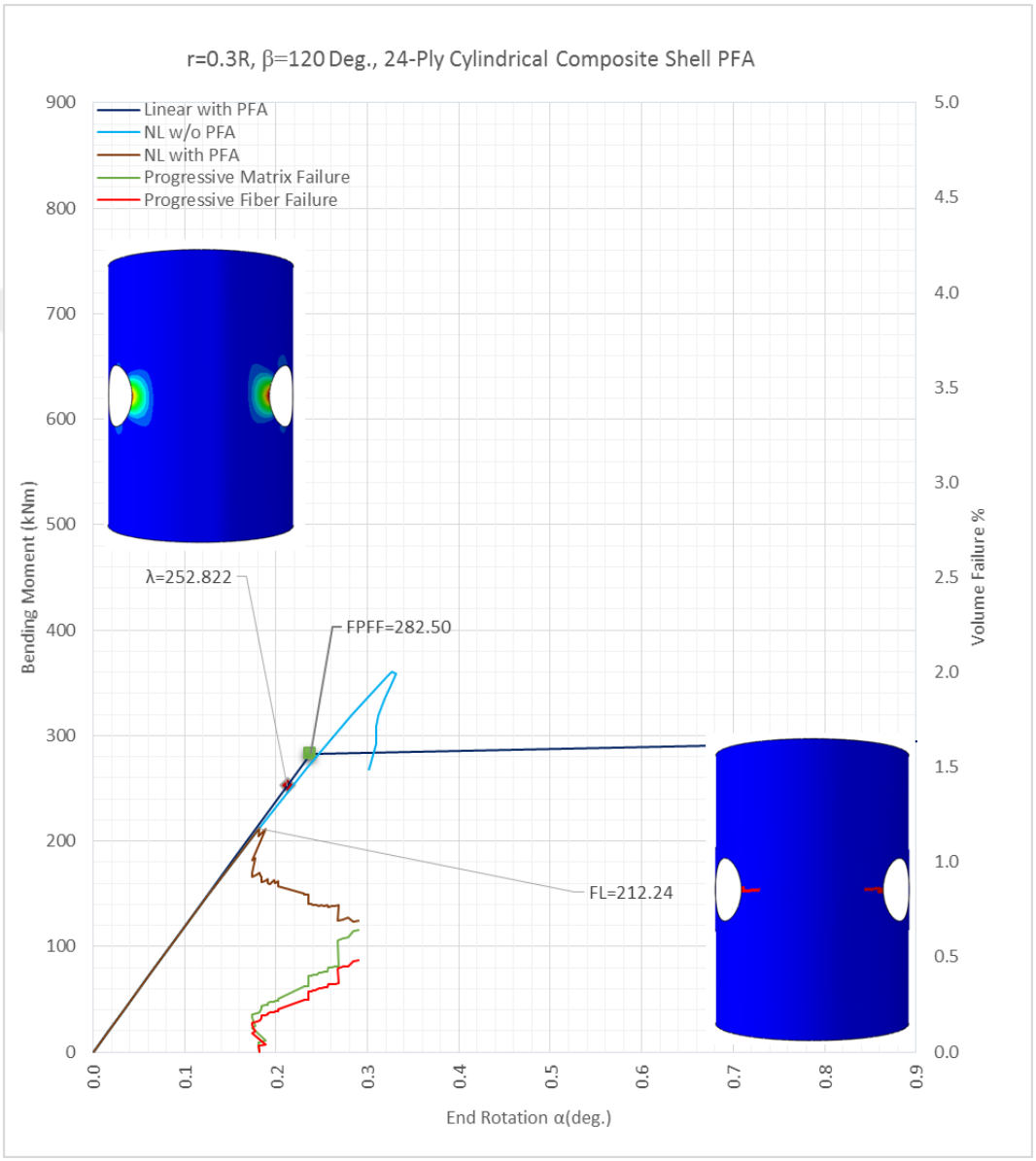


Figure L.7 : 0.3R/120 analysis result.

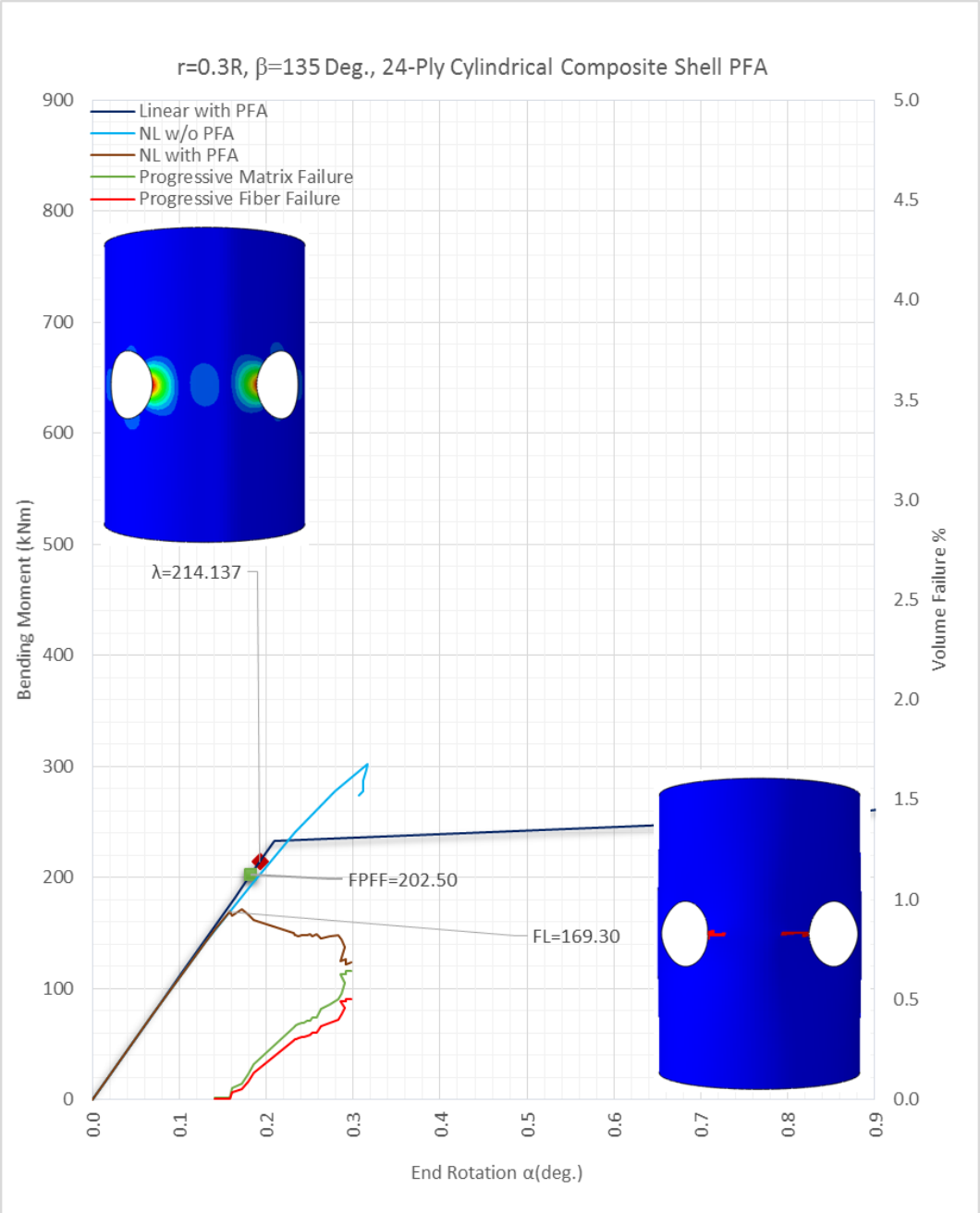


Figure L.8 : 0.3R/135 analysis result.

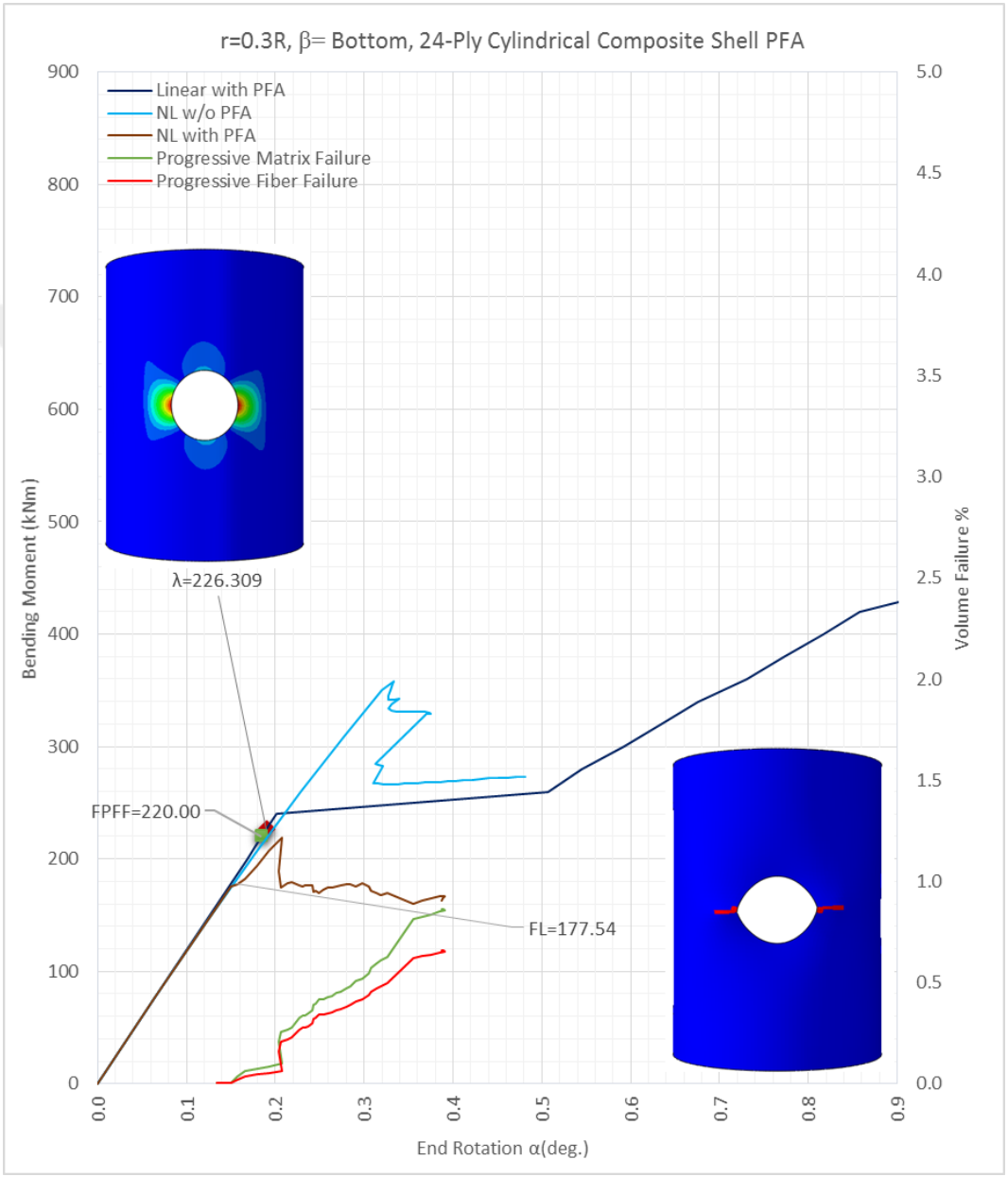


Figure L.9 : 0.3R/180 analysis result.

APPENDIX M: VS, 0.5R Cutout Analysis Results

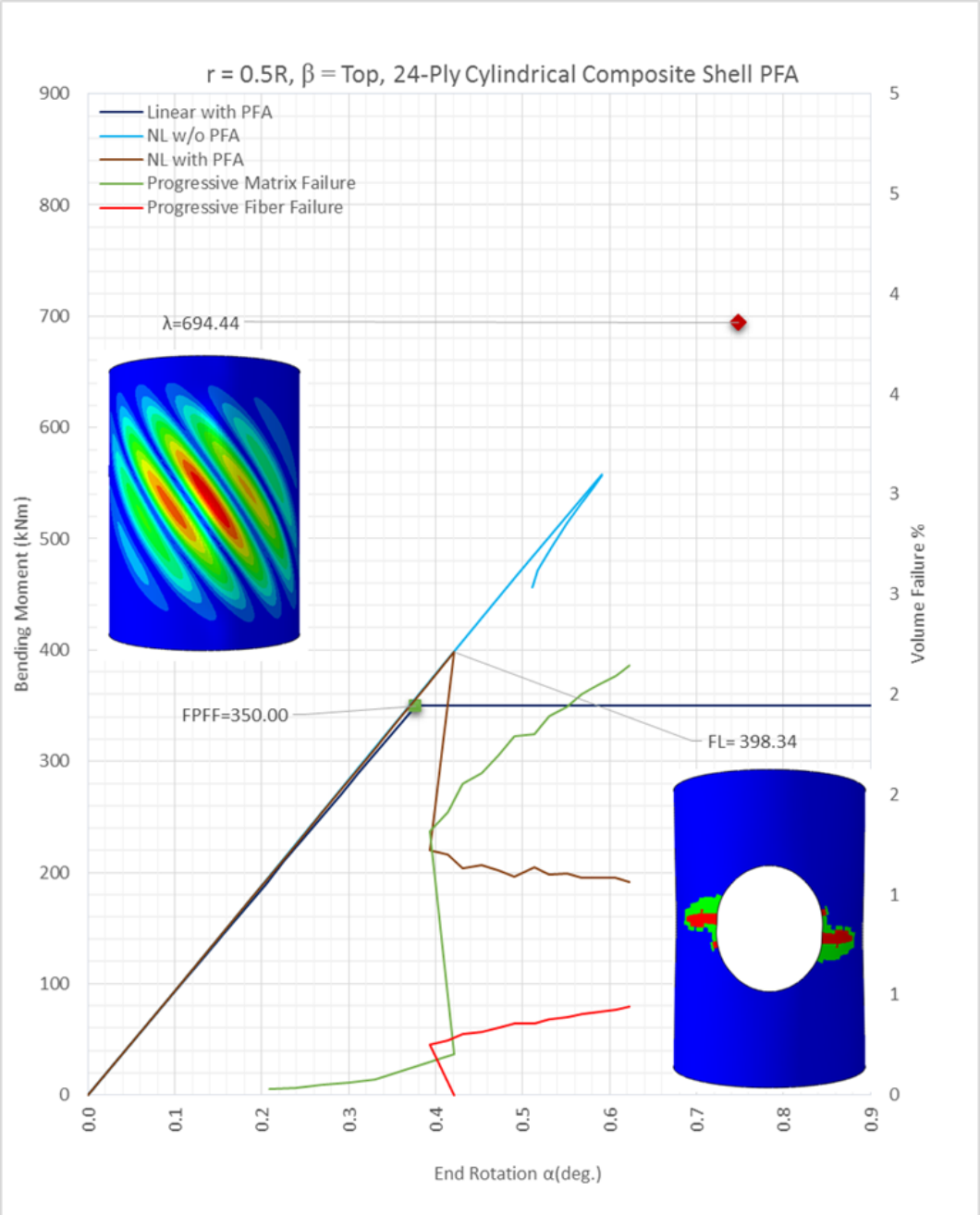


Figure M.1 : 0.5R/0 analysis result.

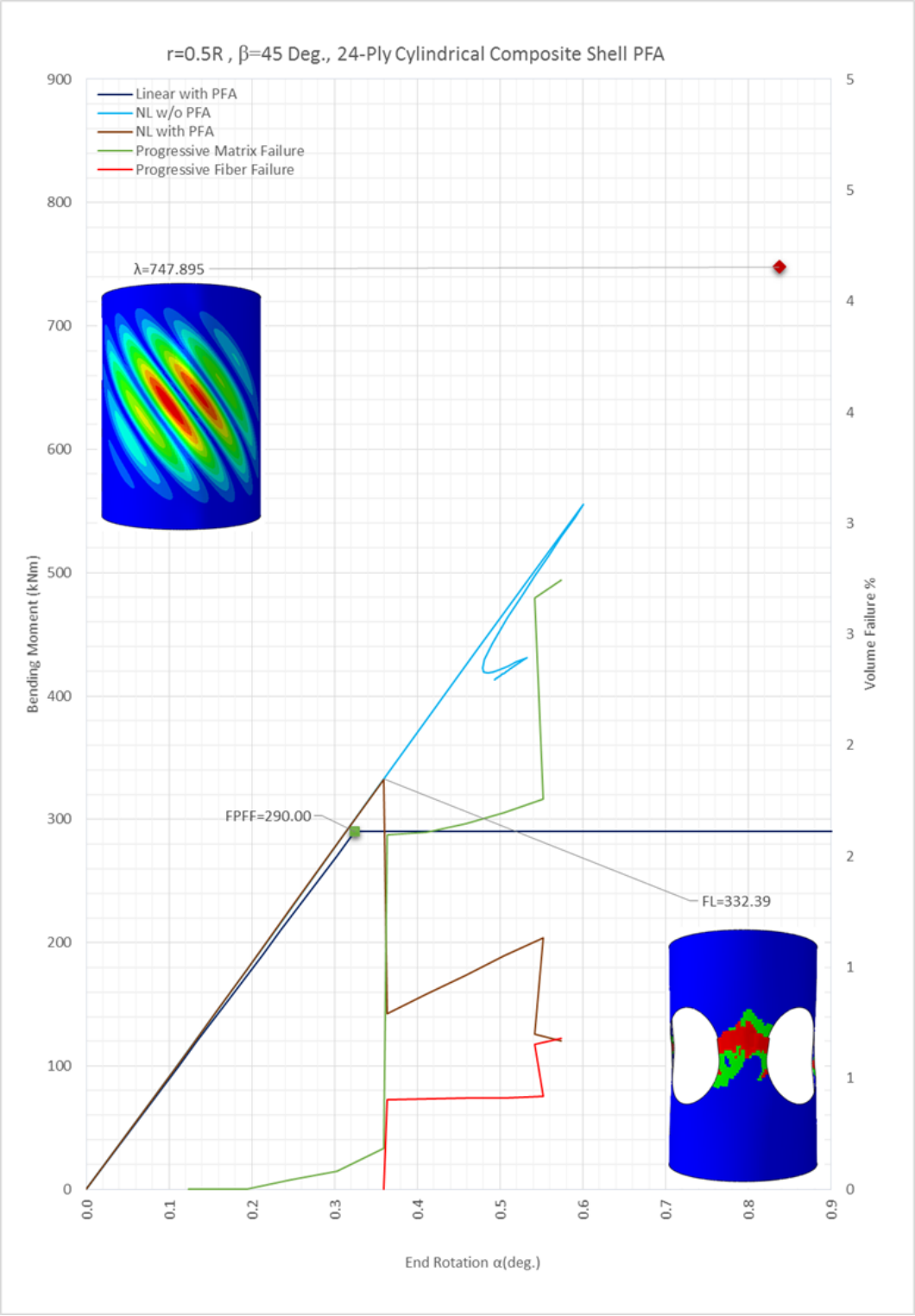


Figure M.2 : 0.5R/45 analysis result.

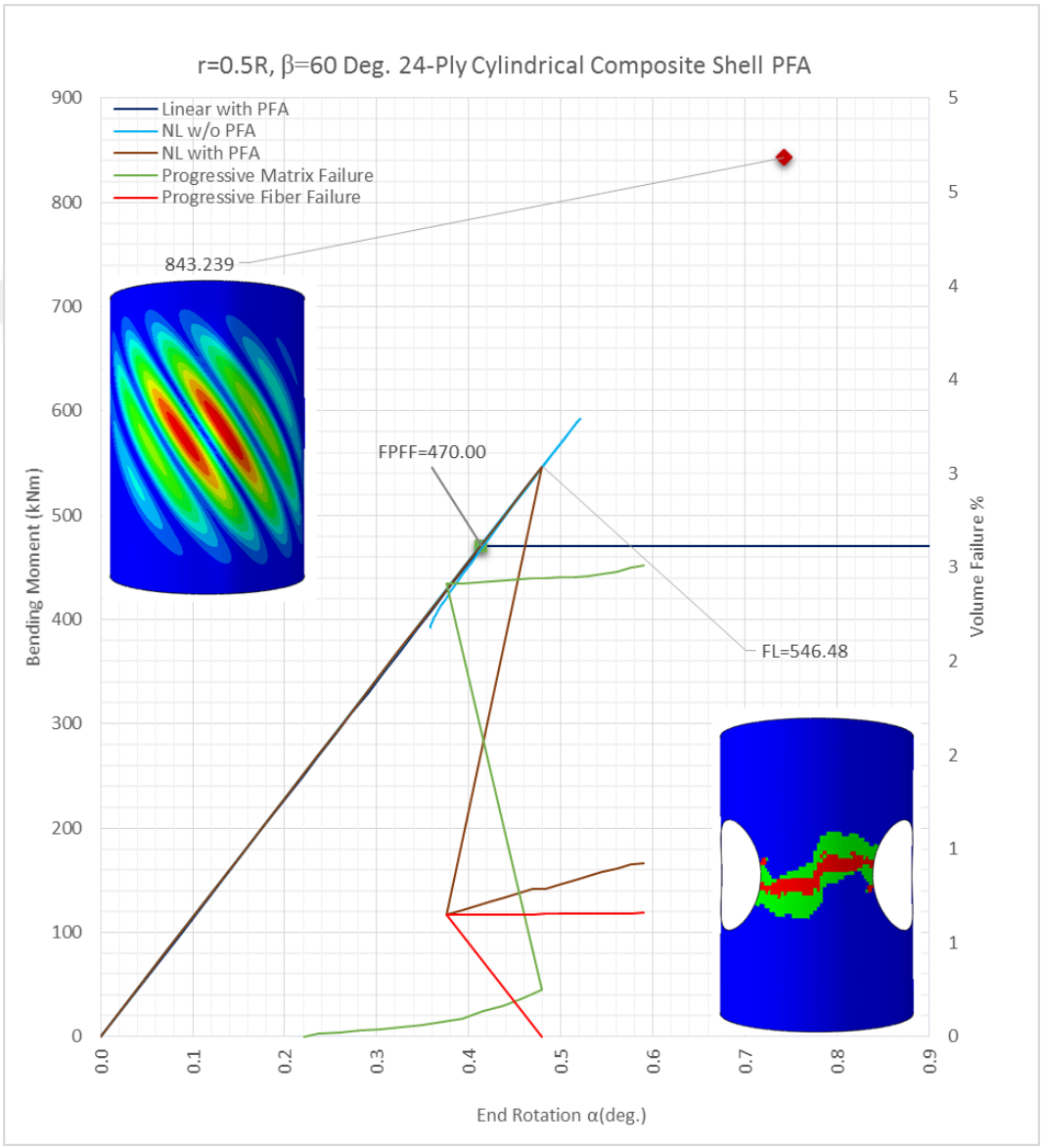


Figure M.3 : 0.5R/60 analysis result.

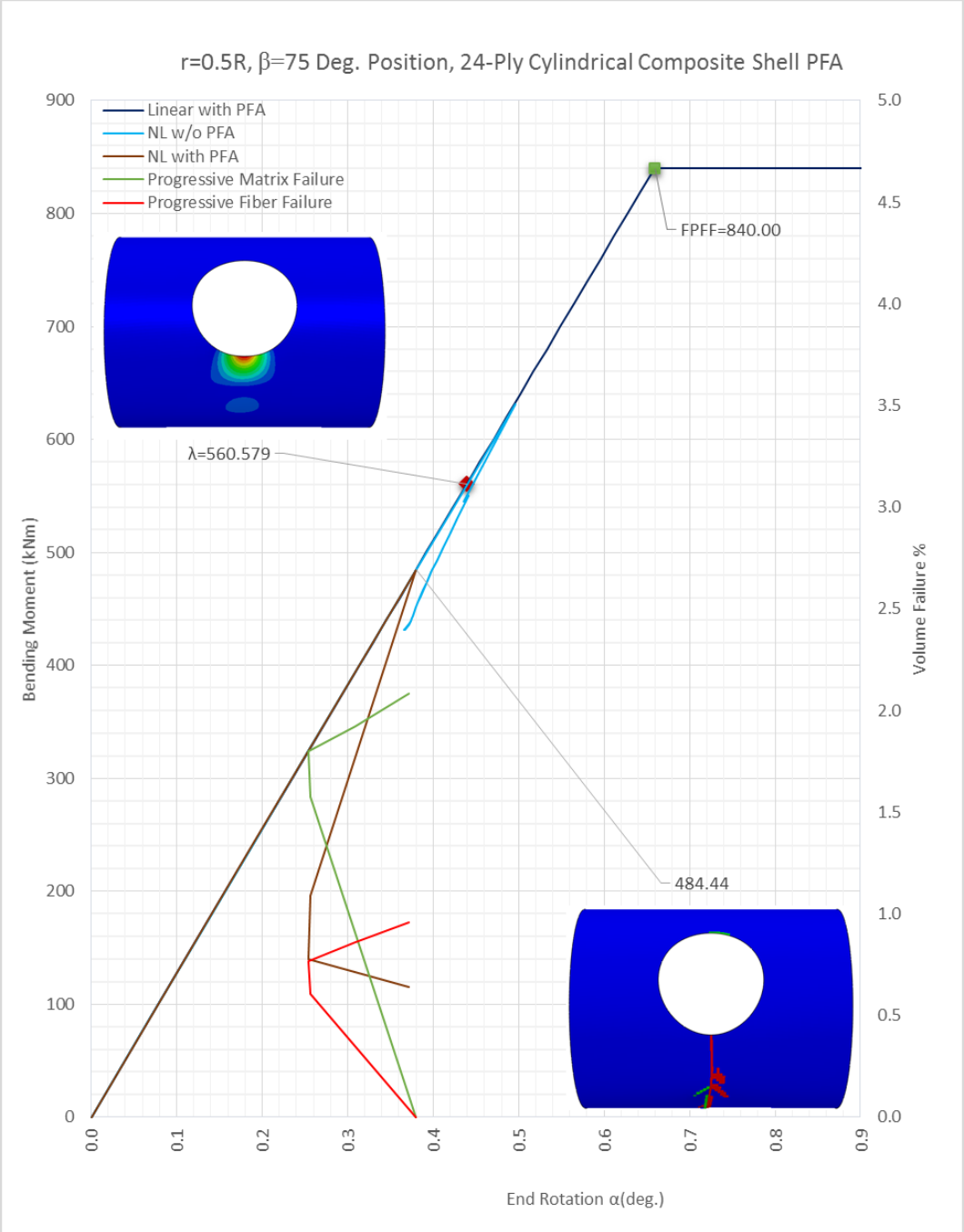


Figure M.4 : 0.5R/75 analysis result.

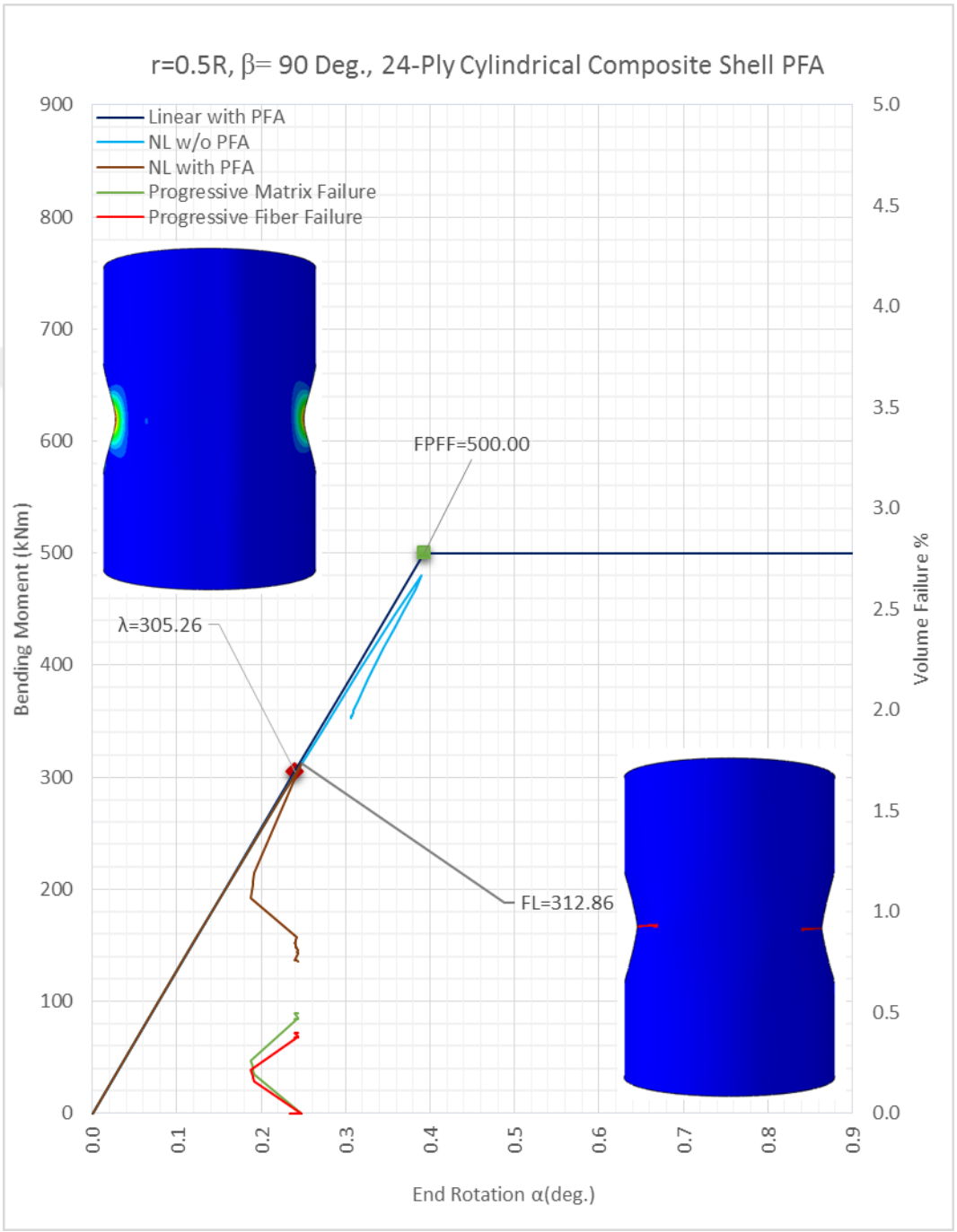


Figure M.5 : 0.5R/90 analysis result.

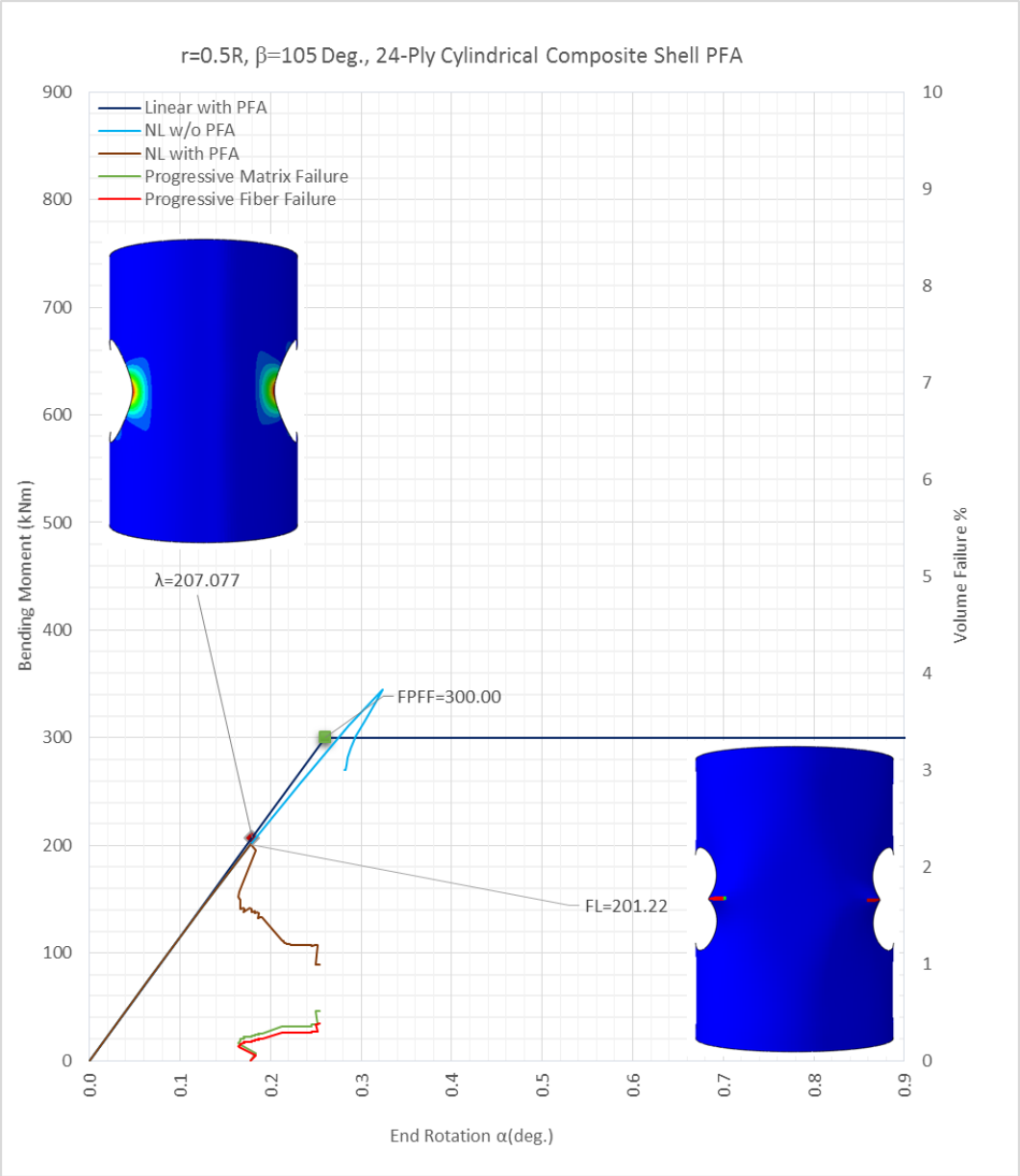


Figure M.6 : 0.5R/105 analysis result.

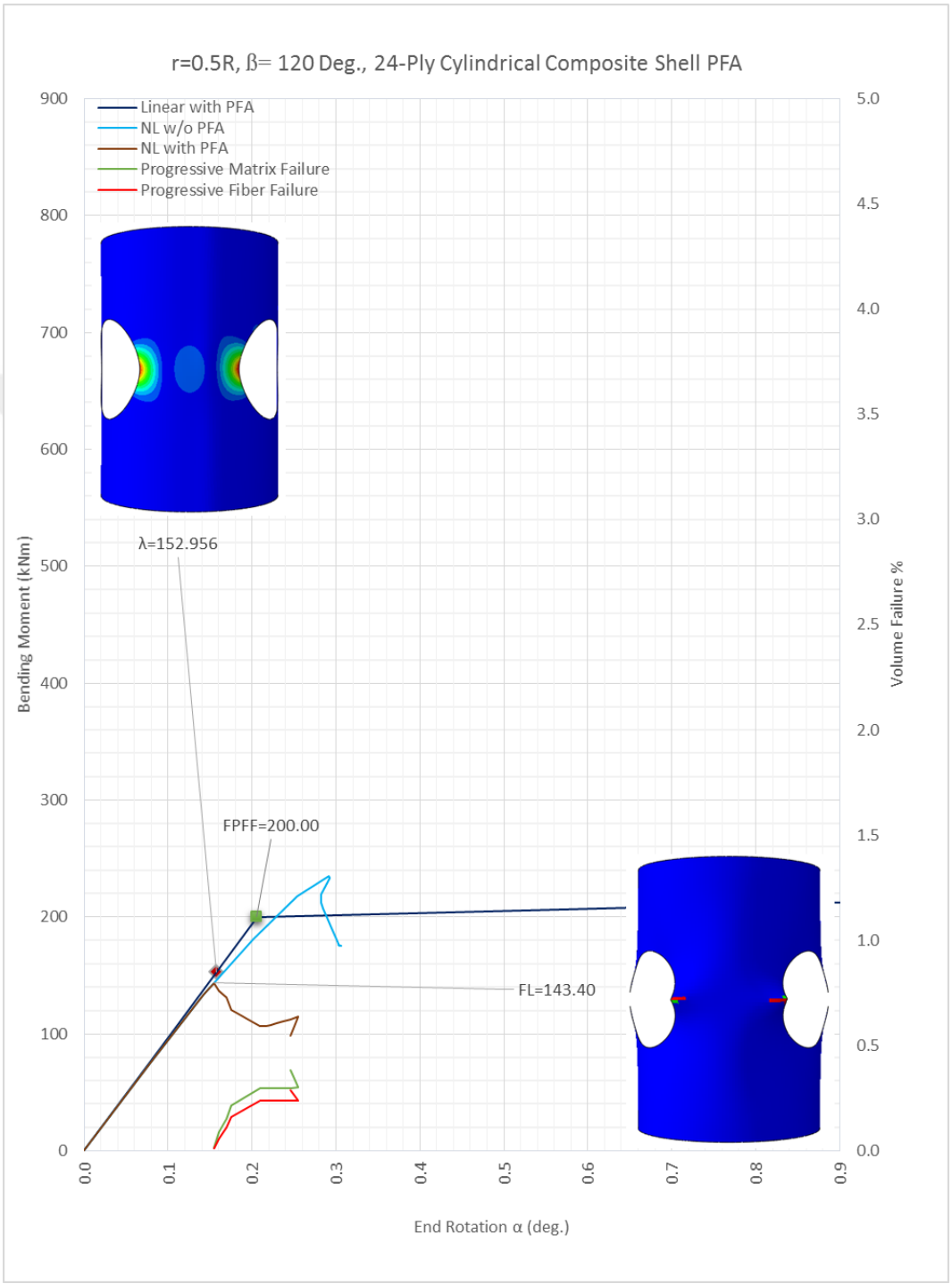


Figure M.7 : 0.5R/120 analysis result.

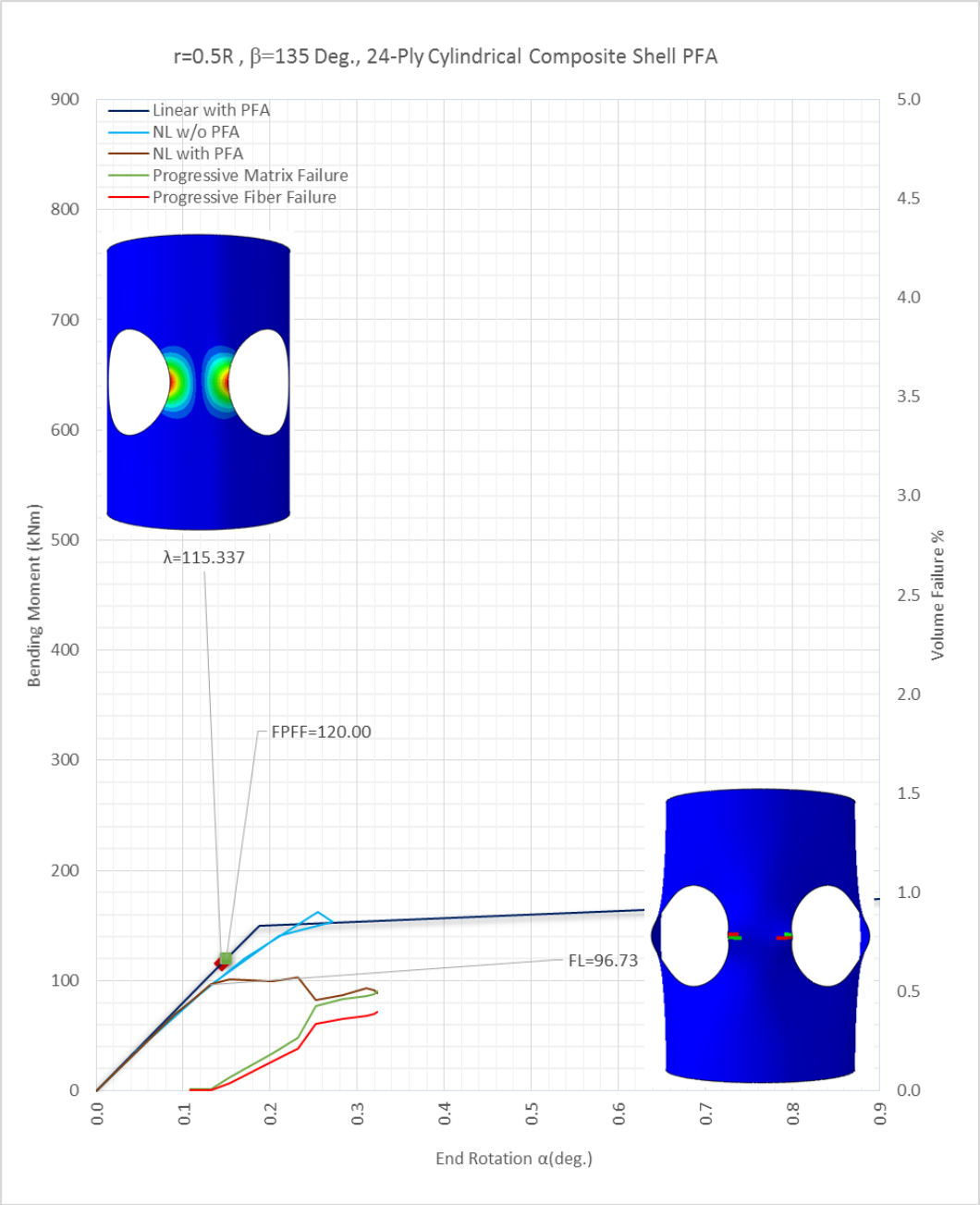


Figure M.8 : 0.5R/135 analysis result.

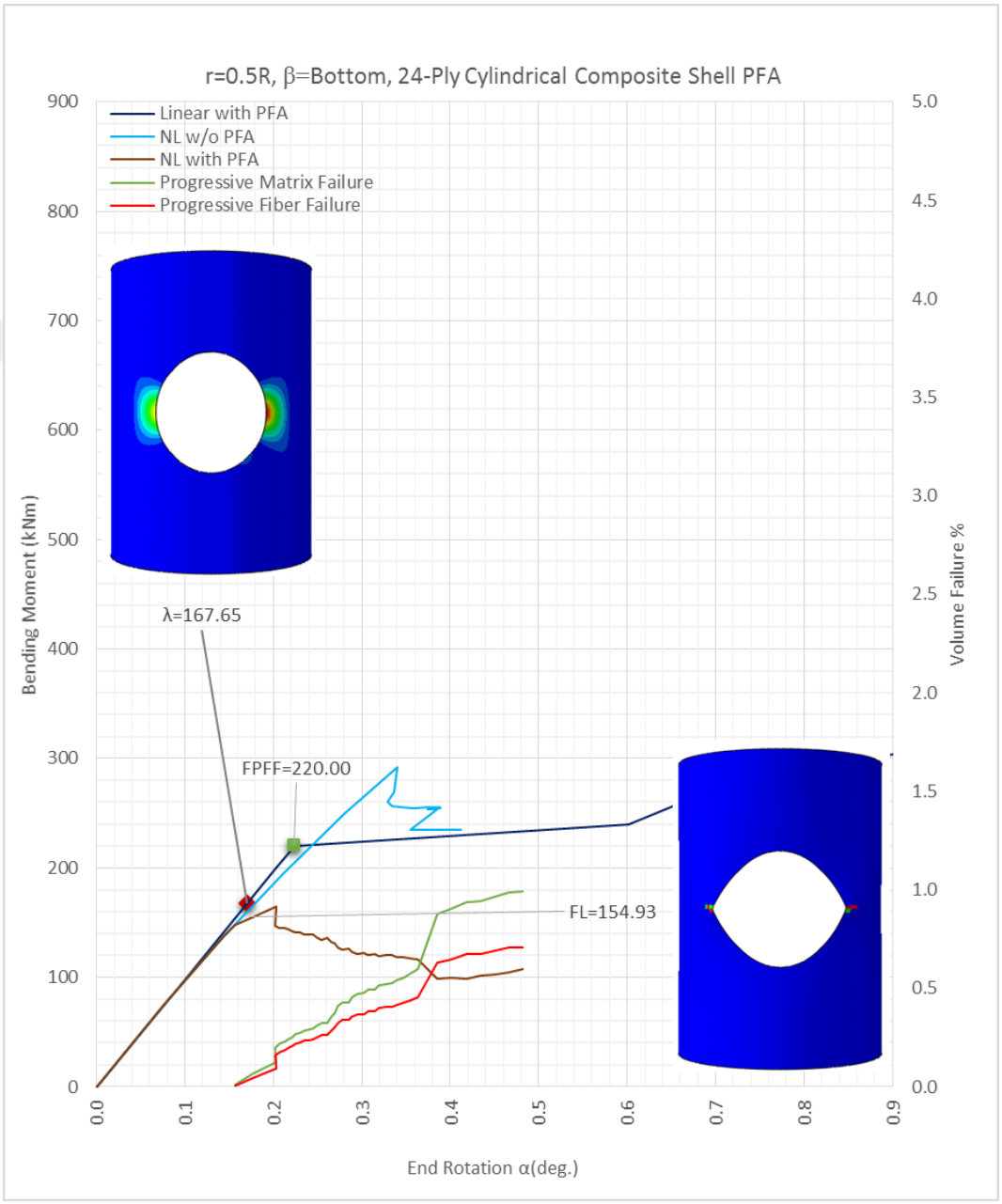


Figure M.9 : 0.5R/180 analysis result.

APPENDIX N: Drawing for Machining of Planned Cutout Configurations

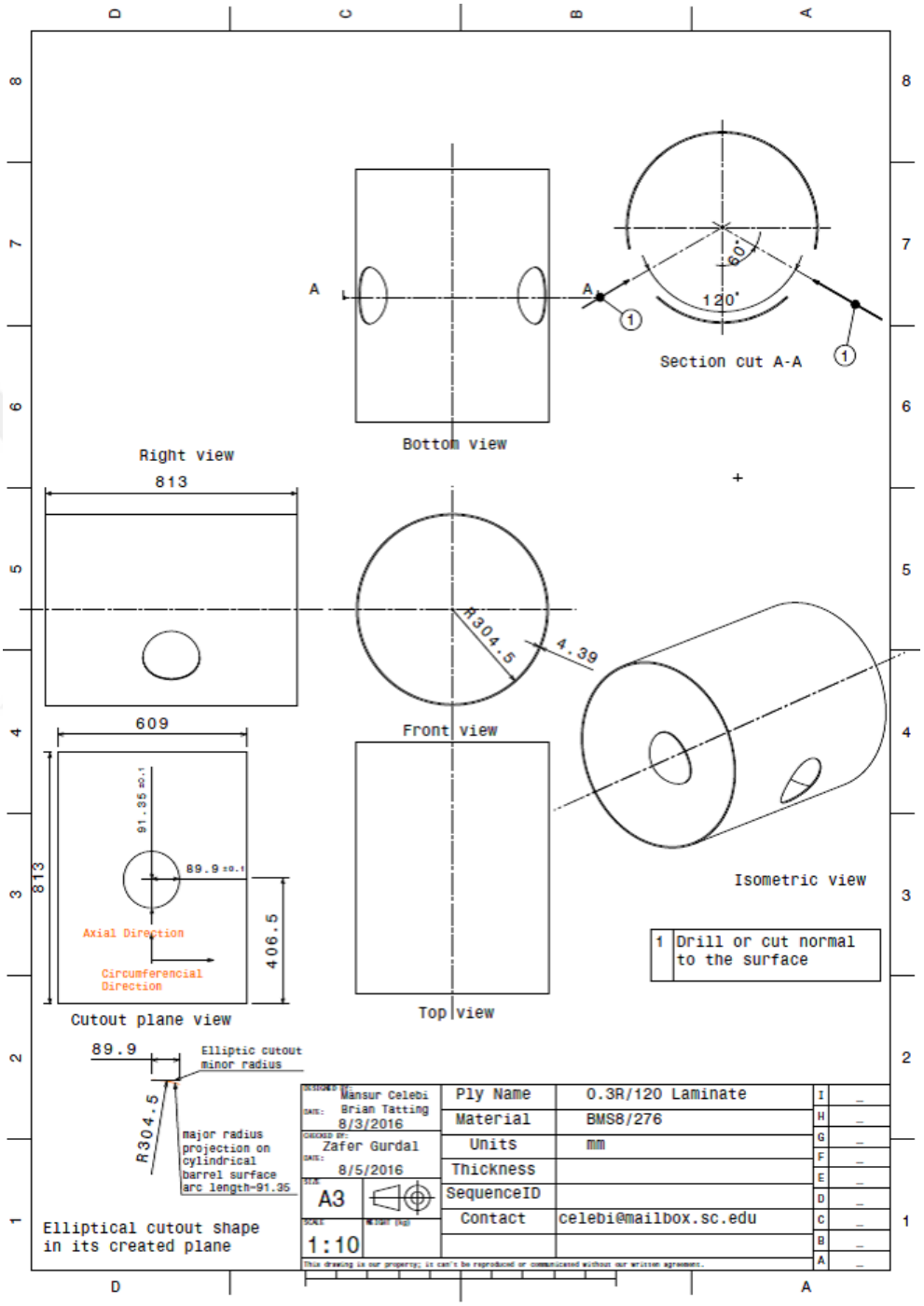


Figure N.1 : Planned cutout configurations and machining dimensions.



CURRICULUM VITAE

Name Surname: Mansur ÇELEBİ

Place and Date of Birth: Muş / 21.01.1976

E-Mail: mansurcelebi@sabanciuniv.edu

EDUCATION:

- **B.Sc.:** 1998, Middle East Technical University, Faculty of Engineering, Aeronautical Engineering Department
- **M.Sc.:** 2004, Anadolu University, Faculty of Engineering, Computer Engineering Department

PROFESSIONAL EXPERIENCE AND REWARDS:

- 1998 Aircraft Structural Engineer, 1st Air Supply and Maintenance Center, Eskişehir, Turkey
- 1999 Structural Life Extension Program Training, Israeli Aircraft Industry, Israel
- 2004 Head of Structural Engineering Branch of Technical Management, 1st Air Supply and Maintenance Center, Eskişehir, Turkey
- 2006 Aircraft Structural Integrity Program, Structural Analysis Training, Lockheed Martin Company, Fortworth, TX, USA
- 2009 System Engineering and Airworthiness Training, Lockheed Martin Company, Fortworth, TX, USA
- 2009 Instructor, Turkish Air Force Academy, Istanbul, Turkey
- 2011 CanSAT Leadership Training, Wakayama University, Wakayama, Japan
- 2011 Turkish Armed Forces Science Prize
- 2011 Coordinator, Turkish Union of Space Technologies and Education
- 2011-2013 Deputy Director of Education, Aeronautics and Space Technologies Institute, Istanbul, Turkey
- 2013 International “Future Flight Design” Competition First Prize
- 2013 CubeSAT Technology and Applications Training, von Karman Instituut voor Stromingsdynamica, Brussel, Belgium

- 2013 Head of Space Sciences, Aeronautics and Space Technologies Institute, Istanbul, Turkey
- 2015-2017 Research Scholar, McNAIR Center for Aerospace and Innovation, University of South Carolina, Columbia, SC, USA

PUBLICATIONS, PRESENTATIONS AND PATENTS ON THE THESIS:

- Mansur Celebi, Halit S. Turkmen. "Mechanical Behavior of a Tubular Composite Structure Under the Effects of a Combined Loading", 4th International Conference on INTEGRITY, RELIABILITY & FAILURE, Pg.289, 23-27 June 2013, Funchal, Portugal
- Mansur Celebi, Zafer Gürdal, Brian Tatting, Agnes Blom-Schieber, Mostafa Rassaian, Steven P. Wanthal. "Effects of Size and Location of a Circular Cutout on Buckling and Failure of a Cylindrical Shell in Bending", 58th AIAA/ASCE/AHS/ASC Structures, Structural Dynamics and Materials Conference, AIAA SciTech 2017, January 9-13, 2017, Grapevine Texas, USA
- Mansur Celebi, Zafer Gürdal,Halit S. Türkmen "Buckling Analysis of CFRP Composite Cylindrical Shell with Cutouts in Bending", Journal of Aeronautics and Space Technologies, accepted in April 26, 2017.

OTHER PUBLICATIONS, PRESENTATIONS AND PATENTS:

- H. Çakır, E. Özbek, M.B. Özbilgin, M. Bent, S. Akgül, M. Çelebi, Z. Kazancı, A. Hacıoğlu, "Design Process of Cevheri-3", International Unmanned Vehicles Workshop-UVW2010, İstanbul, Turkey
- S. Metin, A. Başar, S. Gökalp, S. Korkusuz, S. Akgül, M. Çelebi, Z. Kazancı, A. Hacıoğlu, "Design Process of Anatolian Eagle", International Unmanned Vehicles Workshop-UVW2010, İstanbul, Turkey
- Aydemir M.E., Celebi M, , Ay S, Vivas E.V., Bustinza F.C., Phan D., "Design and Implementation of a Rover-Back CANSAT", RAST 2011, 5th International Conference on recent Advances in Space Technologies, June 09-11, Istanbul, Turkey
- Mansur Celebi, Mustafa Emre Aydemir, Serdar Ay, Mohammed Khalil Ibrahim Khalil, Lewis Hennedige Jayathu Dimuthu Kumara Fernando, Messaoud Bensaada, Hiroaki Akıyama, Shusaku Yamaura, "Design and Navigation Control of an Advanced Level CANSAT", RAST 2011, 5th International Conference on recent Advances in Space Technologies, June 09-11, Istanbul, Turkey
- Cihan Cabuloglu, Mansur Çelebi, Mustafa Emre Aydemir, Erhan Calıskan, Hüseyin Aykıs, Yasin Karataş, Resul Yapacak, Ömer Agırbas, Şaban Abur, Süleyman Soyer, Halit Türkmen, Serdar Ay, "Mission Analysis and Planning of a CANSAT", 5th International Conference on recent Advances in Space Technologies, June 09-11, Istanbul, Turkey
- M. Celebi, "Mission and Scale Analysis on SHM of UAV's", The 8th International Workshop on Structural Health Monitoring - Stanford University, 12-15 September 2011 Stanford, CA, USA

- M.Çelebi, “Reliability Improvement of Spacecraft by Structural Health Monitoring Using MEMS Devices”, NATO AVT-210 “Risk and Reliability Assessment and Validation for Small Spacecraft” Specialist Meeting, 13-16 May 2013, Karlstad, Sweeden

- A. Rüstem Aslan, Mustafa İlarslan, Mansur Celebi, “Turkish University Consortium for Space Technologies and Education (UTEB)-UNISEC Prospects for Turkey”, 6th International Conference on Recent Advances in Space Technologies, 12-14 June 2013 Istanbul, Turkey

- Emre Aydemir, Erhan Güleç, Mustafa İlarslan, Mansur Çelebi, Ekrem Demirel, Fatih Üstüner, “Antenna radiation pattern measurement using an unmanned aerial vehicle (UAV)”, 2014 XXXIth URSI General Assembly & Scientific Symposium (URSI GASS), p1-4, 28-30 August 2014, Elazığ, Turkey

- Osman Ergüven Vatandaş, Yılmaz Altuntaş, Mansur Çelebi. "Improvement of forward swept wing optimization in the compressible flow by using a hybrid method", RAST 2015 Proceedings, pp.21-25, 16-19 June 2015, Istanbul, Turkey.

- A.Rüstem ASLAN, Abdurrahman Hacıoglu, Mansur Çelebi, Emrah Kalemci and Ömer Soykasap, “Space Education at UNISEC-TR (UTEB) Universities”, 30th International Symposium on Space Technology and Science, 4-10 July 2015 Kobe, Japan.